Structure-Based Drug Design on Enzymes of the Fatty Acid Biosynthesis Pathway

Strukturbasiertes Wirkstoffdesign an Enzymen der Fettsäurebiosynthese

Doctoral thesis

for a doctoral degree at the Graduate School of Life Sciences,
Julius-Maximilians-Universität Würzburg,
Sections Infection and Immunity / Biomedicine

submitted by

Johannes Schiebel

from Nürnberg

Würzburg 2013

Submitted on: …………………………………………………………..……..

Office stamp

Members of the *Promotionskomitee*:

Chairperson:	**Prof. Dr. Utz Fischer** University of Würzburg
Primary Supervisor:	**Prof. Dr. Caroline Kisker** University of Würzburg
Supervisor (Second):	**Prof. Dr. Christoph Sotriffer** University of Würzburg
Supervisor (Third):	**Prof. Dr. Peter Tonge** Stony Brook University, USA

Date of Public Defence: ……………………………………………………………

Date of Receipt of Certificates: ……………………………………………….

This dissertation is based on the following manuscripts:

1) Schiebel, J.*, Chang, A.*, Lu, H., Baxter, M. V., Tonge, P. J., and Kisker, C. (2012) *Staphylococcus aureus* FabI: Inhibition, Substrate Recognition, and Potential Implications for In Vivo Essentiality. *Structure* **20**, 802-813

2) Chang, A.*, Schiebel, J.*, Yu, W., Bommineni, G. R., Pan, P., Baxter, M. V., Khanna, A., Sotriffer, C. A., Kisker, C., and Tonge, P. J. (2013) Rational Optimization of Drug-Target Residence Time: Insights from Inhibitor Binding to the *Staphylococcus aureus* FabI Enzyme-Product Complex. *Biochemistry* **52**, 4217-4228

3) Schiebel, J.*, Chang, A.*, Shah, S., Lu, Y., Liu, L., Pan, P., Hirschbeck, M. W., Tareilus, M., Eltschkner, S., Cummings, J. E., Knudson, S. E., Bommineni, G. R., Yu, W., Walker, S. G., Slayden, R. A., Sotriffer, C. A., Tonge, P. J., and Kisker, C. (in preparation) Molecular Basis for the Narrow-spectrum Activity of the Clinical Candidate CG400549 and the Rational Design of a Potent Broad-spectrum Pyridone-based FabI Inhibitor.

4) Schiebel, J., Chang, A., Merget, B., Bommineni, G. R., Yu, W., Spagnuolo, L. A., Baxter, M. V., Tareilus, M., Tonge, P. J., Kisker, C., and Sotriffer, C. A. (in preparation) Protons and Hydrides - Wherefrom and Whereto: From a Chemical Binding Pocket Analysis to a Biological Substrate Recognition Process.

5) Schiebel, J., Kapilashrami, K., Fekete, A., Bommineni, G. R., Schaefer, C. M., Mueller, M. J., Tonge, P. J., and Kisker, C. (in preparation) Acyl Channel Opening Reveals How the Condensing Enzyme KasA from *Mycobacterium tuberculosis* Recognizes Mycolic Acid Precursors.

*These authors contributed equally

“Dissertation Based on Several Published Manuscripts“

Statement of individual author contributions and of legal second publication rights

(if required use more than one sheet)

Publication (complete reference): Schiebel, J., Chang, A., Lu, H., Baxter, M. V., Tonge, P. J., and Kisker, C. (2012) *Staphylococcus aureus* FabI: Inhibition, Substrate Recognition, and Potential Implications for In Vivo Essentiality. *Structure* **20**, 802-813

Participated in	**Author Initials,** Responsibility decreasing from left to right				
Study Design	JS, AC, CK, PJT				
Data Collection	JS, AC	HL	MVB		
Data Analysis and Interpretation	JS, AC, CK, PJT	HL	MVB		
Manuscript Writing	JS, AC	CK, PJT			

Explanations (if applicable):

Publication (complete reference): Chang, A., Schiebel, J., Yu, W., Bommineni, G. R., Pan, P., Baxter, M. V., Khanna, A., Sotriffer, C. A., Kisker, C., and Tonge, P. J. (2013) Rational Optimization of Drug-Target Residence Time: Insights from Inhibitor Binding to the *Staphylococcus aureus* FabI Enzyme-Product Complex. *Biochemistry* **52**, 4217-4228

Participated in	**Author Initials,** Responsibility decreasing from left to right				
Study Design	AC, JS, PJT, CK	CAS			
Data Collection	AC, JS	WY	GRB	PP	MVB, AK
Data Analysis and Interpretation	AC, JS, PJT, CK	WY, CAS	GRB	PP	MVB, AK
Manuscript Writing	AC, JS	PJT, CK, CAS	WY	GRB	PP

Explanations (if applicable):

Publication (complete reference): Schiebel, J., Chang, A., Shah, S., Lu, Y., Liu, L., Pan, P., Hirschbeck, M. W., Tareilus, M., Eltschkner, S., Cummings, J. E., Knudson, S. E., Bommineni, G. R., Yu, W., Walker, S. G., Slayden, R. A., Sotriffer, C. A., Tonge, P. J., and Kisker, C. (in preparation) Molecular Basis for the Narrow-spectrum Activity of the Clinical Candidate CG400549 and the Rational Design of a Potent Broad-spectrum Pyridone-based FabI Inhibitor.

Participated in	**Author Initials,** Responsibility decreasing from left to right				
Study Design	JS, AC, PJT, CK	CAS	RAS, SGW		
Data Collection	JS, AC	SS	YL, LL, PP	MWH, MT, SE	JEC,SEK,GRB,WY
Data Analysis and Interpretation	JS, AC, PJT, CK	CAS	SS, YL, LL, PP	MWH, MT, SE	JEC,SEK,GRB,WY
Manuscript Writing	JS, AC	CAS, PJT, CK	SS, YL, LL, PP	MWH, MT, SE	SGW, RAS

Explanations (if applicable):

Publication (complete reference): Schiebel, J., Chang, A., Merget, B., Bommineni, G. R., Yu, W., Spagnuolo, L. A., Baxter, M. V., Tareilus, M., Tonge, P. J., Kisker, C., and Sotriffer, C. A. (in preparation) Protons and Hydrides - Wherefrom and Whereto: From a Chemical Binding Pocket Analysis to a Biological Substrate Recognition Process.

Participated in	**Author Initials,** Responsibility decreasing from left to right				
Study Design	JS, CAS	PJT, CK	AC, BM		
Data Collection	JS	AC	BM	GRB, WY, LAS	MVB, MT
Data Analysis and Interpretation	JS, CAS	AC	BM	GRB, WY, LAS	MVB, MT
Manuscript Writing	JS	AC, CAS	PJT, CK	BM	

Explanations (if applicable):

Publication (complete reference): Schiebel, J., Kapilashrami, K., Fekete, A., Bommineni, G. R., Schaefer, C. M., Mueller, M. J., Tonge, P. J., and Kisker, C. (in preparation) Acyl Channel Opening Reveals How the Condensing Enzyme KasA from *Mycobacterium tuberculosis* Recognizes Mycolic Acid Precursors.					
Participated in	**Author Initials,** Responsibility decreasing from left to right				
Study Design	JS, KK, PJT, CK	GRB	AF, MJM		
Data Collection	JS	KK, AF, GRB	CMS		
Data Analysis and Interpretation	JS, PJT, CK	KK, AF	GRB	CMS	
Manuscript Writing	JS	KK, AF, PJT, CK	GRB, MJM	CMS	

Explanations (if applicable):

I confirm that I have obtained permission from both the publishers and the co-authors for legal second publication.

I also confirm my primary supervisor's acceptance.

Johannes Schiebel	07/24/13	Würzburg	
Doctoral Researcher's Name	Date	Place	Signature

Table of Contents

Table of Contents ...... **i**

Summary ...... **vi**

Zusammenfassung ...... **viii**

1 Introduction **1**

1.1 Antibiotic Resistance *1*
- 1.1.1 Clinically Relevant Classes of Antibacterial Drugs 1
- 1.1.2 Resistance Mechanisms 1
- 1.1.3 Methicillin-resistant *Staphylococcus aureus* (MRSA) 2
- 1.1.4 Tuberculosis 3

1.2 Antibacterial Drug Discovery *3*
- 1.2.1 History of Antibacterial Discovery 3
- 1.2.2 Challenges of Antibacterial Discovery 3
- 1.2.3 New Concepts and Strategies of Antibacterial Drug Development 4
- 1.2.4 Importance of Drug-Target Kinetics 5

1.3 Bacterial Fatty Acid Biosynthesis as a Drug Target *6*
- 1.3.1 Fatty Acid Biosynthesis 6
- 1.3.2 The Acyl Carrier Protein 8
- 1.3.3 Diversity in the Fatty Acid Synthesis Pathway 9
- 1.3.4 Essentiality of the Bacterial Fatty Acid Biosynthesis 10
- 1.3.5 Mycolic Acid Synthesis in Mycobacteria 10

1.4 Targeting Key Steps of the FAS-II Pathway *11*
- 1.4.1 The Enoyl-ACP Reductase FabI of *S. aureus* and other Bacteria 11
- 1.4.2 FabI Inhibition 13
- 1.4.3 *M. tuberculosis* KasA 16
- 1.4.4 Inhibition of the FAS-II Condensing Enzymes 17

1.5 Research Objective *18*
- 1.5.1 General Questions Concerning the FAS-II Pathway 18
- 1.5.2 Questions Concerning SaFabI, KasA and their Natural Substrates 18
- 1.5.3 Questions Concerning the Inhibition of SaFabI and KasA 19

2 *Staphylococcus aureus* FabI: Inhibition, Substrate Recognition, and Potential Implications for In Vivo Essentiality **20**

2.1 Summary *22*

2.2 Highlights *22*

2.3 Introduction *22*

2.4 Results *24*
- 2.4.1 Overall Structure 24
- 2.4.2 SaFabI Inhibition 25
- 2.4.3 Induced Fit Ligand Binding 26
- 2.4.4 Dimer - Tetramer Transition 28
- 2.4.5 Cooperativity 29
- 2.4.6 Cofactor Specificity 30
- 2.4.7 Branched-Chain Substrate Specificity 32

2.5 Discussion 32

2.6 Experimental Procedures 34
  2.6.1 Cloning, Expression and Purification 34
  2.6.2 Site-directed Mutagenesis, Expression and Purification of SaFabI Mutants 34
  2.6.3 Crystallization, Data Collection and Structure Determination 34
  2.6.4 Analytical Size Exclusion Chromatography 35
  2.6.5 Synthesis of trans-2-enoyl-CoA Substrates 35
  2.6.6 Steady-state Kinetic Assays 35
  2.6.7 Inhibition Kinetics 35

2.7 Accession Numbers 36

2.8 Acknowledgements 36

2.9 Supplemental Information 36
  2.9.1 Supplemental Data 36
  2.9.2 Supplemental Results 42
    2.9.2.1 Inhibition Kinetics 42
    2.9.2.2 Reduction of Straight-chain Substrates by SaFabI 42
    2.9.2.3 Substrate Specificity of SaFabI 42
  2.9.3 Supplemental Discussion 43
    2.9.3.1 Glutamate Sensitivity 43
  2.9.4 Supplemental Experimental Procedures 43
    2.9.4.1 Cloning 43
    2.9.4.2 Expression and Purification 44
    2.9.4.3 Crystallization, Data Collection and Structure Determination 44
    2.9.4.4 Steady-state Kinetic Assays 45
    2.9.4.5 Inhibition Kinetics 46

3 Rational Optimization of Drug-Target Residence Time: Insights from Inhibitor Binding to the *Staphylococcus aureus* FabI Enzyme-Product Complex 48

3.1 Keywords 50

3.2 Abstract 50

3.3 Introduction 50

3.4 Experimental Procedures 51

3.5 Results 54

3.6 Discussion 64

3.7 Associated Content 66

3.8 Author Information 66

3.9 Acknowledgments 67

3.10 Abbreviations 67

3.11 Supporting Information 68

4 Molecular Basis for the Narrow-spectrum Activity of the Clinical Candidate CG400549 and the Rational Design of a Potent Broad-spectrum Pyridone-based FabI Inhibitor. 74

4.1 Keywords 76

4.2 Capsule 76

4.3 Summary 76

4.4 Introduction 76

4.5 Experimental Procedures ... 78
4.5.1 Compound synthesis ... 78
4.5.2 Expression and Purification ... 78
4.5.3 Crystallization ... 78
4.5.4 Data Collection and Structure Determination ... 79
4.5.5 Inhibition Kinetics ... 80
4.5.6 Thermal Shift Assay ... 81
4.5.7 Docking Studies ... 81
4.5.8 Determination of MIC Values ... 81
4.5.9 *In vivo* Pharmacokinetics ... 81
4.5.10 *In vivo* Efficacy ... 82

4.6 Results ... 82

4.7 Discussion ... 96

4.8 Acknowledgements ... 99

4.9 Footnotes ... 100

4.10 Supplementary Information ... 101
4.10.1 Supplemental Tables ... 101
4.10.2 Supplemental Figures ... 104

5 Protons and Hydrides - Wherefrom and Whereto: From a Chemical Binding Pocket Analysis to a Biological Substrate Recognition Process ... 105

5.1 Abstract ... 107

5.2 Introduction ... 107

5.3 Results and Discussion ... 110
5.3.1 Analysis of the SaFabI Binding Pocket Characteristics ... 110
5.3.2 Putative Substrate Binding Modes ... 113
5.3.3 Hydride Transfer and Proton Delivery ... 114
5.3.4 Protein Fluctuations Relevant for Substrate Recognition ... 118
5.3.5 Location and Binding Process of ACP-substrates ... 119
5.3.6 Concluding Remarks ... 121

5.4 Methods ... 121
5.4.1 Crystallization, Data Collection and Structure Determination ... 121
5.4.2 Site-Directed Mutagenesis, Expression and Purification of SaFabI Variants ... 122
5.4.3 Steady-State Kinetics ... 122
5.4.4 Inhibition Kinetics ... 122
5.4.5 Thermal Shift Assay ... 122
5.4.6 Circular Dichroism ... 122
5.4.7 Molecular Dynamics Simulations ... 123
5.4.8 Computational Docking ... 124

5.5 Associated Content ... 124
5.5.1 Supporting Information ... 124

5.6 Author Information ... 124
5.6.1 Corresponding Author ... 124
5.6.2 Notes ... 124

5.7 Acknowledgments ... 124

5.8 Supplementary Information ... 125
5.8.1 Supplemental Tables ... 125
5.8.2 Supplemental Figures ... 129

5.8.3 Supplemental Movies 135
5.8.4 Supplemental Results and Discussion 136
5.8.4.1 Inhibition of SaFabI 136
5.8.4.2 Molecular Dynamics Simulations 136
5.8.4.3 Cofactor Binding Process 137
5.8.4.4 Substrate Recognition 138

6 Acyl Channel Opening Reveals How the Condensing Enzyme KasA from *Mycobacterium tuberculosis* Recognizes Mycolic Acid Precursors 139

6.1 Keywords 141

6.2 Capsule 141

6.3 Summary 141

6.4 Introduction 141

6.5 Experimental Procedures 143
6.5.1 Expression and Purification 143
6.5.2 Crystallization and Data Collection 143
6.5.3 Structure Determination 144
6.5.4 Lipidomics 144
6.5.5 Synthesis of 3-Substituted TLM-Derivatives 144
6.5.6 Inhibition Kinetics 144

6.6 Results 145
6.6.1 KasA Inhibition by 3-Substituted TLM-Derivatives 145
6.6.2 Identification of a Phospholipid Bound to KasA 147
6.6.3 Location of the KasA Substrate Binding Sites 148
6.6.4 Structural Explanation for the KasA Substrate Preferences 150
6.6.5 Acyl-Channel Opening Mechanism 151

6.7 Discussion 154

6.8 Acknowledgements 157

6.9 Footnotes 158

6.10 Supplementary Information 159
6.10.1 Supplemental Tables 159
6.10.2 Supplemental Figures 163
6.10.3 Supplemental Movies 165
6.10.4 Supplemental Experimental Procedures 166
6.10.4.1 Lipidomics 166

7 Discussion 167

7.1 S. aureus FabI 167
7.1.1 Substrate, Cofactor and Inhibitor Recognition 167
7.1.2 Molecular Determinants of Affinity and Selectivity 169
7.1.3 Rational Residence Time Optimization - a Case Study with SaFabI 171
7.1.4 New Concepts for Inhibitor Design 172

7.2 M. tuberculosis KasA 173
7.2.1 Substrate and Inhibitor Recognition 173
7.2.2 New Concepts for Inhibitor Design 174

7.3 Interaction between ACP and FAS-II Enzymes 175

8 References I

9 Appendix XIX

9.1 Abbreviations XIX

9.2 Supplementary Materials and Methods XXIII

9.2.1 Expression and Purification of Crotonyl-saACP XXIII

9.2.2 Expression and Purification of Acetoacetyl-AcpM XXVI

9.3 DNA and Protein Sequences XXIX

9.3.1 SaFabI XXIX

9.3.2 SaACP XXX

9.3.3 EcFabI XXXI

9.3.4 KasA XXXI

9.3.5 AcpM XXXII

10 Acknowledgements XXXIII

11 Curriculum Vitae XXXIV

12 List of Publications XXXVI

13 Affidavit XXXVII

14 Eidesstattliche Erklärung XXXVII

Summary

The rise of antibiotic-resistant pathogens such as methicillin-resistant *Staphylococcus aureus* (MRSA) strains and drug-resistant forms of *Mycobacterium tuberculosis* is one of the major problems modern medicine faces and constitutes a severe threat to human health. The successful treatment of infections caused by drug-resistant bacteria now and in the future, requires the urgent development of novel antibacterials.

Whereas most currently used antibiotics act by interfering with essential bacterial processes, a smaller group of antibacterials disturbs the integrity of the cell membrane. Since fatty acids are a vital component of membrane phospholipids, the type-II fatty acid biosynthesis pathway (FAS-II) of bacteria constitutes a promising drug target. The front-line anti-tuberculosis prodrug isoniazid blocks the FAS-II pathway in *M. tuberculosis* thereby leading to morphological changes and finally to cell lysis. When it became evident that the enoyl-ACP reductase in the FAS-II pathway is the target of the activated isoniazid, several programs were initiated to develop novel inhibitors directed against this protein in different pathogens.

The *S. aureus* enoyl-ACP reductase (saFabI) is of particular interest since three promising drug candidates inhibiting this homologue have reached clinical trials. However, despite these prospects, no crystal structures of saFabI were publicly available at the time the present work was initiated. Thus, one major goal of this thesis was the generation of high-resolution atomic models by means of X-ray crystallography. The development of a highly reproducible approach to co-crystallize saFabI in complex with $NADP^+$ and diphenyl ether-based inhibitors led to crystal structures of 17 different ternary complexes. Additional crystallographic experiments permitted the view into two apo-structures and two atomic models of saFabI in complex with NADPH and 2-pyridone inhibitors. Based on the established saFabI structure, molecular dynamics (MD) simulations were performed to improve our understanding of the conformational mobility of this protein. Taken together, these investigations of the saFabI structure and its flexibility served as an ideal platform to address important questions surrounding substrate and inhibitor recognition by this enzyme. Intriguingly, our saFabI structures provide several vastly different snapshots along the reaction coordinate of ligand binding and hydride transfer, including the closure of the flexible substrate binding loop (SBL). The extraordinary mobility of saFabI was confirmed by MD simulations suggesting that conformational motions indeed play a pivotal role during substrate delivery and turnover. A water chain linking the active site with a water-basin inside the homo-tetrameric enzyme was found likely to be crucial for the closure and opening of the SBL and, thus, for the catalyzed reaction. Notably, the induced-fit ligand binding process involves a dimer-tetramer transition, which could be related to the observed positive cooperativity of cofactor and substrate binding. Overall, saFabI displays several unique characteristics compared to FabI proteins from other organisms that might be necessary for the synthesis of branched-chain fatty acids, which in turn are required for *S. aureus* fitness *in vivo*. This finding may explain why *S. aureus* is sensitive to FAS-II inhibitors even in the presence of exogenous fatty acids. Accordingly, saFabI remains a valid drug target and our structures can be used as a molecular basis for rational drug design efforts. In fact, binding affinity trends of diphenyl ether inhibitors and, more importantly, the correlated residence times could be rationalized at the molecular level. Furthermore, the structure of saFabI in complex with the 2-pyridone inhibitor CG400549 revealed unique interactions in the wider binding crevice of saFabI compared to other FabI homologues explaining the narrow activity spectrum of this clinical candidate with proven human efficacy. In summary, these studies provide an ideal platform for the development of new, effective saFabI inhibitors as exemplified by the promising 4-pyridone PT166.

In the context of this dissertation, crystal structures of the condensing enzyme KasA in complex with several analogs of the naturally occurring inhibitor thiolactomycin have been solved. KasA is an essential enzyme involved in the FAS-II system of *M. tuberculosis*, which is capable of producing very long fatty acid chains. The solved structures help to clarify the mechanism of the catalyzed reaction and, importantly, reveal successive snapshots of an induced-fit binding mechanism enabling the uptake of the long and hydrophobic acyl-substrate. Intriguingly, a phospholipid molecule was found to be trapped inside the acyl-binding channel, thus permitting the observation which conformational changes in the capping region of the protein are necessary to enable binding of the acyl-chain.

The different conformational states observed in this study for the two FAS-II enzymes saFabI and KasA likely represent intermediate structures of the proceeding enzymatic reactions and, thus, provide ideal starting points for the rational optimization and design of small molecules that are active against *S. aureus* and *M. tuberculosis* infections.

Zusammenfassung

Die Zunahme Antibiotika-resistenter pathogener Erreger stellt eines der größten Probleme der modernen Medizin dar. Eine besondere Gefährdung für die Gesundheit der Bevölkerung sind methicillin-resistente *Staphylococcus aureus* (MRSA) und Antibiotika-resistente *Mycobacterium tuberculosis* Bakterien. Um die Behandlung von Infektionen, die von diesen Bakterien verursacht werden, auch in Zukunft gewährleisten zu können, werden dringend neue antibakteriell wirksame Substanzen benötigt.

Während die Wirkung der meisten gebräuchlichen Antibiotika auf einer Beeinträchtigung wichtiger bakterieller Prozesse beruht, wirken manche Substanzen durch die Störung der Zellmembran-Struktur. Da Fettsäuren ein essentieller Bestandteil von Membran-Phospholipiden sind, stellt die bakterielle Fettsäurebiosynthese II (FAS-II) einen relativ wenig erforschten, aber dennoch vielversprechenden Angriffspunkt für die Entwicklung neuer Antibiotika dar. Das wichtige Antituberkulotikum Isoniazid blockiert die mykobakterielle Fettsäurebiosynthese und ruft dadurch morphologische Änderungen sowie letztlich die Lyse des Bakteriums hervor. Eine wichtige Erkenntnis war, dass Isoniazid den letzten Schritt des FAS-II Elongationszyklus inhibiert, der durch die Enoyl-ACP Reduktase katalysiert wird. Darauf aufbauend wurden mehrere Programme ins Leben gerufen, die sich zum Ziel gesetzt hatten, neue Moleküle zu entwickeln, welche dieses Protein verschiedener Pathogene hemmen.

Die *S. aureus* Enoyl-ACP Reduktase (saFabI) ist von besonders großem Interesse, da drei vielversprechende Inhibitoren dieses Proteins entwickelt werden konnten, die momentan in klinischen Studien eingehend untersucht werden. Trotz dieser Erfolgsaussichten waren zum Zeitpunkt, als die vorliegenden Arbeiten aufgenommen wurden, keine Kristallstrukturen von saFabI öffentlich verfügbar. Daher war es eines der Hauptziele dieser Doktorarbeit, auf der Basis von kristallographischen Experimenten atomar aufgelöste Modelle für dieses wichtige Protein zu erzeugen. Durch die Entwicklung einer verlässlichen Methode zur Kristallisation von saFabI im Komplex mit $NADP^+$ und Diphenylether-Inhibitoren konnten Kristallstrukturen von 17 verschiedenen ternären Komplexen gelöst werden. Weitere kristallographische Experimente ergaben zwei apo-Strukturen sowie zwei Strukturen von saFabI im Komplex mit NADPH und 2-Pyridon-Inhibitoren. Basierend auf der nun bekannten saFabI-Struktur konnten Molekulardynamik-Simulationen durchgeführt werden, um zusätzliche Erkenntnisse über die Flexibilität dieses Proteins zu erhalten. Die so gewonnenen Informationen über die Struktur und Beweglichkeit des Enzyms dienten in Folge als ideale Grundlage dafür, den Erkennungsprozess von Substrat und Inhibitor zu verstehen. Besonders bemerkenswert dabei ist, dass die verschiedenen saFabI Kristallstrukturen Momentaufnahmen entlang der Reaktionskoordinate der Ligandenbindung und des Hydrid-Transfers repräsentieren. Dabei verschließt der so genannte Substratbindungsloop das aktive Zentrum des Enzyms allmählich. Die außergewöhnlich hohe Mobilität von saFabI konnte durch molekulardynamische Simulationen bestätigt werden. Dies legt nahe, dass die beobachteten Änderungen der Konformation tatsächlich an der Aufnahme und Umsetzung des Substrates beteiligt sind. Eine Kette von Wassermolekülen zwischen dem aktiven Zentrum und einer wassergefüllten Kavität im Inneren des Tetramers scheint für die Beweglichkeit des Substratbindungsloops und somit für die katalysierte Reaktion von entscheidender Bedeutung zu sein. Außerdem wurde die erstaunliche Beobachtung gemacht, dass der

adaptive Substratbindungsprozess mit einem Dimer-Tetramer Übergang gekoppelt ist, welcher die beobachtete positive Kooperativität der Ligandenbindung erklären kann. Alles in allem weist saFabI im Vergleich zu FabI Proteinen aus anderen Organismen mehrere außergewöhnliche Eigenschaften auf, die für die Synthese von verzweigten Fettsäuren nötig sein könnten, welche wiederum für die Überlebensfähigkeit von *S. aureus* im Wirt von Bedeutung sind. Diese Erkenntnis könnte erklären, warum *S. aureus* selbst bei Anwesenheit von exogenen Fettsäuren von FAS-II Inhibitoren abgetötet werden kann. Somit können die gewonnenen atomaren saFabI Modelle einen entscheidenden Beitrag zur Entwicklung neuer Hemmstoffe dieses validierten Angriffszieles leisten. Tatsächlich konnten die neuen Strukturen genutzt werden, um die Bindungsstärken sowie die Verweilzeiten verschiedener saFabI Inhibitoren molekular zu erklären. Die Struktur von saFabI im Komplex mit dem 2-Pyridon Inhibitor CG400549 hingegen enthüllte spezifische Wechselwirkungen in der geweiteten Bindetasche des *S. aureus* Enzyms, welche das geringe Aktivitätsspektrum dieses derzeit klinisch erprobten Inhibitors erklären. Diese Studien schaffen somit eine ideale Voraussetzung für die Entwicklung neuer wirksamer saFabI Inhibitoren, was am Beispiel des 4-Pyridons PT166 belegt werden kann.

Im Rahmen der vorliegenden Dissertation konnten außerdem die Strukturen des Enzyms KasA im Komplex mit mehreren Derivaten des Naturstoffs Thiolactomycin gelöst werden. Dieses Protein ist ein essentielles, an der Fettsäurebiosynthese von *M. tuberculosis* beteiligtes Enzym, welches in der Lage ist, sehr lange Fettsäuren zu produzieren. Die gelösten Strukturen leisten einen entscheidenden Beitrag dazu, den Mechanismus der katalysierten Reaktion zu verstehen. Gleichzeitig legen sie einen adaptiven Bindungsprozess des langen hydrophoben Acyl-Substrates nahe. Ein Phospholipid-Molekül bindet dabei innerhalb des langen Acyl-Kanals und ermöglicht somit die Beobachtung der Konformationsänderungen des Proteins, die für die Bindung der Acyl-Kette nötig sind.

Die verschiedenen Zustände, die in dieser Studie für die beiden FAS-II Enzyme saFabI und KasA beobachtet wurden, repräsentieren aller Wahrscheinlichkeit nach während der enzymatischen Reaktion auftretende Strukturen und bilden somit eine gute Grundlage für das rationale Design neuartiger Wirkstoffe gegen *S. aureus* und *M. tuberculosis* Infektionen.

1 Introduction

1.1 Antibiotic Resistance

1.1.1 Clinically Relevant Classes of Antibacterial Drugs

The treatment of infectious diseases becomes increasingly difficult due to the development of antibiotic resistances (20). Alarmingly, resistances have been reported for all clinically relevant antibacterials (1). The antibiotics currently in use block a limited number of essential biological processes to harm the pathogenic bacterium which is the underlying cause for certain human infections (1). Most antibacterial drugs interfere with ribosomal protein biosynthesis, DNA replication and transcription, nucleotide biosynthesis and cell wall synthesis or disturb the integrity of the cell membrane (Table 1-1) (1-4).

Table 1-1. Antibiotic classes and their targets (1-4).

Cellular target	Antibiotic classes
ribosomal protein biosynthesis	macrolides, tetracyclines, aminoglycosides, streptogramins, oxazolidinones, chloramphenicol, lincosamides
cell wall biosynthesis	β-lactams (penicillins, cephalosporins, carbapenems, monobactams), glycopeptides, fosfomycin
DNA replication and transcription	quinolones, rifamycins
nucleotide biosynthesis	sulfonamides
cell membrane integrity	lipopeptides, polymyxins

Interestingly, most antibiotics (70%) were derived from natural products and only some classes are completely synthetic in origin (e.g. oxazolidinones, fluoroquinolones) (2,20). Thus, new antibacterial chemical scaffolds with novel mechanisms of action are required to combat the increasing threat of antibiotic-resistant pathogens (20).

1.1.2 Resistance Mechanisms

Understanding the underlying principles of antibiotic resistance is key to prevent its initial occurrence or to specifically target the resistance mechanism (21). The bacterial cell envelope constitutes a physical barrier that hinders the penetration of several xenobiotics into the cell. In particular, Gram-negative bacteria are intrinsically resistant to many antibiotics due to an additional membrane layer outside of the peptidoglycan layer (21). In addition to a reduced influx, an enhanced efflux of the antibacterial agent can lead to resistance (21). Due to the reduced uptake of the antibiotic and its export via efflux pumps, it is particularly difficult to develop novel effective antibiotics to treat infections caused by multidrug-resistant Gram-negative pathogens such as *Pseudomonas aeruginosa*, *Acinetobacter baumannii*, *Klebsiella pneumoniae* and *Escherichia coli* (20). Similarly, *Mycobacterium tuberculosis* - the causative agent of tuberculosis (TB) - is intrinsically resistant to most commonly used antibiotics due to its lipid-rich waxy cell wall (for further details see also chapters 1.1.4 and 1.3.5) (22-24).

Although import of antibiotics is more easily achieved for Gram-positive bacteria, diverse other resistance mechanisms are known which render pathogens such as *Staphylococcus aureus* a major threat to human health (see also chapter 1.1.3) (20). Antibiotics can be inactivated by specific enzymes which modify the antibacterial agent. For instance, β-lactamases hydrolyze the 4-membered ring of β-lactam antibiotics (21,25). The associated resistance genes presumably developed already two billion years ago, which explains the almost instantaneous occurrence of resistance in *S. aureus* after the introduction of penicillin to the market (4,21). In contrast, the formation of resistance against vancomycin was believed to be highly unlikely since this glycopeptide antibiotic acts outside the cell via its interaction with lipid II (21,26). However, after 33 years of clinical vancomycin usage, first resistant *Enterococcus* strains (VRE) were reported in 1988 (4,27). This resistance is based on the modification of the entire peptidoglycan biosynthesis pathway, which finally results in the production of lipid II molecules containing a C-terminal D-lactate or D-serine instead of D-alanine, which in turn leads to a 1,000-fold reduction in affinity towards vancomycin (21,26). In most cases less complex mechanisms are operative in order to modify the cellular target of an antibiotic. For instance, overexpression as well as single or multiple mutations of a target protein can cause resistance to an antibacterial agent (21,28).

1.1.3 Methicillin-resistant *Staphylococcus aureus* (MRSA)

The Gram-positive bacterium *Staphylococcus aureus* readily acquires resistance genes and, thus, methicillin-resistant *Staphylococcus aureus* (MRSA) strains have been reported already two years after the market launch of this β-lactam antibiotic (29). Unfortunately, MRSA strains are often additionally insensitive to other β-lactam antibiotics, aminoglycosides, tetracyclines, macrolides, lincosamides and/or fluoroquinolones, which complicates the treatment of infections caused by these strains (29). Today, MRSA constitutes a major clinical problem all over the world - methicillin-resistance rates were 70%, 64% and 24% for *S. aureus* isolates from hospitals in Korea (1998), the USA (2003) and Australia/New Zealand (2008), respectively (30-32). In Europe, resistance rates vary between 0 and 50% (2007) with the maximal occurrence in the southern countries (29).

S. aureus colonizes approximately 50% of all adults and can mainly be found in the anterior nares (29). This bacterium can cause manifold diseases such as skin infections, nosocomial pneumonia or severe bloodstream infections (29). The risk to acquire a *S. aureus* infection is increased in elderly, immuno-compromised patients (32,33). According to a study performed in Australia and New Zealand, the mortality rate of *S. aureus* infections ranges from 2.5 to 40% depending on the group of people (32). In the case of MRSA infections, the mortality rates are increased compared to infections caused by methicillin-sensitive *S. aureus* (MSSA) (29). Hence, MRSA infections cause approximately 19,000 deaths annually in the USA (20,34). Serious MRSA infections can be treated with the "antibiotic of the last resort" vancomycin. However, the initial emergence of vancomycin-resistant *S. aureus* strains (VRSA), which likely arose via a horizontal gene transfer from VRE to MRSA in co-infected patients, will further aggravate the treatment of such infections in the future (29,33).

In recent years, the epidemiology of MRSA changed and the related infections are not limited to hospitals anymore (29). Community-acquired MRSA (CA-MRSA) can cause diseases in otherwise healthy persons which account for approximately 1,400 deaths per year in the USA (29,34). In addition, animals were identified as a reservoir for the zoonotic MRSA strain

ST398 which has the ability to cause re-infections in humans (29,34). In the Netherlands, a country with otherwise low MRSA proportions, over 30% of all pigs at the slaughterhouse were found to be colonized by this *S. aureus* strain (29). In the light of these developments it will be critical to discover new antibiotics to ensure an effective treatment of *S. aureus* infections in the future.

1.1.4 Tuberculosis

At the beginning of the 20th century, 12 % of all deaths were caused by tuberculosis (TB) (35). After the "golden era" of antibacterial discovery between 1945 and 1960 it was believed that this disease might soon be eradicated (see also chapter 1.2.1) (36). However, in 2011 the WHO estimated an annual rate of 8.7 million new infections and 1.4 million TB-related deaths (37). Over time, *M. tuberculosis*, the pathogen inducing this disease, developed resistances against several anti-mycobacterial drugs. Infections caused by multidrug-resistant *M. tuberculosis* (MDR-TB), which are insensitive to the most important first-line drugs isoniazid and rifampicin, have to be treated for 2 years and can account for up to 40% of all TB-infections in certain parts of the world (20,36,38). Even more severely, extensively drug-resistant forms of this pathogen (XDR-TB) are additionally insensitive to several second-line drugs and "totally drug-resistant" *M. tuberculosis* (TDR-TB) strains were initially reported in 2009 underlining the urgent need for novel remedies allowing for an effective and shortened treatment of tuberculosis (39).

1.2 Antibacterial Drug Discovery

1.2.1 History of Antibacterial Discovery

The increasing occurrence of antibiotic-resistant pathogens is not only one of the major challenges modern medicine faces, but also a main driving force for antibacterial development (21). Whereas infectious diseases had often been fatal in the 19th century, the development of anti-infectives starting with the 20th century resulted in effective remedies to cure bacterial infections (3). Most antibiotics currently in use were identified during the "golden era" of antibacterial discovery between 1945 and 1960 (21). In the following two decades, the scaffolds of these antibiotics were improved via medicinal chemistry efforts (20,21). However, no new major classes of antibacterials were introduced to the market between 1962 and 2000 and, even more worryingly, no new antibiotics were discovered after 1987 (4,20). The estimated rate of success to market an antibacterial agent (0.17%) is rather low compared to other therapeutic areas (1). This raises the questions why antibacterial drug development is such a challenging task and what we can learn from the failures after 1987.

1.2.2 Challenges of Antibacterial Discovery

The sequencing of the first bacterial genome (*Haemophilus influenzae*) in 1995 raised hope for the identification of novel targets and associated drugs that block the function of these entities (1,3). In an extensive genomics-based study, GlaxoSmithKline (GSK) identified 127 essential bacterial genes among the 258 genes investigated between 1995 and 2001 (1). Although 67 high-throughput screening (HTS) campaigns were undertaken with large compound libraries (260,000 to 530,000 molecules per screen), hits could be identified for only 16 targets which in turn led to the development of lead compounds in 5 cases. In relation to the long duration of these studies and the huge investments made, this is a very disappointing result (1). Nevertheless, the identified lead compounds could be the starting point for the development of new classes of antibiotics. GSK synthesized lead compounds that target the peptide deformylase (PDF) as well as the methionyl- and phenylalanyl-tRNA synthetases (MetRS and PheRS, respectively) (1). Moreover, lead compounds with related whole-cell activity could be developed for two targets of the fatty acid biosynthesis pathway - the enoyl-acyl carrier protein (ACP) reductase (FabI) and the 3-ketoacyl-ACP synthase III (FabH). Out of these five projects, GSK decided to only further pursue the PheRS target (1). As only narrow-spectrum compounds could be developed for FabI and MetRS, these projects were outsourced to the biotechnology industry (Affinium Pharmaceuticals and Replidyne, respectively) (1,4). Compounds inhibiting FabH did not gain drug-like properties and those inhibiting PDF were replaced by more promising drug candidates originating from structure-based drug design efforts (1).

Although the genomics and HTS-based approach was not as successful as expected, important lessons can be learned from the failures within the past two decades (1,3,4). It is necessary but not sufficient that a chosen target is essential for the survival of the pathogen of interest. In addition, it has to be druggable and different, absent or nonessential in humans (2). Furthermore, drug candidates have to exhibit important characteristics such as high-affinity and specific inhibition of the target with related antibacterial activity, drug-like properties and a low propensity for the formation of resistances (2,4). Although many orally bioavailable drugs fulfill the "Lipinski's rules of five" (40), antibacterials are an exception of this rule and possess different physicochemical properties that are likely necessary for the drug to penetrate the bacterial cell which differs from its mammalian counterpart (1,2). In particular, antibiotics are characterized by a higher molecular weight and increased polarity (2). However, the physicochemical property space of the HTS libraries applied by the pharmaceutical industry does not fully match these requirements as those libraries tend to contain molecules which are too lipophilic for antibacterial research (1,2). This limitation in the chemical space may in part explain the relatively low success of the GSK study described above (1,4).

1.2.3 New Concepts and Strategies of Antibacterial Drug Development

In order to combat multidrug-resistant pathogens, new concepts and strategies are required to develop novel antibiotics after the failure of the genomics-based approach (3). Clearly, it will be central to broaden the chemical diversity of the current HTS libraries and to adapt them with respect to the stringent requirements of antibacterials (1,2,4). Thus, one focus must be on the synthesis of new molecules combined with screening for potential antibacterial properties in whole-cell instead of target-specific HTS campaigns (1). It might be advantageous to search for novel bacteriocidal compounds rather than looking for novel targets because it is usually easier to elucidate the mode of action of an antibiotic than to tailor an *in vivo* active antibiotic for a given target (1).

On the other hand, known lead compounds of validated drug targets have to be improved to render them efficacious against multidrug-resistant pathogens (1). The usage of the structure-based drug design (SBDD) approach has been advocated for this task (1,3,4). During this iterative and highly interdisciplinary approach, structural information of drug-target complexes is used to rationally improve the properties of a lead compound using computational and experimental means (Figure 1-1) (41,42). SBDD has already been used successfully for the design of anti-(retro)viral drugs such as the influenza therapeutic zanamivir (GSK) and the HIV protease inhibitor amprenavir (GSK) (3,4).

For the success of SBDD efforts, target selection will be of particular importance. Clearly, the classical targets of antibacterials such as the ribosome are still very promising (see also Table 1-1) (1,3). Furthermore, naturally occurring antibiotics can hint at the suitability of a selected target. To ensure the prolonged applicability of a developed antibiotic, the target should be characterized by a low propensity to form resistances (4). The success of glycopeptides and the long duration until resistance formation, suggests that extracellular targets are ideally suited to fulfill this requirement (1,4,27). In addition, compounds which interfere with multiple instead of just a single target usually are characterized by a reduced rate of resistance formation (1,4). Drug combinations should be used to suppress the formation of resistances for single enzyme targets (20). For instance, combination therapies have been shown to be efficacious and are routinely used for the treatment of tuberculosis and malaria (20,43).

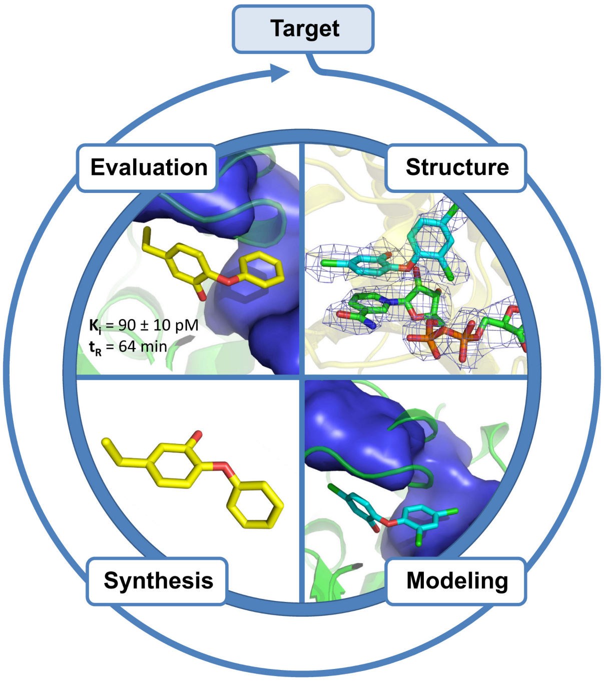

Figure 1-1. The structure-based drug design approach. A drug-target complex structure is used to design improved inhibitors using computational methods. After the synthesis of the most promising compounds, they are evaluated with respect to the properties which are aimed to be improved. Several further cycles of this iterative approach can lead to the identification of drug candidates. The inner circle contains an example of this work (saFabI inhibition by the diphenyl ether inhibitors triclosan (cyan) and 5-ethyl-2-phenoxyphenol (yellow)) (see also chapter 2).

1.2.4 Importance of Drug-Target Kinetics

The availability of a reliable *in vitro* early-stage indicator for the *in vivo* efficacy of a compound is pivotal for effective drug design efforts. Classically, many researchers optimize the thermodynamic affinity K_d or the related metrics K_i and IC_{50} (10,44). However, in an open *in vivo* system, the drug concentration will decrease over time and rebinding only occurs efficiently as long as the drug concentration is above the K_d (10). Hence, the drug-target residence time is a very important kinetic quantity because the drug will only be active as long as it is bound to its target (10). Importantly, slowly dissociating compounds stay bound to their receptor despite the decreasing *in vivo* drug concentration and, thus, the duration of efficacy might be enhanced for molecules with long dissociative half-lifes (10,44,45). Indeed, the drug-target residence time has been shown to be a suitable predictor of *in vivo* activity for several targets (10,45). A recent example demonstrates the applicability of this concept for antibacterial research - the residence times of several slow-off inhibitors targeting the *F. tularensis* FabI protein (ftFabI) were shown to be highly correlated with the survival rate in a mouse model of infection (46). In addition to a prolonged pharmacological effect, long residence times can also lead to improved drug selectivity and safety if the low off-rates are unique for the investigated target and dissociation occurs faster in the case of secondary targets (45,47). Consequently, a relatively large proportion of the drugs approved by the FDA between 2001 and 2004 (26% of all drugs with known target) exhibit slow-off characteristics highlighting the importance of drug-target kinetics for future drug discovery efforts (10).

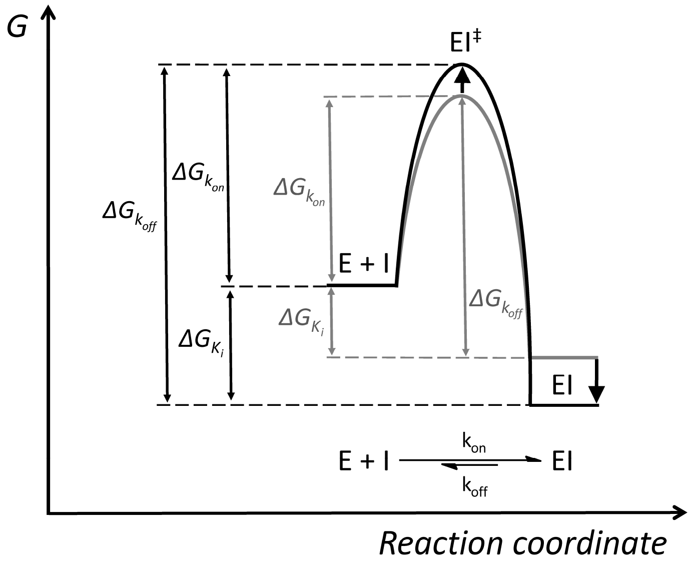

Figure 1-2. Energy plot for the formation of an enzyme-inhibitor complex via a simple one-step mechanism (10). E = enzyme, $EI^‡$ = transition state (TS) of EI formation, EI = enzyme-inhibitor complex, $K_i = k_{off}/k_{on}$. The residence time, which is defined as the reciprocal of k_{off}, can be increased by decreasing the relative free energy G of EI and/or increasing the relative free energy of $EI^‡$ (indicated by bold black arrows). A superimposed second energy plot is depicted for a hypothetical inhibitor with increased residence time (colored in black).

The residence time t_R, which is used to quantify the lifetime of a receptor-ligand complex, is defined as the reciprocal of the dissociation rate constant k_{off} of this complex and is related to the dissociative half-life, which is given as $\ln 2/k_{off}$ (10,44,45). Usually, the residence times of enzyme-bound substrates or products are rather short ranging from milliseconds to seconds (47,48). High-affinity rapid-reversible inhibitors typically exhibit residence times of a few seconds, whereas slow-onset inhibitors are characterized by residence times ranging from minutes to several days (10,44,45). In extreme cases the (*in vitro*) residence time can even be longer - for instance, the basic pancreatic trypsin inhibitor stays bound to its target for approximately 6 months (47).

Despite the importance of drug-target kinetics for drug discovery, it still remains very challenging to modulate the residence time using a rational approach (10,44). Accordingly, it is pivotal to unravel the molecular characteristics which determine a long dissociative half-life (44). The dissociation rate constant k_{off} can be decreased (and thus t_R increased) by either stabilizing the EI ground state and/or destabilizing the $EI^‡$ transition state (TS) along the reaction coordinate of the inhibitor binding process (Figure 1-2) (10). Whereas the relative free energy of the EI ground state is classically minimized during affinity optimization, the rational modulation of the relative free energy of the TS is much more challenging (10,44). In this regard the lack of structural information about the TS is a major obstacle and techniques such as (time-resolved) X-ray crystallography and molecular dynamics (MD) simulations may provide valuable information about such transient conformational states (44).

1.3 Bacterial Fatty Acid Biosynthesis as a Drug Target

1.3.1 Fatty Acid Biosynthesis

Fatty acids are pivotal for life and play important roles as integral components of cell membranes, in energy metabolism and storage, and as second messengers (12,49-51). Due to its essentiality, the bacterial fatty acid biosynthesis pathway provides a promising target for the development of new antibacterial agents (52). Isoniazid, one of the most effective anti-tuberculosis drugs, is in clinical use since 1952 and successfully inhibits the type II fatty acid biosynthesis (FAS-II) in *M. tuberculosis*, thus validating this pathway as an attractive target for antibacterial discovery (Table 1-2, compound **10**) (38,53-55). Importantly, the FAS-II pathway in bacteria, plants and protozoa differs fundamentally from the mammalian type I fatty acid synthesis (FAS-I) and can therefore be inhibited selectively (7,12,19,50). Whereas the mammalian fatty acid synthase (mFAS) is a large homo-dimeric multifunctional protein (Figure 1-3A), separate monofunctional enzymes are responsible for the synthesis of fatty acids in the FAS-II system (Figure 1-4) (7,12,51).

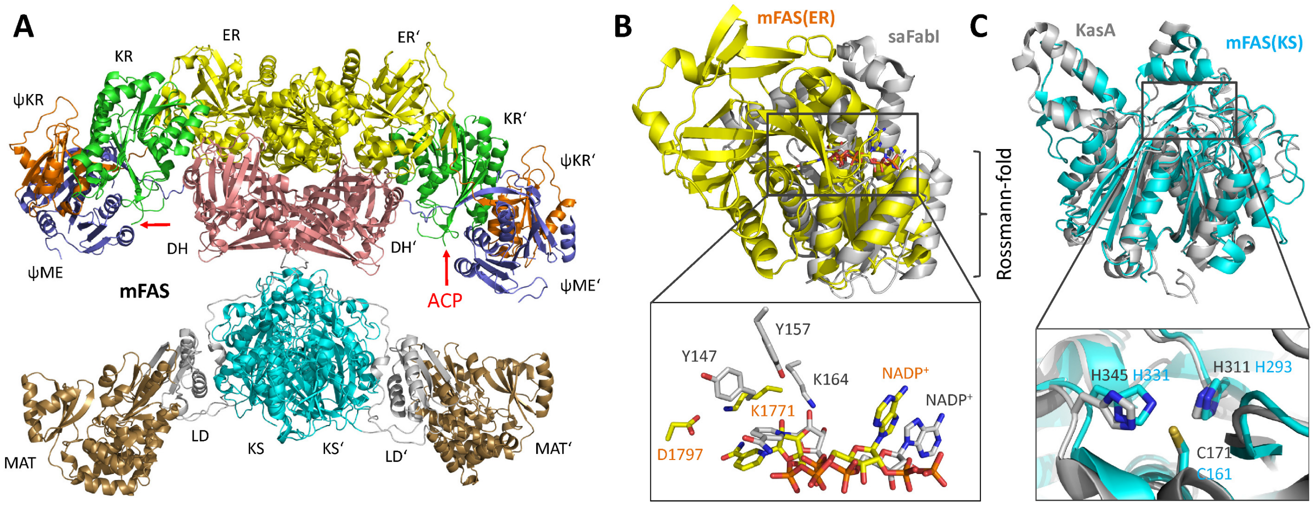

Figure 1-3. The mammalian fatty acid synthase (12). (A) Crystal structure of the mammalian fatty acid synthase (mFAS). The overall homo-dimeric structure of the mammalian fatty acid synthase (source: pig; PDB-code: 2VZ8) is characterized by an "X"-like shape. The reaction steps leading to the formation of fatty acids are catalyzed by several distinct domains: the malonyl-acetyl transferase (MAT), β-ketoacyl-ACP synthase (KS), β-ketoacyl-ACP reductase (KR), β-hydroxyacyl-ACP dehydratase (DH), and enoyl-ACP reductase (ER) domains. During fatty acid biosynthesis the substrate is tethered to the acyl carrier protein (ACP) domain, which was not identified in the crystal structure (the site at which ACP is attached is highlighted by red arrows and the proposed location of this small domain is indicated by the word "ACP" in red) (12). **(B)** Superimposition of the *S. aureus* enoyl-ACP reductase FabI (gray; PDB-code: 4ALI) with the mFAS ER domain (yellow; PDB-code: 2VZ9) (12,19). Although the Rossmann-fold (lower right part of the structures as indicated in black), which builds up the NADPH binding site, is structurally conserved between *S. aureus* FabI and the mFAS ER domain, the active site located above the Rossmann-fold differs between the two structures. The box contains the cofactors and (proposed) active site residues for each structure and highlights the fundamental differences between the mFAS ER domain and *S. aureus* FabI. **(C)** Superimposition of the *M. tuberculosis* β-ketoacyl-ACP synthase KasA (gray; PDB-code: 2WGD) with the mFAS KS domain (cyan; PDB-code: 2VZ8) (12,17). The thiolase fold as well as the active site residues are highly conserved between both structures (insert).

Despite these differences in the structural organization, the single catalytic steps necessary for the synthesis of fatty acids are conserved among all organisms (12). As the nucleophile during the C-C bond forming reactions, the malonyl-acyl carrier protein (ACP; see also chapter 1.3.2) plays a central role in this pathway and provides two additional carbon atoms in each elongation cycle (Figure 1-4). In bacteria, malonyl-ACP is generated from acetyl-coenzyme A (CoA) via the subsequent actions of AccABCD and FabD. The acetyl-CoA carboxylase AccABCD carboxylates acetyl-CoA to yield malonyl-CoA, which subsequently is transferred onto the acyl carrier protein by the malonyl-CoA:ACP transacylase FabD (see also Figure 2-1) (12,54). In the mammalian FAS-I system, the mFAS malonyl-acetyl transferase (MAT) domain catalyzes the corresponding transfer of the malonyl group onto ACP (12). In the final initiation step of the FAS-II pathway, the β-ketoacyl-ACP synthase III (KAS III) FabH catalyzes the Claisen condensation reaction between malonyl-ACP and an acyl-CoA primer, which can differ based on the organism (see also Figure 2-1) (56,57). In addition to the KAS III enzyme, two additional types of bacterial condensing enzymes are known, which catalyze the analogous reaction within the elongation cycle of the FAS-II pathway (Figure 1-4), namely KAS I (usually referred to as FabB; KasA in *M. tuberculosis*) and KAS II (usually referred to as FabF; KasB in *M. tuberculosis*) (18,58,59). Whereas the mFAS β-ketoacyl-ACP synthase (KS) domain as well as the KAS I and KAS II enzymes utilize acetyl-ACP as the electrophile during the condensation reaction, the bacterial KAS III enzyme FabH is unique with respect to its selectivity towards acyl-CoA substrates (12,18,58).

During the elongation cycle, the β-keto group of the generated β-ketoacyl-ACP is reduced to a methylene group via the subsequent actions of a β-ketoacyl-ACP reductase (KR), a β-hydroxyacyl-ACP dehydratase (DH) and an enoyl-ACP reductase (ER) (Figure 1-4) (12,60). The FAS-II system contains a single KR termed FabG (MabA in *M. tuberculosis*), which catalyzes the NADPH-dependent reduction of the β-keto function to a hydroxyl group (51,54,61). Subsequently, one of the two bacterial DH enzymes (FabZ and FabA; HadAB and HadBC in *M. tuberculosis*) dehydrates the β-hydroxyacyl-ACP to yield an enoyl-ACP (8,60,62). This is the substrate for the last enzyme of the elongation cycle, the enoyl reductase FabI or one of its isoforms FabK, FabL and FabV (63-66), which reduce the *trans*-2-enoyl double bond to a single bond (12,60,67). The enoyl-ACP reductase of *M. tuberculosis*, InhA, has been shown to be the target for the front-line anti-tuberculosis prodrug isoniazid after its activation by the mycobacterial catalase/peroxidase KatG (for details see Table 1-2, **10**-**11**) (55,68-71). Overall, the fatty acid synthesis elongation cycle generates a fatty acyl substrate which is elongated by two carbon atoms and the next round is subsequently initiated by the condensing KAS I/II enzymes (54).

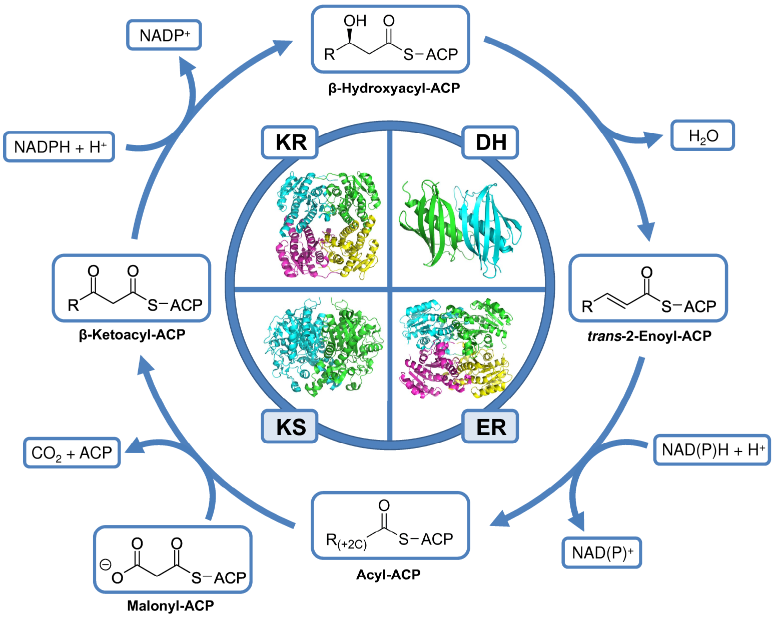

Figure 1-4. Elongation cycle of the type II fatty acid biosynthesis pathway. The inner circle contains the overall structures of the involved enzymes β-ketoacyl-ACP synthase (KS) (KasA of *M. tuberculosis* is shown exemplarily, PDB-code: 2WGG), the β-ketoacyl-ACP reductase (KR) (MabA of *M. tuberculosis* is depicted, PDB-code: 1UZM), the β-hydroxyacyl-ACP dehydratase (DH) (FabZ of *Plasmodium falciparum* is shown, PDB-code: 1ZHG) and the enoyl-ACP reductase (ER) (FabI of *S. aureus* is depicted, PDB-code: 4ALL, this work). The targets of this work are highlighted in light blue (KS and ER). The KS, KR, DH and ER enzymes of *S. aureus* and *M. tuberculosis* are FabF, FabG, FabZ and FabI or KasA/B, MabA, HadAB/BC and InhA, respectively (7,8). R = alkyl chains of different lengths (elongated by 2 carbons per cycle).

1.3.2 The Acyl Carrier Protein

During the mammalian and bacterial fatty acid biosynthesis elongation cycles, all fatty acyl intermediates are tethered to the acyl carrier protein (ACP), which transports the substrates to the different catalytic centers (12,72). Whereas this small acidic protein is an integral part of the mammalian fatty acid synthase, ACP is a separate entity in the FAS-II system. To reach the buried active sites of the involved enzymatic domains/proteins, the substrate is attached to the terminal thiol group of a long and flexible 4'-phosphopantetheine (PPant) linker which in turn is esterified with a conserved serine of ACP (Figure 1-5) (72-75). This highly abundant and conserved protein is structurally organized in a 4-helix bundle with a right-handed twist (76,77). During the bacterial fatty acid synthesis, the acyl substrate must be released from the ACP and injected into the binding pocket of the individual enzymes (74). Accordingly, two slightly different crystal structures have been reported for *E. coli* butyryl-ACP with the acylated PPant buried in a hydrophobic cavity or exposed to the solvent, respectively (77). Thus, a 3-step substrate binding and turnover process is currently envisioned - a weak interaction between ACP and its partner enzyme induces a conformational change in ACP leading to the injection of the substrate into the binding site, followed by catalysis and removal of the product, which in turn is re-buried inside the hydrophobic ACP cavity (74,77). In this regard, it is discussed controversially whether the FAS-II enzymes specifically interact with those ACP molecules modified with the correct partner substrate or whether the different intermediates are rather distinguished upon injection into the binding crevice (76).

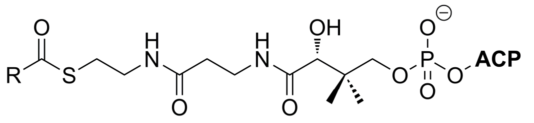

Figure 1-5. ACP esterified with an acylated 4'-phosphopantetheine moiety. The substituent R varies depending on the intermediate (see also Figure 1-4).

Despite the importance of the ACP molecule for fatty acid biosynthesis, only little is known about the interactions between FAS-II enzymes and ACP (74). In part, this might be due to the fact that ACP interacts with a plethora of different enzymes involved in fatty acid, polyketide, non-ribosomal peptide and vitamin biosynthesis (74,77). To enable this multitude of interactions with different enzymes, ACP is a very flexible and thus adaptable protein (76). Moreover, the interactions between ACP and FAS-II enzymes are usually rather weak (reported K_d and K_M values are in the low µM range), which additionally aggravates successful crystallographic studies (18,74,76,78,79). Nevertheless, evidence is accumulating that the helix α2 in ACP provides a common binding site for enzymes of different functional backgrounds (including FAS-II) (76,80-82). In contrast, combined computational, biochemical and biophysical studies with *E. coli* FabH and FabG suggested that no conserved ACP binding motif exists among the different FAS-II enzymes themselves (74,76). Instead, the acidic helix α2 in ACP is presumably recognized by a basic, hydrophobic surface patch close to the binding site entrance of FAS-II enzymes (74,76).

1.3.3 Diversity in the Fatty Acid Synthesis Pathway

Although fatty acid biosynthesis is a vital cellular process for most bacteria, in recent years an increasing number of species-specific differences were recognized (83,84). For instance, different organisms contain different isoenzymes, which catalyze the required biochemical reactions during the synthesis of fatty acids (7). In part, the necessity for additional enzymes can be explained by the requirement of certain bacteria (such as *E. coli*) to synthesize unsaturated fatty acids (UFA) (72). Gram-negative bacteria usually contain additional FabA and FabB enzymes (see also Figure 2-1), which are responsible for the synthesis of UFA. The dehydratase FabA dehydrates and isomerizes β-hydroxydecanoyl-ACP to the associated *cis*-3-enoyl-ACP, which is directly condensed with malonyl-ACP through the action of FabB without prior reduction of the double bond (63,72). In contrast, the Gram-positive organism *Streptococcus pneumoniae* does not contain FabA and FabB and thus produces UFA via an alternative mechanism (83). The DH enzyme FabZ dehydrates β-hydroxydecanoyl-ACP to yield the corresponding *trans*-2-enoyl-ACP, which in turn is isomerized to the *cis*-3-decenoyl-ACP by an additional enzyme termed FabM. As for *E. coli*, the reductive step, which is catalyzed by FabK instead of FabI, is skipped and the *cis*-double bond is maintained after the FabF-catalyzed condensation reaction (83).

Certain Gram-positive bacteria including *S. aureus* lack FabA, FabB and FabM and thus are not able to synthesize UFA (7,72,85). Whereas membrane fluidity in most bacteria is controlled via phospholipids containing UFA, some species utilize methyl-branched fatty acids (BCFA) for this purpose; *S. aureus* contains 81% of these fatty acids (72,86). In particular, the Gram-positive *Bacillus* and *Staphylococcus* as well as the Gram-negative *Legionella* genera are members of the relatively small family of BCFA-synthesizing bacteria (86). For such bacteria UFA are not pivotal, but BCFAs were shown to be essential for *Bacillus subtilis* instead (86,87). The requirement for different fatty acids might in part explain the diversity in the fatty acid biosynthesis pathway found among various bacteria.

1.3.4 Essentiality of the Bacterial Fatty Acid Biosynthesis

The heterogeneity of bacterial species with respect to the synthesis of fatty acids also raises the question whether the FAS-II pathway is essential, and thus a valid target, for all or just for certain bacteria (88). For Gram-negative bacteria, the FAS-II pathway has been shown to be essential due to their need to synthesize β-hydroxy fatty acids as lipid A precursor molecules (89). In contrast, Brinster *et al.* recently have shown that the Gram-positive bacterium *Streptococcus agalactiae* can take up exogenous fatty acids from the host blood serum during a septic infection to circumvent the inhibition of the FAS-II pathway (90). Initially, these findings were extrapolated to all Gram-positive bacteria despite the lack of *in vivo* data supporting this conclusion (90). However, two proximate studies provide compelling evidence that this generalization does not hold true for *S. aureus* (88,89). Parsons *et al.* have demonstrated that, in contrast to *S. pneumoniae*, the uptake of exogenous fatty acids cannot fully compensate for the synthesis of endogenous fatty acids in *S. aureus* (89). Accordingly, only 50% of the endogenous fatty acids of *S. aureus* were replaced by exogenous fatty acids (89). In the case of *S. pneumoniae*, for which a full replacement of endogenous fatty acids is feasible, exogenous fatty acids genetically or biochemically block the AccABCD catalyzed reaction. Due to the resulting depletion of malonyl-CoA levels, ACP accumulates since it is not consumed in the malonyl-CoA:ACP transacylation reaction and, thus, can be used for the incorporation of exogenous fatty acids into bacterial phospholipids (Figure 2-1). The absence of a comparable mechanism in *S. aureus*, which down-regulates the synthesis of endogenous fatty acids and simultaneously triggers the incorporation of exogenous fatty acids, provides the metabolic basis for the susceptibility of this organism to FAS-II inhibitors (89), which has been demonstrated in several *in vivo* models of infection (50,88,91,92).

1.3.5 Mycolic Acid Synthesis in Mycobacteria

Mycobacteria are an additional striking example highlighting the diversity of the bacterial fatty acid biosynthesis. The waxy mycobacterial cell wall, which confers intrinsic antibiotic resistance (see also chapter 1.1.2) (23), consists of three covalently linked macromolecular structures - the peptidoglycan is attached to an arabinogalactan layer, which in turn is esterified with mycolic acids (24,58,93). Mycolic acids are C_{60} - C_{90} α-alkyl-β-hydroxy fatty acids that are essential for the survival of *M. tuberculosis* and related mycobacteria (Figure 1-6) (23).

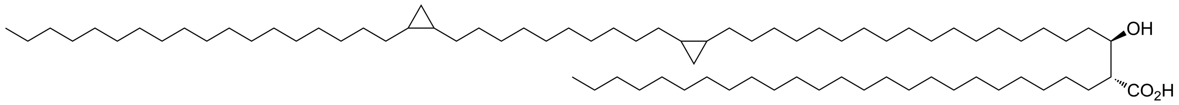

Figure 1-6. α-Mycolic acid. The α-mycolic acid is the most abundant mycolic acid in *M. tuberculosis* (11).

To enable the synthesis of these very long fatty acids, mycobacteria require both, the FAS-I and the FAS-II system (11). During mycolate synthesis, the 640 kDa homo-dimeric fatty acid synthase of the FAS-I system generates short acyl-CoA primers (C_{16} - C_{18}), which are then elongated via the FAS-II pathway to yield C_{50} - C_{56} meromycolate chains (for further details see also chapter 6.4 and Figure 6-1) (11,22,23). Thus, the mycobacterial FAS-II system is unique amongst bacteria since it does not enable the *de novo* synthesis of fatty acids but rather elongates medium-chain precursors to very long fatty acids (23). In this regard, the *M. tuberculosis* KAS III enzyme (mtFabH) plays a pivotal role as it links the two biosynthetic pathways and specifically utilizes medium-chain acyl-CoA primers instead of acetyl-CoA (58,94). Moreover, the mycobacterial ACP (termed AcpM) contains an extended flexible C-terminus, which was suggested to be required for the transport and delivery of long-chain substrates, and thereby differs from common bacterial ACPs (75). In addition, growing evidence indicates that the mycobacterial FAS-II enzymes are organized in distinct complexes and that certain proteins might act as assembly chaperons (in *M. tuberculosis* this role was proposed for the chaperon GroEL1 during biofilm maturation) (38,95,96).

1.4 Targeting Key Steps of the FAS-II Pathway

1.4.1 The Enoyl-ACP Reductase FabI of *S. aureus* and other Bacteria

Based on the findings that the antibacterial agent triclosan and the front-line anti-TB drug isoniazid target the enoyl-ACP reductase FabI (EC 1.3.1.9/10; also referred to as ENR (63,97) and InhA in *M. tuberculosis*) (71,98,99), this enzyme was the major focus among all FAS-II components (67). However, with the identification of the FabI isoforms FabK, FabL or FabV in several important pathogenic bacteria such as *S. pneumoniae*, *Enterococcus faecalis*, *P. aeruginosa*, *Listeria monocytogenes* and *Vibrio cholerae* it became clear that FabI inhibitors will not exhibit broad-spectrum characteristics (64-66,100) and, consequently, major pharmaceutical companies such as GlaxoSmithKline (see also chapter 1.2.2) lost their interest in this target (1). However, given the urgent need for novel antibiotics for specific pathogens such as *S. aureus* (see also chapter 1.1.3), the development of narrow-spectrum antibiotics is strongly advocated (20). Alarmingly, it appears to be difficult in general to discover new broad-spectrum antibacterials due to the heterogeneity of bacteria. For instance, an ideal antibiotic for the treatment of lung infections should be active against *S. aureus*, *S. pneumoniae*, *Haemophila influenzae*, *Moraxella catarrhalis*, *Legionella pneumonphila* and *Mycoplasma pneumoniae*. Unfortunately, already *S. pneumoniae* and *H. influenzae* differ genetically more than humans differ from paramecia, a freshwater protozoon (1). Hence, small-spectrum antibiotics should be developed and applied in combination with improved diagnostic methods. In this regard, *S. aureus* FabI (saFabI) constitutes a very promising target since it is the sole *trans*-2-enoyl-ACP reductase in this organism (100-102) and, consequently, three inhibitors are currently investigated in clinical trials (for details see chapter 1.4.2) (103). Although these compounds inhibit a single target, resistance frequencies were shown to be rather low (surrounding 10^{-9}) (89,92,100). Since bacterial counts can reach 10^{10} during a human infection, an ideal antibiotic should display resistance rates below 10^{-10}, which is usually only achieved for antibiotics which interfere with multiple targets (4). Thus, saFabI inhibitors might be used in combination with other antibacterials to further reduce the probability of resistance formation. For instance, combination therapy is successfully used for the treatment of malaria and tuberculosis and was recommended to enable the application of antibiotics with relatively high resistance frequencies (20,43).

Similar to the second reductase of the FAS-II cycle, FabG, the FabI protein is a member of the short-chain dehydrogenase/reductase (SDR) superfamily and usually exists as homo-tetramer (Figure 1-4) (51). Each monomer is characterized by a chair-like structure containing an extended Rossmann-fold, which consists of a 7-stranded parallel β-sheet surrounded by 3 α-helices on either side (Figure 2-2B) (67,72,104,105). Although the Rossmann-fold, which defines the binding site for NAD(P)H, is also present in the mFAS ER domain (12), the primary sequence identity shared with saFabI is low (11.6%, calculated with ClustalW (106)). Accordingly, a superimposition of the mFAS ER domain with saFabI reveals major differences in the substrate binding region residing above the Rossmann-fold (Figure 1-3B).

The tube-like FabI substrate binding cavity is in contact with the surrounding solvent at both ends and, based on the extent of solvent-exposure, the two entries were termed minor and major portal, respectively (Figure 5-2B) (70,101,107). The NAD(P)H cofactor is located at the bottom of this binding channel and is oriented with the nicotinamide and adenine rings pointing towards the minor and major portals, respectively (Figure 5-2B). Whereas most FabI enzymes utilize NADH as reducing agent, saFabI prefers to bind NADPH in a cooperative fashion (51,52,78,108). Cofactor binding is followed by the uptake of the enoyl-ACP substrate according to an ordered bi-bi mechanism, which is probably common to all SDR proteins (105,109,110). Whether ACP delivers the enoyl-substrate via the minor or major portal of FabI is currently not clear due to conflicting findings (see also chapter 5) (70,107). As a consequence, also the mechanism of the FabI-catalyzed reaction is discussed controversially.

Usually, the FabI catalytic triad consists of Tyr147, Tyr157 and Lys164 (saFabI numbering). Similar to other SDR members, the very conserved active site lysine likely plays a pivotal role in the correct positioning of the NAD(P)H nicotinamide ribose (70,105,111). However, it is currently unclear whether Tyr147 or Tyr157 binds the enoyl-ACP thioester carbonyl group and what the role of the remaining catalytic residue might be (70,107). These two possibilities correspond to the delivery of the substrate via the minor or major portal, respectively. Irrespective of which active site tyrosine binds the thioester carbonyl, FabI catalyzes the last step of the FAS-II elongation cycle via the transfer of the pro-*4S* hydride ion of NAD(P)H to the 3-carbon of the *trans*-C2-C3 double bond of the enoyl-ACP substrate (51,78,108,112,113). Subsequently, the generated enolate anion is protonated at the C2 carbon, forming an acyl-ACP, which is elongated by two carbon atoms with respect to the educt of this particular FAS-II elongation round (113). Similar to other SDR members, FabI proteins contain a flexible loop which is usually disordered in the apo-enzymes and becomes ordered upon ligand binding (6,105). Despite the importance of this substrate binding loop (SBL) for substrate recognition and specificity, little is known about the conformational states sampled along the reaction coordinate of substrate binding and turnover (114,115).

1.4.2 FabI Inhibition

The substrate binding loop of FabI was not only found to be important for the binding of substrates, but is also involved in the recognition of FabI inhibitors (67). Since more than 40 years the FabI inhibitor triclosan is used as antibacterial agent in many consumer products and antiseptic soaps to reduce MRSA colonization of the human skin in hospitals (Table 1-2, compound **1**) (72,97-99,116,117). Triclosan and related diphenyl ether inhibitors were found to be slow-binding inhibitors of FabI and this property was attributed to the closure of the SBL (for details about slow-binding inhibition, see chapter 1.2.4) (67). Although the small triclosan molecule exhibits remarkable affinity towards most FabI enzymes, the metabolically labile hydroxyl group complicates the application of such inhibitors as antibiotics (6,102,118). Consequently, the pharmaceutical company Mutabilis introduced a fluorine *para* to the hydroxyl moiety to prevent metabolic conjugation reactions (119). Based on the lead compound triclosan, Mutabilis developed the potent inhibitor MUT056399 (Table 1-2, compound **2**), which is currently analyzed in clinical trials and is active against *S. aureus* and several clinically important Gram-negative pathogens for which FabI is the sole enoyl-ACP reductase such as *E. coli*, *H. influenzae* and *M. catarrhalis* (92). Using an alternative strategy, CrystalGenomics developed the clinical trial inhibitor CG400549 by replacing the phenol A-ring of the diphenyl ether scaffold by a 2-pyridone to overcome the pharmacokinetic drawback of these compounds (Table 1-2, compound **3**) (103). In contrast to MUT056399, this inhibitor is *Staphylococcus*-specific and thus might be used as a narrow-spectrum antibiotic (31,100). The third clinical candidate AFN-1252 with a completely different scaffold (Table 1-2, compound **4**) originated from the work of GSK and Affinium Pharmaceuticals (see also chapter 1.2.2) and is similarly specific for *Staphylococci* (4,101,103). Importantly, these three clinical trial compounds were shown to possess *in vivo* efficacy in murine models of infection (92,100,101).

Table 1-2. Inhibitors of the enoyl-ACP reductase FabI.

Compound [a]	Inhibition characteristics [b]	Antibacterial activity
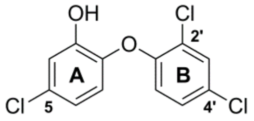 **Triclosan (1)**	K_i = 50 pM (saFabI, chapter 3) K_i = 7 pM (ecFabI) (97) K_i = 51 pM (ftFabI) (46) K_i = 100 nM (pfENR) (120) K_i = 220 nM (InhA) (69)	MIC = 0.03 µg/ml (*S. aureus*) (78,121,122)
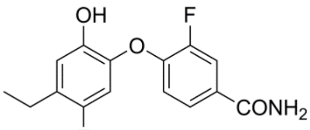 **MUT056399 (2)**	IC_{50} = 12 nM (saFabI) (92) IC_{50} = 58 nM (ecFabI) (92)	MIC_{90} = 0.03 - 0.12 µg/ml (*S. aureus*) (92)

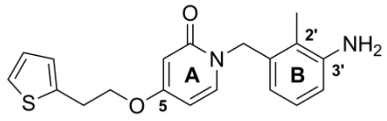 **CG400549 (3)**	K_i = 1 nM (saFabI, chapter 4) K_i = 82 nM (ecFabI, chapter 4)	MIC_{90} = 0.25 µg/ml (*S. aureus*) (31,100)
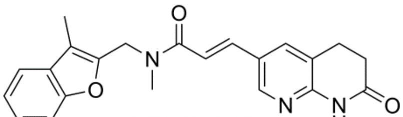 **AFN-1252 (4)**	K_i = 13 nM (saFabI) (101)	MIC_{90} = 0.015 µg/ml (*S. aureus*) (4,101)
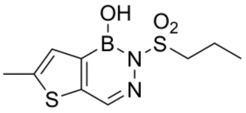 **Thieno-diazaborine (5)**	not available	MIC = 1.25 µg/ml (*E. coli*) (67)
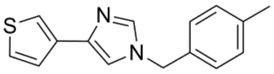 **imidazole (6)**	IC_{50} = 250 nM (saFabI) (121) IC_{50} = 6.4 µM (ecFabI) (121)	MIC = 8 µg/ml (*S. aureus*) (121)
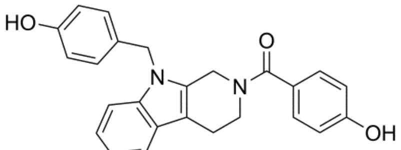 **indole (7)**	IC_{50} = 110 nM (saFabI) (122) IC_{50} = 4.2 µM (ecFabI) (122)	MIC = 0.5 µg/ml (*S. aureus*) (122) MIC = >64 µg/ml (*E. coli*) (122)
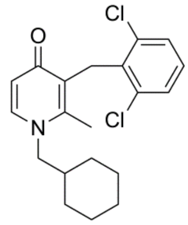 **4-pyridone (8)**	IC_{50} = 220 nM (ecFabI) (123)	MIC = 0.25 µg/ml (*S. aureus*) (123)
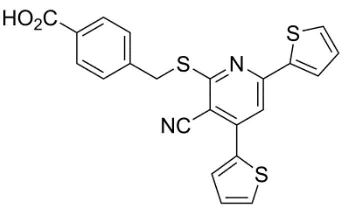 **thiopyridine (9)**	IC_{50} = 3.0 µM (ecFabI) (124)	MIC = 0.75 µg/ml (*S. aureus*) (124)
Activation of the prodrug isoniazid (60): 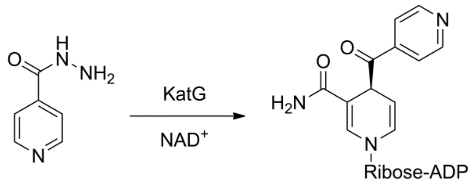 **Isoniazid (INH) (10)** **INH-NAD (11)**	K_i = 750 pM (InhA) (69,125)	MIC = 0.05 µg/ml (*M. tuberculosis*) (69)

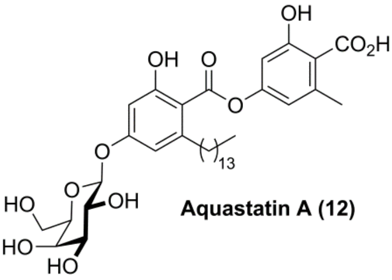 **Aquastatin A (12)**	IC_{50} = 3.2 µM (saFabI) (110)	MIC = 16-32 µg/ml (*S. aureus*) (110)
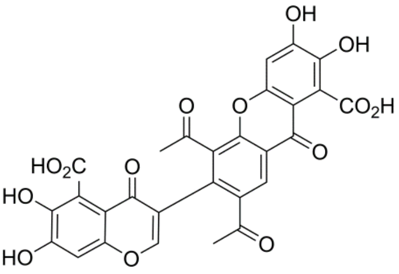 **Vinaxanthone (13)**	IC_{50} = 900 nM (saFabI) (126)	MIC = 32 µg/ml (*S. aureus*) (126)
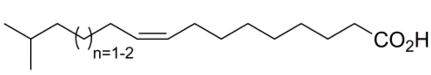 **methyl-branched fatty acids (14)** 14-methyl-9(Z)-pentadecenoic acid (n = 1, MPDA) 15-methyl-9(Z)-hexadecenoic acid (n = 2, MHDA)	IC_{50} = 16.0 µM (saFabI) (127) IC_{50} = 16.3 µM (saFabI) (127)	MIC = 32 µg/ml (*S. aureus*) (127)
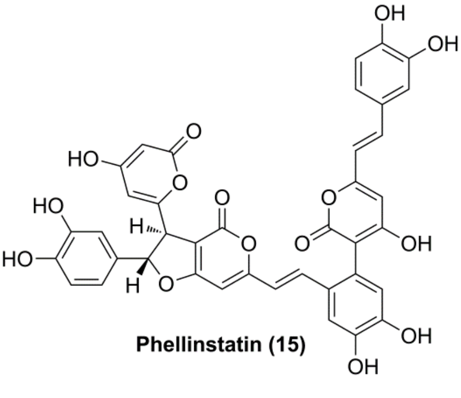 **Phellinstatin (15)**	IC_{50} = 6.0 µM (saFabI) (128)	MIC = 128 µg/ml (*S. aureus*) (128)

a. Compounds **6**, **7**, **8** and **9** are amongst the most potent inhibitors of large series of 1,4-disubstituted imidazoles, 2,9-disubstituted 1,2,3,4-tetrahydropyrido[3,4-*b*]indoles, 4-pyridones, and thiopyridines, respectively.

b. saFabI = *S. aureus* FabI, ecFabI = *E. coli* FabI, ftFabI = *F. tularensis* FabI, pfENR = *Plasmodium falciparum* enoyl-ACP reductase, InhA = *M. tuberculosis* enoyl-ACP reductase.

In addition, several other potent FabI inhibitors such as diazaborines (67), 1,4-disubstituted imidazoles (121), 2,9-disubstituted 1,2,3,4-tetrahydropyrido[3,4-*b*]indoles (122), 4-pyridones (123) and thiopyridines (124) were developed (Table 1-2, compounds **5**-**9**). Importantly, after the activation by the catalase/peroxidase KatG isoniazid (INH) is a slow-binding inhibitor of the mycobacterial FabI homologue InhA (Table 1-2, **10**-**11**) (125). The suitability of FabI as a drug target is further emphasized by the identification of several natural product FabI inhibitors such as Aquastatin A (isolated from the fungus *Sporothrix* sp. FN611) (110), Vinaxanthone (isolated from a *Penicillium* sp.) (126), two different methyl-branched fatty acids (isolated from *Streptomyces* sp. A251) (127) and Phellinstatin (isolated from the fungus *Phellinus linteus*) (128) (Table 1-2, compounds **11**-**14**).

1.4.3 *M. tuberculosis* KasA

Table 1-3. Inhibitors of the FAS-II condensing enzymes.

Compound	Inhibition characteristics	Antibacterial activity
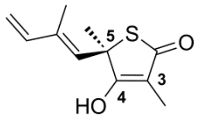 **Thiolactomycin (16)**	IC_{50} = 20 µM (KasA) (129) IC_{50} = 90 µM (KasB) (129) IC_{50} = 12 µM (*E. coli* FabB) (59) IC_{50} = 5 µM (*E. coli* FabF) (59)	MIC = 25 µg/ml (*M. tuberculosis*) (130)
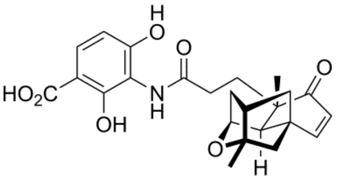 **Platensimycin (17)**	IC_{50} = 4.5 µM (KasA) (129) IC_{50} = 9.5 µM (KasB) (129) IC_{50} = 160 nM (*E. coli* FabF) (131) IC_{50} = 48 nM (*S. aureus* FabF) (131)	MIC = 12 µg/ml (*M. tuberculosis*) (129) MIC = 0.5 µg/ml (*S. aureus*) (131)
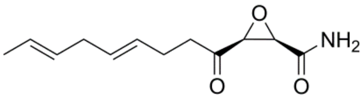 **Cerulenin (18)**	IC_{50} = 3 µM (*E. coli* FabB) (132)	not available
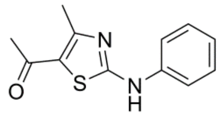 **aminothiazole (19)**	K_d = 25 µM (*E. coli* FabB) (133)	not available
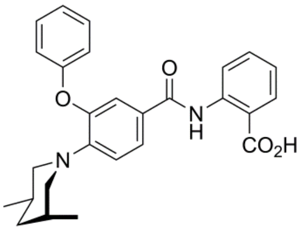 **benzoylaminobenzoic acid (20)**	IC_{50} = 270 nM (*E. faecalis* FabH) (134)	not available

Similar to the isoniazid target InhA, the β-ketoacyl-ACP synthase I of *M. tuberculosis* (KasA) has been shown to be essential for the survival of this pathogen, which confirms KasA as a promising drug target (22,135). In contrast to KasA, the mycobacterial KAS II enzyme KasB is non-essential. In the model organism *Mycobacterium smegmatis*, the depletion of KasA leads to changes in the composition of cell wall mycolates, morphological alterations and finally to cell lysis (135). Importantly, all three KAS enzymes (KasA, KasB and mtFabH in the case of *M. tuberculosis*) are inhibited by the natural product thiolactomycin (TLM, Table 1-3, compound **16**) (24,58,136,137). Such compounds which block multiple targets are particularly promising for the development of new antibiotics due to the reduced propensity for the formation of resistances (see also chapter 1.2.3) (4). However, since the inhibition of several targets by one common molecule concomitantly implies reduced specificity, special attention must be paid on the existence of potential secondary targets, which might lead to side effects during the application of such compounds. Indeed, KasA shares 22.2% primary sequence identity, a common fold and the catalytic triad with the mFAS KS domain (Figure 1-3C) (12,106). Accordingly, McFadden *et al.* were able to design TLM-analogs which inhibit the mFAS KS domain and thereby display anticancer and weight loss effects (138). Furthermore, a second naturally occurring β-ketoacyl-ACP synthase inhibitor, cerulenin, does also inhibit both, the bacterial and mammalian fatty acid synthesis (Table 1-3, compound **18**) (132). Nevertheless, distinct differences between bacterial KAS enzymes and the mFAS KS domain allow the development of selective and very promising inhibitors as exemplified by thiolactomycin (4,130,138).

The homo-dimeric KasA protein contains a thiolase fold and catalyzes the condensation reaction via a ping-pong bi-bi mechanism (13,17,59). First, acyl-AcpM binds to the KasA enzyme and acylates the active site cysteine (Cys171). After the deacylated AcpM left the KasA binding site, malonyl-AcpM can enter and delivers its malonyl group, which is decarboxylated and subsequently condenses with the acyl-chain esterified with Cys171. Finally, the formed β-ketoacyl-AcpM leaves the binding site and KasA including the nucleophile Cys171 are restored for additional rounds of catalysis (13,17,59,131). The catalytic triad of KasA is completed by the two histidines His311 and His345 (17,59,139,140). However, it is currently debated controversially whether and how both histidines are involved in the decarboxylation of the malonyl-substrate, and further studies with the acyl-enzyme intermediate are necessary to reveal the exact location of the malonyl group in the catalytically competent complex (for details see chapter 6) (141). Since the preparation of a homogenous acyl-KAS enzyme for crystallographic studies turned out to be problematic, an active site cysteine mutant is commonly used (C171Q for KasA) which mimics the acylated form of the KAS-enzyme (13,17,131).

1.4.4 Inhibition of the FAS-II Condensing Enzymes

Interestingly, the natural products thiolactomycin (isolated from *Nocardia* and *Streptomyces* sp.) and platensimycin (isolated from *Streptomyces platensis*) preferably inhibit the acyl-intermediates rather than the apo-forms of condensing enzymes (59,131). Despite its moderate MIC values, TLM displayed *in vivo* efficacy against *Serratia marcescens* and *K. pneumoniae* in murine models of infection (59,137). Moreover, the small size, moderate polarity (logP = 3) and broad-spectrum activity of this molecule underscores the potential of TLM as a lead compound for the development of a new antibiotic (Table 1-3, compound **16**) (138,142). Platensimycin constitutes the most potent KAS-inhibitor currently known - the IC_{50} towards *S. aureus* FabF is 48 nM (Table 1-3, compound **17**) (131). In addition, promising antibacterial activities have been reported for *S. aureus* (MIC = 0.5 µg/ml) and *M. tuberculosis* (MIC = 12 µg/ml) (129,131). In contrast to TLM and platensimycin, the natural product cerulenin (isolated from *Cephalosporium caerulens*) is a covalent inhibitor of KAS-enzymes (Table 1-3, compound **18**) (23,132). Mechanistically, the nucleophilic active site cysteine attacks the C2 atom of the electrophilic epoxide ring to yield a covalent protein-inhibitor adduct (132). In addition to the naturally occurring antibacterial agents, some completely synthetic KAS-inhibitors have been developed. For instance, the aminothiazole derivative 2-phenylamino-4-methyl-5-acetylthiazole was identified by means of virtual screening and was found to inhibit the *E. coli* FabB enzyme with a K_d value of 25 µM (Table 1-3, compound **19**) (133). In addition, a high-throughput screening campaign (with 2,500 compounds) and subsequent hit optimization resulted in a series of benzoylaminobenzoic acids with IC_{50} values for the *E. faecalis* FabH enzyme in the high nM to low µM range (Table 1-3, compound **20**) (134).

1.5 Research Objective

During this work, some of the key questions surrounding the important drug targets saFabI and KasA were addressed. For this purpose, we used a highly interdisciplinary and collaborative structure-based drug design approach which included methodologies such as X-ray crystallography, molecular dynamics simulations, computational modeling, biochemistry, mass spectrometry, chemical synthesis, enzyme kinetics and microbiology (individual experimental contributions are listed in the preamble of chapters 2, 3, 4, 5 and 6).

1.5.1 General Questions Concerning the FAS-II Pathway

- Does saFabI differ from other enoyl-ACP reductases given the unique capability of the staphylococcal FAS-II system to generate BCFAs? Does KasA differ from orthologous β-ketoacyl-ACP synthases in the light of its special competence to turnover long-chain mycolic acid precursors? Is the diversity in fatty acid synthesis thus also reflected in these key enzymes? For details on this topic see also chapters 1.3.3 and 1.3.5.
- Why does *S. aureus* differ from other Gram-positive organisms and established a (protective?) mechanism which does not allow the bypass of its FAS-II system through the complete uptake of exogenous fatty acids leading to the sensitivity of this organism to FAS-II inhibitors (88,89)? For which other Gram-positive pathogens does the FAS-II pathway constitute a valid target? For details on this topic see also chapter 1.3.4.

1.5.2 Questions Concerning SaFabI, KasA and their Natural Substrates

- What are the determinants for the unique NADPH specificity of saFabI?
- Does the thioester carbonyl of the saFabI enoyl-substrate bind to Tyr147 or Tyr157? For details on this topic see also chapter 1.4.1.
- What are the substrate binding modes of the enoyl-, acyl-, and malonyl-substrates? Where is the phosphopantetheine linker located in the catalytically competent saFabI and KasA complexes?
- Which reaction mechanisms are operative in saFabI and KasA? What is the proton source for the protonation of the enolate intermediate formed during the saFabI catalyzed reaction? How is the malonyl-group positioned within the KasA active site and which residue is responsible for the decarboxylation of the second AcpM substrate? For details on this topic see also chapters 1.4.1 and 1.4.3.
- Where does the acyl carrier protein bind on the surface of saFabI and KasA? For details on this topic see also chapter 1.3.2.

- How do the saFabI and KasA enzymes recognize their ligands? Which conformational changes occur upon substrate binding? Can we target such conformational states along the reaction coordinate? For details on this topic see also chapters 1.4.1 and 1.4.3.
- How does KasA achieve recognition and binding of very long and hydrophobic mycolic acid precursors? For details on this topic see also chapters 1.3.5 and 1.4.3.
- How do saFabI and KasA differ from orthologous proteins given their unique capability to turnover BCFA or mycolic acid precursors, respectively? Can this knowledge be used for the design of new antibacterials?

1.5.3 Questions Concerning the Inhibition of SaFabI and KasA

- What are the binding modes of saFabI diphenyl ether and pyridone inhibitors? Do these two inhibitor scaffolds differ with respect to their binding poses and inhibitory mechanisms despite their structural similarity? How does the saFabI-NADPH-CG400549 ternary complex look like? Can the observed intermolecular interactions be related to binding affinity? Can we rationalize the residence time of these inhibitors? For details on this topic see also chapters 1.2.4 and 1.4.2.
- Is the *Staphylococcus*-restricted activity spectrum of CG400549 and AFN-1252 reflected in the affinity of these molecules towards FabI enzymes of different organisms? Why does MUT056399 display a broader antibacterial activity spectrum? For details on this topic see also chapter 1.4.2.
- What are the key features of high-affinity FabI inhibitors? Can we rationally improve the affinity and residence time of saFabI inhibitors? What can we learn from our saFabI case study for the residence time concept in general? Can we use the combined knowledge about saFabI to derive new promising inhibitors which are active against MRSA? For details on this topic see also chapters 1.2.4 and 1.4.2.
- How do C3-substitued TLM-derivates bind to KasA? Do these findings correlate to binding affinity trends (16)? For details on this topic see also chapter 1.4.4.
- How can the TLM scaffold be rationally improved with respect to its inhibitory properties? For details on this topic see also chapter 1.4.4.
- Can we derive alternative strategies to target saFabI or KasA?

2 *Staphylococcus aureus* FabI: Inhibition, Substrate Recognition, and Potential Implications for In Vivo Essentiality

This chapter is based on the following publication:

Schiebel, J.*, Chang, A.*, Lu, H., Baxter, M. V., Tonge, P. J., and Kisker, C. (2012) *Staphylococcus aureus* FabI: Inhibition, Substrate Recognition, and Potential Implications for In Vivo Essentiality. *Structure* **20**, 802-813

Copyright:

Reprinted with permission from (19). Copyright 2012 Elsevier.

Author contributions with respect to data collection:

Schiebel, J.:	Expression and purification[‡], X-ray crystallography[‡], analytical size exclusion chromatography
Chang, A.:	Enzyme kinetics, mutagenesis
Lu, H.:	Enzyme kinetics
Baxter, M.V.:	Synthesis of branched-chain fatty acid substrate analogs

*These authors contributed equally

[‡] Initial work had already been performed in the context of the diploma thesis (the main result was the low-resolution $P2_12_12_1$ saFabI-$NADP^+$-triclosan crystal structure) and provided a basis for these studies.

Staphylococcus aureus FabI: Inhibition, Substrate Recognition and Potential Implications for *In Vivo* Essentiality

Johannes Schiebel,[1,¶] Andrew Chang,[2,3,¶] Hao Lu,[2] Michael V. Baxter,[2] Peter J. Tonge,[2,*] Caroline Kisker[1,*]

[1]Rudolf Virchow Center for Experimental Biomedicine, Institute for Structural Biology, University of Würzburg, Josef-Schneider-Str. 2, D-97080 Würzburg, Germany

[2]Institute for Chemical Biology & Drug Discovery, Department of Chemistry, Stony Brook University, Stony Brook, New York 11794-3400, USA

[3]Medical Scientist Training Program, Stony Brook University, Stony Brook, New York 11794-3400, USA

[*]Correspondence: peter.tonge@sunysb.edu (P.J.T.)
caroline.kisker@virchow.uni-wuerzburg.de (C.K.)

[¶]These authors contributed equally to this work.

2.1 Summary

Methicillin-resistant *Staphylococcus aureus* (MRSA) infections constitute a serious health threat worldwide, and novel antibiotics are therefore urgently needed. The enoyl-ACP reductase (saFabI) is essential for the *S. aureus* fatty acid biosynthesis and, hence, serves as an attractive drug target. We have obtained a series of snapshots of this enzyme which provide a mechanistic picture of ligand and inhibitor binding including a dimer-tetramer transition combined with extensive conformational changes. Significantly, our results reveal key differences in ligand binding and recognition compared to orthologous proteins. The remarkable observed protein flexibility rationalizes our finding that saFabI is capable of efficiently reducing branched-chain fatty acid precursors. Importantly, branched-chain fatty acids represent a major fraction of the *S. aureus* cell membrane and are crucial for its *in vivo* fitness. Our discovery thus addresses a long-standing controversy regarding the essentiality of the fatty acid biosynthesis pathway in *S. aureus* and validates saFabI as a drug target.

2.2 Highlights

- Insights into saFabI ligand binding including a dimer-tetramer transition
- Identification of a loop motif that determines altered cofactor specificity
- Increased flexibility modulates substrate and inhibitor recognition
- Ability of saFabI to reduce branched-chain fatty acid precursor molecules

2.3 Introduction

Resistant strains of the Gram-positive human pathogen *Staphylococcus aureus* emerged only two years after the introduction of the antibiotic methicillin in 1959. Since then, methicillin-resistant *S. aureus* (MRSA) infections have become an increasing problem in hospitals worldwide. To treat severe MRSA infections, vancomycin is currently used as the drug of last resort (29). Thus, the initial occurrence of a vancomycin-resistant *S. aureus* (VRSA) strain in June 2002 is especially alarming (143). Unfortunately, antibiotic resistance has drastically outpaced new antibiotic discovery, which flourished between the 1940s and 1960s. Between 1962 and 2000 only a few novel scaffolds like the carbapenems were approved, and novel antibiotics with alternative modes of actions are therefore urgently needed. Accordingly, from 2000 onwards oxazolidinones (e.g. linezolid), the lipopeptide daptomycin and the mutilins were introduced (20).

One strategy that targets the bacterial cell envelope involves the inhibition of the type II fatty acid biosynthesis pathway (FAS II), which is responsible for the *de novo* production of phospholipid precursor molecules (50). In contrast to the large multifunctional mammalian FAS I synthase, the FAS II system of bacteria, protozoa and plants consists of individual monofunctional enzymes, allowing selective inhibition (7). In this pathway, the fatty acid chain, which is attached to the acyl carrier protein (ACP), is elongated by two carbon atoms per cycle (Figure 2-1). The final reduction is catalyzed by the NAD(P)H-dependent *trans*-2-enoyl-ACP reductase (FabI), which is known to play a key regulatory role in this pathway (63,78). This enzyme is highly conserved across many pathogens, however, the *S. aureus* enoyl-ACP reductase (saFabI) is the only known FabI with a clear preference for NADPH (51,78,108,144). The clinical success of FabI inhibitors, such as the first-line tuberculosis prodrug isoniazid (67) and several compounds currently in phase I clinical trials (103), validates this enzyme as an attractive drug target. Furthermore, the FabI diphenyl ether inhibitor triclosan (TCL) is recommended as topical antiseptic to reduce MRSA skin colonization (116).

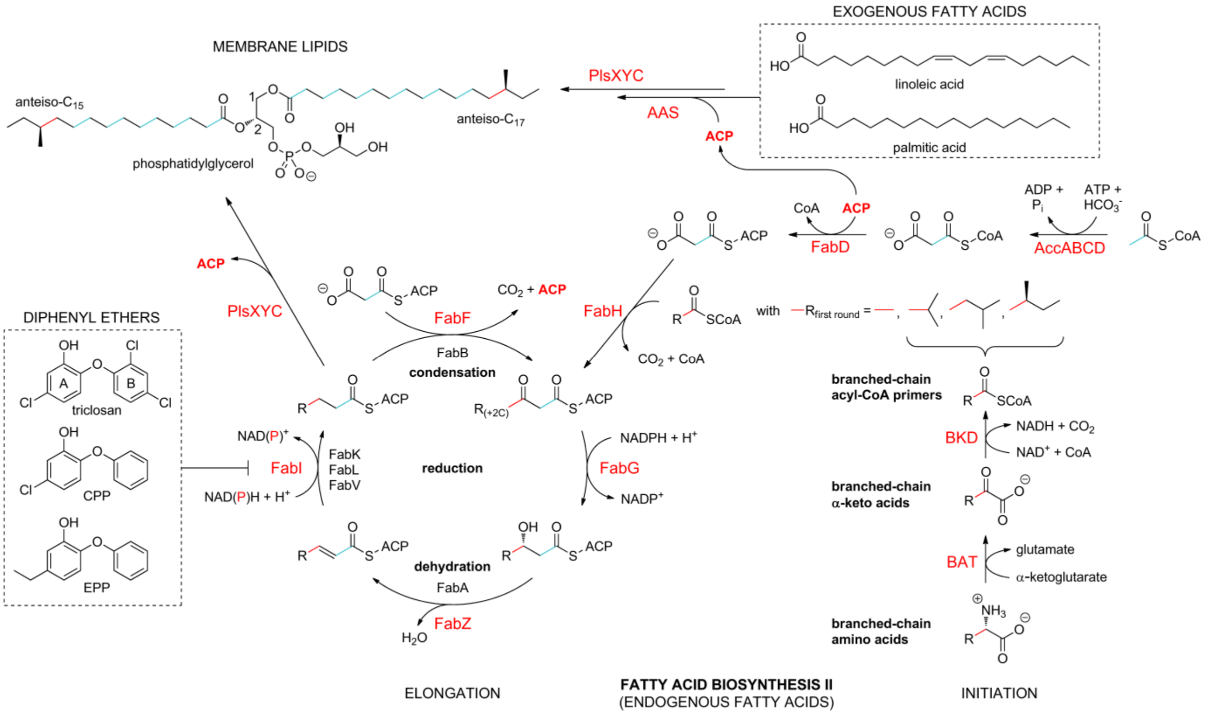
EXOGENOUS FATTY ACIDS
linoleic acid
palmitic acid
MEMBRANE LIPIDS
anteiso-C_{15}
anteiso-C_{17}
phosphatidylglycerol
PlsXYC
AAS
ACP
CoA
ACP
FabD
ADP + P_i
ATP + HCO_3^-
AccABCD
ACP
PlsXYC
FabF
CO_2 + ACP
FabB
condensation
FabH
with $-R_{first\ round}$ =
CO_2 + CoA
branched-chain acyl-CoA primers
BKD
NADH + CO_2
NAD^+ + CoA
branched-chain α-keto acids
BAT
glutamate
α-ketoglutarate
branched-chain amino acids
DIPHENYL ETHERS
triclosan
CPP
EPP
$NAD(P)^+$
FabI
FabK
FabL
FabV
NAD(P)H + H^+
reduction
NADPH + H^+
FabG
$NADP^+$
dehydration
FabA
FabZ
H_2O
ELONGATION
FATTY ACID BIOSYNTHESIS II
(ENDOGENOUS FATTY ACIDS)
INITIATION

Figure 2-1. The bacterial type II fatty acid biosynthesis pathway as a drug target. *S. aureus* enzymes are shown in red, while isoforms in other organisms are depicted in black (7). Initiation of fatty acid biosynthesis requires malonyl-ACP, formed from acetyl-CoA by acetyl-CoA carboxylase (Acc) and malonyl-CoA:ACP transacylase (FabD). The β-ketoacyl-ACP synthase FabH (KAS III) performs the first Claisen condensation yielding a β-ketoacyl-ACP from malonyl-ACP and an acyl-CoA primer. The two carbons originating from malonyl-ACP are shown in cyan and the first two primer carbons in red. Subsequently, the β-ketoacyl-ACP is converted to a saturated acyl-ACP by the actions of the NADPH-dependent reductase FabG, the dehydrase FabZ, and the mostly NADH-dependent enzyme FabI. The saturated acyl-ACP is a substrate for additional rounds of elongation in which FabF catalyzes the condensation reaction. The long-chain acyl-ACP products are subsequently partially transformed into membrane lipids (a typical *S. aureus* phosphatidylglycerol is shown (89)). Most bacteria use acetyl-CoA as the primer which results in straight-chain fatty acids (C_{14} and C_{16}) (56), however, *S. aureus* FabH prefers branched-chain acyl-CoAs which yield branched-chain fatty acids (57). The branched-chain primers isobutyryl-CoA, isovaleryl-CoA and 2-methylbutyryl-CoA are derived from valine, leucine and isoleucine, respectively, through the actions of the branched-chain aminotransferase BAT (*ilvE* (145)), and the branched-chain α-ketoacid dehydrogenase BKD (*lpd*, *bkdA1*, *bkdA2* and *bkdB* (146)). The branched-chain acyl-CoAs yield iso-C_{14} and iso-C_{16} (isobutyryl), iso-C_{15} and iso-C_{17} (isovaleryl), and anteiso-C_{15} and anteiso-C_{17} (2-methylbutyryl) fatty acids (56). Exogenous fatty acids are converted into acyl-ACPs by the acyl-ACP synthetase (AAS) for incorporation into cell membranes. Typical fatty acids of the human blood plasma are palmitic (21.3%) and linoleic acid (23.7%) (147). For *S. aureus*, exogenous oleic acid was only incorporated in the 1-position of phosphatidylglycerol (89). Inhibitors of the NADPH-dependent FabI from *S. aureus* (saFabI) used in this study include 5-chloro-2-(2,4-dichlorophenoxy)phenol (triclosan), 5-chloro-2-phenoxyphenol (CPP) and 5-ethyl-2-phenoxyphenol (EPP) (78). See also Figure S 2-1.

Recently, however, Brinster et al. challenged the validity of FAS II inhibitors as *Streptococcus agalactiae* can utilize exogenous fatty acids from the host blood serum to survive inhibition of its FAS II machinery (90). Whether this resistance mechanism extends to all Gram-positive bacteria including *S. aureus* is currently controversially discussed (88,89). Importantly, *S. aureus* remains sensitive to FabI inhibitors *in vivo,* as shown in several rodent models (50,88,91,92).

To investigate the suitability of saFabI as a drug target, we have structurally and biochemically characterized this enzyme with respect to inhibitor binding, conformational flexibility, ligand binding mechanism, cofactor and substrate specificity, quaternary structure and cooperativity. We identified significant differences in the *S. aureus* and *Bacillus* FabIs compared to the classical FabI proteins from organisms such as *Escherichia coli*, *Burkholderia pseudomallei* and *Francisella tularensis*; and of our structures with respect to the recently determined *S. aureus* FabI structures in complex with triclosan and in its apo-state (144). Importantly, our analysis revealed that the substrate specificity of saFabI displays an increased specificity for branched-chain (BCFA) relative to straight-chain fatty acid (SCFA) precursors (Figure S 2-1), consistent with the high content of BCFAs in the membranes of *Staphylococci* and *Bacilli* (86). Since BCFAs, which are barely found in human serum (147), are likely required for *S. aureus* fitness *in vivo*, we conclude that saFabI is a suitable target for drug discovery.

2.4 Results

2.4.1 Overall Structure

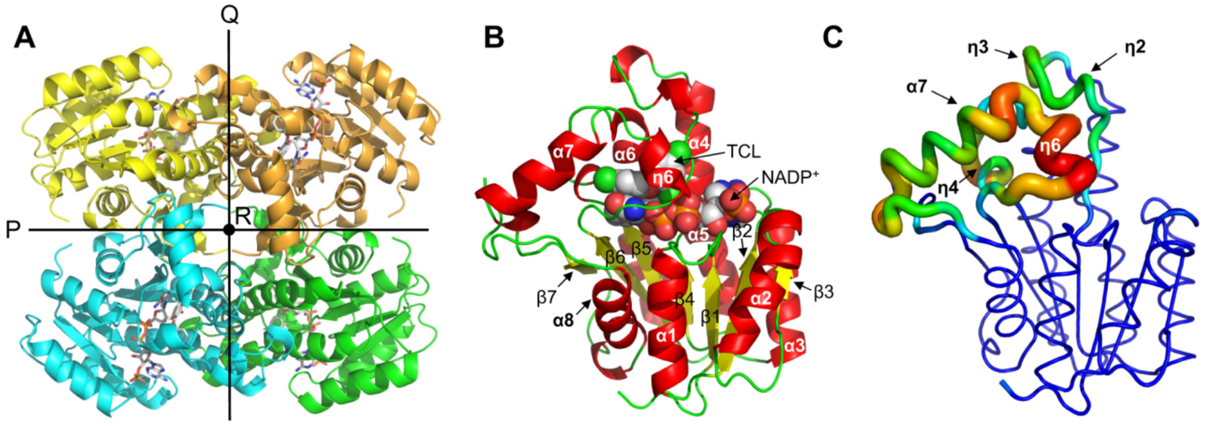

Figure 2-2. Overall structure and flexibility of saFabI. (A) Homo-tetrameric structure of saFabI. Each subunit of the TCL-2 structure is shown in a different color. The three perpendicular 2 fold non-crystallographic symmetry axes P, Q and R are indicated. The interfaces spanned by the axes P and R (Q and R) are referred to as the PR-(QR-) interface. **(B)** Structure of the saFabI monomer. α-Helices are shown in red, β-strands in yellow, loops in green, cofactor and inhibitor as space-filling models in grey. The chair-like structure consists of the Rossmann-fold (seat, lower part) and the active site (back, upper part). **(C)** Flexibility of the saFabI active site in its ligand-free form. Multi-rmsd values were calculated for the C_α atoms of the apo-1 (one subunit), apo-2 (all subunits) and TCL-2 (one subunit) structures using LSQMAN (148). These values varied from 0.2 to 20.5 Å and are represented by color (from blue to red) and width of the TCL-2 model (residues 2-256). Rmsd-values for the missing residues 199-201 were interpolated in a linear fashion based on the values for the two adjacent amino acids 198 and 202. See also Figure S 2-2.

To provide a molecular basis for the rational design of compounds that target saFabI, we solved the structures of ternary FabI complexes with the cofactor $NADP^+$ and the diphenyl ether inhibitors triclosan (TCL), 5-chloro-2-phenoxyphenol (CPP) or 5-ethyl-2-phenoxyphenol (EPP), respectively (Figure 2-1, Figure S 2-1 and Figure S 2-2). As a member of the short-chain dehydrogenase/reductase (SDR) superfamily, saFabI contains an extended Rossmann-fold comprised of a central seven-stranded parallel β-sheet surrounded by three α-helices on either side (Figure 2-2B) (67,105). Furthermore, the structures of our saFabI inhibitor complexes clearly show the presence of homo-tetramers (Figure 2-2A) as observed in other organisms (51). The closest relationship is found with the FabI structures from the Gram-positive organisms *Bacillus anthracis* and *B. subtilis* as well as with the incorrectly designated "FabL" from *B. cereus* which is 100% identical to *B. anthracis* FabI (Figure 2-3).

In addition, we solved two apo saFabI structures which display unexpected flexibility in close proximity to the binding site (Figure 2-2C). In one of the two apo structures all four monomers (apo-2; nomenclature of all structures according to Table S 2-1 and Table S 2-2) differ in their active site (pairwise rmsd of 0.84 Å) and display conformations that, to our knowledge, have never been observed before. Compared to the inhibitor-bound complexes, three regions - the active site and two substrate-binding loops (Figure 2-3) - are either disordered or visible in a rearranged architecture. In contrast, previously published apo structures of FabI proteins from Gram-negative bacteria (PDB codes: 2JJY, 2P91, 2WYU, 3EK2, 3GRK, 3K2E) show disorder in only one region, the substrate-binding loop.

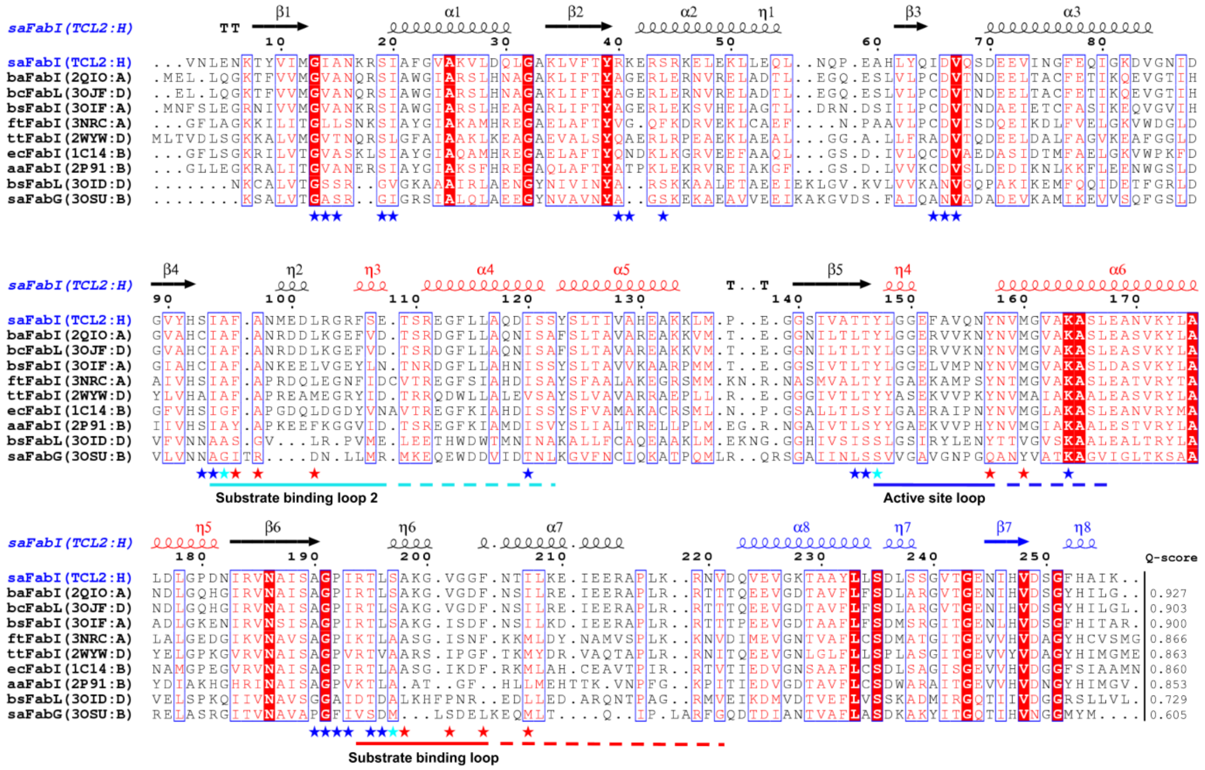
saFabI(TCL2:H)
TT
β1
α1
β2
α2
η1
β3
α3
β4
η2
η3
α4
α5
T..T
β5
η4
α6
η5
β6
η6
α7
α8
η7
β7
η8
Q-score
saFabI(TCL2:H)
baFabI(2QIO:A)
bcFabL(3OJF:D)
bsFabI(3OIF:A)
ftFabI(3NRC:A)
ttFabI(2WYW:D)
ecFabI(1C14:B)
aaFabI(2P91:B)
bsFabL(3OID:D)
saFabG(3OSU:B)
0.927
0.903
0.900
0.866
0.863
0.860
0.853
0.729
0.605
Substrate binding loop 2
Active site loop
Substrate binding loop

Figure 2-3. Secondary structure of saFabI and alignment with similar proteins. Secondary structure matching (SSM) was performed for the TCL-2 structure using PDBe Fold (149). The secondary structure of saFabI is shown in the first line according to the program DSSP (150). Secondary structure elements participating in the QR and PR-interfaces are depicted in red and blue, respectively. Amino acids highlighted in red are conserved. The alignment comprises the 7 best SSM hits (Q-scores are indicated behind the sequences) including bsFabL and saFabG. The first two letters of the protein names indicate the bacterial source (sa = *S. aureus*, ba = *Bacillus anthracis*, bc = *B. cereus*, bs = *B. subtilis*, ft = *Francisella tularensis*, tt = *Thermus thermophilus*, ec = *Escherichia coli*, aa = *Aquifex aeolicus*). PDB codes and subunits are given in parentheses. Blue, red and cyan stars mark residues interacting with the cofactor, inhibitor or cofactor and inhibitor, respectively. Disordered or rearranged regions in all four available saFabI apo structures (apo-1, apo-2, 3GNS, 3GNT) are marked with a continuous line, regions which are additionally disordered or rearranged for distinct apo structures are represented by a dashed line. This Figure was prepared with ESPript (151).

2.4.2 SaFabI Inhibition

Table 2-1. Potency of saFabI inhibition by diphenyl ether analogues.

Inhibitor	$K_i^{*,app}$ (nM)
CPP	161.2 ± 8.4
EPP	106.6 ± 7.9
Triclosan	60.9 ± 5.6

In contrast to the previously described saFabI-NADP$^+$-TCL structure (PDB code: 3GR6) (144), our high-resolution saFabI complex structures with the unsymmetrically substituted inhibitors EPP and CPP unequivocally reveal a similar binding mode of diphenyl ethers including triclosan to saFabI as reported for homologous FabI proteins (67,78) which allows the formation of two key hydrogen bonds connecting the A-ring hydroxyl group to Tyr157 and to the 2'-OH of the nicotinamide ribose at 2.5 ± 0.1 and 2.6 ± 0.1 Å, respectively (Figure 2-4B). TCL, CPP and EPP bind to a pocket composed of $NADP^+$ and several mainly hydrophobic residues with average distances of 3.8 ± 0.4 Å (Figure 2-4B and Figure 2-4C). Notably, the carbonyl oxygen of Ala97 forms a geometrically favorable halogen bond (152) with the TCL B-ring chlorine at position 4 (3.2 ± 0.1 Å). At the same time the chlorine is weakly hydrogen bonded to the amide NH group of Ala97 (3.2 ± 0.1 Å, Figure 2-4B). Accordingly, TCL exhibits an almost 3-fold lower $K_i{}^{*,app}$ value as compared to CPP, which lacks the two B-ring chlorines and is rotated by 11 ± 2° into the binding crevice (Table 2-1, Figure 2-4D and Supplemental Results).

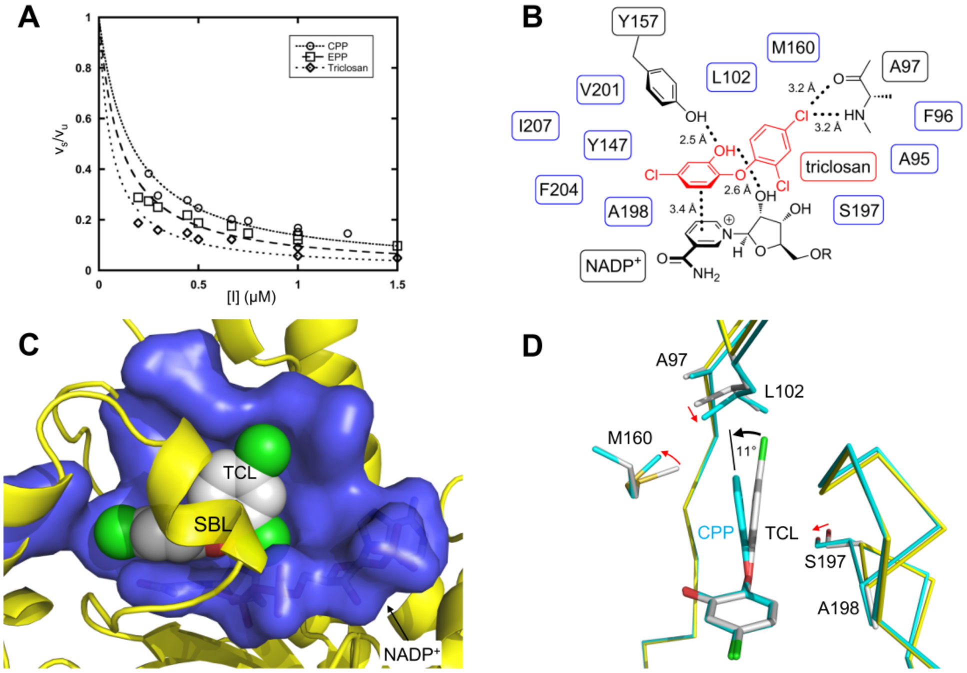

Figure 2-4. SaFabI inhibition with diphenyl ethers. (A) Dose-response curves of diphenyl ether analogues. The steady-state reaction velocities (v_s) at various inhibitor (CPP, EPP, triclosan) concentrations are plotted as a fraction of the uninhibited reaction velocity (v_u). Each plot is fitted to the standard binding isotherm. R^2 = 0.88, 0.75 and 0.73 for the best fit curves to the binding isotherm for CPP, EPP and triclosan, respectively. **(B)** Schematic representation of all residues interacting with triclosan (TCL in red). The interaction pattern was derived from the TCL-2 structure. Directional interactions are depicted explicitly (black residues), amino acids creating the hydrophobic pocket are included in 1-letter code (residues in blue boxes). R = adenosine diphosphate. **(C)** Fit of triclosan in its binding pocket. Triclosan is shown as space filling model in grey. Ala95, Phe96, Ala97, Leu102, Tyr147, Tyr157, Met160, Ile207 and $NADP^+$ are shown in surface representation in blue. Additionally interacting residues Ser197, Ala198, Val201 and Phe204 are located within the substrate-binding loop (SBL). **(D)** Comparison of the TCL and CPP inhibitor binding modes. The TCL-2 structure is shown in grey and yellow, the CPP structure in blue. The cofactor and some protein regions are omitted for clarity. Arrows indicate differences between the two structures. The B-ring is rotated by ~11 ± 2° upon removal of the two chlorine atoms. Simultaneously, the C_α atoms of Ala97, Leu102, Ser197 and Ala198 move towards the inhibitor by about 0.4 ± 0.1 Å, 0.3 ± 0.1 Å, 0.3 ± 0.1 Å and 0.2 ± 0.1 Å, respectively, and the side chain of Met160 rotates away from the inhibitor by ~13 ± 3°.

2.4.3 Induced Fit Ligand Binding

SaFabI undergoes several major conformational changes upon cofactor and inhibitor binding, which have, to our knowledge, never been observed previously for its Gram-negative FabI orthologs, thus allowing us to describe a fundamentally expanded mechanism for ligand binding. All residues interacting with the diphenyl ether inhibitors are located in three distinct regions (Figure 2-3), which exhibit substantial flexibility prior to cofactor and inhibitor binding. As described for numerous FabI orthologs and other SDR proteins, the substrate-binding loop (SBL, 194-204) is disordered or rearranged in our apo structures (6,105). In contrast to other FabI structures, however, the saFabI structures reveal flexibility of a second substrate-binding loop (SBL-2, 94-108) as well as the active site loop (ASL, 147-157).

Superposition of the apo-1 structure with TCL-2 shows that the active site is wide open prior to cofactor and inhibitor or substrate binding (Figure 2-5A). In addition to the three aforementioned loop regions, the C-terminal SBL extension α7 is disordered. The apo-2 structure provides informative snapshots of α7's motion on its way to the ternary complex conformation as every subunit shows a different arrangement of this helix (Figure 2-5B-F and Movie S 2-1). In one subunit, this helix is shifted ~13 Å away from the active site (Figure 2-5B). When helix α7 moves towards the protein core, it is still rotated about 105° relative to the ternary complex conformation (Figure 2-5C) and assumes its final conformation via rotation angles of 70° and 20° (Figure 2-5D-F). Intermittently, the adjacent helix α8 is elongated by up to two turns (Figure 2-5C-D). Finally, the N-terminally attached SBL closes upon actual cofactor and inhibitor binding.

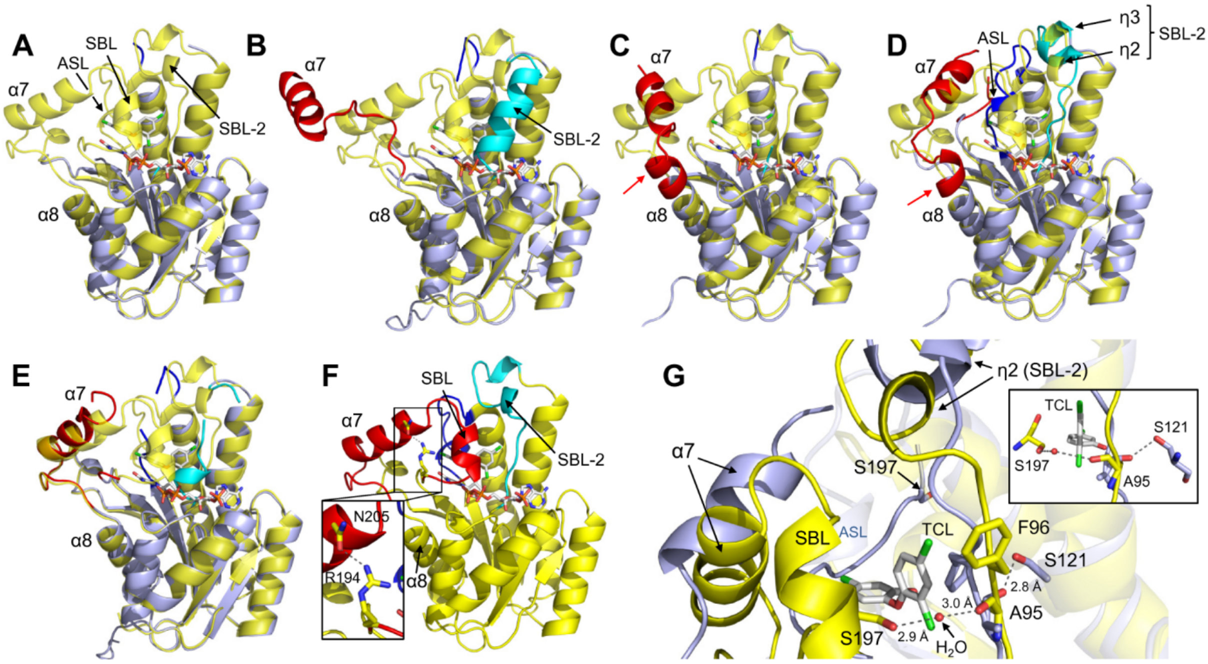

Figure 2-5. Cofactor and inhibitor binding mechanism. Panels A to F show consecutive conformations of saFabI proposed to be adopted during cofactor and inhibitor binding. The three regions undergoing the most extensive conformational changes are highlighted (SBL-2 in cyan, ASL in dark blue and the C-terminally extended SBL in red as in Figure 2-3). One subunit of TCL-2 is continuously shown as a reference in yellow. **(A)** Superposition of the apo-1 and TCL-2 structures. Apo-1 is shown in light blue. **(B-E)** Superposition of the apo-2 and TCL-2 structures. Subunits B, C, A and D of apo-2 are shown in light blue. **(F)** Final ternary complex conformation. The hydrogen bonded residues Arg194 and Asn205 can act as a hinge for SBL-1 closure and are displayed in a larger scale in the black box (153). **(G)** Peptide flip mechanism and SBL-2 closure observed upon superposition of TCL-2 (yellow) with apo-2 (light blue, subunit A). The carbonyl oxygen of Ala95 flips between Ser121 in the apo structure and a water molecule bound to Ser197 in the ternary complex (a rotated view is displayed in the insert). See also Figure S 2-4 and Movie S 2-1.

During this process, the ASL is visible inside the ligand-binding pocket (Figure 2-5D) and SBL-2 adopts an entirely α-helical conformation (Figure 2-5B). Subsequently, SBL-2 is split into the 3_{10}-helices η2 and η3 and adopts a more open conformation (Figure 2-5D,G). A comparison with the ternary complex structure TCL-2 shows that a backbone flip of Ala95 propagates the movements of adjacent residues and leads to the subsequent closure of SBL-2 (Figure 2-5G). This peptide flip may be induced by the ordering of Ser197 located on the SBL, which allows the formation of a water-mediated hydrogen bond interaction with the carbonyl oxygen of Ala95. Simultaneously, the movement of Phe96 creates space for the binding of the TCL B-ring and establishes an elongated acyl-channel. During NADP$^+$ binding, a similar peptide flip mechanism was observed for the NADPH-dependent β-ketoacyl-ACP reductase ecFabG, which also belongs to the SDR family of proteins (154).

We speculate that the concerted closure of both SBLs, instead of just the classical SBL, is the conformational change corresponding to the slow step of the slow-binding inhibition (67). Based on sequence similarities, this mechanism should mainly be feasible for *Staphylococci*, several *Bacilli* and some *Listeria* strains since they contain a serine at position 197, which connects the SBLs (Figure 2-5G). Most other Gram-negative and Gram-positive bacteria harbor an alanine at this position and, thus, lack the required hydrogen bond acceptor (Figure 2-3). Consistently, all structurally characterized FabIs from Gram-negative organisms contain just a single flexible SBL (PDB codes: 2JJY, 2P91, 2WYU, 3EK2, 3GRK, 3K2E), as opposed to *Bacillus* FabIs (3OIF, 3OJE) and the related proteins bsFabL (3OIC) and ecFabG (1I01) which all feature three disordered or rearranged regions in their apo structure.

2.4.4 Dimer - Tetramer Transition

The apo FabI structures from Gram-negative bacteria contain homo-tetramers, whereas bcFabI/baFabI, in the absence of cofactor and inhibitor, were reported to be dimers in the crystal and in solution (155). So far, reports regarding the oligomeric state of saFabI have been inconsistent. It was noted that the published apo structures of saFabI (3GNS, 3GNT) are comprised of dimers, though the enzyme was found to be a tetramer in solution (144,155). Therefore two questions arose: What is the oligomeric state of saFabI prior to ligand binding? If dimers are present, does tetramerization and active site formation occur in a concerted fashion with cofactor and inhibitor binding as hypothesized for bsFabL (156)?

Our results clearly show that NADP$^+$ and triclosan binding to dimeric saFabI induces simultaneous active site formation and tetramerization. In contrast to a previous report but in accordance with the respective apo saFabI structures (3GNS, 3GNT) (144), we identified a dimer through analytical size exclusion chromatography (SEC) experiments at pH 8.0 (Figure S 2-3A), whereas tetramers are present at pH 5.6 (see Experimental Procedures for details). We performed further analytical SEC experiments with the dimeric enzyme in its apo form or incubated with NADP$^+$, NADPH or NADP$^+$ and TCL. Our results unambiguously demonstrate a transition between dimers and tetramers upon both inhibitor and cofactor binding (Figure S 2-3B), whereas binding of oxidized or reduced cofactor alone is not sufficient to induce tetramerization.

A structure and interface analysis of all available saFabI structures provides snapshots of the dimer - tetramer transition in the order 3GNT, 3GNS, apo-1, apo-2, TCL-2 (Figure 2-6 and Movie S 2-2). During this process, the buried surface area of the QR-interface, about which the association occurs, increases significantly, as does the number of hydrogen bonds and salt bridges between interface residues (Figure 2-6C). The QR-interface is established via a 4-helix bundle comprising the long helices α4/α5 (kinked) and α6 (Figure 2-6, last column). Additionally, the corresponding N-terminal extensions η3 and η4 further stabilize this interface (Figure 2-3). Since the SBL-2 and ASL regions including these 3_{10}-helices are disordered in our apo structures, the QR-interface is destabilized and the dimers move slightly (~2 Å) away from one another. During the ordering of the ASL, the full tetramer interface and the catalytic active site are simultaneously established (Figure S 2-4). The 3GNS structure clearly contains dimers due to the additionally disordered α4 region (Figure 2-3). This helix is therefore essential for the maintenance of the QR-interface. Whereas helix α6 of 3GNS is almost completely structured and just slightly shifted, the N-terminal portion of this helix is unstructured and partially disordered in 3GNT.

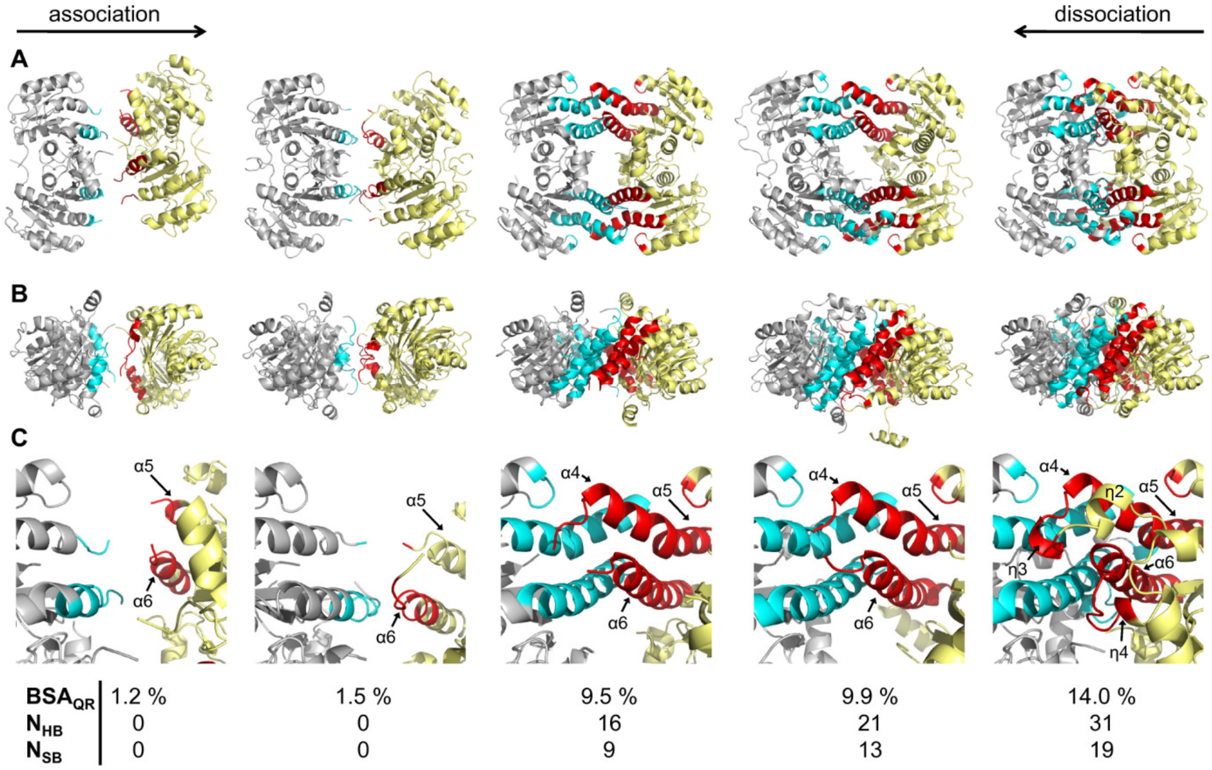
association
dissociation
A
B
C
α5
α6
α5
α6
α4
α5
α6
α4
α5
α6
α4
η2
α5
η3
α6
η4
BSA_{QR} | 1.2 % | 1.5 % | 9.5 % | 9.9 % | 14.0 %
N_{HB} | 0 | 0 | 16 | 21 | 31
N_{SB} | 0 | 0 | 9 | 13 | 19

Figure 2-6. Dimer - tetramer transition. From left to right the QR-interface in the saFabI crystal structures 3GNT, 3GNS (144), apo-1, apo-2 and TCL-2 is shown to illustrate tetramer association and dissociation (view as in Figure 2-2A). The two associating dimers are shown in grey and yellow with the respective QR-interface residues (according to the PDBe PISA server (157)) in cyan and red. **(A)** Front view of the dimer - tetramer transition. **(B)** Side view of the dimer - tetramer transition. **(C)** Close up view of the upper QR-interface half. Buried surface areas of the monomeric QR-interface (BSA_{QR}) as well as the numbers of the corresponding hydrogen bonds (N_{HB}) and salt bridges (N_{SB}) are given below according to PISA. See also Figure S 2-3 and Figure S 2-5 as well as Movie S 2-2.

2.4.5 Cooperativity

We hypothesize that the dimer - tetramer transition also applies to substrate binding, representing the molecular basis for the previously reported positive cooperative binding of NADPH to saFabI (108). Our data clearly show that NADPH binds cooperatively to saFabI with an approximate Hill coefficient h = 2 (Figure S 2-5). Additionally, *trans*-2-octenoyl-CoA bound cooperatively to saFabI with a Hill coefficient h = 2.3. However, glutamate, which enhances the catalytic activity of the enzyme (Supplemental Discussion), was found to alter the cooperativity of binding to saFabI. In the presence of 1 M potassium glutamate, no cooperativity was observed for the binding of NADPH or *trans*-2-octenoyl-CoA to saFabI. Since cooperativity was still observed in the presence of 250 mM potassium glutamate, which is an upper limit estimate of the average *S. aureus* intracellular glutamate concentration (158,159), it is likely to be physiologically relevant. Mechanistically, the observed positive cooperativity of substrate binding could be transferred via the ligand-interacting SBL-2 and ASL regions and the attached long helices α4 and α6, which primarily constitute the QR-interface. The formation of such an interface would enhance cofactor and inhibitor/substrate binding due to the rearrangement of the two loop regions and vice versa. Cooperativity has, to our knowledge, never been observed for NADH-dependent wild-type FabI enzymes, which already exist as tetramers in their apo forms (72). In contrast, a similar FabI tetramerization process might be possible for *Bacillus* species as α4 is additionally disordered in the dimeric bcFabI/baFabI apo structure (PDB code: 3OJE:A) (155). Similarly, the twisted tetramer architecture of the bsFabL apo structure (3OIC:A) comprises N-terminally shifted α4 and α6-helices and therefore links this protein to saFabI (156).

2.4.6 Cofactor Specificity

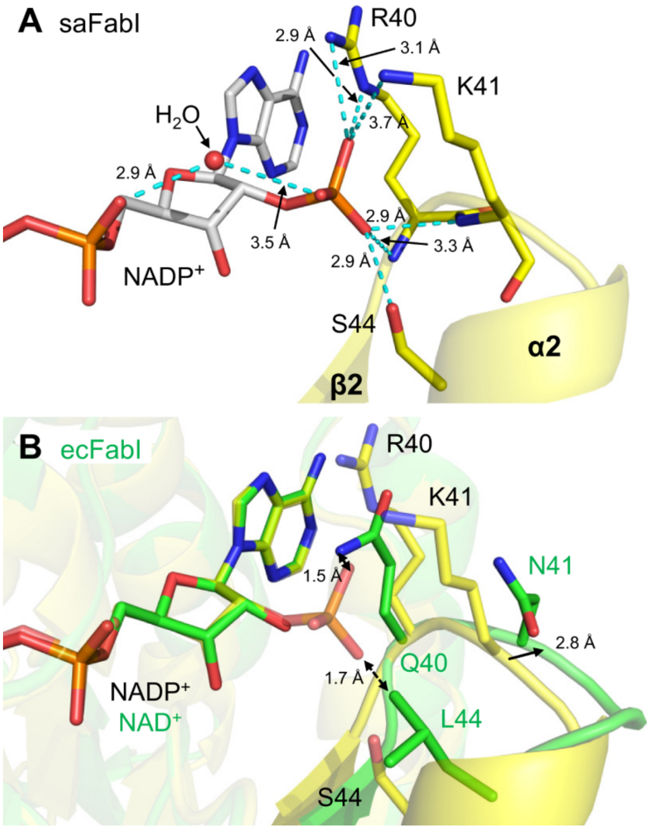

Figure 2-7. Structural basis of NADPH specificity. (A) The 2'-phosphate binding motif. $NADP^+$ is shown in grey, saFabI (CPP structure) in yellow. Additional parts of the protein are omitted for clarity. **(B)** Superposition of saFabI and ecFabI. SaFabI is shown in yellow, ecFabI (1QSG:A) in green. Asn41 is shifted 2.8 ± 0.3 Å towards the solvent compared to Lys41 preventing 2'-phosphate stabilization by an Asn41 backbone interaction.

The studies described above reveal fundamental differences between saFabI and classical FabI proteins. Hence, we also investigated cofactor specificity since, in contrast to all Gram-negative FabI homologues studied thus far, saFabI prefers NADPH instead of NADH as the reducing agent (51,108). Our structural analysis confirmed that the positively charged side chains of Arg40 and Lys41 are important for binding the additional 2'-phosphate of NADPH (78,144) (Figure 2-7A). However, we identified an RKXXS-motif that confers this unique specificity to saFabI. While the R40Q/K41N saFabI double mutant exhibited a drastically decreased k_{cat}/K_m value for NADPH, the specificity constant remained low for NADH (78). Our structures revealed Ser44 as a third crucial residue for NADPH specificity. The serine hydroxyl group forms a hydrogen bond to one of the phosphate oxygen atoms at a distance of 2.9 ± 0.1 Å, while the Ser44-bound phosphate oxygen forms additional hydrogen bonding interactions with the backbone amide nitrogens of Arg40 and Lys41, which are located in a tight loop between β2 and α2 (Figure 2-7A).

Unlike saFabI, the enoyl-ACP reductase from *E. coli* (ecFabI) is NADH-dependent (111). Superposition of saFabI with ecFabI shows that Leu44 and Gln40 clash with the 2'-phosphate of a hypothetically bound NADPH (shortest distances of 1.7 ± 0.1 and 1.5 ± 0.2 Å, Figure 2-7B). Bulky substituents at position 44 (numbers according to saFabI), such as Leu or Phe (Figure 2-3), appear to shrink the adenine ribose-binding pocket, thus decreasing the affinity towards NADPH.

Table 2-2. Kinetic parameters for saFabI wild-type, double and triple mutant utilizing NADPH (top) and NADH (bottom) at saturating *trans*-2-octenoyl-CoA concentrations (150 µM).

	$K_{m,NADPH}$ (µM)	k_{cat} (min^{-1})	$k_{cat}/K_{m,NADPH}$ ($\text{min}^{-1}\ \mu\text{M}^{-1}$)
wt saFabI	189.4 ± 20.9	2171.2 ± 123.3	11.5 ± 1.4[1]
saFabI R40Q/K41N	> 300		0.066 ± 0.001[2]
saFabI R40Q/K41N/S44L	> 300		0.0038 ± 0.0002[2]

	$K_{m,NADH}$ (µM)	k_{cat} (min^{-1})	$k_{cat}/K_{m,NADH}$ ($\text{min}^{-1}\ \mu\text{M}^{-1}$)
wt saFabI	> 300		4.7 ± 0.2[2]
saFabI R40Q/K41N	139.8 ± 23.2	1852.1 ± 132.6	13.2 ± 2.4
saFabI R40Q/K41N/S44L	72.2 ± 26.4	1846.6 ± 266.3	25.6 ± 10.1

[1] Agrees with the linear slope (11.1 ± 0.3) of the Michaelis-Menten plot at low [NADPH]

[2] Estimated based on linear slope of the Michaelis-Menten plot at low [NAD(P)H]

To test the hypothesis that the RKXXS-motif is responsible for cofactor specificity, we generated a triple mutant with all three phosphate-interacting amino acids replaced by the respective *E. coli* residues (R40Q/K41N/S44L). Interestingly, compared to results reported in the absence of glutamate (78), there is only a 2.5-fold increase in the specificity constant of wild-type saFabI for NADPH relative to NADH in the presence of glutamate (Table 2-2). The glutamate-containing conditions also strongly affected the specificity constant of the R40Q/K41N mutant for NADH, which recovered to that of the wild-type enzyme for NADPH. Additionally, the specificity constant of the double mutant for NADH was 200-fold higher than for NADPH, compared to the 19-fold difference reported in the absence of glutamate. The triple mutant displayed an even more dramatic inversion of cofactor specificity with the specificity constant for NADPH nearly 10,000-fold lower than for NADH. This was driven mostly by a decrease in the ability to utilize NADPH, consistent with our prediction that Leu44 would clash with the 2'-phosphate. Interestingly, the $K_{m,NADPH}$ of wild-type saFabI is higher than the $K_{m,NADH}$ of the triple mutant (Table 2-2 and Table S 2-3) and other FabI homologues (109,160) which correlates well with the estimated higher microbial intracellular pool of NADPH compared to NADH (161,162).

Using BLAST and PHI-BLAST searches (163) with the newly identified RKXXS-motif, we found that this preference for NADPH links saFabI to all *Staphylococcus* and some *Bacillus* FabIs, as well as FabL and FabG, rather than to classical NADH-dependent FabIs.

2.4.7 Branched-Chain Substrate Specificity

What is the underlying biological significance of the structural variations we observed for the FabIs from *Staphylococci* and *Bacilli*? Notably, the membranes of *Staphylococcus* and *Bacillus* genera contain branched-chain fatty acids (BCFA) as a major component (86). In contrast, most other bacteria (86) predominantly synthesize straight-chain fatty acids (SCFA). For the more common SCFA family members, membrane fluidity is controlled by unsaturated fatty acids (UFA), whereas, for BCFA family members, 12-methyltetradecanoic acid (anteiso-C_{15}) primarily fulfills this purpose (86). Thus, we speculated that the increased mobility of FabI from *Staphylococci* and *Bacilli* allows the preferential binding of branched-chain substrates.

In addition to different straight-chain substrates (see Supplemental Results), we analyzed two branched-chain substrate analogues - *trans*-5-methyl-2-hexenoyl-CoA and **(±)-*trans*-4-**methyl-2-hexenoyl-CoA, which contains the precursor analog to the anteiso fatty acids found predominantly in the *S. aureus* membrane (89). Among the first-round substrates (Figure 2-1), the ratio of specificity constants is approximately 1:24:1 (straight = *trans*-2-butenoyl-CoA : iso : anteiso) (Table 2-3), although the substrate specificity of the anteiso-substrate may be higher depending on the stereospecificity of the enzyme. Considering that FabI is the rate-limiting enzyme in the FAS II pathway (63), this ratio is likely to be physiologically significant in determining the composition of fatty acids synthesized and incorporated into the cell membrane. Moreover, since the pool of first-round substrates entering the FAS II cycle is generated by the branched-chain specific *S. aureus* FabH enzyme, the synthesis of BCFAs should be highly favored in this pathway (see Supplemental Results for further details) (57). To substantiate the relevance of this observation, we explored the branched-chain substrate specificity of the NADH-dependent FabI enzyme from the Gram-negative pathogen *F. tularensis* (ftFabI). The ratio of specificity constants (Table S 2-3) for the shortest chain substrates is approximately 800:72:1 (straight : iso : anteiso) and hence fundamentally different from saFabI.

Table 2-3. Kinetic parameters for wild-type saFabI utilizing various *trans*-2-enoyl-CoA substrates. See also Figure S 2-1 and Table S 2-3.

	$K_{m,acyl\text{-}CoA}$ (µM)[1]	k_{cat} (min^{-1})[1]	$k_{cat}/K_{m,acyl\text{-}CoA}$ (min^{-1} μM^{-1})
trans-2-butenoyl-CoA	1278.3 ± 120.2	40.1 ± 1.8	0.031 ± 0.003
trans-2-hexenoyl-CoA	138.6 ± 18.8	588.3 ± 25.3	4.2 ± 0.6
trans-2-octenoyl-CoA	20.7 ± 2.7	2645.4 ± 107.3	127.8 ± 17.5
trans-2-decenoyl-CoA	29.1 ± 7.5	323.7 ± 29.5	11.1 ± 3.0
trans-5-methyl-2-hexenoyl-CoA (iso-)	307.0 ± 41.5	172.9 ± 8.1	0.56 ± 0.08
(±)-*trans*-4-methyl-2-hexenoyl-CoA (anteiso-)	599.2 ± 119.1	13.8 ± 1.2	0.023 ± 0.005

[1] $K_{m,acyl\text{-}CoA}$ and k_{cat} values were determined at a fixed NADPH concentration (350 µM)

2.5 Discussion

Our combined results clearly indicate that saFabI possesses distinct characteristics that markedly differentiate it from classical FabI enzymes, while exhibiting similarities to

Staphylococcus and *Bacillus* FabIs and FabL. We identified an RKXXS-motif, which is responsible for the preferential binding of NADPH to saFabI and most likely to FabI proteins of other *Staphylococci* and some *Bacillus* species. Our analysis also reveals a fundamental extension of the classical inhibitor binding mechanism including conformational changes in three regions and a dimer - tetramer transition upon cofactor and inhibitor binding that may also be applicable for FabI enzymes of related *Staphylococcus* and *Bacillus* species. The oligomeric transition is coupled to ligand binding and hence may provide the mechanistic underpinnings for the observed cooperativity upon substrate binding. Glutamate was shown to influence cofactor differentiation and to increase the activity of saFabI while reducing the cooperativity of substrate binding. Nevertheless, cooperativity was still observed at a physiologically relevant glutamate concentration, suggesting that glutamate may function as an intracellular metabolite that regulates enzyme activity (for further details see Supplemental Discussion and Figure S 2-5).

In contrast to many other bacteria including *Streptococci*, the cell membranes of *Staphylococcus* and *Bacillus* species mainly comprise branched-chain fatty acids (85,86,88-90,164). We propose that *S. aureus* FabI, as well as *Bacillus* FabI and FabL proteins, have evolved differently compared to classical FabI proteins to enable the production of BCFAs. The additional flexibility observed in the saFabI structures and other characterized *Bacillus* FabIs may play a role in altering the substrate specificity to accommodate the more bulky branched-chain substrates. Accordingly, Ser197 in saFabI, which links the two flexible substrate binding loops after ligand binding (Figure 2-5G), is conserved in *Staphylococci*, several *Bacilli* and some *Listeria*. Furthermore, we found that FabI enzymes capable of utilizing NADPH belong mostly to the BCFA family of organisms, however, the rationale behind this observation is currently not clear. To generate a membrane containing mostly branched-chain fatty acids, *S. aureus* and *B. subtilis* FabH enzymes are known to prefer branched-chain acyl-CoA primers instead of acetyl-CoA (Figure 2-1, Supplemental Results) (57,165). Our data clearly show that this preference is carried on in the FAS II cycle as the substrate specificity for the first-round branched-chain substrates relative to the first-round straight-chain substrate is markedly increased for saFabI compared to FabIs from organisms producing mainly SCFAs.

Since BCFAs are known to be important for the *in vivo* fitness of *S. aureus* and *Listeria monocytogenes* (146,166), the requirement of some organisms for these fatty acids may explain the different susceptibility of Gram-positive bacteria to inhibitors of the fatty acid biosynthesis pathway. Importantly, only a minimal amount of BCFAs are present in the human and murine blood (1% of all plasma fatty acids in humans (147) and less than 1% in mice (167,168)). It is known that the modulation of membrane lipids enables bacteria to survive under distinct stress situations (146). Even though both types of fatty acids serve to increase the fluidity of the membrane bilayer, the structural and morphological membrane characteristics differ for BCFAs and UFAs (169). Hence, compared to UFAs, supplementing with BCFAs did not confer the same level of fitness to *E. coli* UFA auxotrophs in response to cold stress (170). Similarly, other evidence suggests that *S. aureus* and *L. monocytogenes* fitness is reduced in the absence of BCFAs. The survival of branched-chain α-ketoacid dehydrogenase (BKD) deficient mutant strains in murine animal models was significantly reduced (146,166). Nevertheless, future experiments should clarify whether the defined composition of the human blood lipid pool, comprising mainly SCFAs and UFAs, can fulfill the *in vivo* survival and virulence requirements of *Staphylococci* and other BCFA family members (90,147).

As the essentiality of the FAS II pathway for *S. aureus* infection *in vivo* is re-validated, a detailed structural and kinetic characterization of targets within the pathway becomes increasingly relevant. FabI is one such target, which has spurred many inhibitor discovery efforts. We have shown that the drug target FabI in *S. aureus* and closely related pathogens differs from its homologous proteins with respect to cofactor and substrate specificity, cofactor/inhibitor binding and quaternary structure. Knowledge of these differences, as well as the structures solved here and in similar studies, can aid in the development of antibiotics specifically targeting FabI enzymes from the important human pathogens *S. aureus, S. epidermidis, B. anthracis and B. cereus*, which all synthesize branched-chain fatty acids. Remarkably, three saFabI inhibitors are in phase I clinical trials since 2009, providing substantial hope for new MRSA drugs (103).

2.6 Experimental Procedures

2.6.1 Cloning, Expression and Purification

We optimized the saFabI purification protocol with respect to plasmid usage, *E. coli* expression strain, cultivation and buffer composition (see Supplemental Experimental Procedures for further details) based on previously described procedures (78,144). A detailed description of the protocols is provided in Table S 2-4. FtFabI was prepared as described previously (46).

2.6.2 Site-directed Mutagenesis, Expression and Purification of SaFabI Mutants

Site-directed mutagenesis was performed using the QuikChange Mutagenesis Kit from Stratagene to add a single point mutation (*S44L*) to the previously constructed saFabI R40Q/K41N mutant (primers: 5’-ACCAGAACGAACGTCTGCGTAAAGAGCTTGAA-3’ and 5'-TTCAAGCTCTTTACGCAGACGTTCGTTCTGGT-3') (78). The sequence of saFabI R40Q/K41N/S44L was confirmed by DNA sequencing. Expression and purification of the double and triple mutant was performed as described in Table S 2-4.

2.6.3 Crystallization, Data Collection and Structure Determination

Prior to co-crystallization utilizing the vapor diffusion method, purified saFabI was incubated for 2 h at 4 °C with a 10-fold molar excess of $NADP^+$ (100 mg/ml stock solution in water) and a 20-fold molar excess of the respective inhibitor supplemented as solid powder or dissolved in DMSO (for the P1 structures, 100 mg/ml stock solutions), respectively. The complexes were crystallized by the hanging drop vapor diffusion method using different precipitants (see Supplemental Experimental Procedures). Diffraction data of the flash-frozen crystals were collected at BESSY II (Berlin) or the ESRF (Grenoble), respectively. All structures were solved by molecular replacement with baFabI (2QIO) as the initial search model (see Supplemental Experimental Procedures and Table S 2-1 and Table S 2-2 for further details).

2.6.4 Analytical Size Exclusion Chromatography

SaFabI was dialyzed into a buffer containing 20 mM Tris pH 8.0 and 200 mM NaCl. Equal sample volumes were applied to a calibrated 10/300 Superdex 200 GL column (GE Healthcare) pre-equilibrated with dialysis buffer. Prior to analytical SEC the protein (5 mg/ml) was supplemented with a 10-fold molar excess of $NADP^+$, NADPH or an equal volume of water and a 20-fold molar excess of TCL (100 mg/ml stock solution in DMSO) or an equal volume of DMSO, respectively. All four samples (apo, $NADP^+$, NADPH and $NADP^+$/TCL) were incubated at 20 °C for 2 h. Experiments were performed in triplicate and the peak shift confirmed for a different protein batch at pH 8.0 (Figure S 2-3B). Additionally, one saFabI sample was analyzed at pH 5.6 in 20 mM trisodium citrate pH 5.6, 500 mM NaCl and 100 mM EDTA (Figure S 2-3A).

2.6.5 Synthesis of trans-2-enoyl-CoA Substrates

Trans-5-methyl-2-hexenoic acid and (±)-*trans*-4-methyl-2-hexenoic acid were synthesized from isovaleraldehyde (Sigma-Aldrich) and (±)-2-methylbutyraldehyde (Sigma-Aldrich), respectively, via a Horner-Wadsworth-Emmons reaction with methyl (triphenylphosphoranylidene)acetate, as described previously (171).

Trans-2-enoyl-CoA substrates were synthesized from their respective *trans*-2-enoic acid using the mixed anhydride method (160). Products were characterized by electrospray ionization mass spectrometry. *Trans*-2-butenoyl-CoA was purchased from Sigma-Aldrich.

2.6.6 Steady-state Kinetic Assays

Kinetic experiments were performed on a Cary 100 spectrophotometer (Varian) at 20°C in 50 mM potassium phosphate, 150 mM NaCl and 1 M potassium glutamate pH 7.5 containing 8% glycerol (v/v) and 0.1 mg/mL bovine serum albumin (BSA). Reaction velocities were measured by monitoring the oxidation of NAD(P)H to $NAD(P)^+$ at 340 nm (ε = 6220 M^{-1} cm^{-1}). Kinetic parameters for saFabI were determined by measuring initial velocities at varying concentrations of one substrate, holding the other substrate concentration constant (for further details see Supplemental Experimental Procedures).

2.6.7 Inhibition Kinetics

Progress curves were used to determine the steady-state inhibition of saFabI by the slow-onset inhibitors TCL, EPP and CPP. The final reaction mixture contained saFabI (100 nM), *trans*-2-butenoyl-CoA (1.5 mM), NADPH (350 µM), $NADP^+$ (400 µM) and inhibitor (2% v/v DMSO). $K_i^{*,app}$ values, corresponding to the final steady-state inhibition following slow isomerization of the initial enzyme-inhibitor complex, were determined by plotting the fractional steady-state velocities as a function of inhibitor concentration and fitting to the standard isotherm equation (Equation 1).

$$\frac{v_s}{v_u} = \frac{1}{1 + \frac{[I]}{K_i^{*,app}}} \qquad (1)$$

where v_u is the initial velocity of the uninhibited reaction (for further details see Supplemental Experimental Procedures).

2.7 Accession Numbers

The coordinates and structure factors of saFabI in its unliganded form (space groups $P3_2$ and $P4_32_12$) as well as in complex with $NADP^+$ and triclosan (space groups $P2_12_12_1$ and P1), CPP or EPP have been deposited in the PDB with the codes 4ALN, 4ALM, 4ALL, 4ALI, 4ALJ and 4ALK, respectively.

2.8 Acknowledgements

We thank the staff at the ESRF beamlines ID 14-4 and ID 29 (Grenoble) and at the BESSY II beamline 14.1 (Berlin) for technical support. This work was supported in part by NIH grants AI044639 and AI070383 to P.J.T., and through the Deutsche Forschungsgemeinschaft to C.K. (SFB630 and Forschungszentrum FZ82). J.S. was supported by a grant of the German Excellence Initiative to the Graduate School of Life Sciences, University of Würzburg. A.C. was supported by the Medical Scientist Training Program (MSTP, NIH T32GM008444) and by the Chemical Biology Training Program (CBTP, NIH T32GM092714). The authors declare that no conflict of interest exists.

2.9 Supplemental Information

2.9.1 Supplemental Data

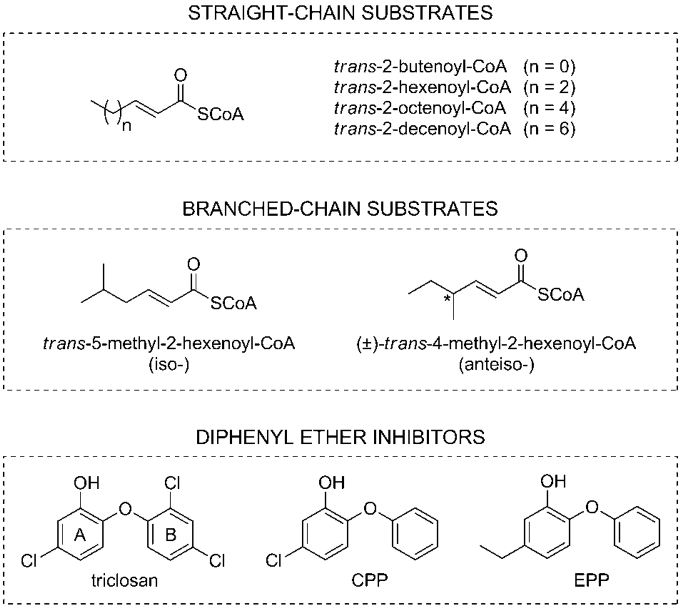
STRAIGHT-CHAIN SUBSTRATES
O
SCoA
n
trans-2-butenoyl-CoA (n = 0)
trans-2-hexenoyl-CoA (n = 2)
trans-2-octenoyl-CoA (n = 4)
trans-2-decenoyl-CoA (n = 6)
BRANCHED-CHAIN SUBSTRATES
O
SCoA
trans-5-methyl-2-hexenoyl-CoA
(iso-)
O
SCoA
*
(±)-trans-4-methyl-2-hexenoyl-CoA
(anteiso-)
DIPHENYL ETHER INHIBITORS
OH
Cl
O
A
B
Cl
Cl
triclosan
OH
O
Cl
CPP
OH
O
EPP

Figure S 2-1, related to Figure 2-1. Substrate and inhibitor structures. The chemical structures of the saFabI substrates and inhibitors, which were analyzed in this study, are shown.

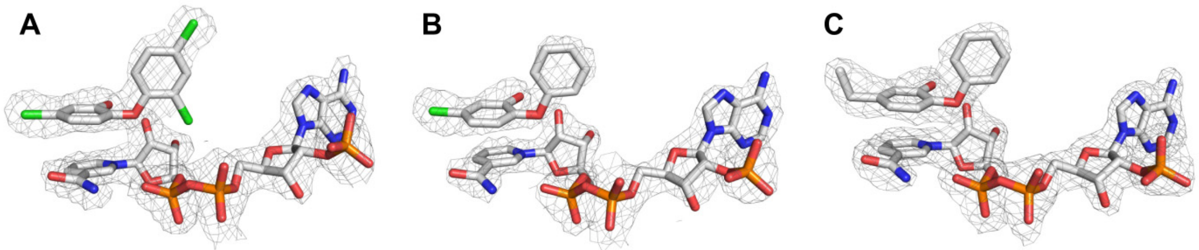

Figure S 2-2, related to Figure 2-2. Inhibitor and cofactor electron densities. (A-C) $2F_o$-F_c omit maps of triclosan (CPP, EPP) and $NADP^+$ in the TCL-2 (CPP, EPP) structure (subunit H) contoured at one time the standard deviation of the mean electron density.

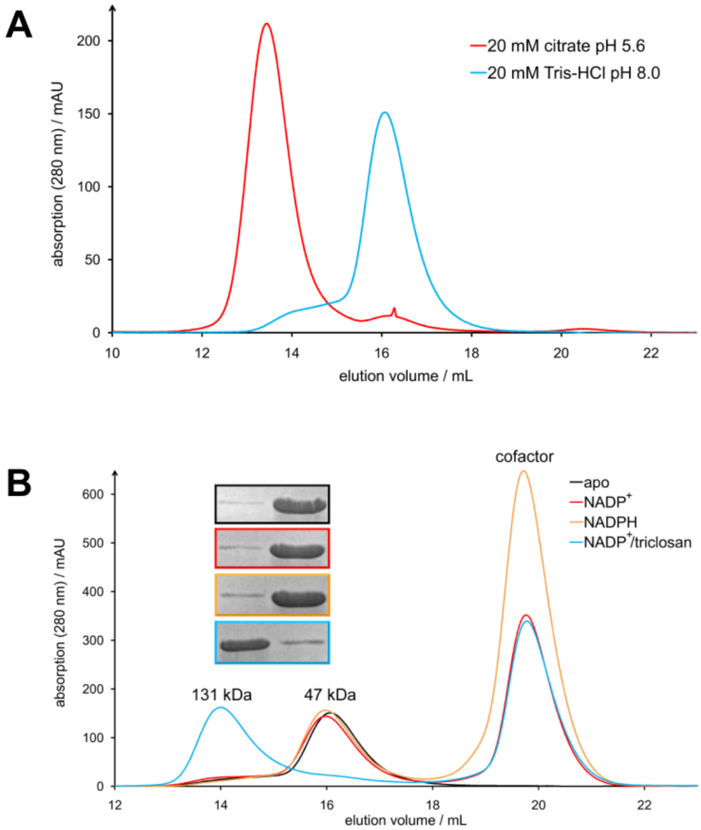

Figure S 2-3, related to Figure 2-6. Quaternary structure of saFabI in solution. (A) Dimeric and tetrameric structure of saFabI. Overlay of two different analytical SEC chromatograms using buffers at pH 5.6 (20 mM trisodium citrate pH 5.6, 500 mM NaCl and 100 mM EDTA) shown in red, or at pH 8.0 (20 mM Tris pH 8.0 and 200 mM NaCl) shown in blue, respectively. **(B)** Dimer - tetramer transition. Four different analytical SEC chromatograms and the respective cropped SDS-PAGE gel bands for the peak fractions (elution volumes of 14.0 and 16.0 ml) running at the same height (~33 kDa, calculated monomeric saFabI molecular mass is 31 kDa) are shown with apo saFabI in black, and saFabI treated with NADP$^+$, NADPH or NADP$^+$ and TCL in red, orange or blue, respectively. The front peak corresponds to a molecular mass of 131 kDa, the middle peak to 47 kDa. Excess of unbound NADP$^+$ and NADPH elutes at 19.8 ml.

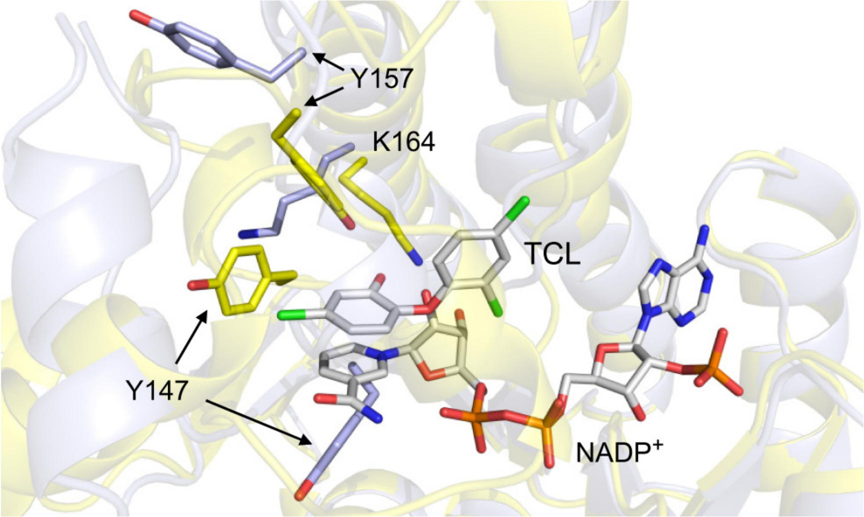

Figure S 2-4, related to Figure 2-5. Active site formation. Superposition of the apo-2 (blue, subunit A) and TCL-2 (yellow) structures. All three active site residues are depicted as stick representations for both structures. TCL and NADP$^+$ are shown in grey. The three active site residues (Tyr147, Tyr157, Lys164) move significantly upon cofactor and inhibitor binding. Tyr147 is shifted by ~5 Å out of the nicotinamide binding pocket whereas Tyr157 rotates about 130° towards the TCL hydroxyl group (70,144). At the same time, the 80° rotation of Lys164 allows the correct placement of the cofactors nicotinamide ring (70).

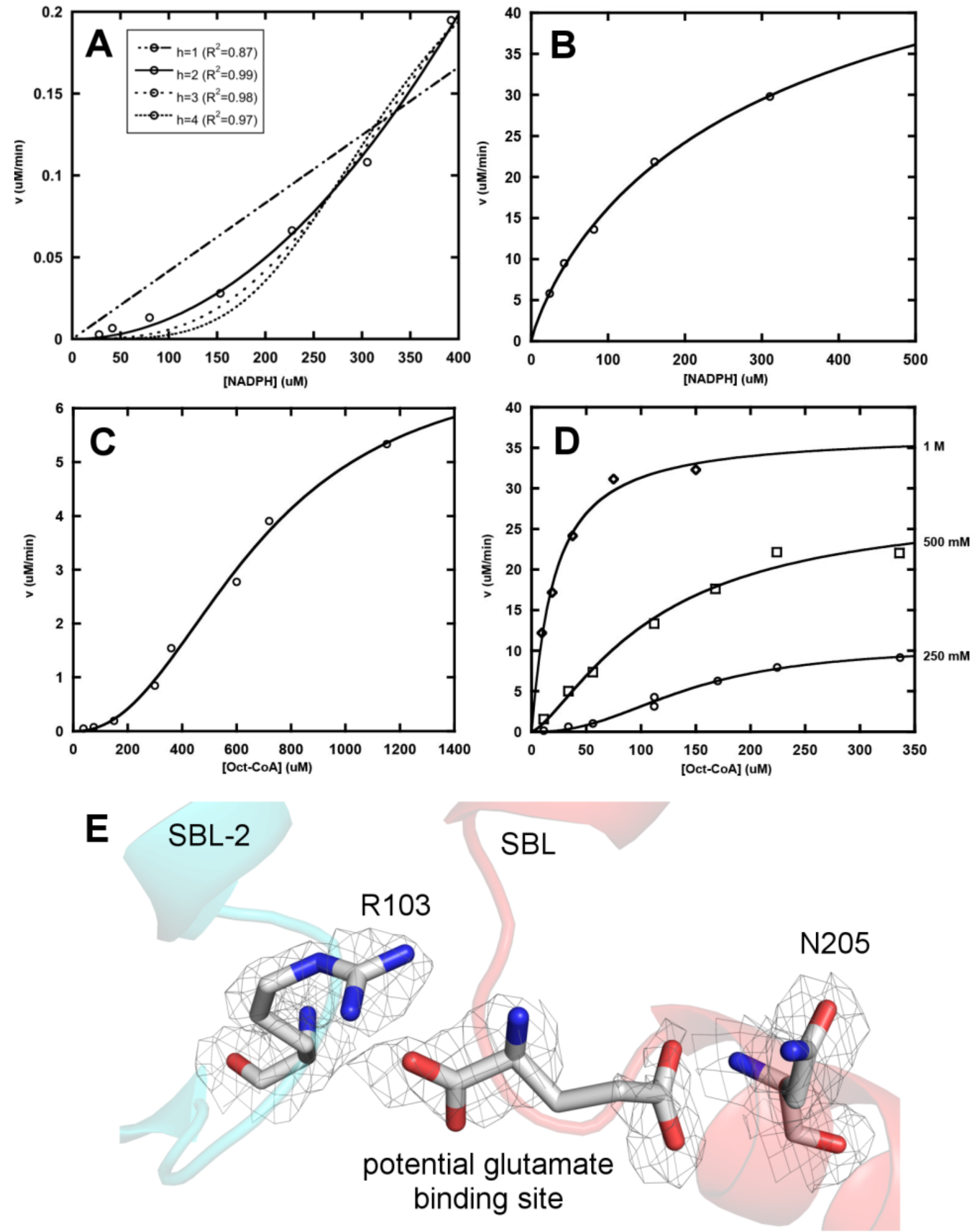

Figure S 2-5, related to Figure 2-6. Cooperativity of substrate binding to saFabI. Reaction velocities with 22 nM saFabI are plotted as a function of substrate concentration, holding the other substrate concentration constant. **(A)** In the absence of potassium glutamate, cooperative binding of NADPH at 100 µM *trans*-2-octenoyl-CoA can be observed. To approximate the Hill coefficient (h) despite the truncated data set, best-fit curves to h = 1, 2, 3 and 4 are displayed. Note that h = 2.2 was previously reported for the binding of NADPH to saFabI (108). **(B)** In the presence of 1 M potassium glutamate, h = 0.9 ± 0.1 for the binding of NADPH at 100 µM *trans*-2-octenoyl-CoA. **(C)** In the absence of potassium glutamate, h = 2.3 ± 0.3 for the binding of *trans*-2-octenoyl-CoA at 350 µM NADPH (R^2 = 0.99). **(D)** In the presence of 250 mM, 500 mM and 1 M potassium glutamate, h = 2.4 ± 0.4, 1.4 ± 0.3 and 1.1 ± 0.3, respectively, for the binding of *trans*-2-octenoyl-CoA at 350 µM NADPH (R^2 = 0.99 for each curve-fit). In addition, note the rise in V_{max} as the concentration of glutamate increases. **(E)** Potential glutamate binding site. The ambiguous density of the $2F_o$-F_c omit map (CPP structure, subunit G) contoured at one time the standard deviation of the mean electron density is shown between Arg103 located on SBL-2 (cyan) and Asn205 located on SBL (red). The remainder of the protein is omitted for clarity.

Table S 2-1, related to Experimental Procedures. Data collection and refinement statistics (apo structures).

	Apo-1	**Apo-2**
Data collection		
Cell dimensions		
a, b, c (Å)	123.8, 123.8, 190.1	87.5, 87.5, 307.2
α, β, γ (°)	90.0, 90.0, 120.0	90.0, 90.0, 90.0
Space group	$P3_2$	$P4_32_12$
Resolution[1] (Å)	50.0-3.05 (3.20-3.05)	50.0-2.45 (2.60-2.45)
Observed reflections	160,521 (21,802)	319,536 (52,121)
Unique reflections	61,623 (8,296)	44,583 (7,185)
Completeness (%)	99.3 (99.7)	98.9 (99.8)
Average redundancy	2.6 (2.6)	7.2 (7.3)
R_{merge}[2] (%)	11.7 (49.9)	8.8 (78.0)
<I / σ(I)>	6.8 (2.1)	16.4 (2.8)
Monomers per AU	12	4
Refinement		
Resolution (Å)	44.3-3.05	48.2-2.45
R_{cryst}[3] (%)	20.3	18.5
R_{free} (%)	24.6	25.1
Twin fraction	0.33	-
Number of atoms	20,062	7,820
rmsd bond lengths (Å)	0.015	0.007
rmsd bond angles (°)	1.482	0.980
Average B-factor ($Å^2$)	67.1	62.9
Ramachandran-plot[4]		
Favored (%)	91.5	96.7
Allowed (%)	7.9	3.1
Outliers (%)	0.6	0.2
Maximum likelihood based estimated coordinate error (Å)	0.28	0.30
PDB code	4ALN	4ALM

[1] Values in parenthesis refer to the highest resolution shell

[2] $$R_{merge} = \sum_{hkl}\sum_{i}\left|I_i - \langle I \rangle\right| \Big/ \sum_{hkl}\sum_{i} I_i$$

[3] $$R_{cryst} = \sum_{hkl}\left|F_{obs} - F_{calc}\right| \Big/ \sum_{hkl} F_{obs}$$

[4] According to Molprobity (172)

Table S 2-2, related to Experimental Procedures. Data collection and refinement statistics (ternary complex structures).

	TCL-1	**TCL-2**	**CPP**	**EPP**
Data collection				
Cell dimensions				
a, b, c (Å)	83.5, 111.9, 111.6	90.0, 94.8, 94.9	90.2, 94.8, 94.8	90.2, 95.1, 95.3
α, β, γ (°)	90.0, 90.0, 90.0	98.1, 112.0, 97.3	98.0, 112.4, 97.4	98.2, 112.3, 97.3
Space group	$P2_12_12_1$	P1	P1	P1
Resolution[1] (Å)	42.9-2.80 (2.95-2.80)	38.5-2.10 (2.21-2.10)	49.1-2.20 (2.32-2.20)	49.3-1.90 (2.00-1.90)
Observed reflections	119,875 (17,343)	640,244 (92,983)	249,699 (35,984)	427,322 (63,042)
Unique reflections	22,827 (3,361)	161,229 (23,385)	135,192 (19,491)	206,602 (30,427)
Completeness (%)	87.2 (89.6)	97.8 (97.0)	94.4 (93.2)	92.1 (92.6)
Average redundancy	5.3 (5.2)	4.0 (4.0)	1.8 (1.8)	2.1 (2.1)
R_{merge}[2] (%)	15.3 (35.7)	14.1 (84.3)	8.2 (34.8)	6.9 (40.4)
R_{pim}[3] (%)	6.8 (16.2)	8.2 (48.8)	8.2 (34.8)	6.4 (38.0)
<I / σ(I)>	6.5 (2.5)	8.0 (2.0)	5.9 (1.9)	6.4 (2.0)
Monomers per AU	4	8	8	8
Refinement				
Resolution (Å)	79.0-2.80	38.5-2.10	49.1-2.20	40.9-1.90
R_{cryst}[4] (%)	21.4	14.9	15.8	15.0
R_{free} (%)	26.2	19.8	21.9	19.3
Twin fraction	-	-	-	-
Number of atoms	8,101	18,131	17,947	18,573
rmsd bond lengths (Å)	0.013	0.013	0.012	0.015
rmsd bond angles (°)	1.591	1.839	1.788	1.767
Average B-factor ($Å^2$)	66.4	31.3	47.7	30.1
Ramachandran-plot[5]				
Favored (%)	96.2	96.3	96.8	97.0
Allowed (%)	3.6	3.6	3.2	3.0
Outliers (%)	0.2	0.1	0.0	0.0
Maximum likelihood based estimated coordinate error (Å)	0.38	0.12	0.14	0.09
PDB code	4ALL	4ALI	4ALJ	4ALK

[1] Values in parenthesis refer to the highest resolution shell

[2] $$R_{merge} = \sum_{hkl}\sum_{i}\left|I_i - \langle I \rangle\right| \Big/ \sum_{hkl}\sum_{i} I_i$$

[3] $$R_{pim} = \sum_{hkl}\left[1/(N-1)\right]^{1/2}\sum_{i}\left|I_i - \langle I \rangle\right| \Big/ \sum_{hkl}\sum_{i} I_i \quad (173)$$

[4] $$R_{cryst} = \sum_{hkl}\left|F_{obs} - F_{calc}\right| \Big/ \sum_{hkl} F_{obs}$$

[5] According to Molprobity (172)

Table S 2-3, related to Table 2-3. Kinetic parameters for ftFabI utilizing NADH and various *trans*-2-enoyl-CoA substrates.

	K_m (µM)	k_{cat} (min^{-1})	$k_{cat}/K_{m,acyl\text{-}CoA}$ (min^{-1} $µM^{-1}$)
trans-2-butenoyl-CoA	353 ± 5	1140 ± 60	3.2 ± 0.2
trans-2-octenoyl-CoA	33.3 ± 0.4	1200 ± 60	36.0 ± 1.9
trans-2-decenoyl-CoA	11.2 ± 0.8	1260 ± 60	112.5 ± 9.7
trans-2-dodecenoyl-CoA	1.7 ± 0.1	1200 ± 60	705.9 ± 54.5
trans-5-methyl-2-hexenoyl-CoA (iso-)			0.287 ± 0.007[1]
(±)-*trans*-4-methyl-2-hexenoyl-CoA (anteiso-)			0.0040 ± 0.0002[1]
NADH	18.8 ± 0.6	1140 ± 60	60.0 ± 6.0

[1] Estimated based on linear slope of the Michaelis-Menten plot at low [NADH]

Table S 2-4, related to Experimental Procedures. Details of the saFabI purification protocols.[*]

	A	B	C	D	E
Plasmid	pET-16b(+)	pETM-11	pETM-11[2]	pETM-11	pETM-11
***E. coli* strain**	BL21 (DE3) pLysS	BL21 (DE3)	BL21 (DE3)	BL21 (DE3)	BL21 (DE3)
antibiotics	100 µg/ml ampicillin and 34 µg/ml chloramphenicol	50 µg/ml kanamycin	50 µg/ml kanamycin[2]	50 µg/ml kanamycin	50 µg/ml kanamycin
cultivation temperature, time	28 °C, 5 h	18 °C, 18 h	18 °C, 18 h[2]	18 °C, 18 h	18 °C, 18 h
lysis buffer	50 mM Tris-HCl pH 8.0, 500 mM NaCl	50 mM Tris-HCl pH 8.0, 500 mM NaCl	50 mM Tris-HCl pH 8.0, 500 mM NaCl	50 mM Tris-HCl pH 8.0, 500 mM NaCl	50 mM Tris-HCl pH 8.0, 200 mM NaCl, 2 mM β-mercaptoethanol, 5% glycerol
wash buffer	50 mM Tris-HCl pH 8.0, 500 mM NaCl, 10 mM imidazole	50 mM Tris-HCl pH 8.0, 1 M NaCl	50 mM Tris-HCl pH 8.0, 1 M NaCl[2]	50 mM Tris-HCl pH 8.0, 1 M NaCl	50 mM Tris-HCl pH 8.0, 500 mM NaCl, 2 mM β-mercaptoethanol, 5% glycerol
elution buffer	100 mM trisodium citrate pH 5.6, 500 mM NaCl, 100 mM EDTA	50 mM Tris-HCl pH 8.0, 500 mM NaCl, 250 mM imidazole	50 mM Tris-HCl pH 8.0, 500 mM NaCl, 250 mM imidazole	50 mM Tris-HCl pH 8.0, 500 mM NaCl, 250 mM imidazole	50 mM Tris-HCl pH 8.0, 200 mM NaCl, 2 mM β-mercaptoethanol, 5% glycerol, 250 mM imidazole
TEV cleavage	no	yes[1]	no	no	no
storage buffer	20 mM trisodium citrate pH 5.6, 500 mM NaCl, 100 mM EDTA	20 mM trisodium citrate pH 5.6, 500 mM NaCl, 100 mM EDTA	20 mM trisodium citrate pH 5.6, 500 mM NaCl, 100 mM EDTA[3]	20 mM trisodium citrate pH 5.6, 280 mM NaCl, 1 mM EDTA, 280 mM K-glutamate	25 mM Tris-HCl pH 8.0, 200 mM NaCl, 1 mM DTT
final concentration	9.8 mg/ml (0.32 mM)	38.6 mg/ml (1.24 mM)	13.0 mg/ml (0.42 mM) [2,3]	15.0 mg/ml (0.48 mM)	15.2 mg/ml (0.49 mM)

[1] After Ni^{2+} affinity chromatography the protein sample was incubated with TEV-protease in 50 mM Tris pH 8.0 and 500 mM NaCl at 4 °C for 10 h, yielding a 50% removal of the His_6-tag. Subsequently, the sample was re-applied to Ni-TED followed by size exclusion chromatography as described above.

[2] Alternatively (**C'**), the saFabI mutants were expressed and purified (final concentrations of 1.0 mg/ml) using the pET-16b(+) plasmid, 100 µg/ml ampicillin, a cultivation temperature of 25 °C and the wash buffer described in procedure A.

[3] Alternatively (**C''**), the storage buffer of the pooled SEC-fractions was exchanged to 20 mM trisodium citrate pH 5.6, 150 mM NaCl and 1 mM EDTA before concentrating to 8.5 mg/ml (0.27 mM).

[*] In general, the procedure described in the Supplemental Experimental Procedures was applied to obtain ≥ 95% pure saFabI protein. The crystals leading to the TCL-1, apo-1 and apo-2 structures were obtained using purifications A, B or C'', respectively. For the EPP, TCL-2 and CPP complex structures a FabI batch was used which was obtained by procedure D. The analytical size exclusion chromatography experiments were performed with protein batches E and C. The double and triple mutants were purified applying procedure C'.

Movie S 2-1, related to Figure 2-5. Ordering of the substrate binding loop region. This model is based on the TCL-2 structure (one monomer is shown in cyan, TCL in yellow and NADP+ in green). Helix α7 was rearranged in PyMol according to the different geometries of the apo-2 structure. The motion of helix α7 was visualized by interpolating between these different arrangements. The loop region between α7 and α8 was omitted for clarity (the associated termini are shown in red). The initial states of the SBL (shown in green), cofactor and inhibitor were not obtained directly in our apo structures. Conformational changes in additional regions (SBL-2 and ASL) were omitted in the animation. This animation was prepared using PyMol, VirtualDub and Xvid (174).

Movie S 2-2, related to Figure 2-6. Dimer - tetramer transition. This animation was prepared using the structures 3GNT, 3GNS, apo-1, apo-2 and TCL-2. One dimer is shown in blue, the other in red. All structures were superimposed using the lower left monomer. LSQMAN was used to interpolate between C_α positions of consecutive structure pairs for the amino acids which were ordered in both structures (148). C_α traces of these consecutive states were visualized using PyMol, VirtualDub and Xvid (174).

2.9.2 Supplemental Results

2.9.2.1 Inhibition Kinetics

Based on the relative $K_i{}^{*,app}$ measurements, the gain in affinity from the additional buried surface area (BSA) for the inhibitors CPP and EPP (BSA_{TCL} = 72.9%, BSA_{CPP} = 74.7%, BSA_{EPP} = 76.2%) does not completely compensate for the loss of the halogen bond observed for TCL (Table 2-1 and Figure 2-4). The relative affinities of the diphenyl ether analogues for saFabI increase in the order CPP < EPP < TCL. $K_i{}^{*,app}$ includes the affinity of the more potent enzyme-inhibitor complex (E-I*) formed following slow isomerization of the initial, rapid-reversible enzyme-inhibitor complex (E-I; affinity described by $K_i{}^{app}$), according to a two-step slow-binding mechanism of inhibition. Since saFabI exhibited greatly improved activity and stability in the presence of glutamate (see Supplemental Discussion), we were able to perform a more reliable progress curve-based analysis of steady-state inhibition as compared to previous studies (78,108).

2.9.2.2 Reduction of Straight-chain Substrates by SaFabI

Among the straight-chain fatty acyl substrates, we observed an increase in the specificity constant as the chain length increases from 4 to 8 carbons (Table 2-3), consistent with previous results noting a preference for longer chain substrates in the case of *S. aureus* FabI (78). However, in contrast to other FabI homologues, the specificity constant decreases beyond a chain length of 8 carbons. These variations are driven by both an increase in k_{cat} and a decrease in K_m, as opposed to ftFabI (Table S 2-3) and ecFabI, where changes in straight-chain substrate specificity are driven primarily by changes in K_m (107,175).

2.9.2.3 Substrate Specificity of SaFabI

The ratio of specificity constants amongst the first-round straight- and branched-chain substrates of saFabI was approximately 1:24:1 (straight : iso : anteiso) (Table 2-3). Since the ratio of velocities $v_X : v_Y$ for competing substrates S_X and S_Y is equal to the ratio of $[S_X]\ k^X{}_{cat}/K^X{}_m$ to $[S_Y]\ k^Y{}_{cat}/K^Y{}_m$, the available substrate pool also determines the membrane fatty acid composition (176). FabH, which catalyzes the initial condensation reaction in the FAS II pathway, controls the pool of substrates that enter the FAS II cycle (Figure 2-1). Accordingly, *S. aureus* and *B. subtilis* FabH exhibit a preference for branched-chain acyl-CoA primers over the typical acetyl-CoA primer (57,165). Since the *S. aureus* membrane is composed mostly of anteiso-C_{15} fatty acids (89), our results are consistent with the current thought that FabH is the main determining factor in branched-chain fatty acid biosynthesis. For the SCFA family of organisms, FabH tends to prefer the acetyl-CoA primer, resulting in a smaller pool of available branched-chain substrates (57). Although FabIs from these organisms are capable of utilizing branched chain (iso-) substrates (165,177), the relative rate of BCFA substrate reduction catalyzed by SCFA FabIs like ftFabI is much lower than for the BCFA family member saFabI (Table S 2-3). Thus, as expected, the pool of substrates and specificity constants both heavily favor the synthesis and incorporation of straight-chain fatty acids by this organism.

2.9.3 Supplemental Discussion

2.9.3.1 Glutamate Sensitivity

We investigated the glutamate sensitivity of saFabI as glutamate is known to be present at high intracellular concentrations (> 100 mM) in Gram-positive organisms, such as *S. aureus*, and has been found to increase the *in vitro* activity of *S. aureus* gyrase and topoisomerase IV (158,159). Glutamate markedly improved the catalytic activity of saFabI (~5-fold for 1 M potassium glutamate, ~4-fold for 500 mM potassium glutamate), such that the maximum k_{cat} obtained was similar to other FabI homologues with CoA-based substrates (k_{cat} > 500 min^{-1}; Table 2-3) (78,107,108,160,175). In contrast, the catalytic activity of ftFabI is unaffected by glutamate. The reaction velocity of 25 nM ftFabI with 10 µM oct-CoA and 250 µM NADH was 11.25 µM/min both in the presence and absence of 1 M glutamate. To screen for salt effects, we performed single-point reaction velocity measurements. Unlike the *S. aureus* gyrase and topoisomerase IV enzymes (159), the activation of saFabI by glutamate is not cation-specific though K^+ is slightly preferred over Na^+. Among the anions tested, glutamate provided the greatest rate enhancement. At 50 nM saFabI with 30 µM oct-CoA and 200 µM NADPH, the reaction velocities relative to sodium glutamate were 0, 0.16, 0.22, 0.49 with sodium chloride, sodium aspartate, sodium acetate and sodium ADA, respectively. Thus, enhancement of activity is not a general salt effect but appears to be mediated by a carboxylate motif. Interestingly, there is evidence of this effect in the literature. To avoid protein precipitation, previous saFabI purification protocols required buffers containing 100 mM EDTA (78,108). Furthermore, some saFabI inhibition assays were performed in the presence of 100 mM sodium ADA pH 6.5 (50).

Notably, there is a physiological link between glutamate and BCFA synthesis - the first step of BCFA biosynthesis is the transamination of branched-chain amino acids to α-ketoglutarate, forming the corresponding α-keto acid and glutamate (Figure 2-1) (56). We have shown that glutamate not only enhances enzyme activity but also affects the cofactor specificity as well as the cooperativity of substrate binding (Figure S 2-5). In fact, the dimer-tetramer transition may provide a mechanism of regulation by glutamate or similar metabolites. Based on ambiguous densities in the saFabI P1 crystal structures (Figure S 2-5E) obtained in the presence of the saFabI-stabilizing anions glutamate, citrate and EDTA which share the glutaric acid motif, a potential glutamate binding site is located between Arg103 of SBL-2 and Asn205 of SBL. Molecules occupying this site could interconnect the SBLs, thereby enhancing substrate binding and stabilizing the tetrameric state. However, future experiments should clarify the role of glutamate and similar metabolites for saFabI functioning *in vivo*.

2.9.4 Supplemental Experimental Procedures

2.9.4.1 Cloning

SaFabI from the *S. aureus* strain NCTC 8325 was purified using the *safabI*$_{NCTC8325}$:pET-16b(+) plasmid (78). We also amplified the same *safabI* gene from *S. aureus* strain N315 via PCR (originating from *safabI*$_{N315}$:pET-16b(+)) and cloned it into pETM-11 (EMBL) using the NcoI and HindIII (New England Biolabs) restriction sites (primers: 5'-CGAAGGTCGTCCCATGGTAAATCTTGAAAAC-3' and 5'-CCAATAACGTGAACAAAGCTTCTGAATG-3' (Biomers)). The saFabI isoform from *S. aureus* NCTC 8325 was used only for kinetic experiments. It differs from the *S. aureus* N315 isoform by a single amino acid (*G191S*). Although residue 191 is positioned in close proximity to the nicotinamide ring of NADPH, the K_m of saFabI-G191 with respect to NADPH was identical to that reported previously under similar assay conditions for saFabI-S191 (78).

2.9.4.2 Expression and Purification

E. coli BL21 (DE3) bacteria (Novagen) containing the *safabI:*pETM-11 plasmid were grown in Luria-Bertani (LB) medium (Lennox) supplemented with 50 µg/ml kanamycin at 37 °C. After induction with 0.5 mM isopropyl-β-D-1-thiogalactopyranoside (IPTG) at an $OD_{600\ nm}$ of 0.6 the temperature was reduced to 18 °C. Cells were harvested after 18 hours post-induction, resuspended in lysis buffer (50 mM Tris-HCl pH 8.0, 500 mM NaCl) and lysed through a cell disruptor at 1.5 kbar. The lysate was centrifuged at 50,000 g and the supernatant loaded onto a Protino Ni-TED column (Macherey-Nagel). After washing (50 mM Tris-HCl pH 8.0, 1 M NaCl), the protein was eluted (50 mM Tris-HCl pH 8.0, 500 mM NaCl, 250 mM imidazole). A buffer exchange with PD-10 desalting columns (Amersham Biosciences) was followed by size exclusion chromatography (SEC) on a HiLoad 26/60 Superdex 200 pg column (GE Healthcare) pre-equilibrated with storage buffer (20 mM trisodium citrate pH 5.6, 280 mM NaCl, 1mM EDTA, 280 mM potassium glutamate). Protein containing fractions were pooled and concentrated to 15 mg/ml prior to shock-freezing in liquid nitrogen and storage at -80 °C. For further details see also Table S 2-4 (this protocol refers to procedure D in Table S 2-4).

2.9.4.3 Crystallization, Data Collection and Structure Determination

In a vapor diffusion experiment containing equal amounts of protein and precipitant solution (0.1 M K/Na-phosphate pH 6.5, 35% 2-methyl-2,4-pentanediol (MPD)), a single TCL-1 crystal (nomenclature according to Table S 2-2) of space group $P2_12_12_1$ grew within 3 weeks. Diffraction data of the directly flash-frozen crystal were collected to 2.8 Å at the MX beamline 14.1 at BESSY II (Berlin) utilizing a MarMosaic 225 detector (λ = 0.976 Å, T = 100 K). Data were processed with iMosflm (178) and Scala (179). Phases were determined with Phaser (180) by molecular replacement using the FabI structure of *B. anthracis* (PDB code: 2QIO:A) as search model (6). Alternate cycles of maximum likelihood refinement and model building were performed in Refmac 5 (181) and Coot (Table S 2-2) (182). Refinement was improved with the implementation of TLS-refinement and NCS-restraints excluding Met99. After the first rounds of refinement triclosan, $NADP^+$ and water molecules were included into the model according to the F_o-F_c map.

Rod-shaped apo-1 crystals of space group $P3_2$ were obtained in a vapor diffusion setup using 0.61 M $NH_4H_2PO_4$, 9% *t*-butanol, 0.01 M EDTA pH 7.0 as precipitant. For data collection at ID 29 (λ = 0.919 Å, T = 100 K) of the European Synchrotron Radiation Facility (ESRF, Grenoble) the crystals were briefly transferred into cryoprotectant solution (0.61 M $NH_4H_2PO_4$, 9% *t*-butanol, 0.01 M EDTA pH 7.0, 25% glycerol) and cryocooled in liquid nitrogen. After data processing with XDS (183), twinning was detected using Phenix.xtriage (184). Phaser molecular replacement was performed with the TCL-1 structure omitting regions 95-108, 149-158 and 190-221 of the protein as well as all small molecules. To avoid model bias due to high non-crystallographic symmetry (12 molecules per asymmetric unit) and twinning, R_{free} flags were assigned in 20 thin resolution shells. Model building in Coot was alternated with a combined refinement using Phenix.refine (185) and Refmac 5 (Table S 2-1). As no additional electron density for the cofactor and inhibitor was observed, this structure is referred to as the apo-form.

Cube-shaped apo-2 crystals of space group $P4_32_12$ grew in 1.15 M $(NH_4)_2SO_4$, 0.1 M sodium acetate pH 5.0, 1% ethanol as precipitant in a vapor diffusion experiment. Crystals were cryocooled (30% glycerol) and diffraction data were collected to 2.45 Å at beamline ID 29 (ESRF) using an ADSC Quantum Q315r detector (λ = 0.919 Å, T = 100 K). Data were analyzed as described for the apo-1 structure and refined (including TLS refinement) with Phenix.refine (Table S 2-1). As in the case of apo-1, no interpretable cofactor or inhibitor density was present.

Ternary saFabI-$NADP^+$-EPP crystals were obtained with 0.1 M K/Na-phosphate pH 6.5 and 36% MPD as precipitant. Data were collected with an ADSC Quantum Q315r detector at beamline ID 14-4 (ESRF, λ = 0.980 Å, T = 100 K) and were processed to 1.9 Å using iMosflm and Scala. Molecular replacement was performed with Phaser using the TCL-1 structure lacking all small molecules as search model. Refinement (including TLS refinement (186)) and model building were performed using Refmac 5 and Coot (Table S 2-2). $NADP^+$ and EPP were included in the model (187) after molecular replacement and initial refinement. Additionally, the F_o-F_c map indicated an alternative conformation of the amino acid stretch 99-105. The second conformation was modeled for all subunits with clear densities for this feature.

A vapor diffusion experiment with TCL-treated saFabI protein and a similar precipitant solution (0.1 M K/Na-phosphate pH 6.5 and 38% MPD) resulted in TCL-2 crystals of space group P1. Diffraction data were collected to 2.1 Å at beamline 14.1 (BESSY II) using a MarMosaic 225 detector (λ = 0.918 Å, T = 100 K) and processed with iMosflm and Scala. The EPP structure without alternative conformations served as a search model for molecular replacement in Phaser. Refmac 5 and Coot were used for refinement (including TLS refinement) and model building (Table S 2-2).

Similarly, CPP crystals of saFabI were grown with a precipitant solution containing 0.1 M K/Na-phosphate pH 6.5 and 35% MPD. Diffraction data of a directly cryocooled crystal were collected at beamline ID 29 (ESRF) with a PILATUS 6M detector (λ = 0.976 Å, T = 100 K). Indexing and integration were performed with the XDS package. Scala was used for scaling. Structure determination and refinement followed the procedure as described for TCL-2 (Table S 2-2).

As saFabI crystallized in space group P1 with similar cell parameters for the different inhibitors, comparability is warranted (Table S 2-2). For further analysis we used the subunits H of the different structures which display no significant crystal contacts at the active site and therefore approximate the natural state in solution despite the increased flexibility that results in weaker electron densities. Distances and angles were measured for all subunits and are given as mean values ± standard deviations.

To avoid model bias, omit maps were calculated directly after molecular replacement and an initial refinement prior to inclusion of any small molecule (Figure S 2-2). All structural figures were prepared with PyMol (174).

2.9.4.4 Steady-state Kinetic Assays

Kinetic parameters for the wild-type saFabI catalyzed reduction of *trans*-2-octenoyl-CoA (oct-CoA) using NADPH were determined by varying the concentration of oct-CoA at several fixed concentrations of NADPH. Previous mechanistic studies suggest that saFabI catalyzes its reaction via an ordered Bi Bi mechanism with the fatty acyl substrate binding first (78). However, our structural studies suggest that NADP$^+$ likely binds first, followed by the inhibitor. We believe this extends to substrate binding with NADPH binding before the fatty acyl substrate, in accordance with other FabI homologues. Thus, the data were fitted to equations 2 and 3, assuming an ordered Bi Bi system with NADPH binding first. Kinetic parameters for saFabI R40Q/K41N/S44L using oct-CoA and NADH were determined in the same way. The exact $K_{m,NADH}$ and $K_{m,NADPH}$ values for the wild-type enzyme and triple mutant, respectively, could not be accurately calculated because of the maximum usable absorbance range of the UV/VIS instrument. Instead, the specificity constants were estimated via the linear slope of the Michaelis-Menten plot at low NAD(P)H concentrations and saturating acyl-CoA substrate.

$$V_{\max}{}^{app} = \frac{V_{\max}[NADPH]}{K_{m,NADPH} + [NADPH]} \tag{2}$$

$$K_{m,oct-CoA}{}^{app} = \frac{K_{i,NADPH}K_{m,oct-CoA} + K_{m,oct-CoA}[NADPH]}{K_{m,NADPH} + [NADPH]} \tag{3}$$

To compare kinetic parameters for wild-type saFabI using various fatty acyl-CoA substrates, initial velocities were plotted as a function of fatty acyl substrate concentration [S] at a fixed concentration of NADPH (350 µM). These data were fit to the ordered Bi Bi velocity equation (Equation 4). In the case of oct-CoA, $K_{m,S}{}^{app}$ remained constant at varying NADPH concentrations, which indicates that $K_{m,NADPH}$ with this substrate approximates the actual value of $K_{i,NADPH}$. By the definition of kinetic constants in an ordered Bi Bi system, $K_{m,NADPH}$ decreases when utilized with fatty acyl substrates exhibiting lower enzyme k_{cat} values. Since most fatty acyl substrates exhibit a lower k_{cat} than oct-CoA, we are confident that the true values of V_{max} and K_m for these substrates were determined at 350 µM NADPH.

$$v = \frac{V_{\max}[NADPH][S]}{K_{i,NADPH}K_{m,S} + K_{m,S}[NADPH] + K_{m,NADPH}[S] + [NADPH][S]} \tag{4}$$

To test for cooperative binding of substrate to saFabI, data were fit to a Hill plot (Equation 5).

$$v = \frac{V_{\max}[S]^h}{K' + [S]^h} \tag{5}$$

Kinetic experiments with ftFabI were conducted as described previously (46). All plots and curve-fits were generated using KaleidaGraph 4.1.

2.9.4.5 Inhibition Kinetics

The assay buffer is the same as described above, excluding BSA. For dissociation progress curves, saFabI (1 µM), NADP$^+$ (500 µM), inhibitor and DMSO were pre-incubated overnight at 20°C prior to dilution (1:100). Reactions were allowed to proceed until the progress curve reached a steady-state velocity, within the limits of the linear control. Progress curves were fit to the integrated rate equation (Equation 6).

$$A_t = A_0 - v_s t - \frac{v_i - v_s}{k_{obs}}[1 - e^{-k_{obs}t}] \tag{6}$$

where v_i and v_s are the respective initial and steady-state velocities and k_{obs} is the pseudo-first order rate constant.

Since these are tight-binding inhibitors of saFabI, the value of $K_i^{*,app}$ determined in this assay may conceal the true affinity of these compounds, particularly in the case of the most potent compound, triclosan. Although we were unable to obtain the recommended data points to accurately fit the dose-response curves to the Morrison equation, the curvature of the dose-response plots suggest that the inhibitors are not sufficiently potent to titrate the enzyme at the concentrations used in the assay (Figure 2-4A). Thus, we can reasonably expect the true $K_i^{*,app}$ value for each inhibitor to lie close to the fitted value using the standard isotherm equation (Equation 1).

3 Rational Optimization of Drug-Target Residence Time: Insights from Inhibitor Binding to the *Staphylococcus aureus* FabI Enzyme-Product Complex

This chapter is based on the following publication:

Chang, A.*, Schiebel, J.*, Yu, W., Bommineni, G. R., Pan, P., Baxter, M. V., Khanna, A., Sotriffer, C. A., Kisker, C., and Tonge, P. J. (2013) Rational Optimization of Drug-Target Residence Time: Insights from Inhibitor Binding to the *Staphylococcus aureus* FabI Enzyme-Product Complex. *Biochemistry* **52**, 4217-4228

Copyright:

Reprinted with permission from (188). Copyright 2013 American Chemical Society.

Author contributions with respect to data collection:

Chang, A.:	Enzyme kinetics, thermal shift assays
Schiebel, J.:	X-ray crystallography
Yu, W.:	Radioactive dissociation assay
Bommineni, G.R.:	Synthesis of inhibitors
Pan, P.:	Synthesis of inhibitors
Baxter, M. V.:	Synthesis of inhibitors
Khanna, A.:	Synthesis of inhibitors

*These authors contributed equally

Rational Optimization of Drug-Target Residence Time: Insights from Inhibitor Binding to the *Staphylococcus aureus* FabI Enzyme-Product Complex

Andrew Chang[1,‡], Johannes Schiebel[2,3,‡], Weixuan Yu[1], Gopal R. Bommineni[1], Pan Pan[1,†], Michael V. Baxter[1], Avinash Khanna[1,¶], Christoph A. Sotriffer[3], Caroline Kisker[2,*], Peter J. Tonge[1,*]

[1]Institute for Chemical Biology & Drug Discovery, Department of Chemistry, Stony Brook University, Stony Brook, NY 11794-3400, USA

[2]Rudolf Virchow Center for Experimental Biomedicine, Institute for Structural Biology, University of Wuerzburg, D-97080 Wuerzburg, Germany

[3]Institute of Pharmacy and Food Chemistry, University of Wuerzburg, Am Hubland, D-97074 Wuerzburg, Germany

[‡]These authors contributed equally.

3.1 Keywords

residence time; fatty acid biosynthesis; *Staphylococcus aureus* FabI; enoyl-ACP reductase; enzyme kinetics; crystallography; structure-based drug design

3.2 Abstract

Drug-target kinetics has recently emerged as an especially important facet of the drug discovery process. In particular, prolonged drug-target residence times may confer enhanced efficacy and selectivity in the open *in vivo* system. However, the lack of accurate kinetic and structural data for series of congeneric compounds hinders the rational design of inhibitors with decreased off-rates. Therefore, we chose the *Staphylococcus aureus* enoyl-ACP reductase (saFabI) - an important target for the development of new anti-staphylococcal drugs - as a model system to rationalize and optimize the drug-target residence time on a structural basis. Using our new, efficient and widely applicable mechanistically informed kinetic approach, we obtained a full characterization of saFabI inhibition by a series of 20 diphenyl ethers complemented by a collection of 9 saFabI-inhibitor crystal structures. We identified a strong correlation between the affinities of the investigated saFabI diphenyl ether inhibitors and their corresponding residence times, which can be rationalized on a structural basis. Due to its favorable interactions with the enzyme, the residence time of our most potent compound exceeds 10 hours. In addition, we found that affinity and residence time in this system can be significantly enhanced by modifications predictable by a careful consideration of catalysis. Our study provides a blueprint for investigating and prolonging drug-target kinetics and may aid in the rational design of long-residence-time inhibitors targeting the essential saFabI enzyme.

3.3 Introduction

When developing lead compounds against a validated drug target, the traditional drug discovery paradigm has focused primarily on optimizing drug-target thermodynamics and *in vivo* pharmacokinetics (45). However, there has been a recent realization that efficacy and selectivity may also be driven by drug-target kinetics, an overlooked dimension in the conventional SAR profile (10,45,189). In particular, drug-target residence time, which is defined as the reciprocal of the dissociation rate constant, has been shown to be a promising early stage indicator of *in vivo* drug activity. In agreement with this proposal, 26 % of the drugs approved by the FDA between 2001 and 2004 exhibit time-dependent inhibition of their targets (10,45).

In a recent study, the residence time of inhibitors targeting the *Francisella tularensis* enoyl-ACP reductase (ftFabI) was strongly correlated with survival rate in a tularemia mouse model of infection (46). Understanding the molecular interactions that modulate the rate of dissociation from the FabI enzyme would, therefore, greatly aid in the design of new and effective antibiotics, which are urgently needed.

Staphylococcus aureus is a particularly dangerous pathogen in settings such as hospitals because it is carried by healthy people, mostly in the anterior nares, and is readily transferred to immunocompromised patients (190,191). The evolution of antibiotic-resistant strains is, hence, of particularly grave concern since it can very rapidly lead to uncontrolled nosocomial outbreaks (192). Unfortunately, methicillin-resistant strains (MRSA) are widespread, and the severity of this problem has been further compounded by the development of resistance against vancomycin, the “drug of last resort” (193-195). Thus, there is an urgent need for new drugs against orthogonal targets to combat these constantly adapting pathogens.

The type II fatty acid biosynthesis pathway (FAS II), which is involved in the endogenous production of lipids to be incorporated into the bacterial cell membrane, is a promising source for new drug targets (Figure 3-1). There has been a recent controversy regarding the essentiality of this pathway for septic infections caused by Gram-positive bacteria, such as *S. aureus*, given the lipid-rich environment of human serum (90). However, several studies have emerged in support of FAS II as a valid drug target in *S. aureus* by demonstrating *in vivo* efficacy in animal models of infection and revealing heterogeneity in the incorporation and composition of fatty acids among Gram-positive bacteria (19,88,89). Among the FAS II enzymes, FabI, which catalyzes the final step in the catalytic cycle, has garnered the most attention as an antibacterial target (67). This was spurred by the discoveries that diazaborines, triclosan and isoniazid, the latter a front-line anti-tuberculosis prodrug, all target this enoyl-ACP reductase (54,67,71,117,196). In fact, three separate *S. aureus* FabI (saFabI) inhibitors are currently in clinical trials (92,100,101,197).

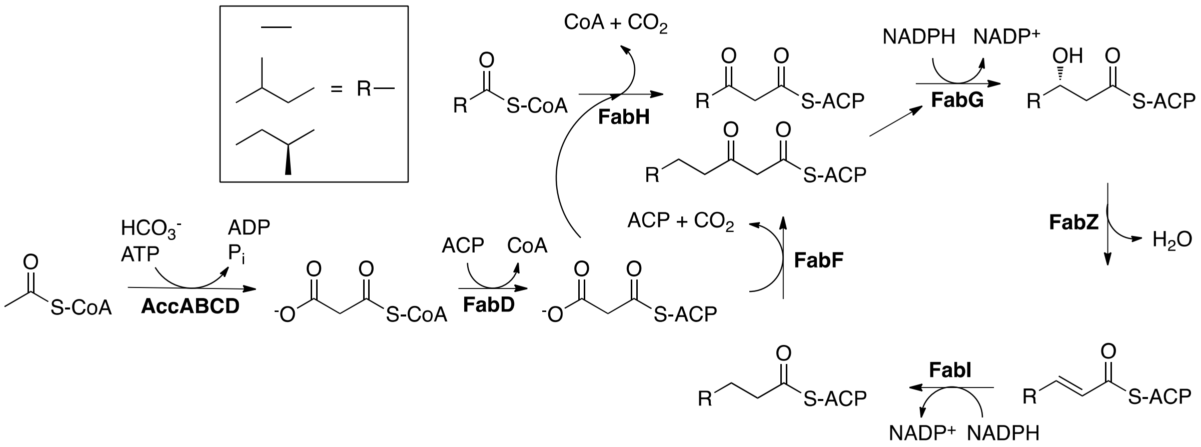

Figure 3-1. The bacterial fatty acid biosynthesis pathway in *S. aureus*. FabI is the enoyl-ACP reductase in the pathway.

Here, we aim to rationally improve the residence time of saFabI inhibitors by analyzing a series of enzyme-product-drug ternary complex inhibitors using X-ray crystallography and a simple, widely applicable mechanistic approach for kinetics-informed drug discovery efforts. We identified a strong correlation between the affinities of the investigated saFabI diphenyl ether inhibitors and their corresponding residence times, which could be rationalized on a structural basis. The mechanistic insights garnered through a consideration of both catalysis and inhibition may prove significant in the rational improvement of small molecules targeting saFabI.

3.4 Experimental Procedures

Compound synthesis. Synthesis of PT51, PT55, PT52, PT103, PT53, PT01, PT02, PT03, PT04, PT05 and PT13 were described previously (69,97,198). PT68, PT89, PT162, PT446, PT447, PT448 and PT119 were synthesized from their corresponding A-rings with 2-fluoro-benzonitrile in the presence of K_2CO_3/dimethylformamide at 170 °C. Similarly, PT104 was synthesized from 1-fluoro-2-methoxy-4-nitro-benzene and phenol at 120 °C. Finally, all the compounds were demethylated using BBr_3. Triclosan was purchased from EMD Millipore Chemicals.

Expression and purification of saFabI. SaFabI was expressed and purified as described previously (19). Briefly, we expressed the *safabi* gene in *Escherichia coli* BL21 (DE3), lysed the cells and isolated the saFabI enzyme via Ni^{2+} affinity chromatography. Finally, size exclusion chromatography yielded > 95% pure protein in 20 mM trisodium citrate pH 5.6, 280 mM NaCl, 280 mM potassium glutamate and 1 mM EDTA.

Crystallization, data collection and structure determination. As described previously, saFabI was concentrated to 15 mg/ml for co-crystallization experiments (19). Prior to crystallization, saFabI was incubated for 2 hours at 4 °C with a 10-fold molar excess of $NADP^+$ and a 20-fold molar excess of the respective diphenyl ether inhibitor. In vapor diffusion experiments, diffraction-quality crystals of space group P1 were obtained using a precipitant solution composed of 0.1 M Na/K-phosphate pH 6.5 and 35 - 47% 2-methyl-2,4-pentanediol (MPD). In order to obtain saFabI-$NADP^+$-PT55 crystals, the protein had to be incubated with the ligands in 25 mM Tris pH 8.0 and 200 mM NaCl at 20 °C prior to concentrating the enzyme from 1 to 15 mg/ml. After directly flash-freezing the crystals in liquid nitrogen, diffraction data were collected to a resolution ranging from 2.15 to 2.50 Å at the MX beamline 14.1 at BESSY II (199) (λ = 0.918 Å, T = 100 K) utilizing a MarMosaic 225 detector (PT02, PT04, PT13, PT55, PT68, PT70 and PT119), beamlines ID14-1 (λ = 0.933 Å, T = 100 K) with an ADSC Quantum Q210 detector (PT03) and ID29 (λ = 0.976 Å, T = 100 K) equipped with a Pilatus 6M detector (PT53) at the ESRF as well as on a Rigaku MicroMax-007 HF X-ray generator (λ = 1.542 Å, T = 100 K) using a R-Axis HTC detector (PT53). Data processing was performed with Imosflm (178) and Scala (179) (PT02, PT04, PT13, PT55, PT68, PT70 and PT119) or the XDS package (183) (PT03, PT53), respectively. The structures were solved by molecular replacement with Phaser (180) using our previously published saFabI structure as search model (PDB-code: 4ALK) (19). Maximum likelihood refinement with Refmac 5 (181) (including TLS refinement (200)) was alternated with model building in Coot (182) to obtain the final structures including $NADP^+$ and inhibitors, which were unambiguously identified in the resulting electron density maps. Data collection and refinement statistics are given in Table S 3-1. Structure analysis was performed as described previously (19) and Figures were prepared with PyMOL (201). The model coordinates and structure factors for the saFabI-$NADP^+$-inhibitor ternary complexes have been deposited in the Protein Data Bank with the codes 4BNF (inhibitor PT02), 4BNG (PT03), 4BNH (PT04), 4BNI (PT13), 4BNJ (PT53), 4BNK (PT55), 4BNL (PT68), 4BNM (PT70), and 4BNN (PT119).

Thermal shift assay. ThermoFluor experiments were carried out in 96-well plates (Concord) using the CFX96 Real-Time PCR Detection System and C1000 Thermal Cycler (Bio-Rad). Samples contained 7.4 µM saFabI, 2.5 mM $NADP^+$ or NADPH, 25 µM inhibitor (2% DMSO) and 5X Sypro Orange (Sigma) in 20 µL final volume of 50 mM potassium phosphate pH 7.5, 150 mM NaCl, 1 M potassium glutamate and 8% glycerol. The plates were sealed with Microseal 'B' Film (Bio-Rad) and heated from 25 to 90 °C in increments of 0.2 °C/10 s. Data were processed by the Bio-Rad CFX Manager.

Progress curve kinetics. Kinetic experiments were performed on a Cary 100 spectrophotometer (Varian) at 20 °C. Reaction velocities were measured by monitoring the oxidation of NADPH to $NADP^+$ at 340 nm (ε = 6220 M^{-1} cm^{-1}). The reaction mixture for forward progress curve experiments has been described previously (19). In the absence of inhibitor, the time window of progress curve linearity was generally limited by substrate consumption rather than enzyme stability (Figure S 3-1). The resulting progress curves were analyzed via the Morrison & Walsh integrated rate equation (Equation 1) (202),

$$A_t = A_0 - v_S t - (v_i - v_s) \cdot \left(\frac{1 - e^{-k_{obs} t}}{k_{obs}} \right) \tag{Eq 1}$$

where A_t and A_0 are the absorbance at time t and time 0, v_i and v_s are the initial and steady state velocities and k_{obs} is the pseudo-first order rate constant for the approach to steady-state. K_i^{app} values, which correspond to the steady-state inhibition IC_{50}, were determined by plotting the fractional steady-state velocities as a function of inhibition concentration and fitting to the isotherm equation (Equation 2),

$$\frac{v_s}{v_u} = \frac{1}{1 + \frac{[I]}{K_i^{app}}} \tag{Eq 2}$$

where v_u is the control, uninhibited reaction velocity. To calculate k_{-1}, which corresponds to the dissociation rate (k_{off}) of the inhibitor, from each progress curve, we used Equation 3.

$$k_{-1} = k_{obs} \cdot \frac{v_s}{v_i} \tag{Eq 3}$$

We can also determine k_{-1} by fitting the k_{obs} values from each progress curve to Equation 4.

$$k_{obs} = k_{-1} \cdot \left(1 + \frac{[I]}{K_i^{app}} \right) \tag{Eq 4}$$

The commonly used jump dilution assay (45,202,203) was used to monitor the recovery of enzyme activity following ternary complex formation. 10 µM saFabI, 15 µM inhibitor and 500 µM $NADP^+$ were preincubated overnight at room temperature followed by 1:200 dilution into reaction buffer (50 mM potassium phosphate pH 7.5, 150 mM NaCl, 1 M potassium glutamate, 8% glycerol) containing 1.5 mM crotonyl-CoA (Sigma; Advent Bio) and 350 µM NADPH. The resulting progress curve was fitted to Eq 1. All curve fitting was performed using KaleidaGraph Version 4.1.

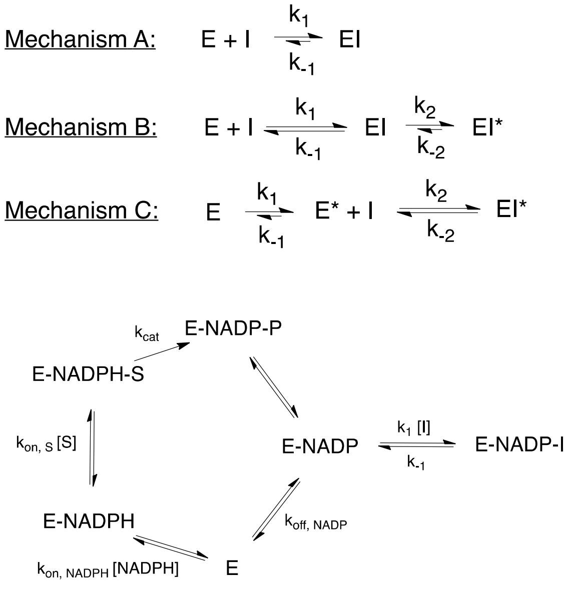

Figure 3-2. Mechanistic model for slow-binding kinetics. Three possible mechanisms (A, B and C) of slow-binding inhibition are depicted. In addition, the detailed kinetic mechanism for inhibition of saFabI by diphenyl ethers is shown below.

Kinetic modeling. A set of ordinary differential equations were constructed based on the kinetic mechanism depicted in Figure 3-2 and numerically solved using Wolfram *Mathematica* 8 (204). The rationale behind the chosen kinetic parameters is provided in Table S 3-2.

^{32}P dissociation kinetics. A mixture of 15 μM saFabI R40Q/K41N/S44L, 20 μM NAD$^+$, ^{32}P-NAD$^+$ (800 C$_i$/mmol) and 200 μM inhibitor in reaction buffer was preincubated at room temperature overnight. Following gel filtration to remove excess free ligand, 500 μL of the mixture was rapidly diluted into 60 mL reaction buffer to initiate dissociation of the ternary complex. 600 μL aliquots of the diluted mixture were withdrawn at various time points, followed by immediate loading onto an ultrafiltration spin column (Sartorious, 10 kDa) and centrifugation at 13,400 rpm for 90 seconds. The amount of ^{32}P in the flow through was quantified by a scintillation counter. Data was fit to Equation 5,

$$C(t) = C(0) + C_{max} \cdot \left(1 - e^{-k_{off}t}\right) \qquad \text{(Eq 5)}$$

where C(t) and C(0) are the radioactive counts (cpm) at time t and time 0, C$_{max}$ is the maximum radioactive count and k$_{off}$ is the inhibitor dissociation rate.

3.5 Results

Diphenyl ethers bind to the E-NADP$^+$ complex generated via catalysis. Triclosan and its diphenyl ether analogues are slow-binding inhibitors of the FabI enzymes from a number of organisms, including *S. aureus* and *F. tularensis* (46,78,108). Although we have previously used the Morrison and Walsh equations to analyze the slow-binding inhibition of ftFabI, we are cognizant that the integrated equations used to analyze progress curve data for slow-binding inhibitors were originally developed for a simple model in which a single-substrate reaction is competitively inhibited by a substrate analog (46,202). To confirm that the Morrison and Walsh integrated equations can be used to analyze the more complex inhibition of FabI, it was first necessary to elucidate a more precise mechanism of inhibition by diphenyl ethers.

FabI catalyzes an ordered Bi Bi reaction, and diphenyl ethers bind uncompetitively with respect to the product NAD(P)$^+$ (78,108). To determine the primary origin of the E-NADP$^+$ complex relevant for inhibitor binding, progress curves were obtained for a slow-binding inhibitor (PT53) in the presence of 400 and 2000 μM NADP$^+$. These curves were essentially identical (Figure S 3-2B), suggesting that the product of the catalytic cycle rather than binding of NADP$^+$ to the free enzyme was the dominant source of E-NADP$^+$ under the assay conditions. The significance of the E-NADP$^+$ complex generated via catalysis for saFabI inhibition has been hinted at in a recent publication (102), and is consistent with the very weak NADP$^+$ product inhibition of the free enzyme (Figure S 3-2A). Additionally, the onset and degree of inhibition increased when using substrates with higher k$_{cat}$ (data not shown), consistent with a higher steady-state concentration of E-NADP$^+$ generated via catalysis.

Previous studies proposed that diphenyl ethers bind preferentially to the E-NAD(P)$^+$ complex but still exhibit potent binding to the E-NAD(P)H complex (46,78,97,109,205). However, thermal shift assays revealed exclusive binding of the diphenyl ethers to the saFabI E-NADP$^+$ complex (Figure 3-3). Mechanistic models operating under the assumption that diphenyl ethers bind to the E-NAD(P)H complex are, therefore, erroneous. Instead, the most accurate model is depicted in Figure 3-2, which was initially proposed for the inhibition of saFabI by triclosan (108). Kinetic rate constants were rationally derived for each step of the model on the basis of broad experimental data. By numerically solving the system of differential equations, a set of progress curves was generated for a hypothetical inhibitor with predetermined k$_1$ and k$_{-1}$. Analysis of this theoretical set of curves by the Morrison and

Walsh equations resulted in a reliable estimate of k_{-1} (Table S 3-3). This validated the direct use of these equations to analyze the more complex case of FabI inhibition despite its derivation from a simple mechanistic scheme. Surprisingly, accurate estimates of k_{-1} can be obtained at inhibitor concentrations lower than the enzyme concentration without even accounting for tight-binding inhibition. This is due to the fact that the steady-state population of E-NADP$^+$ at the given reaction velocity is much lower than the concentration of free enzyme.

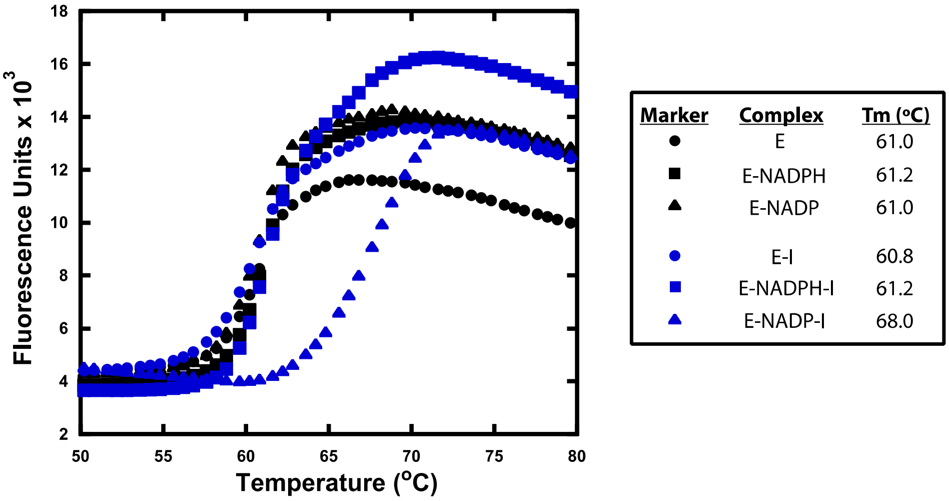

Figure 3-3. Diphenyl ethers bind preferably to the E-NADP$^+$ binary complex. Representative thermal shift curves of saFabI bound to NADPH, NADP$^+$ and/or inhibitor (PT119). The measurement variability is approximately ± 0.2 °C.

Diphenyl ethers bind to saFabI via an induced-fit mechanism. Progress curves corresponding to inhibition of saFabI by diphenyl ethers exhibited curvature characteristic of slow-binding kinetics (Figure 3-4). Slow-binding inhibition generally encompasses one of three kinetic mechanisms (Figure 3-2; top) (10,202,206). The most basic mechanism involves a one-step process with slow inhibitor association accounting for slow formation of the EI complex (Figure 3-2; Mechanism A). A two-step process, which is most often encountered for slow-binding inhibitors, involves rapid formation of EI followed by a slow induced-fit conformational change to the more potent EI* (Figure 3-2; Mechanism B). Alternatively, a two-step process may entail a slow conformational change to an enzyme form that rapidly binds inhibitor (Figure 3-2; Mechanism C). To elucidate the mechanism of slow-binding inhibition, k_{obs} was plotted as a function of inhibitor concentration (Figure 3-4C). The increasing linear plot unambiguously rules out the possibility of a conformational selection mechanism (Mechanism C) (47). Typically, this is characteristic of a single-step slow-binding mechanism of inhibition, whereas the two-step induced-fit mechanism is generally characterized by a hyperbolic relationship. However, the one-step mechanism is kinetically indistinguishable from a special case of the two-step mechanism where EI* is much lower in free energy than EI. In this situation, initial inhibition is not detected at low inhibitor concentrations that still affect the steady-state velocity. In a recent report, we structurally characterized the extensive rearrangements that build the active site upon ligand binding (19). Based on these results, binding of the diphenyl ether inhibitors may induce a directional structural change in the enzyme (special case of Mechanism B). Since the results are analyzed in accordance with Mechanism A (Figure 3-2), k_1 and k_{-1} would, in the special case of Mechanism B, represent the respective overall apparent association and dissociation rate constants between E + I and EI*.

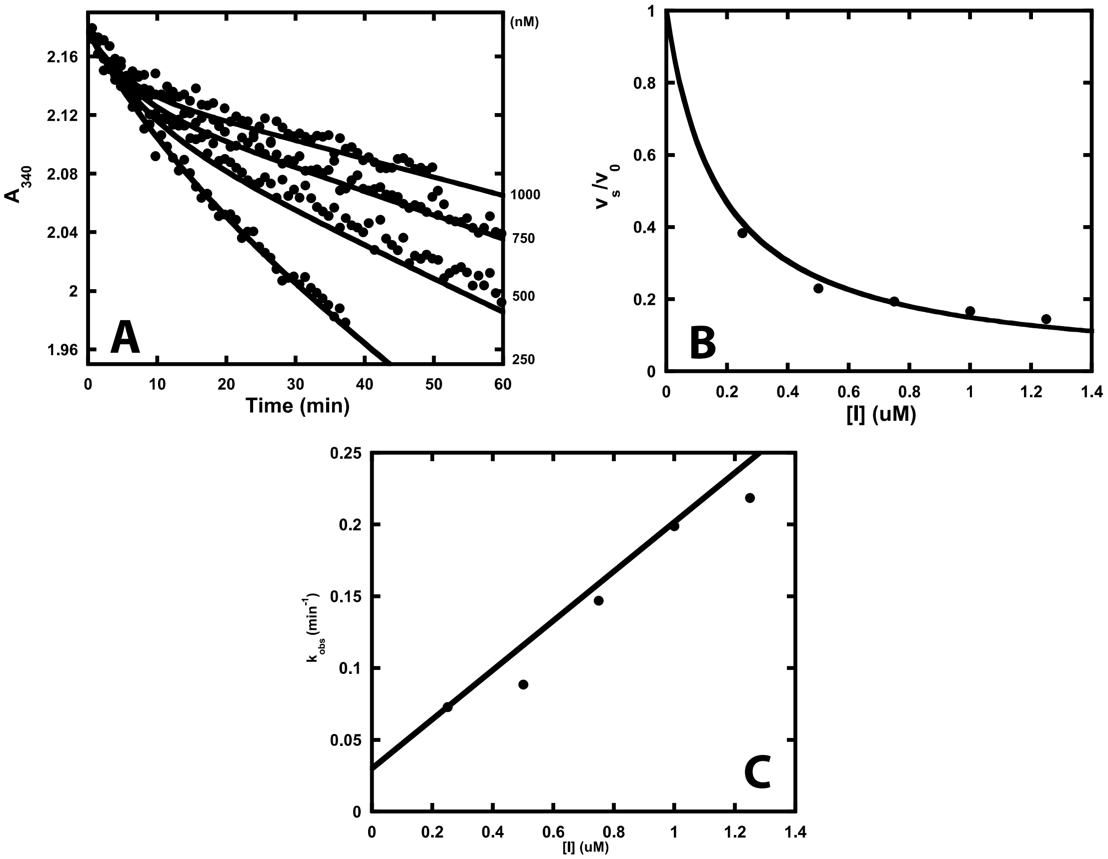

Figure 3-4. Progress curve analysis of saFabI inhibition by diphenyl ether analogues. (A) Representative example of progress curves generated with varying concentrations of PT52 (●). Theoretical curves (—) have been superimposed on the experimental data. These curves were generated using the kinetic parameters in Table 3-1 and Equation 1. R^2 (goodness of fit between theoretical curves and experimental data) = 0.99, 0.95, 0.97 and 0.93 for 250, 500, 750 and 1000 nM PT52, respectively. **(B, C)** These plots display the corresponding fractional steady-state velocity (v_s/v_0) and pseudo-first order rate constant (k_{obs}) as a function of inhibitor concentration. Theoretical curves (—) have been superimposed on the experimental data. These curves were generated using the kinetic parameters in Table 3-1 and Equation 2 or 4. R^2 (goodness of fit between theoretical curves and experimental data) = 0.93 and 0.90 for the IC_{50} and k_{obs} plots, respectively.

Diphenyl ether residence time strongly correlates with affinity. A detailed understanding of the mechanism and interactions that modulate drug-target residence time is particularly important for future drug discovery programs. However, the rational design of inhibitors with decreased off-rates is still very challenging. This task is further hampered by the lack of accurate kinetic data for large compound series (10). Using a mechanistically informed kinetic approach, we analyzed a series of 20 saFabI inhibitors (Table 3-1). The kinetic barrier to dissociation can be increased by either stabilizing the ground state enzyme-inhibitor complex or destabilizing the transition state (Figure 3-5A) (10). Interestingly, the dissociation rate displays a strong linear correlation to K_i in a double logarithmic plot, suggesting that the energetics involved in residence time differentiation are related to stabilization of the final enzyme-inhibitor complex (Figure 3-5B). In addition, the association rate is very similar across the diphenyl ether series, indicating a similar barrier to the transition state. Importantly, this highlights the fact that the following structural rationale for binding affinity trends also applies to residence time.

Table 3-1. Kinetic and thermodynamic parameters for inhibitors of saFabI [a]

Name	Structure	K_i^{app} (nM)	K_i (nM)	k_1 (x 10^{10} M^{-1} hr^{-1}) [h]	k_{-1}(hr^{-1})	t_R (min)[i]
PT51	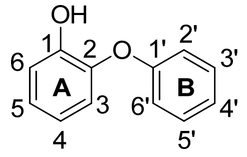	24515.0 ± 1359.8	18.86 ± 1.05	≥ 0.30	rapid [e]	≤ 1
PT55	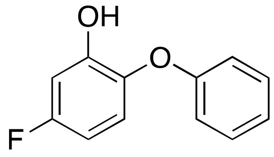	1851.8 ± 127.4	1.42 ± 0.10	0.68 ± 0.23	9.67 ± 3.14 [b] 25.36 ± 2.45 [c]	6.2 [b] 2.4 [c]
PT104	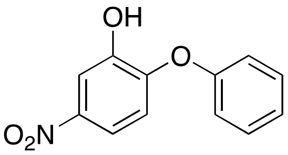	1933.4 ± 345.2	1.49 ± 0.27	0.61 ± 0.46	9.03 ± 6.58 [b]	6.6 [b]
PT52	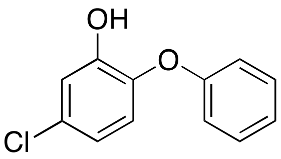	161.2 ± 8.4	0.12 ± 0.01	1.37 ± 0.27	1.70 ± 0.30 [b] 2.33 ± 0.03 [c] 2.13 ± 0.41 [d]	35.3 [b] 25.8 [c] 28.2 [d]
PT103	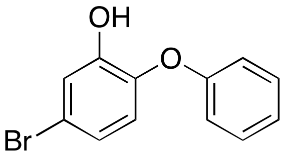	77.7 ± 9.4	0.06 ± 0.01	1.30 ± 0.25	0.78 ± 0.08 [b] 0.73 ± 0.09 [d]	76.9 [b] 82.2 [d]
PT53	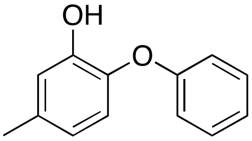	493.7 ± 40.2	0.38 ± 0.03	0.91 ± 0.11	3.46 ± 0.29 [b] 4.53 ± 0.08 [c]	17.3 [b] 13.2 [c]
PT01	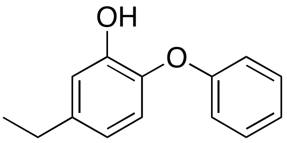	120.8 ± 10.1	0.09 ± 0.01	1.01 ± 0.19	0.94 ± 0.14 [b] 0.72 ± 0.08 [d]	63.8 [b] 83.3 [d]
PT02 [g]	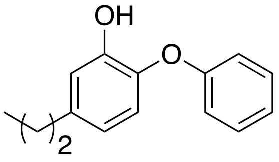		0.07	1.33	0.99 [b] 0.57 ± 0.09 [d]	60.9 [b] 105.3 [d]
PT03 [g]	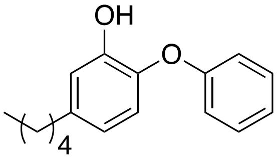		0.04 [f]	0.58	0.20 [b] 0.32 ± 0.17 [d]	300.0 [b] 187.5 [d]

PT04	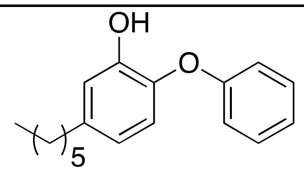		0.01 [f]	1.30	0.13 ± 0.04 [d]	461.5 [d]
PT05 [g]	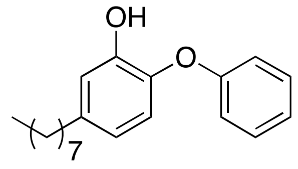		0.82	0.25	2.03 [b] 3.74 ± 0.06 [c]	29.6 [b] 16.0 [c]
PT68	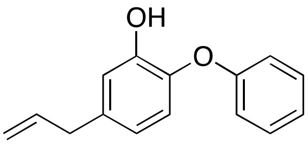	145.2 ± 9.1	0.11 ± 0.01	0.79 ± 0.10	0.87 ± 0.07 [b]	68.7 [b]
PT89	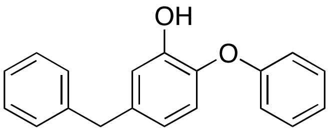	123.2 ± 7.9	0.10 ± 0.01	0.68 ± 0.09	0.64 ± 0.06 [b]	93.5 [b]
PT446	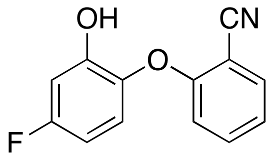	1311.3 ± 246.6	1.01 ± 0.19	0.30 ± 0.16	2.99 ± 1.50 [b]	20.1 [b]
PT447	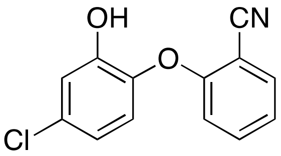	72.0 ± 7.4	0.06 ± 0.01	0.80 ± 0.14	0.44 ± 0.02 [b] 0.47 ± 0.08 [d]	136.4 [b] 127.7 [d]
PT443 [g]	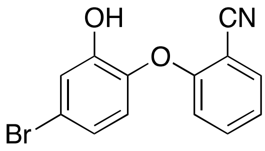		0.05	0.62	0.28 [b]	210.9 [b]
PT119	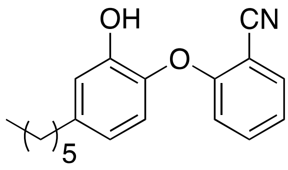		0.01 [f]	0.80	No recovery [c] 0.08 ± 0.01 [d]	750 [d]
PT13 [g]	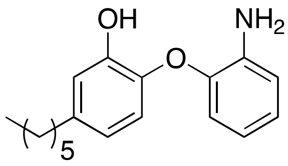		0.12	0.73	0.88 [b]	68.5 [b]
TCL	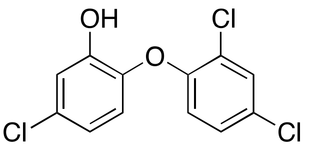	69.2 ± 5.5	0.05 ± 0.01	0.81 ± 0.22	0.43 ± 0.08 [b]	139.5 [b]

PT162 [g]	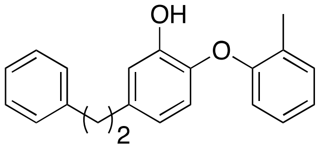	0.5	0.57	2.66 [b]	22.6 [b]

a. Fitting errors are reported for each value in the Table, unless otherwise specified.
b. Mean value calculated from individual progress curves. Errors reflect the standard deviation from the mean.
c. Determined by fitting the jump dilution curve to Eq 1.
d. Determined by fitting the ^{32}P-NAD-based dissociation curve to Eq 5.
e. Defined as ≥ 60 hr^{-1}.
f. Affinity was calculated using the k_{-1} value obtained from the ^{32}P-NAD dissociation assay since the dissociation rate was too slow and/or inhibition was too potent. The k_1 value was obtained from forward progress curve analysis.
g. Values estimated from a single progress curve at a single inhibitor concentration.
h. Errors are propagated from K_i and k_{-1}.
i. Residence time $t_R = 1/k_{-1}$

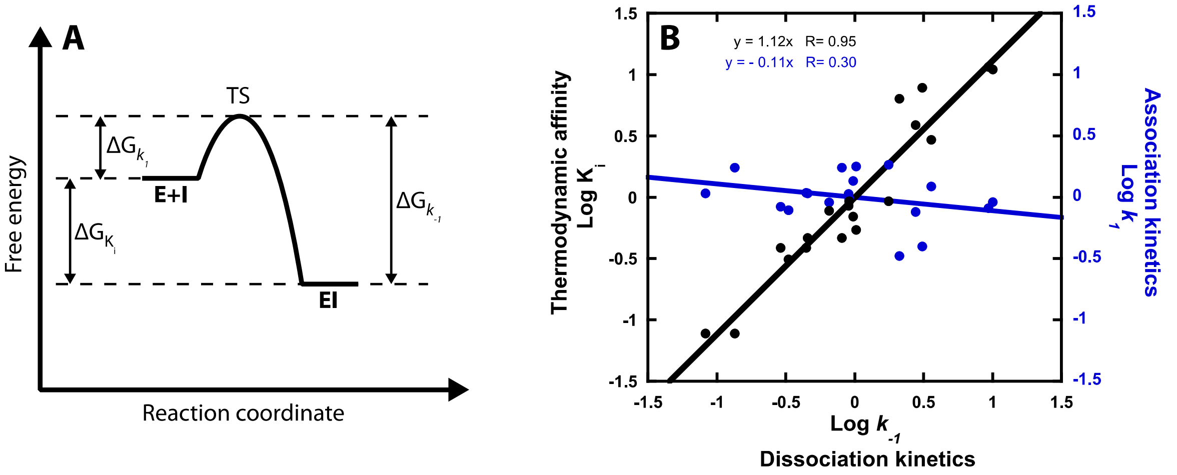

Figure 3-5. Dissociation kinetics drive changes in thermodynamic affinity. (A) Energy diagram corresponding to Mechanism A in Figure 3-2. Residence time ($t_R = 1/k_{-1}$) can be prolonged by either stabilizing EI or destabilizing the transition state (TS). **(B)** A double logarithmic plot depicts a strong correlation between thermodynamic affinity and dissociation kinetics (black) and a weak correlation between association and dissociation kinetics (blue). On each axis, logarithmic values are adjusted such that their mean is equal to zero.

Hydrophobic 5-substituents enhance residence time and affinity. To obtain a detailed understanding of the kinetic and thermodynamic SAR profile, we solved the structures of saFabI in complex with the oxidized cofactor NADP$^+$ and 9 diphenyl ethers differing in their substitution pattern (Figure 3-6, Table 3-1). All investigated inhibitors bind to the predominantly hydrophobic active site pocket and share a common binding pose stabilized by a π-π-stacking interaction with the NADP$^+$ nicotinamide ring (interaction distance of 3.4 ± 0.1 Å) and a central hydrogen bond network between Tyr157, the diphenyl ether hydroxyl group and the 2'-OH of the NADP$^+$ nicotinamide ribose (2.6 ± 0.1 Å or 2.5 ± 0.1 Å, respectively) (Figure 3-6). Substituents at the 5-position of the diphenyl ether A-ring bind to an elongated and very lipophilic binding channel mainly composed of Tyr147, Pro192, Val201, Phe204 and Ile207 (Figure 3-7A, B). Accordingly, we observed clear steric and hydrophobic contributions to binding at the 5-position of the A-ring (Table 3-1).

PT51, PT55 and PT104 comprise a subset of diphenyl ethers lacking hydrophobic bulk at this position. These compounds are noticeably the least potent of the diphenyl ethers tested. Consistently, a similar trend was recently observed for *E. coli* FabI (ecFabI) (102). Such inhibitors were previously characterized as rapid-binding, rather than slow-binding, inhibitors of ftFabI (46). However, similar to slow-onset inhibitors like PT52 (PDB-entry: 4ALJ) (19), the binding of PT55 to saFabI resulted in the closure of the substrate binding loop, which is believed to be responsible for slow-binding inhibition (67). In accordance, PT55 and PT104 exhibited clear slow-binding inhibition of saFabI. Slow-binding kinetics may be more difficult to detect with less potent compounds since higher inhibitor concentrations are required to observe inhibition. This may explain why slow-binding inhibition could not be observed for PT51 and may have been missed in the case of ftFabI (46).

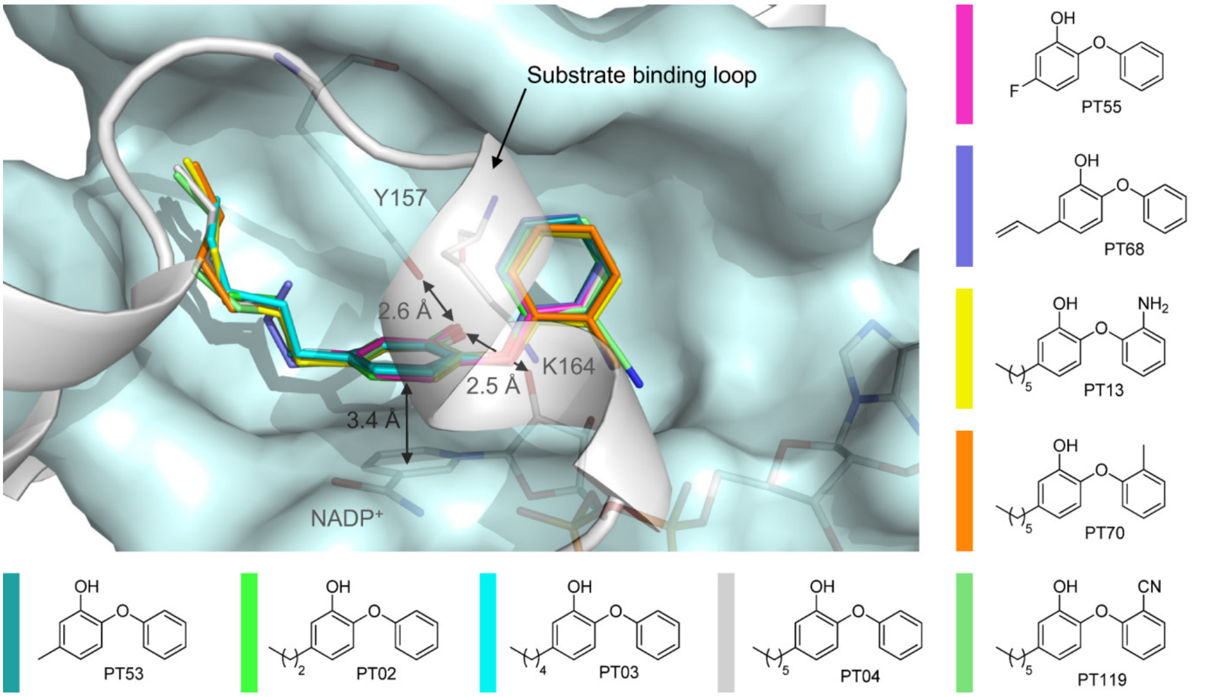

Figure 3-6. Diphenyl ether binding to the binary saFabI-NADP$^+$ complex. Nine diphenyl ether inhibitors are depicted within the saFabI binding pocket (in different colors as defined next to the molecules). All ternary complex structures were superimposed for this purpose. Distances between protein, inhibitor and cofactor atoms are given as mean values (the standard deviations are defined in the main text). All amino acids within a radius of 6 Å of PT04 except the substrate binding loop residues (194-204) are shown in a light blue surface representation. The substrate binding loop, which is in a similarly closed state for all nine structures, is displayed in gray. Main discrepancies between the depicted saFabI binding pocket of the PT04 structure and the remaining structures are discussed in Figure 3-7.

Among compounds with hydrophobic bulk, a steric effect is very prominent. The stabilization conferred by substituting chlorine (PT52; PT447) with bromine (PT103; PT443) provides one such example. Additionally, residence time and affinity increased with aliphatic chain length up to six carbons. Upon elongation of the 5-substituent from methyl (PT53) to ethyl (PT01, PDB-entry: 4ALK), propyl (PT02), pentyl (PT03) and hexyl (PT04), the alkyl chain progressively extends into the aforementioned hydrophobic channel thereby explaining the observed k_{off} and K_i trends (Figure 3-7A, B, E). Beyond this length, however, the alkyl chain is expected to reach the more polar protein surface, rationalizing the decrease in affinity and residence time with PT05. Further striking differences were found between the PT53 and PT04 structures as indicated by an isomorphous difference map. Whereas Ile207 adopts a closed state in the PT53 structure, a conformational change in this gatekeeper residue enables the longer 5-alkyl chains (e.g. the 5-hexyl group of PT04) to bind (Ile207-$C_{\delta 1}$ shifts by 3.4 ± 0.4 Å) (Figure 3-7C, E). The stepwise opening of the hydrophobic channel upon elongation of the alkyl chain is accompanied by its widening via movements of residues Tyr147 and Val201

(Tyr147-OH shifts by 0.5 ± 0.1 Å and Val201-$C_{\gamma1}$ by 0.9 ± 0.1 Å) (Figure 3-7D). A comparable mechanism was observed for the *Mycobacterium tuberculosis* homolog InhA during the binding of 5-octyl-2-phenoxyphenol, which induced a shift of Leu218 (corresponding to Ile207 in saFabI) (69). In contrast, ftFabI has a methionine at this position, which might explain the preference of the enzyme for PT02 (19,46). The finding that this part of the saFabI binding pocket is flexible will be important for future inhibitor design efforts.

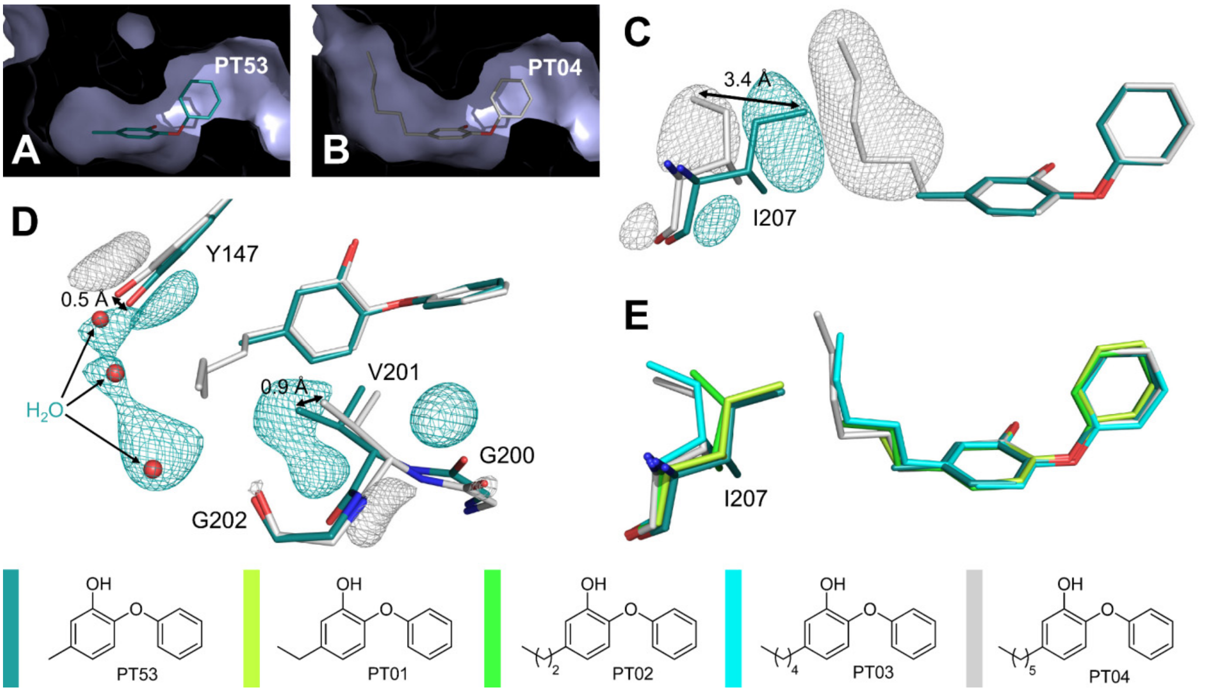

Figure 3-7. Structural changes to saFabI caused by the binding of different 5-alkyldiphenyl ethers. (A) 5-Methyl-2-phenoxyphenol (PT53) is shown as a stick model within its binding pocket. This view shows an intersection through one of the respective saFabI monomers in surface representation. Thus, all parts of the molecule which are in front of an imaginary clipping plane are not visible. **(B)** The corresponding intersection for the 5-hexyl-2-phenoxyphenol (PT04) structure reveals a binding pocket enlarged around the 5-substituent. **(C)** Ile207 and the inhibitors of the superimposed PT53 and PT04 structures are shown. Meshes represent selected parts of the NCS-averaged isomorphous difference map at 5 σ. Additional experimental electron density for each structure is indicated by the associated color and clearly reveals a conformational change of Ile207. **(D)** The same map uncovers supplementary movements of Tyr147 and Val201. In addition, the binding of PT04 leads to a reduced occupancy of three water molecules, which are still bound between Tyr147 and Gly202 in the case of PT53. **(E)** Ile207 and 5-alkyl-2-phenoxyphenols with different alkyl chain lengths are shown. This view was generated via superposition of single monomers of the respective structures (the PT01 structure (PDB-code: 4ALK) was published previously (19)) and indicates a successive opening movement of Ile207. The color code is defined next to the molecules.

Diphenyl ethers likely bind in a deprotonated form to saFabI. Electrostatics of the A-ring 5-position contribute significantly to saFabI binding. Affinity and residence time increase with more electron-withdrawing substituents in the two series PT51, PT55, PT104 and PT53, PT52. The respective pK_a values for the phenolic hydroxyl group are listed in Table S 3-4. We can probe the theoretical contribution of electrostatics to thermodynamic binding if we assume that only the deprotonated oxyanion species can bind to the enzyme. This kinetic simulation resembles the scheme in Figure 3-2 but also includes a rapid equilibrium inhibitor deprotonation step preceding binding to the E-$NADP^+$ binary complex. The equilibrium distribution depends on inhibitor pK_a and buffer pH. Among similarly sized substituents, apparent affinity differences can be almost entirely predicted by pK_a using this theoretical approximation (Table S 3-4), suggesting that the inhibitor is bound in a deprotonated state. The slight disparities from experimental values may be rationalized by other factors, such as differences in sterics. This is a theoretical analysis to rationalize the observed magnitude of electrostatic stabilization. In reality, the similar association rate constants among the various compounds suggest that the protonated species can also bind to the enzyme, followed by subsequent deprotonation. The resulting oxyanion species might contribute to the high affinity binding of these inhibitors to saFabI due to the formation of a strong charge-assisted hydrogen bonding network and an electrostatic interaction between the negatively charged phenolic oxygen and the neighboring positive charges of the catalytic triad residue Lys164 and the oxidized cofactor NADP$^+$ (Figure 3-6). The latter charge-assisted π-π stacking interaction between the inhibitor phenolate ring and the planar oxidized nicotinamide ring of the cofactor might also explain why diphenyl ethers specifically target E-NADP$^+$ despite its lower steady-state abundance relative to E-NADPH. Based on our kinetic parameters (Table S 3-2), the E-NADPH complex is present at more than 300-fold higher concentrations compared to E-NADP$^+$ under our assay conditions (Table S 3-3). However, further studies are required to unequivocally demonstrate that diphenyl ethers are bound to saFabI in their anionic form and to elucidate when deprotonation might occur.

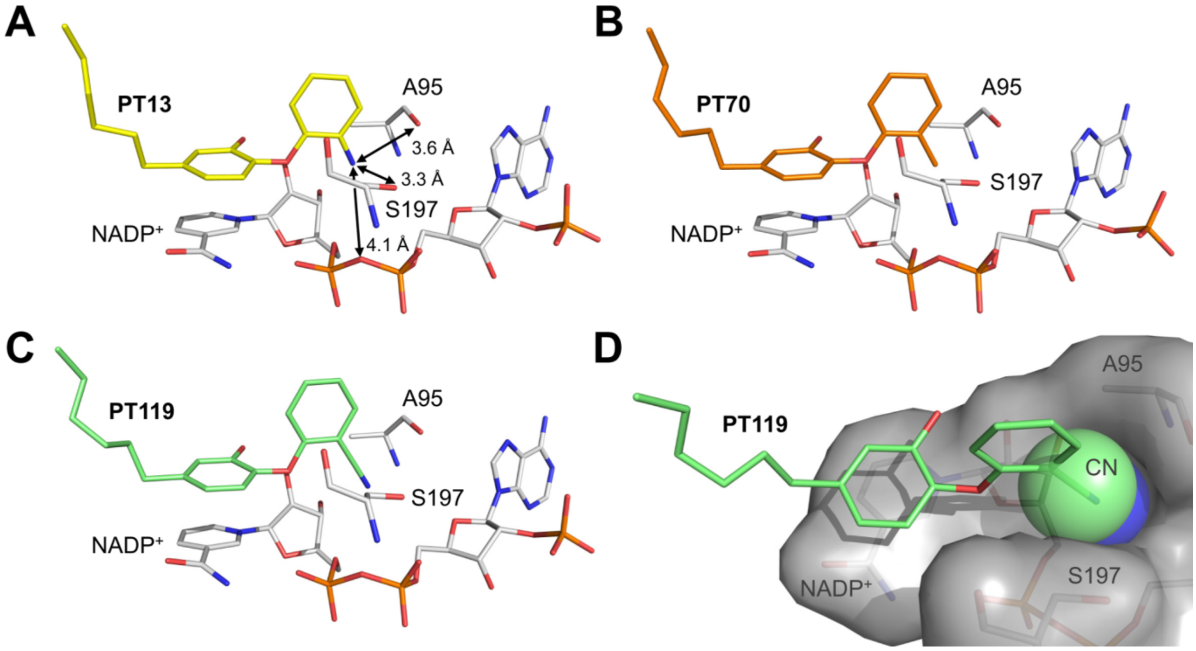

Figure 3-8. Binding modes of different 2'-substituted saFabI diphenyl ether inhibitors. (A-C) Ala95, Ser197 and NADP$^+$ are depicted in stick representation (gray) along with the B-ring *ortho*-substituted inhibitors PT13, PT70 and PT119 (colored according to Figure 3-6). Distances are given as mean values (standard deviation is 0.1 Å in all cases) **(D)** The 2'-cyano group (shown as space filling model) of PT119 fills the saFabI side pocket created by Ala95, Ser197 and NADP$^+$ (shown as gray surface) with a good steric fit.

Small and slightly polar 2'-substituents contribute to binding. We also obtained interesting SAR at the B-ring *ortho* position of the diphenyl ether analogs (Table 3-1). The introduction of a 2'-cyano group enhances affinity and residence time up to 2- and 3-fold, respectively. A methyl substituent (PT70, Figure 3-8B) also increased affinity (data not shown), while PT13 with an amino substituent displayed decreased affinity (Figure 3-8A). All investigated 2'-substituents bind to a narrow, elongated and slightly polar side pocket created by Ala95, Ser197 and the pyrophosphate moiety of NADP$^+$ (Figure 3-8). However, only the linear CN group of PT119 reaches the bottom of this cavity with its polar tip, rendering it ideally suited to fully occupy this space (Figure 3-8D). In contrast, the steric fit is worse for H, CH_3, Cl (triclosan, PDB-code: 4ALI), and NH_2. In particular, the amino substituent is 12-fold less potent as its polar hydrogens have to be desolvated upon binding and cannot engage in geometrically favorable hydrogen bond interactions with surrounding protein residues (Figure 3-8A). Due to the clearly limited space in this region of the saFabI binding pocket, we advocate the usage of small B-ring *ortho* substituents in future drug design studies.

Alternative methods confirm the drug-target dissociation rates. Direct dissociation methods were used to further validate the forward progress curve-based kinetic characterization of diphenyl ethers. In the jump dilution assay, saFabI was pre-incubated overnight with inhibitor in the presence of NADP$^+$ prior to dilution into buffer containing substrate. For less potent inhibitors, dilution allows for full recovery of enzyme activity (Figure 3-9A; see PT55 and PT52). Thus, for these inhibitors, it was found that the k_{obs} values obtained using jump dilution analysis were in good agreement with k_{-1} values obtained via forward progress curve experiments (Table 3-1). Unfortunately, compound rebinding complicated the use of jump dilution assays to quantify dissociation of more potent inhibitors, resulting in only partial recovery of enzyme activity. Since the mechanism of inhibition precluded the use of saturating concentrations of substrate to compete against rebinding, k_{obs} for these jump dilution curves overestimated the true k_{-1}. Long-residence-time inhibitors also required a time window extending beyond the feasible assay limits. Nevertheless, given the kinetic parameters derived from progress curve analysis and the radioactivity-based method described below, we can predict the partially recovered jump dilution curve with great accuracy (Figure 3-9A; see PT447).

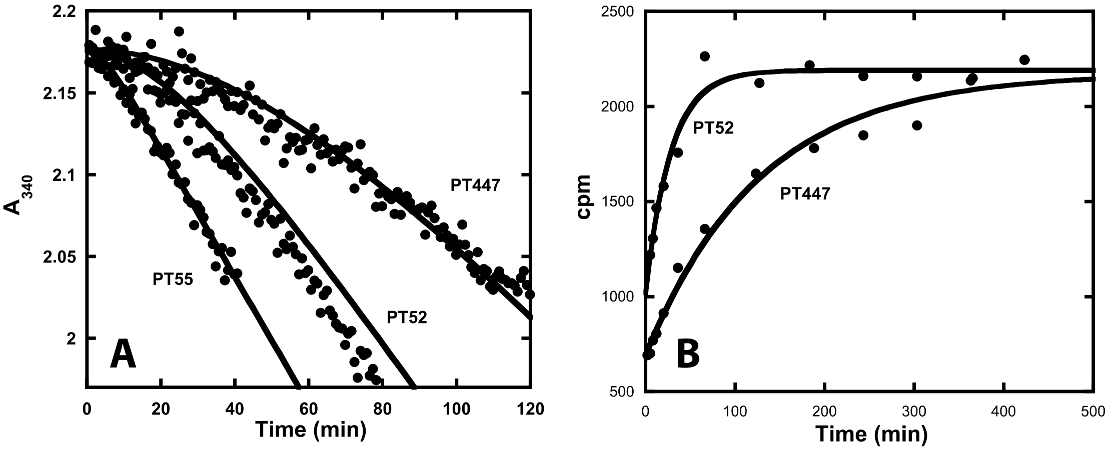

Figure 3-9. Direct measurements of inhibitor dissociation. (A) Experimental jump dilution progress curves (●) are shown for the pre-formed saFabI-NADP$^+$-PT55, saFabI-NADP$^+$-PT52 and saFabI-NADP$^+$-PT447 ternary complexes. Theoretical curves (—) have been superimposed on the experimental data. These curves were generated using the kinetic parameters in Table 3-1 and Equation 1. R^2 (goodness of fit between theoretical curves and experimental data) = 0.98, 0.94 and 0.97 for PT55, PT52 and PT447, respectively. Unlike PT447, there is near recovery to the uninhibited reaction velocity for the less potent compounds PT55 and PT52. **(B)** Release of ^{32}P-NAD$^+$ from the pre-formed ternary complex using the saFabI R40Q/K41N/S44L triple mutant is plotted as a function of time. The lines represent the best fits of the points to Equation 5 (R^2 = 0.97 and 0.98 for PT52 and PT447, respectively). Fitted k_{off} values are listed in Table 3-1.

To enable accurate characterization of long residence time inhibitors, we also developed a ^{32}P-NAD$^+$-based assay of inhibitor dissociation (Figure 3-9B). This was previously used to study dissociation of diphenyl ethers from the FabI homolog in *M. tuberculosis*, InhA (207). Since wild-type saFabI prefers binding to NADP$^+$, we used the R40Q/K41N/S44L triple mutant. We showed previously that this mutant behaves exactly as the wild-type enzyme except for an exclusive preference for NAD(H) (19,46). For all examined inhibitors, we observed good agreement between the k_{-1} values obtained via the different methods. This direct dissociation method is strongly preferred for the characterization of long-residence-time inhibitors which have very slow off rates (Table 3-1). For instance, PT119 had a residence time exceeding 700 minutes that could only be accurately measured using this radioactivity-based direct dissociation technique. For this particular inhibitor, progress curve analysis provided a poor estimate of k_{-1}.

3.6 Discussion

In the quest for new effective therapeutics against increasingly resistant pathogens, it is crucial to understand the precise mechanisms of both pharmacologic and physiologic protein-ligand interactions. An improved molecular understanding of drug-target kinetics can be particularly valuable. Therefore, we chose saFabI - an important target for the development of new anti-staphylococcal drugs (103) - as a model system to rationalize and optimize the drug-target residence time on a structural basis.

A new, multifaceted approach was utilized to obtain a full kinetic characterization of saFabI inhibition by a series of diphenyl ethers. Using a precise, predictive mechanistic model, we can unravel the key kinetic parameters k_1, k_{-1} and K_i for any given inhibitor from only a single progress curve at a single inhibitor concentration. All of this information is contained in the uninhibited and steady state velocity and pseudo-first order rate constant. The amount of time and substrate required for progress curve analysis has traditionally been limiting given the need for multiple progress curves to characterize a single inhibitor. We have, therefore, developed an extremely efficient and information-rich kinetic assay for future drug discovery efforts. The kinetic information attained via forward progress curve analysis was further validated by direct dissociation methods allowing for the accurate characterization of high affinity and long-residence-time saFabI inhibitors.

We found that dissociation rates and thermodynamic affinity are strongly correlated in a double logarithmic plot (Figure 3-5B). Very recently, a comparable correlation between K_i and k_{off} has been demonstrated for the amino-nucleoside-based inhibitors of the human protein methyltransferase DOT1L (48). Interestingly, Maschera and coworkers identified a similar relationship for saquinavir binding to wild-type HIV-protease and three different resistance-conferring mutants (45,208). Thus, nature may select for mutations that promote faster inhibitor dissociation as a primary resistance mechanism. The logarithmic values of k_{-1} and K_i are proportional to the dissociation energy barrier of the ligand ΔG_{-1} and its free energy of binding ΔG_i. The energy barrier of dissociation, and hence the residence time, can be increased by either destabilizing the transition state or stabilizing the ground state of the final enzyme-inhibitor complex (10).

Rational optimization of the residence time is usually difficult as the transition state structure is not readily available (10). For the saFabI system, an exact knowledge of this transient structure is not essential. Based on the observed correlation between k_{off} and K_i, considerations of the saFabI-NADP$^+$-inhibitor complex ground state will be sufficient for the rational improvement of both affinity and residence time. We obtained a wealth of structural information explaining the observed residence time and affinity trends. For example, the addition of bulky hydrophobic diphenyl ether 5-substituents or small slightly polar 2'-substituents (e.g. 2'-cyano) lead to a reduced dissociation rate due to a good steric fit within the protein active site (Figure 3-7 and Figure 3-8). On the other hand, significant variations in the association rate constants were not observed. Further exploration of diverse A-ring and/or B-ring substituents may provide insight on how to modulate the transition state barrier.

In addition, our data suggest that affinity and residence time in this system can be significantly enhanced by modifications predictable by a careful consideration of catalysis. Utilizing our parameter estimations (Table S 3-2), diphenyl ethers have affinities in the low picomolar to low nanomolar range. This is consistent with the expected affinity of transition-state analogues (209). Certainly, the deprotonated diphenyl ether resembles an enolate intermediate (Figure 3-10). This may explain its preference for binding together with the oxidized product NADP$^+$. One can, therefore, imagine an enolate-like, late transition state as the rate-limiting barrier in catalysis. In such a scenario, the delocalized system of the diphenyl ether imitates the breaking and forming of substrate bonds on the way to the enolate. In addition, the acidity of the phenol induces a partial negative charge at the hydroxyl oxygen similar to the transition state (Figure 3-10). As further evidence, the relationship between inhibitor affinity and aliphatic chain length at the A-ring 5-position perfectly reflects the relationship between catalytic activity and substrate chain length (Figure 3-10). Interestingly, the least potent inhibitor of our series, PT51, corresponds to a non-natural substrate smaller than the initial crotonyl-ACP substrate. In this context, the observed opening of a hydrophobic channel for long-chain 5-alkyldiphenyl ethers suggests that the gatekeeper residue Ile207 might also play a critical role for binding of substrates with chain lengths exceeding six carbon atoms (Figure 3-7). Based on our knowledge of catalysis, we can also predictably increase potency by stabilizing the oxyanion via electron-withdrawing substituents on the A-ring.

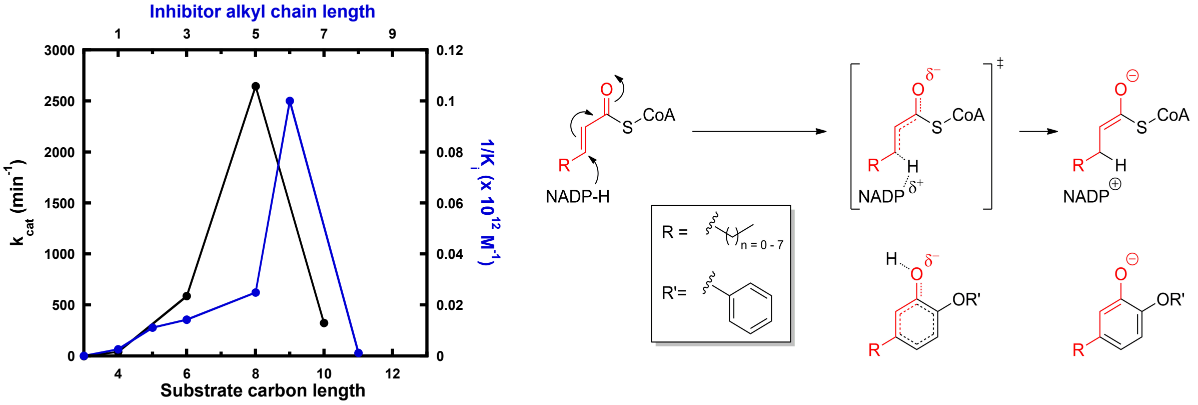

Figure 3-10. Diphenyl ethers as transition state analogues of saFabI. The plot depicts the relationship between fatty acyl-CoA k_{cat} (black; values obtained from our previous work (19)) and inhibitor affinity, plotted as the reciprocal of K_i (blue), as a function of the carbon chain length. An inhibitor with *n* carbons at the A-ring 5-position is equivalent to a substrate with *n*+3 carbon chain length, as depicted on the right. Substrates shorter than 4 carbons in length are catalytically inactive.

Since the diphenyl ethers primarily bind to the E-NADP$^+$ binary complex generated via catalysis, we can predict the evolution of unique kinetic mechanisms of resistance involving mutations away from the inhibitor binding site that accelerate product release. In the case of saFabI, selection experiments have resulted in mutations that do, indeed, lie near the NADP$^+$ binding pocket, particularly I193S (78,92). We believe that this mutation decreases diphenyl ether inhibition by primarily increasing the rate of NADP$^+$ dissociation. However, these mutations are likely to come at a cost since the interactions involved in product binding are also important for binding the reduced cofactor. Accordingly, this mutant was also shown to drastically increase the K_m of the NADPH cofactor (78).

From a thermodynamic perspective, it would seem that there is a disadvantage to having a drug that binds to the enzyme-product complex since enzymes are designed to bind substrates only long enough for catalysis to occur and then release product quickly to allow for additional rounds of catalysis. For this and similar cases of enzyme-product-drug ternary complex inhibition, the focus must be on slowing the dissociation rate of the ternary complex. In the case of saFabI, tighter binding of diphenyl ether transition state analogues corresponds to longer residence times because of minimal perturbations in the kinetic barrier to association. If long residence times correlate with prolonged cellular effects, optimization of residence time may be the key parameter to unlocking *in vivo* efficacy for these series of metabolically labile compounds (210). In this regard, our rigorously determined SAR will facilitate further optimization of promising drug candidates with high activity against *S. aureus*. The ultimate hope is that our multipronged strategy will be applied to diverse, complex enzyme systems to achieve a thorough understanding of the interplay between structure, catalysis and the kinetics and thermodynamics of inhibition. We believe it holds great potential to streamline and facilitate the pursuit of rationality in the early stages of the drug discovery process.

3.7 Associated Content

Supporting Information. Supporting Information Available: 4 supplementary tables and 2 supplementary figures. This material is available free of charge via the Internet at http://pubs.acs.org.

3.8 Author Information

Corresponding Authors

*Peter J. Tonge, Institute for Chemical Biology & Drug Discovery, Department of Chemistry, Stony Brook University, Stony Brook, NY, USA, Tel.: (631) 632-7907; Fax: (631) 632-7934; E-mail: peter.tonge@stonybrook.edu

*Caroline Kisker, Rudolf Virchow Center for Experimental Biomedicine, Institute for Structural Biology, University of Wuerzburg, D-97080 Wuerzburg, Germany, Tel.: +49 931 3180381, E-Mail: caroline.kisker@virchow.uni-wuerzburg.de

Present Addresses

†Arkema Inc., 900 First Avenue, King of Prussia, PA 19406

¶Department of Chemistry, University of California at Irvine, Irvine, CA 92697-2025

Author Contributions

The manuscript was written through contributions of all authors. All authors have given approval to the final version of the manuscript. ‡These authors contributed equally.

Funding Sources

NIH grants GM102864, AI044639, AI070383, T32GM092714 and T32GM008444

Deutsche Forschungsgemeinschaft grants SFB630 and Forschungszentrum FZ82

3.9 Acknowledgments

This work was supported in part by the Deutsche Forschungsgemeinschaft (grants SFB630 to C.K. and C.A.S. and Forschungszentrum FZ82 to C.K.) and by the National Institutes of Health (grants GM102864, AI044639 and AI070383 to P.J.T.). A.C. was supported by the Chemical Biology Training Program (NIH grant T32GM092714) and by the Medical Scientist Training Program (NIH grant T32GM008444). J.S. was supported by a grant of the German Excellence Initiative to the Graduate School of Life Sciences, University of Wuerzburg. We thank the staff at the beamline 14.1 (BESSY II) operated by the Helmholtz-Zentrum Berlin and at the ESRF beamlines ID 14-1 and ID 29 for technical support.

3.10 Abbreviations

ACP, acyl carrier protein; CoA, coenzyme A; FabI, enoyl ACP reductase; FAS II, type 2 fatty acid biosynthesis; NAD^+, nicotinamide adenine dinucleotide; NADH, nicotinamide adenine dinucleotide, reduced form; $NADP^+$, nicotinamide adenine dinucleotide phosphate; NADPH, nicotinamide adenine dinucleotide phosphate, reduced form; TCL, triclosan; t_R, residence time; SAR, structure activity relationship.

3.11 Supporting Information

Table S 3-1. Data collection and refinement statistics.

	PT02	**PT03**	**PT04**
Inhibitor structure	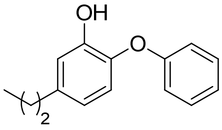	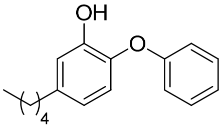	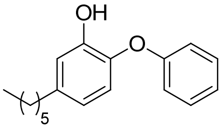
Data collection			
Cell dimensions			
a, b, c (Å)	90.1, 94.9, 94.8	89.1, 94.4, 94.9	90.5, 94.6, 94.8
α, β, γ (°)	98.1, 97.3, 112.3	98.6, 97.2, 111.4	98.0, 112.7, 96.9
Space group	P1	P1	P1
Resolution[1] (Å)	38.5-2.30 (2.42-2.30)	46.2-2.20 (2.32-2.20)	33.5-2.15 (2.27-2.15)
Observed reflections	243,615 (35,310)	239,683 (32,519)	298,031 (43,204)
Unique reflections	122,748 (17,790)	132,692 (19,124)	150,132 (21,758)
Completeness (%)	98.0 (97.3)	93.5 (92.3)	97.9 (97.2)
Average redundancy	2.0 (2.0)	1.8 (1.7)	2.0 (2.0)
R_{merge}[2] (%)	9.7 (41.3)	5.5 (28.0)	6.8 (39.0)
<I / σ(I)>	5.4 (2.0)	10.2 (2.2)	6.8 (2.0)
Refinement			
Resolution (Å)	37.1-2.30	46.0-2.20	33.5-2.15
R_{cryst}[3] (%)	15.8	15.5	14.7
R_{free} (%)	21.9	20.8	19.6
Monomers per AU	8	8	8
Number of atoms	17,905	17,399	17,737
Rmsd bond lengths (Å)	0.010	0.012	0.013
Rmsd bond angles (°)	1.710	1.782	1.854
Average B-factor (Å^2)	33.2	36.6	34.7
Ramachandran-plot[4]			
Favored (%)	95.6	96.3	96.6
Allowed (%)	4.3	3.7	3.4
Outliers (%)	0.1	0.0	0.0
Maximum likelihood based estimated coordinate error (Å)	0.16	0.13	0.12
PDB code	4BNF	4BNG	4BNH

	PT13	**PT53**	**PT55**
Inhibitor structure	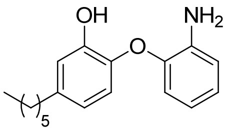	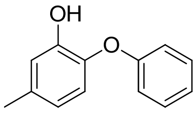	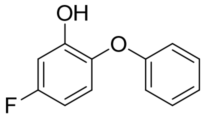
Data collection			
Cell dimensions			
a, b, c (Å)	90.5, 94.6, 94.9	89.9, 94.5, 94.8	90.6, 95.0, 95.0
α, β, γ (°)	97.9, 113.0, 96.9	98.2, 111.9, 97.3	98.1, 97.0, 112.8
Space group	P1	P1	P1
Resolution[1] (Å)	38.6-2.20 (2.32-2.20)	50.0-2.40 (2.50-2.40)	46.1-2.50 (2.64-2.50)
Observed reflections	276,664 (40,119)	421,849 (47,469)	312,430 (45,365)
Unique reflections	139,578 (20,240)	107,887 (12,316)	94,724 (13,764)
Completeness (%)	97.6 (96.8)	98.0 (96.8)	96.6 (96.0)
Average redundancy	2.0 (2.0)	3.9 (3.9)	3.3 (3.3)
R_{merge}[2] (%)	7.5 (39.4)	10.6 (57.1)	12.5 (57.4)
<I / σ(I)>	6.5 (2.0)	8.7 (2.3)	7.2 (2.0)
Refinement			
Resolution (Å)	37.5-2.20	49.3-2.40	46.1-2.50
R_{cryst}[3] (%)	14.7	13.8	18.0
R_{free} (%)	20.0	19.2	25.0
Monomers per AU	8	8	8
Number of atoms	17,719	17,561	17,079
Rmsd bond lengths (Å)	0.012	0.011	0.018
Rmsd bond angles (°)	1.739	1.677	1.814
Average B-factor (Å^2)	34.4	49.5	45.6
Ramachandran-plot[4]			
Favored (%)	95.9	96.3	94.8
Allowed (%)	4.0	3.5	5.1
Outliers (%)	0.1	0.2	0.1
Maximum likelihood based estimated coordinate error (Å)	0.13	0.14	0.21
PDB code	4BNI	4BNJ	4BNK

	PT68	**PT70**	**PT119**
Inhibitor structure	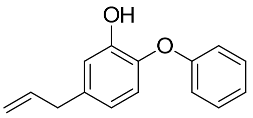	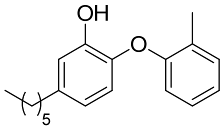	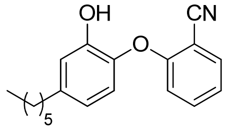
Data collection			
Cell dimensions			
a, b, c (Å)	89.8, 94.5, 94.9	89.1, 94.8, 94.6	89.9, 94.6, 94.3
α, β, γ (°)	97.9, 112.9, 97.0	98.0, 112.2, 97.4	97.9, 112.0, 97.3
Space group	P1	P1	P1
Resolution[1] (Å)	42.8-2.15 (2.27-2.15)	46.4-2.35 (2.48-2.35)	40.9-2.25 (2.37-2.25)
Observed reflections	290,458 (42,164)	223,766 (32,400)	255,816 (37,092)
Unique reflections	147,365 (21,435)	113,028 (16,397)	129,530 (18,781)
Completeness (%)	96.9 (96.2)	97.6 (96.9)	97.5 (96.8)
Average redundancy	2.0 (2.0)	2.0 (2.0)	2.0 (2.0)
R_{merge}[2] (%)	7.0 (40.5)	8.6 (35.4)	8.6 (43.0)
<I / σ(I)>	6.6 (1.9)	6.1 (2.0)	6.0 (2.0)
Refinement			
Resolution (Å)	42.8-2.15	46.4-2.35	40.9-2.25
R_{cryst}[3] (%)	14.6	14.8	15.1
R_{free} (%)	19.6	21.2	20.6
Monomers per AU	8	8	8
Number of atoms	17,874	17,629	17,807
Rmsd bond lengths (Å)	0.012	0.010	0.011
Rmsd bond angles (°)	1.834	1.694	1.761
Average B-factor (Å^2)	34.5	30.5	34.7
Ramachandran-plot[4]			
Favored (%)	96.3	95.8	95.8
Allowed (%)	3.7	4.1	4.1
Outliers (%)	0.0	0.1	0.1
Maximum likelihood based estimated coordinate error (Å)	0.12	0.15	0.14
PDB code	4BNL	4BNM	4BNN

[1] Values in parenthesis refer to the highest resolution shell

[2] $R_{merge} = \sum_{hkl}\sum_{i}\left|I_i - \langle I \rangle\right| \Big/ \sum_{hkl}\sum_{i} I_i$

[3] $R_{cryst} = \sum_{hkl}\left|F_{obs} - F_{calc}\right| \Big/ \sum_{hkl} F_{obs}$

[4] According to Molprobity (172)

Table S 3-2. SaFabI kinetic parameters for the mechanistic model in Figure 3-2.

Parameter	Estimate	Rationale
K_S	0.75 mM for cro-CoA 100 µM for oct-CoA	In the case of cro-CoA, K_d is approximated by K_m since k_{cat} is small. For oct-CoA, a similar approximation is likely to be true since $K_{m,S}^{app}$ stays relatively constant at varying NADPH concentrations.
K_{NADPH}	250 µM	$K_{m,NADPH}^{app}$ stayed relatively constant at varying oct-CoA concentrations. Fluorescence-based direct binding experiments were consistent with weaker binding of NADPH to saFabI than NADH to FabI homologues (< 10 µM).
K_{NADP}	1 M	This is a reasonable lower limit estimate consistent with the lack of observable product inhibition in the presence of 5 mM NADP$^+$ and the minimal effect of 2 mM NADP$^+$ on the kinetics of 500 nM PT53. The true affinity may actually be weaker.
$k_{on,S}$	$6 \cdot 10^8$ M^{-1} min^{-1}	This arbitrary estimate is within an order of magnitude of the diffusion-limited rate constant, which represents the theoretical ceiling. The value will only affect the kinetic system if it is low enough to be rate limiting (approx. $6 \cdot 10^6$ M^{-1} min^{-1}).
$k_{on,NADPH}$	$9 \cdot 10^6$ M^{-1} min^{-1}	A value less than an order of magnitude lower significantly decreases catalytic activity. However, higher values result in lower than observed $K_{m,NADPH}^{app}$.
$k_{off, NADP}$	$3 \cdot 10^4$ min^{-1}	Off rates slower than $3 \cdot 10^3$ min^{-1} result in low $K_{m,NADPH}^{app}$ and activity. Faster off rates require higher estimates of inhibitor (diphenyl ether) affinity to account for observed levels of inhibition. To counterbalance the increased sensitivity of inhibition to added NADP$^+$, the NADP$^+$ affinity must also be proportionally decreased. Based on the diphenyl ether association rate constant, which must not exceed the diffusion-limited rate constant, the upper limit off rate is in the range of $3 \cdot 10^5$ min^{-1}.
k_{cat}	40 min^{-1} for cro-CoA 4000 min^{-1} for oct-CoA	Derived from previously published Michaelis-Menten kinetic data.

Table S 3-3. Morrison-Walsh analysis of theoretically generated progress curves.[a]

[I] (nM)	k_{obs} (hr^{-1})	v_s ($\mu M\ hr^{-1}$)	k_{-1} (hr^{-1}) [b]
0		84.6[c]	
50	2.7089	67.3	2.1919
250	4.4315	36.0	1.8838
500	6.9294	21.8	1.7870
750	9.4962	15.6	1.7448
1000	12.1030	12.1	1.7239
1250	14.7280	9.8	1.7121

a. Parameters: [E] = 65 nM, [Cro-CoA] = 1.5 mM, [NADPH] = 350 µM, [NADP] = 400 µM; for the inhibitor, $k_{on} = 1.37 \times 10^{10}\ hr^{-1}$ and $k_{off} = 1.70\ hr^{-1}$

b. Calculated as $k_{obs} \cdot \frac{v_s}{v_0}$, where v_0 is the uninhibited reaction velocity

c. At this reaction velocity, steady-state [E-NADP$^+$] = 0.051 nM and steady-state [E-NADPH] = 0.017 µM

Table S 3-4. Theoretical analysis of electrostatic contribution to affinity by assuming inhibitor binding solely as a deprotonated species (pH 7.5).

Inhibitor	pK_a	Assumed K_i (nM)	Predicted K_i^{app} (nM)	Experimental K_i^{app} (nM)
PT51	9.12 [a]	0.460	24515.0 [d]	24515.0
PT55	8.12 [a]	0.460	3040.8	1851.8
PT104	7.71 [b]	0.460	1566.4	1933.4
PT53	9.15 [a]	0.007	493.7 [d]	493.7
PT52	8.32 [b,c]	0.007	79.4	161.2

a. Experimental value was obtained from (97).
b. Experimental value was measured in this study.
c. A similar value was reported in (97).
d. Experimental value was used to determine a theoretical K_i. This K_i was assumed to hold true for similarly grouped compounds (blue or green).

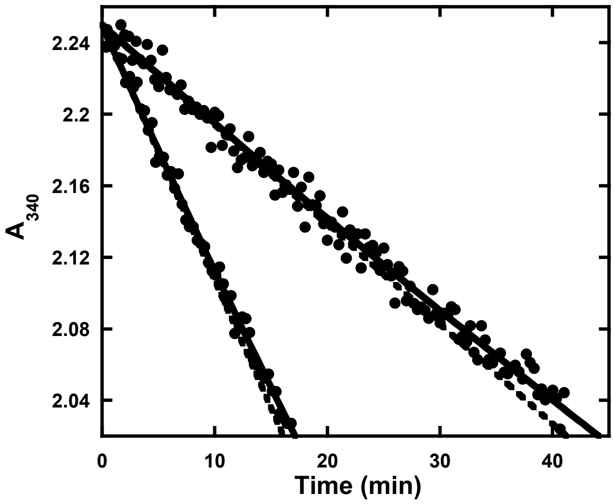

Figure S 3-1. In the absence of inhibitor, ten percent deviation from linearity is achieved at ΔA_{340} of 0.18 and 0.19 for the lower and higher velocity reactions, respectively. Reaction velocities were varied via changes in enzyme concentration. Solid lines depict the experimental fit to Eq. 1; dotted lines depict a linear extrapolation of the initial velocity.

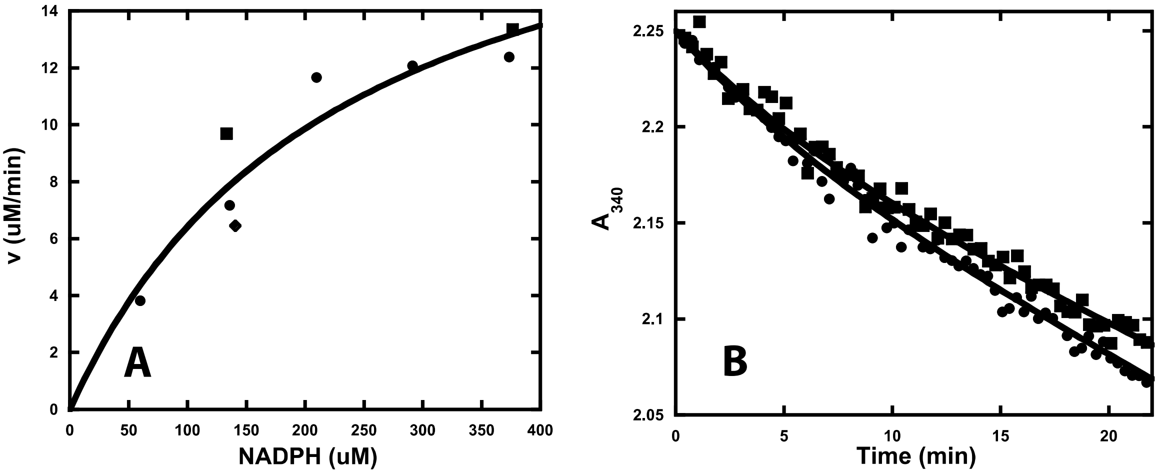

Figure S 3-2. (A) The Michaelis-Menten relationship is plotted for saFabI (20 nM) utilizing octenoyl-CoA (37.5 μM) and varying concentrations of NADPH in the absence of $NADP^+$ (●; trace). Points corresponding to initial velocity measurements in the presence of 1.5 mM (■) and 5 mM (◆) $NADP^+$ are superimposed. **(B)** The progress curves depict saFabI inhibition by 500 nM PT53 in the presence of 400 μM (●) and 2000 μM $NADP^+$ (■). Best-fit parameters for the pseudo-first order rate constant (k_{obs}) and steady-state velocity (v_s) are 0.139 min^{-1} and 0.98 μM min^{-1}, respectively, at 400 μM $NADP^+$ and 0.146 min^{-1} and 0.87 μM min^{-1}, respectively, at 2000 μM $NADP^+$.

4 Molecular Basis for the Narrow-spectrum Activity of the Clinical Candidate CG400549 and the Rational Design of a Potent Broad-spectrum Pyridone-based FabI Inhibitor.

This chapter is based on the following publication:

Schiebel, J.*, Chang, A.*, Shah, S., Lu, Y., Liu, L., Pan, P., Hirschbeck, M. W., Tareilus, M., Eltschkner, S., Cummings, J. E., Knudson, S. E., Bommineni, G. R., Yu, W., Walker, S. G., Slayden, R. A., Sotriffer, C. A., Tonge, P. J., and Kisker, C. (in preparation[‡]) Molecular Basis for the Narrow-spectrum Activity of the Clinical Candidate CG400549 and the Rational Design of a Potent Broad-spectrum Pyridone-based FabI Inhibitor.

Author contributions with respect to data collection:

Schiebel, J.:	X-ray crystallography, computational docking
Chang, A.:	Enzyme kinetics, MIC determination, thermal shift assays
Shah, S.:	Synthesis of 2-pyridone inhibitors (details not shown)
Lu, Y.:	*In vivo* mouse model of infection
Liu, L.:	Pharmacokinetics
Pan, P.:	Synthesis of 4-pyridone inhibitors (details not shown)
Hirschbeck, M. W.:	X-ray crystallography (bpFabI-NAD$^+$-PT155)
Tareilus, M.:	X-ray crystallography (ecFabI-NADH-CG400549)
Eltschkner, S.:	X-ray crystallography (ecFabI-NADH-PT166)
Bommineni, G. R.:	Synthesis of 2-pyridone inhibitors (details not shown)
Cummings, J. E.:	MIC determination
Knudson, S. E.:	MIC determination
Yu, W.:	Protein expression and purification

*These authors contributed equally

[‡] The printed version might be subject to some changes prior to submission

Molecular Basis for the Narrow-spectrum Activity of the Clinical Candidate CG400549 and the Rational Design of a Potent Broad-spectrum Pyridone-based FabI Inhibitor*

Johannes Schiebel[1, 2, 6], Andrew Chang[3, 4, 6], Sonam Shah[3], Yang Lu[3, 4], Li Liu[3], Pan Pan[3], Maria W. Hirschbeck[1], Mona Tareilus[1], Sandra Eltschkner[1], Jason E. Cummings[5], Susan E. Knudson[5], Gopal R. Bommineni[3], Weixuan Yu[3], Stephen G. Walker[4], Richard A. Slayden[5], Christoph A. Sotriffer[2], Peter J. Tonge[3], Caroline Kisker[1]

From the [1]Rudolf Virchow Center for Experimental Biomedicine, Institute for Structural Biology, University of Wuerzburg, D-97080 Wuerzburg, Germany

[2]Institute of Pharmacy and Food Chemistry, University of Wuerzburg, Am Hubland, D-97074 Wuerzburg, Germany

[3]Institute for Chemical Biology & Drug Discovery, Department of Chemistry, Stony Brook University, Stony Brook, NY 11794-3400, USA

[4]School of Dental Medicine, Department of Oral Biology and Pathology, Stony Brook University, Stony Brook, NY 11794-3400, USA

[5]Rocky Mountain Regional Center of Excellence and Department of Microbiology, Immunology and Pathology, Colorado State University, Fort Collins, CO 80523-1682, USA

[6]These authors contributed equally.

To whom correspondence should be addressed: Caroline Kisker, Rudolf Virchow Center for Experimental Biomedicine, Institute for Structural Biology, University of Wuerzburg, D-97080 Wuerzburg, Germany, Tel.: +49 931 3180381, Fax: +49 931 3187320, E-mail: caroline.kisker@virchow.uni-wuerzburg.de

Peter J. Tonge, Institute for Chemical Biology & Drug Discovery, Department of Chemistry, Stony Brook University, Stony Brook, NY, USA, Tel.: (631) 632-7907, Fax: (631) 632-7934, E-mail: peter.tonge@stonybrook.edu

4.1 Keywords

target selectivity; induced-fit substrate recognition; induced-fit inhibitor binding; fatty acid biosynthesis; *Staphylococcus aureus* FabI; enoyl-ACP reductase; pyridones; diphenyl ethers; enzyme kinetics; crystallography; structure based drug design; CG400549

4.2 Capsule

Background: The enoyl-ACP reductase FabI is a promising target for the development of novel antibiotics.

Results: Our data reveal the molecular determinants conferring *S. aureus* FabI selectivity to the clinical candidate CG400549.

Conclusion: The rationally designed FabI inhibitor PT166 has higher intrinsic potency and broad-spectrum activity.

Significance: This study demonstrates how to rationally expand the spectrum of antimicrobial activity.

4.3 Summary

Determining the molecular basis for target selectivity is of particular importance in drug discovery. The ideal antibiotic should be active against a broad spectrum of pathogenic organisms with only a minimal effect on human targets. CG400549 - a *Staphylococcus*-specific 2-pyridone compound that inhibits the enoyl-ACP reductase (FabI) - has recently been confirmed to possess human efficacy for the treatment of methicillin-resistant *Staphylococcus aureus* (MRSA) infections, which constitute a serious threat to human health. In this study, we solved the structures of three different FabI homologues in complex with several pyridones including CG400549. Based on these structures we rationalize the 65-fold reduced affinity of CG400549 towards *Escherichia coli* vs. *S. aureus* FabI and implement concepts to improve the spectrum of antibacterial activity. Specifically, the identification of different conformational states along the reaction coordinate of the enzymatic hydride transfer provides an elegant visual depiction of the relationship between catalysis and inhibition, which facilitates rational drug design. Ultimately, we were able to develop the pyridone compound PT166 that potently inhibits FabI with broad-spectrum *in vitro* activity, favorable pharmacokinetic profile, and efficacy in a mouse model of *S. aureus* infection.

4.4 Introduction

Staphylococcus aureus can cause a variety of bacterial infections ranging from common skin infections to life-threatening pneumonia or bacteraemia (29). In particular, methicillin-resistant *S. aureus* (MRSA)[7] poses an imminent risk to immuno-compromised patients in healthcare settings all over the world. In addition, the incidence of community-acquired MRSA infections has increased amongst otherwise healthy individuals (29,211). The initial occurrence of *S. aureus* strains resistant to vancomycin (VRSA), an antibiotic used to treat severe MRSA infections (143), underlines the urgent need for novel anti-staphylococcal drugs.

Isoniazid, a first-line prodrug for the treatment of tuberculosis, inhibits the type II fatty acid biosynthesis (FAS-II) pathway of *Mycobacterium tuberculosis* (53). The clinical success of isoniazid validates the FAS-II pathway as a valuable target for the development of new antibiotics (54). Importantly, bacterial fatty acid biosynthesis differs from its mammalian counterpart and is pivotal for the production of several cellular components, such as phospholipids (19,50). In the last step of the FAS-II elongation cycle, the enoyl-acyl carrier protein (ACP) reductase (FabI) catalyzes the reduction of the *trans*-2-enoyl-ACP double bond (Figure 4-1) (78,108). The discoveries that activated isoniazid and the antimicrobial agent triclosan inhibit FabI (55,71,111,117,212) generated significant interest in this enzyme as a potential broad-spectrum target shared among many pathogenic organisms (1,67). However, the finding that distinct bacteria like *Streptococcus pneumoniae* or *Vibrio cholerae* utilize FabI isoenzymes including FabK (64), FabL (65) and FabV (66) or can take up exogenous fatty acids from the host blood serum to circumvent the inhibition of FabI (90), has altered the perception that FabI could be a broad-spectrum target (1). Nevertheless, for several clinically relevant pathogens such as *S. aureus*, *Staphylococcus epidermidis*, *Escherichia coli*, *Haemophilus influenzae*, *Francisella tularensis* and *M. tuberculosis* FabI remains a very promising drug target since these organisms require endogenous fatty acids (19,53,88,89) and contain FabI as the sole enoyl-ACP reductase (101,102). Accordingly, several drug design programs have been continued, and three *S. aureus* FabI (saFabI) inhibitors with different scaffolds (Figure 4-1) have been advanced to clinical trials (103).

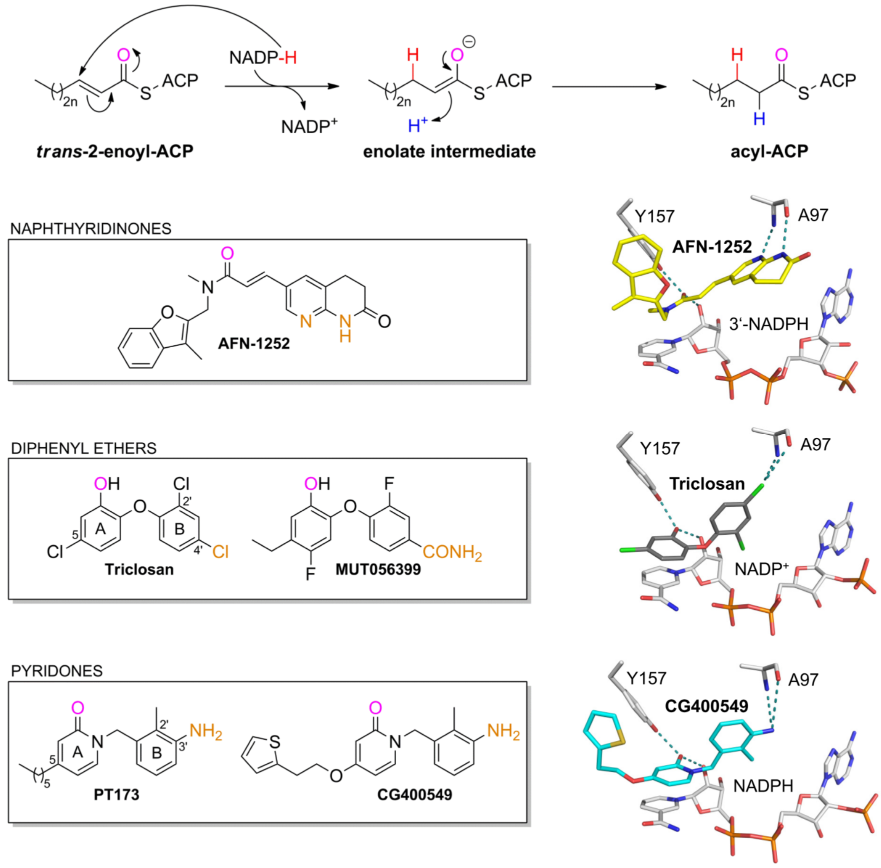

Figure 4-1. Catalyzed reaction and successful inhibitor classes of *S. aureus* FabI. FabI catalyzes the reduction of the *trans*-2-enoyl-ACP substrate via an enolate intermediate (n = 0 - 8) (51). In the case of saFabI, the hydride (shown in red) is delivered by the reducing agent NADPH (19,78,108). During the second step of the reaction the enolate intermediate is protonated, which leads to the formation of the final acyl-ACP product (the proton is depicted in blue). Examples for the most important FabI inhibitor classes are given in the boxes along with their binding mode in the saFabI active site pocket (PDB-codes: 4FS3 and 4ALI (19,101); the CG400549 structure was solved during this study). For each of these inhibitor scaffolds, one compound is currently in clinical trials (AFN-1252, MUT056399 and CG400549) (103). One common feature of these FabI inhibitors is the formation of a hydrogen bond to Tyr157 and the cofactor NADP(H). The oxygen atoms involved in this central interaction are colored in magenta. In addition, all depicted inhibitors directly interact with Ala97 (the interacting inhibitor atoms are highlighted in orange).

Based on the lead compound triclosan, Mutabilis developed the diphenyl ether MUT056399 (Figure 4-1), which displays activity against *S. aureus* and several important Gram-negative pathogens (92,102). In contrast, the pyridone CG400549 (CrystalGenomics) as well as the naphthyridinone AFN-1252 (GlaxoSmithKline and Affinium Pharmaceuticals) were shown to be *Staphylococcus*-specific (Figure 4-1) (1,4,31,100,101,213). Importantly, all three FabI inhibitors have been shown to be efficacious in mouse models of infection (92,100,101). Very recently, CrystalGenomics announced that the Phase 2a study for CG400549 has been completed and confirmed human efficacy without serious adverse events[8].

Extensive studies have been conducted on the molecular recognition of diphenyl ethers by (sa)FabI (19,67,188). However, little is known about the binding of pyridone inhibitors such as CG400549. These compounds were intended to simply improve pharmacokinetic properties by replacing the metabolically labile phenol of the diphenyl ether skeleton with a stable pyridone (103). Despite the structural similarity between pyridones and diphenyl ethers, we reveal fundamental differences in the molecular recognition of these two scaffolds by FabI enzymes, which serve as the underlying basis for their respective narrow- and broad-spectrum activities. We report the first pyridone-bound crystal structures of saFabI, in addition to a complete kinetic profile of inhibition. In particular, we solved the CG400549-bound saFabI and *E. coli* FabI (ecFabI) structures, which help to rationalize the selectivity of this compound for the *S. aureus* homologue. Based on our cumulative insights, we have developed the novel 4-pyridone inhibitor PT166 that exhibits broad-spectrum *in vitro* activity and *in vivo* efficacy in a murine *S. aureus* thigh infection model.

4.5 Experimental Procedures

4.5.1 Compound synthesis

The pyridone compounds PT155, PT159, PT166, PT170, PT171, PT172, PT173, PT179, PT191, PT420 and CG400549 were synthesized as described in the supplement.

4.5.2 Expression and Purification

SaFabI was prepared as described previously (19,144). Briefly, we expressed the *safabi* gene cloned into a pETM-11 vector in *E. coli* BL21(DE3), disrupted the cells and obtained the > 95% pure protein in 25 mM Tris pH 8.0 and 200 mM NaCl via Ni^{2+} affinity and size exclusion chromatography. In addition, *E. coli* FabI (ecFabI) was expressed and purified as described previously (109). *Burkholderia pseudomallei* FabI (bpFabI) was obtained using a previously described procedure (214) with the final size exclusion chromatography step (Superdex 200 26/60, GE Healthcare/ÄKTA) performed in 20 mM Bistris pH 6.5, 500 mM NaCl, 1 mM EDTA.

4.5.3 Crystallization

Prior to concentrating saFabI samples from 2 to 15-19 mg/ml, the protein was incubated for 2 hours at 20 °C with a 12-fold molar excess of NADPH and a 20-fold molar excess of inhibitor dissolved in DMSO (CG400549 or PT173, respectively). Diffraction-quality crystals were grown in vapor diffusion experiments with a precipitant solution containing 0.1-0.2 M Li_2SO_4 and 20-24% PEG 3350. For CG400549, we obtained crystals of space group $P2_12_12_1$ with two different sets of cell parameters (the resulting structures were named CG400549-I and II; Table S 4-1).

Similarly, ecFabI samples at a concentration of 13 mg/ml were incubated for 2 hours at 4°C with a 10-fold molar excess of NADH and a 20-fold molar excess of CG400549 or PT166 (dissolved in DMSO), respectively. Hanging-drop vapor diffusion experiments yielded diffraction-quality crystals in drops composed of 1 µl of this protein-ligand mixture and 1 µl precipitant solution (0.2 M NH_4Ac, 0.1 M CAPS pH 10.5 and 20% PEG 8000 in the case of CG400549; 0.2 M NH_4Ac, 0.1 M sodium citrate pH 5.6 and 10% PEG 8000 in the case of PT166).

BpFabI samples with a concentration of 10-30 mg/ml were incubated for 2 hours at 20 °C with a 10-fold molar excess of NAD^+ and a 20-fold molar excess of PT155 (dissolved in DMSO). Sitting-drop vapor diffusion experiments yielded diffraction-quality crystals in drops composed of 0.3 µl of the protein-ligand mixture and 0.3 µl precipitant solution (20% PEG 3350 and 200 mM $(NH_4)_2HPO_4$).

4.5.4 Data Collection and Structure Determination

Prior to flash-freezing in liquid nitrogen, the saFabI ternary complex crystals were successively transferred into solutions composed of mother liquor supplemented with 10 and 25% ethylene glycol, respectively. Diffraction data were collected at the BESSY II MX beamline 14.1 (199) (λ = 0.918 Å, T = 100 K) equipped with a MarMosaic 225 detector, integrated with Imosflm (CG400549-II and PT173) (178) or XDS (CG400549-I) (183) and further processed using Scala (179). The CG400549 structures were solved by molecular replacement with Phaser (180) using our previously published saFabI structure (PDB-code: 4ALK; lacking amino acids 196-202) as search model (19). For PT173, the fully refined CG400549-I structure was used as a template for the molecular replacement procedure. To avoid model bias, R_{free} flags were copied from the search model (PT173) and assigned in thin resolution shells (CG400549-I and II). The final structures were obtained by several alternate cycles of model building in Coot (182) and refinement in Refmac 5 (CG400549-bound structures) (181) or Phenix (PT173) (185), respectively (including NCS- (PT173, CG400549-II) and TLS-refinement (200)). Amplitude-based twin refinement was used in the case of CG400549-II, for which we detected slightly twinned data. Cofactors and inhibitors could be unambiguously assigned based on the $2F_o$-F_c and F_o-F_c electron density maps.

Crystals of the CG400549 and PT166 ternary complexes were cryo-protected using the corresponding mother liquor supplemented by 25% or 30% ethylene glycol, respectively. Using a Pilatus 6M detector, diffraction data were collected at the MX beamline 14.1 of the BESSY II synchrotron (λ = 0.918 Å, T = 100 K) and at beamline ID 23-1 of the ESRF (λ = 1.064 Å, T = 100 K), integrated using XDSAPP (215) and scaled with Scala. Initial phases were determined by molecular replacement in Phaser with our previously published ecFabI structure (PDB-code: 1QSG) as the search model (111). Model building in Coot and refinement using Refmac 5 (including TLS-refinement) yielded the final structure. We did not model the amino acid range 193 to 209-211 due to only partial and very weak electron density. In addition, we note that the CG400549 electron density in subunit B was still sufficient but not as good as in monomer A. Dictionaries for the cofactors and inhibitors of the *S. aureus* and *E. coli* FabI structures were computed using Grade (216,217).

BpFabI crystals were cryo-cooled in cryo-protectant containing 25% glycerol in the mother liquor. Data collection was performed at an in-house X-ray generator (MicroMax-007 HF, Rigaku) at a wavelength of 1.54 Å and recorded with an imaging plate detector (R-Axis HTC, Rigaku). Data were integrated with Imosflm and scaled in Scala. Molecular replacement was performed in Phaser using the PDB entry 3EK2 as a template. For refinement in Refmac and finally Phenix TLS parameters were created using the TLSMD server (200) and a library file supplying restraints for the cofactor and inhibitor was generated by the Prodrg server (187). The structure was refined until convergence (R/R_{free}= 14/16%) and validated using the Molprobity server (218).

To avoid model bias, omit maps were calculated prior to inclusion of cofactors and inhibitors. Data collection and refinement statistics are given in the Supplemental Table S 4-1 (saFabI) and Table S 4-2 (ecFabI and bpFabI). Distances and angles were measured for all subunits of the asymmetric unit and are given as mean values ± standard deviation. Structural figures were prepared using PyMOL (174).

4.5.5 Inhibition Kinetics

Kinetics were performed on a Cary 100 spectrophotometer (Varian) at 20°C. Reaction velocities were measured by monitoring the oxidation of NAD(P)H to $NAD(P)^+$ at 340 nm (ε = 6220 M^{-1} cm^{-1}). For saFabI, the reaction mixture was identical to that described previously for progress curve experiments (19). For ecFabI, the final reaction mixture contained ecFabI (75 nM), *trans*-2-butenoyl-CoA (800 µM; Sigma and Advent Bio), NADH (300 µM; Sigma), NAD^+ (400 µM; Sigma) and inhibitor (2% v/v DMSO) in 50 mM potassium phosphate pH 7.5, 150 mM NaCl, 8% glycerol. The resulting curves were fit to the Morrison & Walsh integrated rate equation (Equation 1) (202). K_i^{app} was determined using the standard isotherm equation (Equation 2) or Morrison quadratic equation for tight-binding inhibitors (Equation 3) (219). For pyridones, the K_i was extracted from K_i^{app} using Equation 4, where K_S and $K_{NAD(P)H}$ values are provided in Table S 4-3 or (188).

$$A_t = A_0 - v_s t - (v_i - v_s) \cdot \frac{1 - e^{-k_{obs} t}}{k_{obs}} \qquad \text{(Eq 1)}$$

where A_t and A_0 are the absorbance at time t and time 0, v_i and v_s are the initial and steady-state velocities and k_{obs} is the pseudo-first order rate constant for the approach to steady-state.

$$\frac{v_i}{v_u} = \frac{1}{1 + \frac{[I]}{K_i^{app}}} \qquad \text{(Eq 2)}$$

where v_u is the control, uninhibited velocity and K_i^{app} is the IC_{50} value.

$$\frac{v_i}{v_u} = 1 - \frac{([E]_T + [I]_T + K_i^{app}) - \sqrt{([E]_T + [I]_T + K_i^{app})^2 - 4[E]_T[I]_T}}{2[E]_T} \qquad \text{(Eq 3)}$$

where $[E]_T$ and $[I]_T$ are the total enzyme and inhibitor concentrations, respectively.

$$K_i^{app} = K_i \left(1 + \frac{[S]}{K_S} + \frac{K_{NAD(P)H}}{[NAD(P)H]} \right) \qquad \text{(Eq 4)}$$

where K_S and $K_{NAD(P)H}$ are the respective dissociation rate constants for the enoyl-CoA substrate and NAD(P)H.

For the jump dilution assay, 10 µM saFabI, 15 µM inhibitor and 500 µM NADPH were preincubated overnight at room temperature followed by 1:200 dilution into reaction buffer

(50 mM potassium phosphate pH 7.5, 150 mM NaCl, 1 M potassium glutamate, 8% glycerol) containing 1.5 mM *trans*-2-butenoyl-CoA and 350 µM NADPH. The resulting progress curve was fitted to Eq 1. All curve fitting was performed using KaleidaGraph Version 4.1.

4.5.6 Thermal Shift Assay

ThermoFluor experiments were carried out in 96-well plates (Concord) using the CFX96 Real-Time PCR Detection System and C1000 Thermal Cycler (Bio-Rad), as described previously (188).

4.5.7 Docking Studies

A computational docking and scoring procedure was used to generate putative binding modes for all pyridone inhibitors investigated in this study. The binding poses were generated with FlexX (BioSolveIT, Sankt Augustin, 2009), version 3.1.4 (220), and rescored with DrugScore^X (G. Neudert and G. Klebe, University of Marburg, 2008), version 0.21, which builds on DrugScore and utilizes the DrugScore^{CSD} potentials (221-223). To account for the flexibility of the substrate binding loop, we docked all inhibitors into subunits A and C of the saFabI CG400549-I structure, which represent the two experimentally observed states (for details see results section). The selection of the most likely binding pose and receptor was based on the DrugScore^X Score combined with visual inspection (Figure S 4-1). A comparison with the available experimental binding modes revealed rms deviations below 1.1 Å for the ten best-ranked binding poses, with 0.7 Å (CG400549) and 0.8 Å (PT173) for the top-ranked pose, respectively (Figure S 4-1A and Figure S 4-1B). These re-/cross-docking experiments confirm the validity and reliability of our computational approach.

The inhibitors were setup with MOE (Chemical Computing Group, Montreal, 2010), version 2010.10 (224), and energetically minimized (Tripos force field) using SYBYL-X (Tripos, St. Louis, 2009), version 1.0 (225). NADPH was protonated within the saFabI environment using MOE. The saFabI CG400549-I crystal structure was protonated in FlexX and the binding site region defined by NADPH and the amino acids 93-99, 102, 121, 146-147, 154-157, 160, 164, 190-193, 195, 197-204 and 207. Water molecules within a radius of 6 Å around CG400549 were included during the docking procedure and treated as displaceable particles. FlexX was run in command line mode with a default docking procedure, followed by post-docking optimization. Rms deviations were calculated using fconv (G. Neudert and G. Klebe, University of Marburg, 2012), version 1.24 (226).

4.5.8 Determination of MIC Values

MIC values were determined with the microbroth dilution assay according to the Clinical and Laboratory Standards Institute methods for antimicrobial susceptibility tests for aerobically growing bacteria (227).

4.5.9 *In vivo* Pharmacokinetics

Pharmacokinetic (PK) studies were conducted in female ICR mice via intraperitoneal administration of PT04 (200 mg/kg dose) or PT166 (100 mg/kg dose) in a vehicle of 40% PEG / 40% EtOH / 20% H_2O. Blood samples were collected from each animal at eight time points (5 min, 15 min, 30 min, 1 hour, 2 hours, 4 hours, 8 hours and 24 hours post-injection). Three mice were sampled per time point. Plasma concentrations for each sample were measured by LC/MS/MS, and PK parameters were calculated with WinNonlin (Pharsight Corporation, Mountain View, CA, USA).

4.5.10 *In vivo* Efficacy

Anti-bacterial efficacy of 5-hexyl-2-phenoxyphenol (PT04) and PT166 (Table 4-1) was evaluated in a neutropenic mouse thigh infection model. Six week old, male Swiss Webster mice weighing 23 to 27 g were rendered neutropenic by intraperitoneal injection of cyclophosphamide 4 days (150 mg/kg) and 1 day (100 mg/kg) prior to infection. Previous studies have shown that this can produce severe neutropenia in mice for at least 5 days (228).

MRSA strain BAA1762 was cultured in Mueller-Hinton (MH) broth to mid log phase (OD_{600} = 0.4; 3×10^8 CFU/ml) and harvested by centrifugation. Cell pellets were resuspended in freshly sterilized Brain Heart Infusion (BHI) broth to a final inoculum of 1×10^7 CFU/ml. 50 µl of this suspension (5×10^5 CFU) was injected intramuscularly into the left thigh of each mouse while 50 µl of BHI broth was injected into the right thigh as control. Drug was administered by subcutaneous injection at 1 hour and 12 hours post-infection (100 mg/kg dose per injection). Mice were euthanized 24 hours post-infection. Each thigh muscle was subsequently collected and homogenized in saline containing 10% BHI broth. Bacterial load was determined by counting colony-forming units of serial dilutions plated on MH sheep blood agar.

For *in vivo* efficacy and PK studies, all animals were maintained in accordance with criteria set by the American Association for Accreditation of Laboratory Animal Care. This study was approved by the Institutional Animal Care and Use Committee (IACUC) at Stony Brook University.

4.6 Results

CG400549 and related 2-pyridones selectively inhibit growth of S. aureus – The 2-pyridone CG400549 exhibits potent activity against *S. aureus* in contrast to many other bacteria such as *E. coli*, *Listeria monocytogenes*, *Helicobacter pylori* and *Pseudomonas aeruginosa* (31). We confirmed this disparity by comparing growth inhibition of *S. aureus* and *E. coli* by various 2-pyridone inhibitors (Table 4-1 and Table 4-2). An important question to address is whether this narrow-spectrum behavior can be attributed to FabI-specific differences between species.

Table 4-1. Thermodynamic parameters for inhibitors of saFabI [a]

Name	Structure	K_i^{app} (nM) [b]	K_i (nM)	MIC (µM) [c]
CG400549	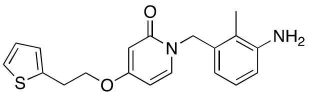	4.73 ± 0.50	1.27 ± 0.13	5.87

PT173	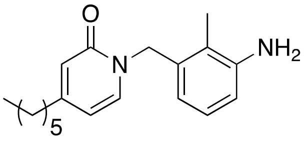	7.30 ± 1.54	1.97 ± 0.42	6.70
PT171	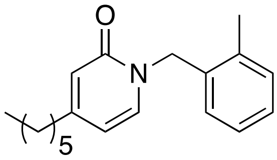	44.28 ± 6.57	11.94 ± 1.77	n.d. [d]
PT179	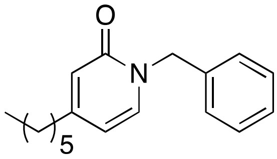	70.44 ± 9.83	18.99 ± 2.65	118.79
PT420	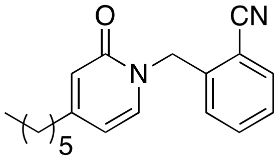	109.75 ± 1.66	29.58 ± 0.45	108.70
PT172	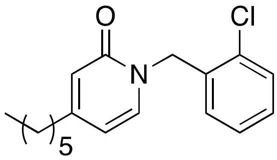	40.74 ± 1.31	10.98 ± 0.35	26.33
PT170	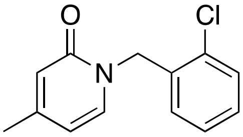	848.61 ± 19.32	228.74 ± 5.21	> 500
PT166	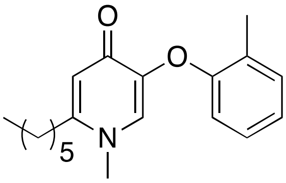	10.05 ± 2.10	2.71 ± 0.57	0.83
PT159	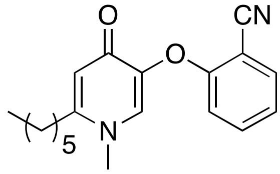	40.97 ± 3.42	11.04 ± 0.92	12.89
PT191	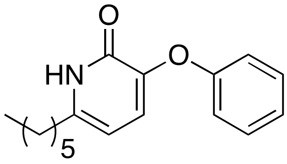	729.09 ± 82.39	196.50 ± 22.21	n.d. [d]
PT01 [e]	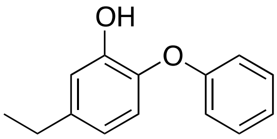	120.8 ± 10.1	0.09 ± 0.01	2.33

PT51 [e]	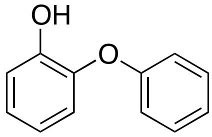	24515.0 ± 1359.8	18.86 ± 1.05	687.40
PT53 [e]	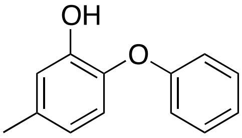	493.7 ± 40.2	0.38 ± 0.03	19.98

a. Curve fitting errors are reported for each value in the table
b. $[S]/K_S = 2$
c. Value reported against *S. aureus* RN4220
d. n.d. = not determined
e. Binds to the E-NADP$^+$ binary complex; K_i and K_i^{app} values obtained from (188).

Table 4-2. Thermodynamic parameters for inhibitors of ecFabI [a]

Name	Structure	K_i^{app} (nM) [b]	K_i (nM)	MIC (μM) [c]
CG400549	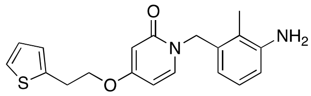	99.38 ± 2.26	81.85 ± 1.86	> 375
PT173	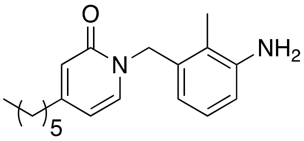	246.04 ± 10.13	202.63 ± 8.34	> 425
PT171	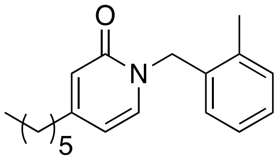	116.23 ± 4.58	95.72 ± 3.77	n.d. [d]
PT166	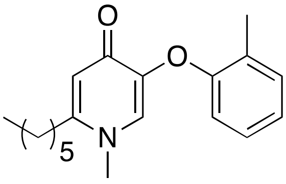	8.51 ± 0.17	7.01 ± 0.14	6.68
PT01 [e]	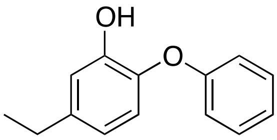	33.58	0.22	0.58
PT04 [e]	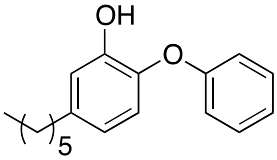	32.24	0.20	14.79

PT52 [e]	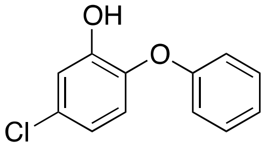	26.88	0.12	0.14
PT55 [e]	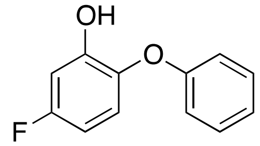	92.59	1.10	1.22

a. Curve fitting errors are reported for each value in the table
b. $[S]/K_S = 0.19$
c. Value reported against *E. coli* MG1655 ΔacrAB
d. n.d. = not determined
e. Binds to the E-NAD$^+$ binary complex. K_i and K_i^{app} values were determined via single point progress curve analysis, as described in (188). Kinetic parameters for each step in the mechanistic model depicted in Figure 4-2B are listed in Table S 4-3.

As expected, the apparent inhibition constant (K_i^{app}) of CG400549 against saFabI was very potent (K_i^{app} = 4.7 nM, Table 4-1) - more so than any of the diphenyl ether compounds previously tested (188). In the case of *E. coli* FabI (ecFabI), the apparent inhibition was weaker relative to saFabI (K_i^{app} = 99.4 nM). However, diphenyl ethers with similar K_i^{app} values still exhibit potent inhibition of *E. coli* cell growth (Table 4-2). This provided the first hint that pyridones may act via a different mode of action.

In contrast to the diphenyl ethers, 2-pyridones bind to the E-NADPH complex and exhibit fast-off kinetics – Very recently, we found that diphenyl ethers bind exclusively to the E-NADP$^+$ enzyme-product complex generated via catalysis (188). Despite the obvious structural similarity between pyridone and diphenyl ether inhibitors (Figure 4-1), thermal shift assays revealed preferable binding of pyridones to the E-NADPH complex (Figure 4-2A, Table 4-1). Thus, these inhibitors are uncompetitive with respect to NADPH but competitive with respect to the acyl substrate (Figure 4-2B). Our kinetic studies confirmed this pattern of saFabI inhibition, showing enhanced inhibition with increasing concentrations of NADPH and decreasing concentrations of the substrate *trans*-2-octenoyl-CoA used in the assay (data not shown). Moreover, we were able to co-crystallize pyridones with saFabI using the reduced form of the cofactor. Accordingly, the saFabI target can be productively inhibited at two different stages of the catalytic cycle, as exemplified by pyridones and diphenyl ethers (Figure 4-2B). This finding is of particular importance for the development of improved FabI inhibitors since most known scaffolds bind adjacent to the nicotinamide ring of the cofactor (67). The absence or presence of a buried positive charge in the E-NADPH vs. E-NADP$^+$ binary complexes likely will have a critical influence on the affinity of potential inhibitors (152). Since NADPH binds with higher affinity to the enzyme compared to NADP$^+$, the E-NADPH binary complex exists at a higher population (78,188). Thus, despite weaker thermodynamic affinity, the apparent inhibition of PT166 and CG400549 was much more potent than observed for the diphenyl ethers (Table 4-1) and required classical tight binding analysis (Figure 4-3D) (188).

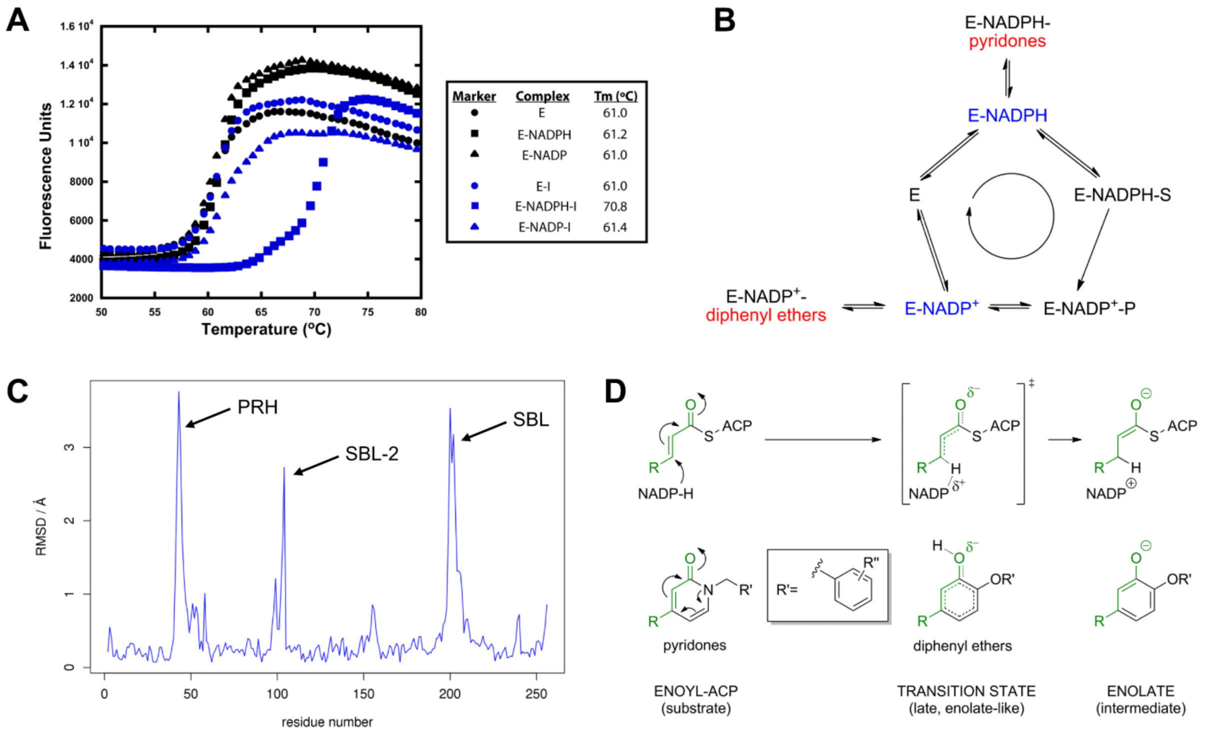

Figure 4-2. Mechanisms of saFabI inhibition. (A) Thermal shift analyses of saFabI bound to NADPH, NADP$^+$ and/or inhibitor (CG400549). The measurement variability is approximately ±0.2 °C. **(B)** Distinct mechanisms of saFabI inhibition. In contrast to diphenyl ethers (highlighted in red), which bind to the enzyme-product complex generated via catalysis (E-NADP$^+$, depicted in blue) (188), pyridone compounds (shown in red) preferentially inhibit saFabI at the enzyme-substrate complex state (E-NADPH, depicted in blue). **(C)** Structural differences between diphenyl ether and pyridone ternary complexes. Per-residue rmsd values between our triclosan- (PDB-code: 4ALI, subunit H) and CG400549-bound (CG400549-I, subunit C) structures were calculated using Theseus (14) and are plotted against the residue number. The inhibitor-bound structures of these two scaffolds differ considerably in three regions of the protein (PRH = phosphate recognition helix α2, SBL-2 = substrate binding loop 2, SBL = substrate binding loop). **(D)** Pyridone and diphenyl ether inhibitors resemble different species along the enzymatic reaction coordinate. In contrast to the enolate-like diphenyl ethers which are transition state analogs (188), pyridones are more substrate-like. The corresponding moieties of inhibitors and species along the reaction coordinate are highlighted in green.

Pyridone and diphenyl ether saFabI inhibitors also differ with respect to their apparent association and dissociation kinetics. Diphenyl ethers exhibit slow-binding kinetics and bind with long residence times to their target (Figure 4-3B and Figure 4-3C) (19,188). In contrast, progress curves of saFabI in the presence of pyridones are linear, displaying apparent rapid-onset kinetics (Figure 4-3A). This is likely attributed to the higher population of E-NADPH compared to E-NADP$^+$. In fact, an estimate of the actual association rate constant yields a value in the same range as for the diphenyl ethers (188). Moreover, the rapid appearance of activity following jump dilution is highly indicative of fast-off kinetics (Figure 4-3C), which may simply reflect the weaker thermodynamic affinity of pyridones compared to diphenyl ethers.

The mode of action has significant implications for cell growth inhibition. In open systems, substrate accumulation may eventually diminish the effect of competitive inhibitors (229). It is, therefore, important to consider the relationship between substrate concentration and K_i^{app} (Figure 4-4B). In Figure 4-4A, we see a strong linear correlation for the double logarithmic plot of K_i vs. MIC for both 2-pyridones and diphenyl ethers, consistent with on-target effects. However, higher overall ternary complex affinity ($K_i \cdot K_{d,NADP(H)}$) is needed for 2-pyridones to obtain a similar cellular potency as diphenyl ethers. This observation can be readily explained by substrate accumulation. The MIC is a thermodynamic parameter that is essentially equivalent to a physiological apparent inhibition constant (K_i^{app}). In the substrate concentration range of 40 to 80 times K_S the relative K_i^{app} values are very predictive of the pattern of MIC values for both 2-pyridones and diphenyl ethers (Figure 4-4C). This may, thus, estimate the levels of substrate accumulation in the cell. Additionally, we can now translate K_i to K_i^{app} values that can be readily compared despite different modes of action.

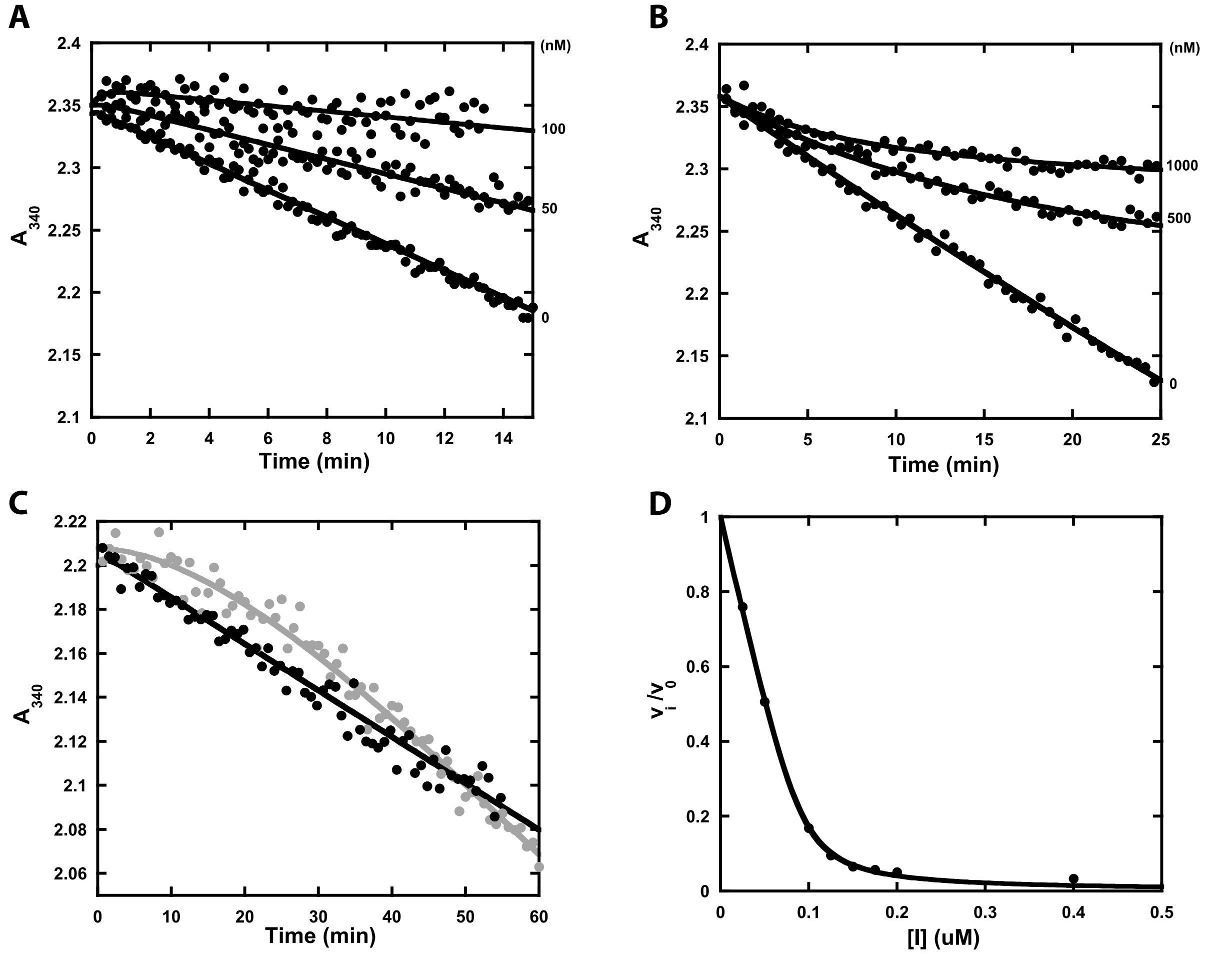

Figure 4-3. Progress curve kinetics. (A) Representative set of forward progress curves with pyridone-based inhibitors of saFabI. The plot depicts rapid-onset inhibition at different PT173 concentrations. **(B)** As a reference, this plot illustrates the slow-onset inhibition of saFabI by the diphenyl ether PT04 (188). Note the clear observation of curvature that is absent in panel A. **(C)** Jump dilution curve for CG400549 (black) following pre-incubation with NADPH and saFabI. The jump dilution curve for the slow-off diphenyl ether inhibitor PT52 (gray) following pre-incubation with $NADP^+$ and saFabI is shown as reference (full recovery of activity; t_R=30 min) (188). The lack of curvature for CG400549 is consistent with rapid-off kinetics. **(D)** Representative plot of fractional velocity (v/v_0) as a function of inhibitor concentration for a potent pyridone (CG400549, in this example). The shape is characteristic of tight-binding inhibition. The best-fit curve to the Morrison quadratic equation (Eq. 3) yields K_i^{app} = 4.73 ± 0.50 nM and $[E]_T$ = 92.73 ± 2.52 nM (R^2 = 0.99).

The utility of a scaffold for lead optimization is related, in part, to its intrinsic potency. We define this as the potency of a relatively unmodified scaffold – i.e. the starting point that determines how much affinity optimization is needed. For instance, PT170 and PT53 represent relatively unmodified 2-pyridone and diphenyl ether scaffolds, respectively. The competitive mode of inhibition likely contributes to the weakening of the intrinsic potency of the 2-pyridone relative to the diphenyl ether scaffold by more than 20-fold (Figure 4-4B). Thus, further optimization of 2-pyridones is needed to achieve potent cellular activity. As we demonstrate below, such optimization is much more easily attained in the case of saFabI compared to other FabI homologues, providing rationale for the narrow spectrum activity of CG400549 and related 2-pyridone compounds.

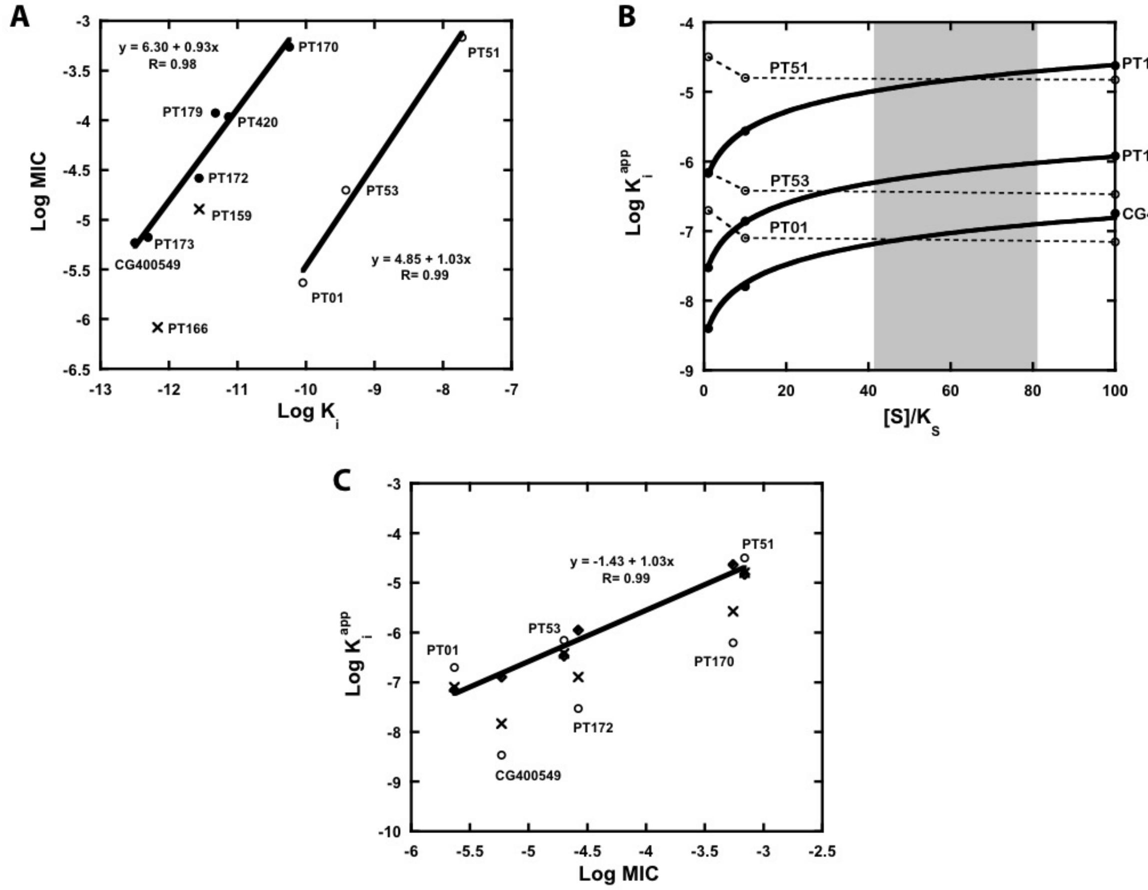

Figure 4-4. Rationalizing the *in vitro* cellular potency of competitive and uncompetitive FabI inhibitors. (A) A double logarithmic plot depicts a strong linear correlation between K_i of the overall ternary complex ($K_i \cdot K_{d,NADP(H)}$) and MIC for the 2-pyridone series (●) and diphenyl ethers (○). Points corresponding to 4-pyridones (X) are superimposed. Note that in this plot, the MIC for PT170 was assumed to be 550 µM, which is a lower limit estimate. **(B)** The relationship between acyl substrate concentration as a multiple of K_S ($[S]/K_S$) and the apparent affinity (K_i^{app}) of pyridones (PT170, PT172, CG400549) and diphenyl ethers (PT51, PT53, PT01) is illustrated. The plots are simulated based on K_i values against saFabI (Table 4-1 and (188)), the mechanism of inhibition shown in Figure 4-2B and the kinetic model described in (188). The range of substrate concentration that best correlates relative K_i^{app} to relative MIC for both classes of compounds is shaded gray. **(C)** This double logarithmic plot of K_i^{app} and MIC illustrates how 2-pyridones and diphenyl ethers can lie on the same linear correlation at the correct substrate concentration [S]. Data points correspond to inhibitor K_i^{app} values at $[S]/K_S$ of 1 (○), 10 (X) and 100 (◆). The linear correlation for points corresponding to $[S]/K_S = 100$ is depicted.

The clinical trial compound CG400549 interacts tightly with saFabI – CG400549 binds with high affinity (K_i = 1.27 nM) to saFabI (Table 4-1). To provide insight into the underlying molecular interactions, we solved two different saFabI-NADPH-CG400549 ternary complex structures (CG400549-I and CG400549-II, respectively; unless stated otherwise, the CG400549-I structure was used for the following analyses; see also Table S 4-1). Based on the associated $2F_o$-F_c omit maps, we unambiguously reveal the binding mode of CG400549 (Figure 4-5B), which enables the formation of two central hydrogen bonds of the pyridone carbonyl oxygen with the Tyr157 hydroxyl and the NADPH nicotinamide ribose 2'-OH at distances of 2.74 ± 0.07 and 2.69 ± 0.10 Å, respectively (Figure 4-5A). Although reminiscent of interactions found for other inhibitor scaffolds (Figure 4-1), these hydrogen bonds are 0.15 Å longer for pyridones in comparison to diphenyl ethers. This supports our suggestion that diphenyl ethers bind to saFabI in their deprotonated form (188) leading to shorter charge-assisted hydrogen bonds. Additional long-range hydrogen bonds are formed between the 3'-amino group of CG400549 (Figure 4-1) and the main chain oxygen and nitrogen of Ala97 at distances of 3.56 ± 0.06 and 3.32 ± 0.09 Å, respectively (Figure 4-5A). Moreover, a water molecule is frequently bound between this B-ring NH_2 group and Ala95 at 3.36 ± 0.18 Å (Figure 4-5A). Interestingly, Ala97 engages in direct interactions for several potent saFabI inhibitors (Figure 4-1). Triclosan and AFN-1252 form halogen and hydrogen bonds with Ala97, respectively, and the amide group of MUT056399 was similarly suggested to interact with this residue (Figure 4-1) (19,101,102).

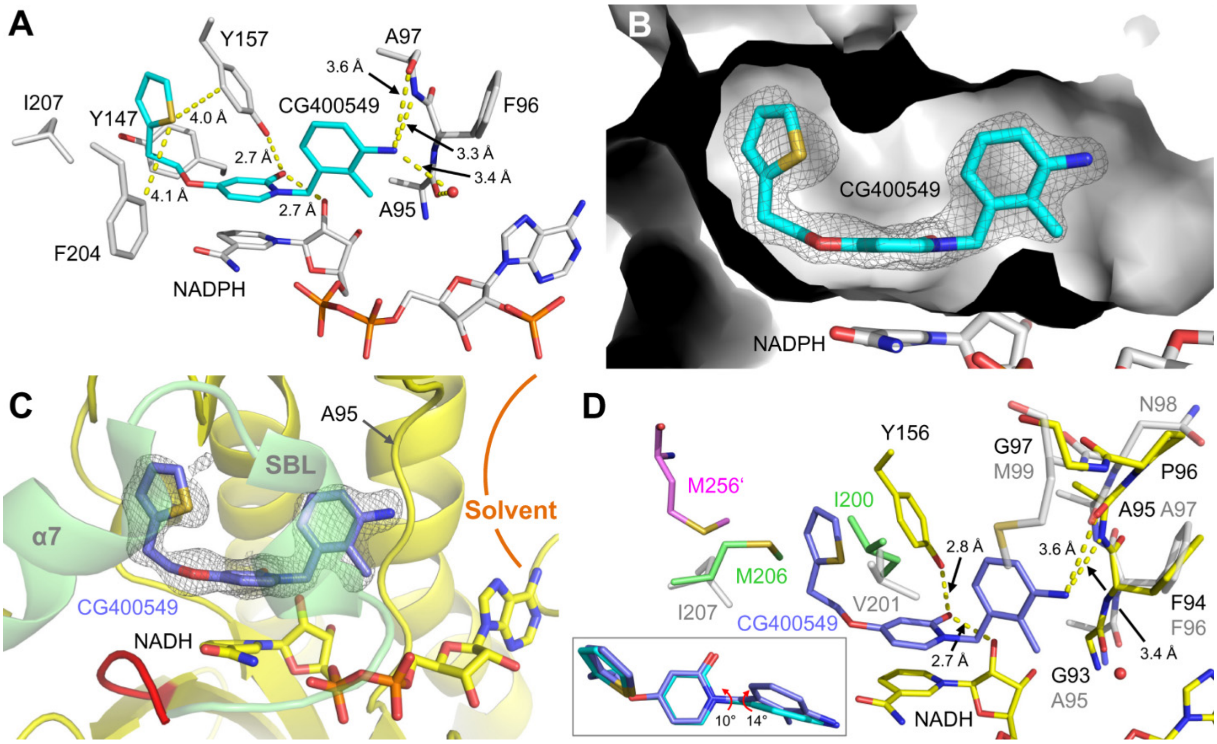

Figure 4-5. Molecular interactions of the *S. aureus* and *E. coli* FabI homologues with the pyridone inhibitor CG400549. (A) Binding mode of CG400549 (cyan) in complex with saFabI and NADPH. Interactions between inhibitor, cofactor and protein are highlighted by yellow dashed lines. Selected residues of the saFabI binding pocket are shown as gray sticks (CG400549-I structure, subunit G). **(B)** $2F_o$-F_c omit map for CG400549 bound to saFabI. According to the omit map (shown as mesh at 1 σ), CG400549 (cyan) unambiguously binds to the hydrophobic saFabI active site pocket. An intersection of the CG400549-I structure (subunit G, depicted in gray surface representation) provides insight into this cavity. **(C)** CG400549 (lilac) in its complex with ecFabI and NADH. The $2F_o$-F_c omit map is depicted for CG400549 (shown as mesh at 1 σ) and clearly reveals the presence of this molecule although the substrate binding loop (SBL) region was found to be disordered in this structure (starting after residue 192 highlighted in red; subunit A of the ecFabI-NADH-CG400549 structure is shown in yellow cartoon representation). As a reference, the SBL of a superimposed ecFabI-NAD^+-triclosan structure is shown in green (PDB-code: 1QSG) (111). Together with the SBL, the loop comprising Ala95 defines a portal towards the solvent. **(D)** Comparison between the CG400549-bound *S. aureus* (inhibitor in cyan - for clarity only present in insert, amino acids in gray) and ecFabI (inhibitor in lilac, amino acids in yellow) ternary complexes. The insert contains a comparison between the CG400549 binding modes, which differ in their B-ring conformations via changes in the torsion angles between the two aromatic rings (indicated by red arrows). Met256' of the subunit on the opposite side of the ecFabI homo-tetramer is depicted in pink. Residues Ile200 and Met206 of the 1QSG structure are shown as reference in green.

The unique 5-substituent of CG400549 binds to a hydrophobic pocket with the thiophene moiety trapped between the three aromatic amino acids Tyr147, Tyr157 and Phe204 (Figure 4-5A and Figure 4-5B). The side-on π-stacking interaction between Tyr157 of the catalytic triad and the thiophene ring may contribute to the high affinity of CG400549 towards saFabI (Figure 4-5, Table 4-1). In particular, the thiophene sulfur interacts with the edge of Tyr157 (C_δ) at a distance of 3.97 ± 0.11 Å (152). A similar interaction is found between this sulfur atom and Phe204 (C_δ) at 4.15 ± 0.16 Å (Figure 4-5A). Remarkably, amongst thirteen CG400549 resistant *S. aureus* strains ten were characterized by a single F204L mutation, whereas the residual three had no mutations in the *fabi* gene (4,100). In contrast, multiple resistance mutations are known for diphenyl ethers (28,78,92,108,230). Accordingly, the Phe204 - thiophene interaction seems to be critical for the activity of CG400549.

In addition to the CG400549 structures, we solved a saFabI structure in complex with NADPH and PT173, which contains a 5-hexyl group that mimics the natural enoyl-ACP substrate (Figure 4-1) (188). Although the resolution was much lower (Table S 4-1), there was clear density for cofactor and inhibitor (Figure 4-6B). The binding mode of PT173 in the saFabI active site pocket is similar to CG400549, and we observed the same central hydrogen bonding network between the inhibitor, cofactor and Tyr157 (Figure 4-6A).

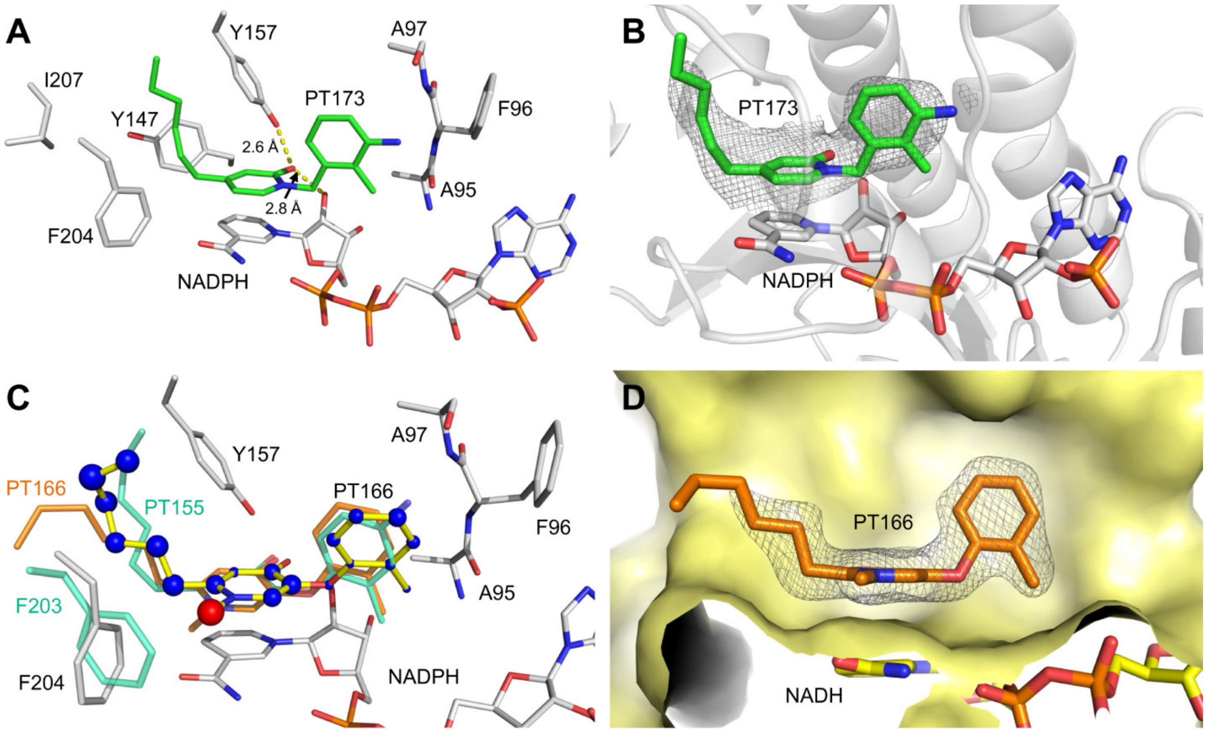

Figure 4-6. Binding modes of different pyridone inhibitors within the FabI active site pocket. (A) Experimental binding geometry of PT173 (green). Selected residues of the saFabI-NADPH-PT173 structure (gray, subunit F) and the central hydrogen bonding network (yellow dashed lines) are depicted. **(B)** NCS-averaged $2F_o$-F_c omit map for PT173. The omit map is shown at 1 σ and reveals the presence of PT173 (shown in green). Subunit F of the PT173 structure is depicted in gray cartoon representation. **(C)** Putative binding mode of PT166 (yellow sticks) within the saFabI pocket (CG400549-I structure, subunit A). PT166 was docked into the saFabI binding cavity using the validated approach described in the Experimental Procedures section. The radii of the blue (red) spheres indicate the values of the favorable (unfavorable) score for each individual atom, as determined with DrugScore^X. Our bpFabI-NAD$^+$-PT155 structure (cyan sticks) confirms this binding mode and suggests a rotation of Phe204 to avoid the steric interference with the *N*-methyl group of 4-pyridone inhibitors (indicated by the red sphere). Moreover, the putative binding mode is in accordance with our PT166-bound ecFabI structure (orange sticks, subunit A). The docking results for the residual pyridone inhibitors of Table 4-1 are summarized in Figure S 4-1. **(D)** $2F_o$-F_c omit map for PT166 (orange sticks) bound to ecFabI (shown as mesh at 1 σ). An intersection of the ecFabI-NADH-PT166 structure (subunit A, depicted in yellow surface representation) is shown. The SBL, which usually covers the binding site (in front of the cavity), was found to be disordered.

Despite the prospects of CG400549, little is known about pyridone FabI inhibitors and their structure-activity relationships (SAR) (123,231,232). Thus, we synthesized a series of pyridone compounds and investigated their ability to inhibit saFabI (Table 4-1). To rationalize the SAR results, we generated putative binding modes for all investigated inhibitors using a validated docking procedure, which could reproduce the CG400549 and PT173 binding geometries with low rms deviations (0.71 Å and 0.83 Å, respectively) (Figure S 4-1). Due to the lipophilic environment, bulky and hydrophobic substituents are preferred at the 5-

position. Hence, PT170 is the least potent compound of our pyridone series. Replacing the 5-methyl group by a 5-hexyl group (PT172) leads to a 21-fold affinity enhancement, which is underlined by the favorable scores for the additional carbon atoms (Figure S 4-1). Similar to the 2'-chloro substituent of PT172, the 2'-methyl group of PT171, which is also present in CG400549, increases affinity by a factor of 2 compared to the unsubstituted analog PT179. In comparison to the 2'-Cl and 2'-Me groups, a 2'-CN substituent leads to decreased potency. Interestingly, the SAR at this position is different from diphenyl ethers for which 2'-cyano is the best substituent (188). Pyridone 2'-substituents are predicted to bind in a similar orientation (Figure S 4-1) as observed for diphenyl ethers. The introduction of a 3'-amino group as present in CG400549 and PT173 further enhances the affinity of PT171 by a factor of 6, which highlights the energetically favorable character of the observed long-range hydrogen bonds between those inhibitors and Ala97 (Figure 4-5A). Interestingly, PT173 was also found to be a competitive inhibitor of *Yersinia pestis* FabV (K_i = 1.5 µM), which raises the possibility of developing compounds that inhibit both FabI and the FabV isoenzyme (118). Replacement of the PT173 5-hexyl group with the thiophene containing 5-substituent of CG400549 further improves the affinity of the clinical trial compound 1.5-fold and might be explained by the additional aromatic interactions we observed.

SaFabI conformational states differ between pyridone and diphenyl ether ternary complex structures – In accordance with the distinct kinetic behavior of pyridone and diphenyl ether inhibitors, we observed considerable structural differences between the corresponding ternary complex structures. A per-residue rmsd plot reveals variations in mainly three regions of the protein (Figure 4-2C) - the two substrate binding loops (SBL and SBL-2; residues 194-204 and 94-108) and the phosphate recognition helix α2 (PRH; residues 40-54), which confers the unique NADPH specificity to saFabI (19). The full closure of the substrate binding loop has been proposed to constitute the rate-limiting step of slow-binding FabI inhibition by diphenyl ethers (67). Indeed, we found more 'open' SBL states in the saFabI-NADPH-CG400549 structures compared to the triclosan-bound structure (Figure 4-7A). Most likely the observation of the 'open' state can be attributed to steric interference between the thiophene moiety of CG400549 and the side chain of Val201 in the SBL if it would adopt the completely 'closed' state (Figure 4-7A, gray). Hence, Val201 is shifted by 2.9 ± 0.1 Å into the more 'open' CG400549-bound structure (Figure 4-7A, cyan). Interestingly, some subunits of the CG400549-I structure reveal a second, even more 'open' SBL state - the rmsd increases from 1.6 to 2.0 Å compared to the triclosan-bound reference structure - with an additional shift in helix α7, which we previously identified to be very flexible prior to ligand binding (Figure 4-7A, yellow) (19). Both SBL conformations in the saFabI-NADPH-CG400549 complex seem to be energetically equally favorable due to the observation of subunits with both states in equilibrium. The more 'closed' state is stabilized by a sulfate ion, which is bound to backbone amides of the SBL; this state differs from the completely 'closed' triclosan-bound structure by a Lys199-Gly200 backbone flip (Figure 4-7A, right insert; ψ_{K199} and ϕ_{G200} change by 156° and 159°, respectively), which is observed for seven of the eight CG400549-I monomers and might be responsible for the opening movement. An additional shift of residues 202-208 with extensive variations for Gly202 and Gly203 leads to the most 'open' form (Figure 4-7A, left insert), which is related to the conformation observed for the AFN-1252 structure (101).

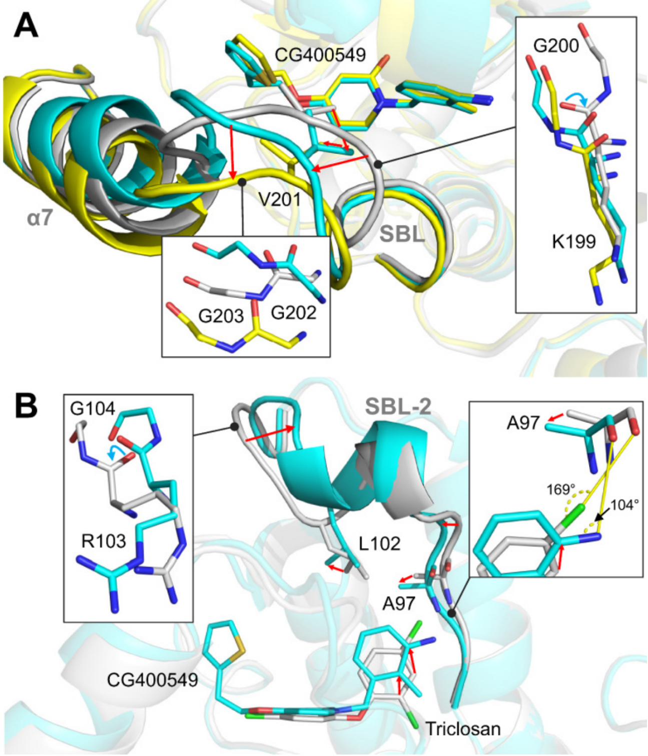

Figure 4-7. Structural variations between pyridone and diphenyl ether ternary complex structures. (A) Conformational states of the substrate binding loop. The different subunits of our CG400549-I structures reveal two distinct states of the substrate binding loop (SBL) and the attached helix α7 (shown in cyan and yellow for subunits A and C, respectively; residual parts of the protein are displayed in transparent colors for clarity). Compared to these conformations, the substrate binding loop is more closed in our triclosan-bound structure (shown in gray; PDB-code: 4ALI, subunit H). Detailed views of the three different conformations are displayed in the inserts. Red arrows indicate the conformational changes from the 'closed' to the 'open' substrate binding loop states. Blue arrows highlight backbone flips. **(B)** Conformational states of the substrate binding loop 2 (SBL-2). Selected residues, the inhibitors and the substrate binding loop 2 are shown for the CG400549-I (cyan; subunit A) and triclosan-bound structures (gray; PDB-code: 4ALI, subunit H).

Similar to the SBL, a second loop that also contributes to the substrate binding pocket (SBL-2) was almost exclusively found to be in an 'open' conformation in the saFabI-NADPH-CG400549 structures (Figure 4-7B, cyan). In contrast, we observed alternative 'closed' and 'open' SBL-2 conformations for the diphenyl ether-bound structures (19). An Arg103-Gly104 backbone flip (Figure 4-7B, left insert; ψ_{R103} and ϕ_{G104} change by 180° and 144°, respectively) clearly differentiates those two states. This flip is induced by (or induces) a 1.5 ± 0.5 Å shift of Leu102 out of the binding pocket, which in turn might be caused by (or causes) a considerable movement of the CG400549 B-ring towards this residue (Figure 4-7B). The resulting differences between the pyridone and diphenyl ether binding poses (Figure 4-7B) rationalize the varying SAR-profiles at the 2'-position for both scaffolds and the success of the 3'-amino substituent in the case of pyridones. In particular, the 2' and 3'-carbon atoms are relocated by 1.3 ± 0.1 Å and 1.6 ± 0.1 Å, respectively, which places the CG400549 3'-carbon at the position of the triclosan 4'-carbon. Consequently, 3'-pyridone and 4'-diphenyl ether substituents are ideally oriented to interact with the important anchor residue Ala97. For instance, the triclosan 4'-Cl is halogen bonded to the free electron pair of the Ala97 carbonyl oxygen via the favorable linear geometry (Figure 4-7B, right insert) (19,152). To enable an equally favorable angular geometry for a hydrogen bond between the CG400549 3'-NH_2 group and Ala97 along one amino hydrogen atom (152), the Ala97 carbonyl oxygen is shifted by 0.8 ± 0.1 Å towards the B-ring of the inhibitor, which in turn approaches Ala97 to reduce the interaction distance (Figure 4-7B, right insert). As exemplified by these considerations, exact knowledge of the different conformations that can be attained by a protein target is pivotal for the design of improved inhibitors.

Comparison of ecFabI and saFabI inhibition by 2-pyridones - To determine whether the narrow-spectrum behavior of CG400549 can be partly attributed to target-specific differences between species, we obtained and compared the structures and inhibition kinetics of CG400549 with respect to *E. coli* and *S. aureus* FabI. Indeed, CG400549 shows a 65-fold reduced affinity to *E. coli* FabI (ecFabI) in comparison to saFabI (Table 4-1 and Table 4-2). Nevertheless, the inhibitor clearly bound to the binary ecFabI-NADH complex with a similar binding geometry as observed for saFabI (Figure 4-5C and Figure 4-5D). However, in contrast to the related saFabI ternary complex, the substrate binding loop and the attached helix α7 were found to be disordered in this ecFabI structure (Figure 4-5C). Based on a comparison of these structures, we propose that Val201 and Ile207 contribute to the specificity of CG400549 towards saFabI. The more bulky Ile200 and Met206 ecFabI residues (corresponding to saFabI positions 201 and 207, respectively) restrict the available space for large 5-substituents as present in CG400549 (Figure 4-5D). Accordingly, the elongation of the 5-substituent in 5-ethyl-2-phenoxyphenol (PT01) to 5-hexyl-2-phenoxyphenol (PT04) does not enhance the affinity towards ecFabI (Table 4-2), whereas affinity increases approx. 10-fold for saFabI (188). We have recently shown that these inhibitors are transition-state analogues with the 5-substituent alkyl chain extending towards the fatty acyl binding channel (188). Consistently, whereas the k_{cat} increases for longer enoyl-substrates in the case of saFabI (188), it is similar among the different substrate chain lengths for *E. coli* and *F. tularensis* FabI, which also carries the V201I and I207M substitutions and is inhibited by PT01 and PT04 with similar potency (19,46,109,175). Thus, the enlarged binding pocket of saFabI might partially explain the specific action of the comparatively bulky CG400549 and AFN-1252 clinical candidates (Figure 4-1). Interestingly, the C-terminus of the ecFabI monomer located on the opposite side of the homo-tetrameric protein (in particular, Met256') seals this acyl-binding cavity and likely restricts the side chain mobility of Met206 (Figure 4-5D). The resulting steric interference between the substrate binding loop residues Met206 and Ile200 and the thiophene moiety of CG400549 presumably results in the experimentally observed enhanced mobility of this loop. In contrast, the C-terminus of saFabI is shorter and lacks a residue corresponding to Met256', thus enabling Ile207 to move away from bulky 5-substituents. Consequently, important contacts between this inhibitor and the substrate binding loop (e.g. with Phe204; see also Figure 4-5A) are more easily attained, partially explaining the selectivity of CG400549 towards the saFabI homologue.

Moreover, hydrogen bonding interactions with Ala97 seem to be particularly favorable in the case of saFabI and are exploited by the three clinical trial compounds, as indicated by crystallographic and computational studies (Figure 4-1) (101,102). In the case of CG400549, the more rigid Pro96 of ecFabI (Asn98 in the case of saFabI) slightly changes the orientation of the Ala95 carbonyl (Ala97 for saFabI) (Figure 4-5D). This might explain the observed rotation in the B-ring of CG400549, which seems to be required for the maintenance of the hydrogen bond to this residue. Interestingly, this interaction is solvent-exposed (Figure 4-5C) and less buried for ecFabI due to the presence of Gly97, which corresponds to Met99 in saFabI (Figure 4-5D). This rationalizes why the 3'-amino substituent decreases affinity in the case of ecFabI (Table 4-2). Furthermore, treatment of *S. aureus* with AFN-1252, which is also hydrogen bonded to Ala97 (Figure 4-1), selects for a M99T mutation (101). Thus, the buried hydrogen bonding interaction with Ala97 likely plays an important role in the selective affinity of CG400549 and AFN-1252 towards saFabI.

The 4-pyridone PT166 is a potent FabI inhibitor with broad-spectrum activity and in vivo efficacy – In contrast to saFabI, the possibilities to optimize binding affinity of 2-pyridones for ecFabI and related homologues may be too limited due to the more constricted space in the binding crevice combined with the relatively low intrinsic potency of 2-pyridones compared to the diphenyl ether scaffold. Instead, to attain broad-spectrum activity, we can design a modified scaffold that possesses a higher intrinsic potency for all FabI homologues. One possibility is to replace the methylene bridge with an ether linkage, thereby changing the conformational preference prior to binding. The biologically active Ar-X-Ar conformation (Figure 4-5 and Figure 4-6) is more readily available for the bisaryl ether system thus leading to an entropic advantage upon binding (9). This was implemented in the design of C-substituted 2-pyridone (2-pyridones such as CG400549 are substituted at the N-atom) and 4-pyridone analogues. As expected, both prefer to bind in a ternary complex with NADPH (similar thermal shift pattern to that depicted in Figure 4-2A for CG400549), thus preserving the 2-pyridone mode of action. Compared to the analogous N-substituted 2-pyridone PT179, the C-substituted 2-pyridone PT191 binds 10-fold less tightly to saFabI (Table 4-1). Although its enol form has a similar putative binding geometry as PT179 (Figure S 4-1) and more closely resembles the potent diphenyl ether PT04 (188,231), the increased desolvation costs for this more polar compound are likely responsible for the decreased affinity. In contrast, the 4-pyridones PT166 and PT159 have 3 to 4-fold enhanced affinities for saFabI with respect to the analogous 2-pyridones PT171 and PT420 (Table 4-1), consistent with a higher intrinsic potency of this scaffold. PT166 also potently inhibited ecFabI (Table 4-2), suggesting that the higher intrinsic potency may, indeed, translate to broad-spectrum activity. Thus, substituting the methylene bridge of the initially reported 4-pyridones (123) with an ether linkage (233) seems to be a successful strategy to further improve FabI pyridone inhibitors.

Based on our docking studies, we suggest a binding mode for the 4-pyridones similar to those observed for 2-pyridones (Figure 4-6C). However, despite the enhanced affinity of PT166 with respect to PT171, the additional 4-methyl group is characterized by an unfavorable score. Thus, we hypothesized that Phe204 will change its conformational state upon 4-pyridone binding to avoid the steric interference with the *N*-methyl group. Since 4-pyridones did not co-crystallize with saFabI, we initially used PT155, which carries an additional 4'-NH_2 group compared to PT166, and determined a ternary complex structure with *Burkholderia pseudomallei* FabI (bpFabI). Indeed, this structure confirmed the predicted 4-pyridone binding mode and Phe203 (corresponding to the saFabI residue Phe204) was found to adopt a different conformation presenting one of its π-faces to the *N*-methyl group of PT155 (Figure 4-6C). Moreover, we were able to solve an ecFabI-NADH-PT166 structure (Figure 4-6D), which further validated the proposed PT166 binding mode (Figure 4-6C). Similar to the ecFabI-NADH-CG400549 structure, the substrate binding loop was found to be disordered or in a very open conformation in these ecFabI and bpFabI structures, respectively (Figure 4-6D).

For the 4-pyridone analogues, *in vitro* MIC measurements against *S. aureus* RN4220 lie near the 2-pyridone linear correlation, consistent with its similar mode of action (Figure 4-4A). In addition, relative to CG400549, PT166 had a >50-fold lower MIC against an efflux pump deficient strain of *E. coli* MG1655, consistent with its more potent inhibition of ecFabI (Table 4-2). At an acyl substrate concentration of 40 to 80 times K_m, the predicted K_i^{app} ranges from 7.6 to 13.9 times higher for PT166 relative to PT01, and in agreement the MIC of PT166 is 11.5 times higher than that of PT01, suggesting that the estimated level of substrate accumulation in *E. coli* is similar to *S. aureus*. Remarkably, PT166 also exhibited antibacterial activity against a broad spectrum of pathogenic organisms, including *F. tularensis*, *M. tuberculosis* and *B. pseudomallei* (Table 4-3). This is a significant finding, as we were able to rationally design a more broad-spectrum pyridone scaffold.

Table 4-3. Spectrum of antibacterial activity for the 4-pyridone PT166

Organism	MIC (µM)
S. aureus RN4220	0.83
E. coli MG1655 ΔacrAB [a]	6.68
F. tularensis LVS	0.85
M. tuberculosis H37Rv	10.02
B. pseudomallei Bp400 [a]	6.68

a. Efflux pump knockout strains

Table 4-4. *In vivo* pharmacokinetic profile for PT166 and PT04

PK parameter	PT04	PT166
Dosage (mg/kg)	200	100
$AUC_{0\text{-}24}$ (µg hr/mL) [a]	11.8	53.0
$t_{1/2}$ (hr) [b]	4.5	2.7
T_{max} (hr) [c]	1.0	0.25
C_{max} (µg/mL) [d]	5.1	45.9

a. $AUC_{0\text{-}24}$ is the area under the plasma concentration-time curve over 24 hours.
b. $t_{1/2}$ is the time taken for plasma concentration to fall to 50% of its original value.
c. T_{max} is the time at which C_{max} occurs.
d. C_{max} is the maximum plasma concentration of drug.

Pyridones are a metabolically stable alternative to diphenyl ethers, which contain a hydroxyl group susceptible to glucuronidation and sulfonation (210). This pharmacokinetic (PK) advantage may be key to the success of the clinical candidates CG400549 and AFN-1252.

Importantly, PT166 maintained a superior PK profile compared to the diphenyl ether PT04 (Table 4-4). C_{max} and $AUC_{0\text{-}24h}$ of PT166 are 9-fold and 5-fold higher than that of PT04, respectively, despite the fact that the dose of PT04 was double that of PT166. We also tested the efficacy of PT166 in a neutropenic mouse model of MRSA infection. As a control, no bacteria were observed in the right thigh muscle of both treated and untreated mice, confirming the lack of significant bacteria migration. In the infected thigh, however, significant bacterial burden was observed in the different treatment groups. As expected, oxacillin, a clinical antibiotic similar to methicillin, exhibited no *in vivo* anti-bacterial efficacy (Figure 4-8). However, PT166 significantly decreased the bacterial burden in the infected thigh by 2.8 Log CFU/g tissue. In comparison, the potent diphenyl ether PT04 only decreased bacterial burden by 0.9 Log CFU/g tissue.

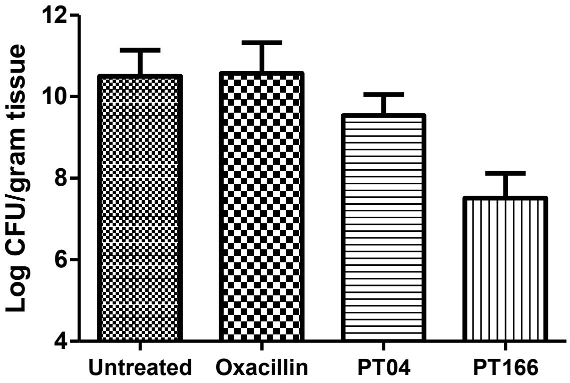

Figure 4-8. *In vivo* efficacy. The efficacy of selected compounds against MRSA strain BAA1762 in a neutropenic mouse thigh infection model is shown. Error bars represent the standard deviation for replicate data (n = 5 in each group).

4.7 Discussion

Pyridones constitute a very promising and relatively new class of FabI inhibitors (67). It has already advanced further along the clinical pipeline than any inhibitor based on the diphenyl ether scaffold. For instance, CG400549 has superior pharmacokinetic properties and proven clinical efficacy against *S. aureus* infection[8]. However, it also has lower activity against many other important pathogens. Understanding the molecular basis for such selectivity can guide the development of pyridone-based FabI inhibitors with greater broad-spectrum potential.

Despite the structural similarity of the pyridone and diphenyl ether scaffolds, we observed surprising differences with respect to their mode of inhibition, which have significant implications for the spectrum of activity. Pyridones bind predominantly to the E-NADPH complex, whereas diphenyl ethers exclusively interact with E-NADP$^+$ generated via catalysis (Figure 4-2A and Figure 4-2B) (188). We recently proposed that diphenyl ethers bind in a deprotonated state to their target (188). In such a scenario, the positively charged and thus electron-deficient oxidized nicotinamide ring of the cofactor forms a charge-assisted π-π stacking interaction with the electron-rich phenolate A-ring (Figure 4-1). The inability of the much less acidic pyridones to form this ionic interaction might explain their reduced affinity for E-NADP$^+$. In fact, pyridones may bind to the E-NADP$^+$ and E-NADPH complexes with similar affinity. Since the E-NADPH complex is energetically more stable and exists at a higher population than E-NADP$^+$ (188), E-NADPH-I is still the predominant and physiologically relevant ternary complex.

The diphenyl ether and pyridone-bound saFabI ternary complexes likely reflect different stages during the hydride transfer step of the enzymatic reaction (Figure 4-2D). We have recently shown that diphenyl ethers are analogs of a late, enolate-like transition state (188). In contrast, the pyridone structure more closely resembles the enoyl-ACP substrate (Figure 4-2D) and thus binds preferably in a ternary complex with the reduced cofactor, which is present prior to the hydride transfer. We envision an incremental closure of the SBL during substrate binding and hydride transfer in which the loop is fully 'closed' at the transition state to minimize its energy (Figure 4-9).

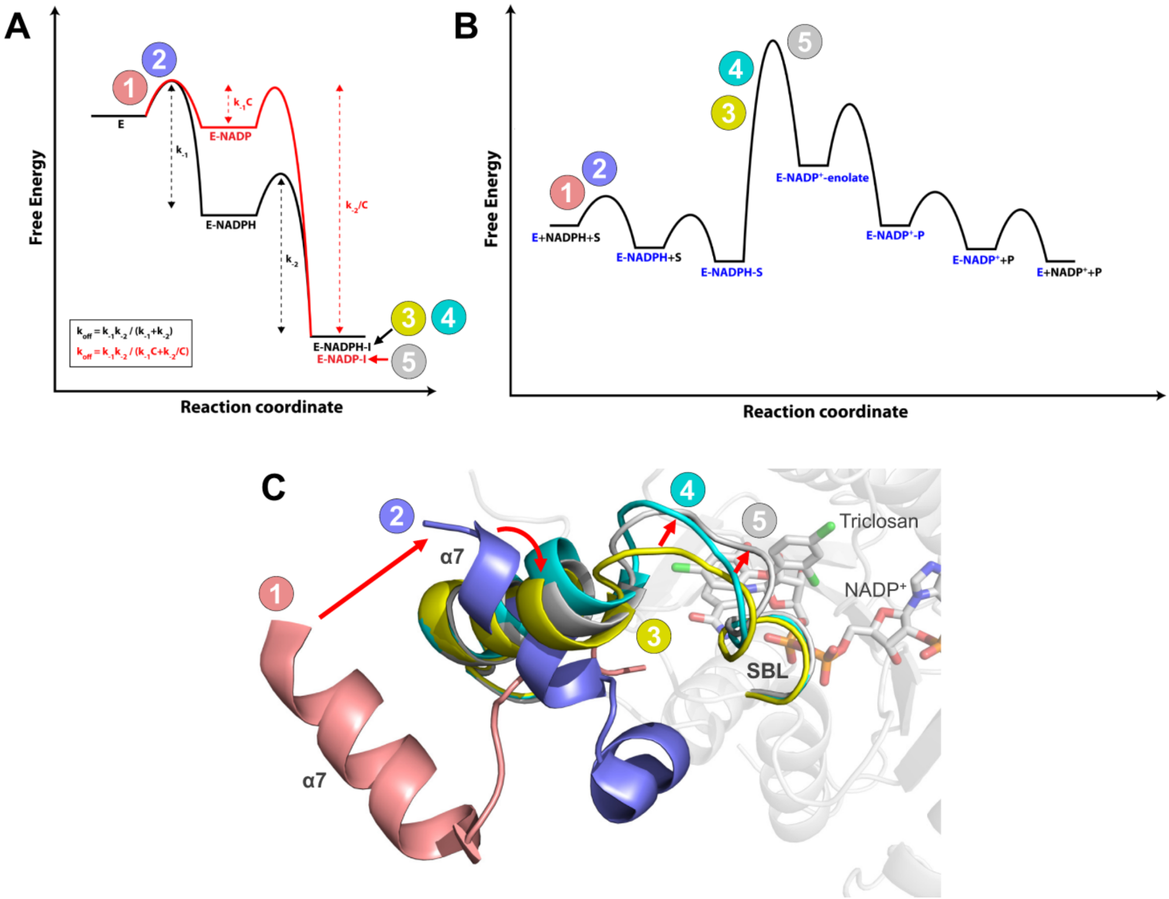

Figure 4-9. Conformational states sampled along the reaction coordinates of inhibitor binding and substrate turnover. (A) Approximate energy diagrams for saFabI in complex with NADPH and pyridone (black) or $NADP^+$ and diphenyl ether inhibitor (red). The overall affinities of both ternary complexes are assumed to be identical. By shifting stabilization from cofactor to inhibitor, the residence time of the overall complex is increased. This rationalizes the difference in off-rate kinetics between the diphenyl ethers and pyridones. Note that, technically, k_{off} for the pyridone complex (E-NADPH-I) is equal to k_{-2} since the E-NADPH complex is catalytically active. C is defined as a constant with a value greater than 1. The numbers 1 to 5 indicate the conformational states (colors according to panel C), which are likely sampled along the reaction coordinate of inhibitor binding (see also panel C). **(B)** Qualitative energy diagram for substrate turnover by saFabI. The numbers 1 to 5 indicate the conformational states (colors according to panel C), which are likely sampled along the reaction coordinate of the enzymatic reaction (see also panel C). **(C)** Conformational states sampled by the SBL and the attached helix α7 of saFabI. Red arrows indicate the conformational changes we propose to occur during the enzymatic reaction (see also panel B). Prior to the binding of cofactor and substrate or inhibitor, the SBL is disordered and helix α7 attains a very open conformation (state 1 colored in pink = PDB-entry 4ALM, subunit B; state 2 colored in lilac = PDB-entry 4ALM, subunit C; further details about the conformational changes upon ligand binding are provided in our previous report (19)). The more substrate-like pyridone inhibitors likely induce a conformational state between the ternary E-NADPH-S complex and the transition state of the hydride transfer (state 3 colored in yellow = CG400549-I structure, subunit C; state 4 colored in cyan = CG400549-I structure, subunit A; see also Figure 4-7A). In contrast, the transition state analog triclosan and several other diphenyl ethers (19,188) induce the likely fully closed state of the SBL (state 5 colored in gray = PDB-entry 4ALI, subunit H).

In this respect, the different conformations of the SBL presented in this study define important structural snapshots along the reaction coordinate of enzyme catalysis (Figure 4-7A). The observation of an 'opened' substrate binding site for pyridones confirms our hypothesis that these inhibitors are more substrate-like compared to the diphenyl ethers. In the light of the two alternatively ordered SBL conformations vs. the disordered loop in the apo enzyme (Figure 4-9C, states 1 and 2) (19,144), it could be argued that the pyridone ternary complexes represent a state between the substrate complex and the transition state for enolate formation (Figure 4-9B). The electron-donating effect of the pyridone nitrogen, which leads to a phenolate-like resonance structure, might thereby mimic the transfer of the negatively charged hydride ion (Figure 4-2D).

As the hydride transfer reaction proceeds, the increasing positive charge on the nicotinamide ring and the closure of the substrate binding loop shifts the balance of ternary complex stabilization more towards the fatty acyl relative to the cofactor component. Diphenyl ethers display affinities which are three orders of magnitude higher compared to analogous 2-pyridones, whereas NADP$^+$ binds approx. 1000-fold less tightly to saFabI with respect to NADPH (Figure 4-9A) (188). Accordingly, the cumulative affinities ($K_i \cdot K_{d,NADP(H)}$) of comparable E-NADP$^+$-diphenyl ether and E-NADPH-pyridone complexes are calculated to be very similar. For instance, there is only a two-fold difference in the cumulative affinity of the E-NADP$^+$-PT04 complex compared to the analogous E-NADPH-PT179 complex. Diphenyl ethers are stabilized to a greater extent partly because of the closure of the SBL that occurs farther along the reaction coordinate. At this stage, NADP$^+$ exists in the ternary complex, which also contributes to enhance the binding affinity of deprotonated diphenyl ethers. However, in comparison to E-NADPH, the steady-state concentration of E-NADP$^+$ is very small due to the fast dissociation of the oxidized cofactor generated via catalysis (188). Hence, the resulting apparent inhibitor association rate ($k_{on}\cdot[\text{E-NADP}^+]\cdot[\text{I}]$) of diphenyl ethers is slow explaining the observed slow-binding phenomenon, although the actual association rate constants k_{on} of pyridones and diphenyl ethers are very similar. Thus, in saFabI the ordering of the substrate binding loop is likely correlated rather than causative with respect to the observation of slow-onset kinetics with diphenyl ethers.

Among the three clinical trial saFabI inhibitors, CG400549 and AFN-1252 have been shown to be *Staphylococcus*-specific (4,31,100,101), whereas the diphenyl ether MUT056399 is also active against several Gram-negative pathogens (102). As shown in Figure 4-4, this is mainly attributed to different modes of inhibition. Substrate accumulation weakens the intrinsic potency of competitive inhibitors in contrast to uncompetitive inhibitors. Thus, relatively unmodified diphenyl ethers are already able to potently inhibit cell growth. In fact, the intrinsic potency of diphenyl ethers is greater in the case of ecFabI compared to saFabI because of the higher k_{cat} with first-round substrates (crotonyl-CoA) and smaller $k_{off,\ NAD}$ (Table S 4-3). This may contribute to the lower MIC values for the *E. coli* pump mutant relative to *S. aureus*. On the other hand, further optimization of binding affinity is necessary for pyridones to achieve cellular efficacy. This argument likely extends to the naphthyridinones, such as AFN-1252, which was recently crystallized in complex with saFabI and 3'-NADPH (Figure 4-1) (101). Our structural data rationalizes the pyridone SAR-profile and clearly reveals the ability of the CG400549 5-, 2'- and 3'-substituents to enhance its affinity towards saFabI (Figure 4-5 and Figure 4-6, Table 4-1). In particular, the CG400549 and PT173 3'-amino group is hydrogen bonded to Ala97, thus leading to a 6-fold increase in affinity (Figure 4-5A). In the case of ecFabI, this hydrogen bond is not protected from solvent-exposure due to a M99G substitution (Figure 4-5D), thereby reducing the affinity of such compounds and increasing the selectivity of CG400549 for saFabI (Table 4-2). Due to the amino acid residues Ile200 and Met206 and an elongated C-terminus including Met256', ecFabI also harbors a smaller binding pocket compared to saFabI (Figure 4-5D). The wider acyl-cavity of saFabI facilitates the accommodation of longer acyl-substrates or, analogously, diphenyl ether 5-substituents (19,109,175,188). Importantly, CG400549 and AFN-1252 contain large moieties at this position, which might further contribute to the *Staphylococcus*-specific spectrum of these two clinical trial inhibitors (Figure 4-1). In fact, bulky pyridone 5-substituents interfere with the ecFabI and bpFabI SBL, whereas it is in a relatively closed state for saFabI with bound AFN-1252 (101) and CG400549 (Figure 4-5C and Figure 4-7A). This important difference might be explained by the presence of an additional C-terminal extension occluding the binding sites of typical FabIs such as ecFabI and bpFabI. In contrast, saFabI contains a significantly shorter C-terminus compared to most other structurally characterized FabI proteins. The wider acyl-cavity, and thus, the enhanced affinity of CG400549 can be related to the ability of saFabI to efficiently utilize bulky branched-chain fatty acyl substrates (19). This is further supported by the relatively mild resistant mutations (F204L) that emerge upon selection with pyridones (4,100). Disrupting the 5-substituent interactions is likely sufficient to abrogate potency against *S. aureus* (see PT170, Table 4-1). On the other hand, more drastic mutations (F204S, A95V) are needed to disrupt the activity of the more intrinsically potent diphenyl ethers (28,78,92,108,230).

Based on the SAR profile of ecFabI, the ability to optimize binding affinity via substituents on the scaffold is very limited. A pyridone-based compound with broad-spectrum activity must necessarily have higher intrinsic potency than the 2-pyridones. To achieve this, we developed a 4-pyridone scaffold that retains the bridging oxygen of diphenyl ethers, thus providing an entropic advantage upon binding to FabI. As expected, the SAR and predicted binding mode is highly reminiscent of the 2-pyridone series, but 4-pyridones possess superior potency at the enzymatic and cellular levels (Table 4-1 and Table 4-2). Importantly, the higher intrinsic potency also translates into broad-spectrum activity for the promising lead compound PT166 (Table 4-3). As with CG400549 (234), replacement of the metabolically labile hydroxyl group with a carbonyl successfully improved the pharmacokinetic profile of PT166 compared to the diphenyl ether PT04 (Table 4-4). Additionally, this compound significantly reduced bacterial burden in a murine model of MRSA infection (Figure 4-8), validating its potential as a drug lead for future optimization and development. Further *in vivo* studies are needed to more precisely compare the pharmacokinetics and efficacy of the diverse FabI inhibitor scaffolds.

In summary, we have elucidated the structural and mechanistic basis for selective saFabI inhibition by pyridones, including the clinical candidate CG400549. Our study has yielded an insightful glimpse into conformational states along the coordinate of the saFabI enzymatic reaction, providing yet another reminder of the elegant connection between catalysis and inhibition. Importantly, we were able to rationally design the promising lead compound PT166, which merges the pharmacokinetic advantages of a pyridone with greater broad-spectrum potential. A similar approach can be applied in the development of much needed narrow- and broad-spectrum antibiotics against novel targets.

4.8 Acknowledgements

We thank the staff at the beamline 14.1 (BESSY II) operated by the Helmholtz-Zentrum Berlin and at ESRF beamline ID 23-1 for technical support. We also thank the staff at the Translational Experimental Therapeutics Lab at Stony Brook.

4.9 Footnotes

*This work was supported in part by the National Institutes of Health (grants GM102864, AI044639 and AI070383 to P.J.T. and the shared instrumentation grant NIH/NCRR 1 S10 RR023680-1) and the Deutsche Forschungsgemeinschaft (grants SFB630 to C.A.S. and C.K. and Forschungszentrum FZ82 to C.K.). J.S. was supported by a grant of the German Excellence Initiative to the Graduate School of Life Sciences, University of Wuerzburg. A.C. was supported by the Chemical Biology Training Program (NIH grant T32GM092714) and by the Medical Scientist Training Program (NIH grant T32GM008444).

[1] Rudolf Virchow Center for Experimental Biomedicine, Institute for Structural Biology, University of Wuerzburg, D-97080 Wuerzburg, Germany

[2] Institute of Pharmacy and Food Chemistry, University of Wuerzburg, Am Hubland, D-97074 Wuerzburg, Germany

[3] Institute for Chemical Biology & Drug Discovery, Department of Chemistry, Stony Brook University, Stony Brook, NY 11794-3400, USA

[4] School of Dental Medicine, Department of Oral Biology and Pathology, Stony Brook University, Stony Brook, NY 11794-3400, USA

[5] Rocky Mountain Regional Center of Excellence and Department of Microbiology, Immunology and Pathology, Colorado State University, Fort Collins, CO 80523-1682, USA

[6] These authors contributed equally to this work

[7] The abbreviations used are: MRSA, methicillin-resistant *Staphylococcus aureus*; VRSA, vancomycin-resistant *Staphylococcus aureus*; FAS-II, type II fatty acid biosynthesis; ACP, acyl carrier protein; FabI, *trans*-2-enoyl-ACP reductase; saFabI, *Staphylococcus aureus* FabI; NADPH, nicotinamide adenine dinucleotide phosphate, reduced form; ecFabI, *Escherichia coli* FabI; DMSO, dimethyl sulfoxide; NAD^+, nicotinamide adenine dinucleotide; $NADP^+$, nicotinamide adenine dinucleotide phosphate; NADH, nicotinamide adenine dinucleotide, reduced form; PK, pharmacokinetics; MIC, minimal inhibitory concentration; SAR, structure-activity relationship; CoA, coenzyme A; SBL, substrate binding loop; SBL-2, substrate binding loop 2; PRH, phosphate recognition helix; t_R, residence time.

[8] http://www.crystalgenomics.com

4.10 Supplementary Information

4.10.1 Supplemental Tables

Table S 4-1. Data Collection and Refinement Statistics (*S. aureus* FabI).

	PT173	**CG400549-I**	**CG400549-II**
Data collection			
Cell dimensions			
a, b, c (Å)	61.5, 109.2, 289.4	61.9, 108.5, 296.8	77.0, 113.1, 117.7
α, β, γ (°)	90, 90, 90	90, 90, 90	90, 90, 90
Space group	$P2_12_12_1$	$P2_12_12_1$	$P2_12_12_1$
Resolution[1] (Å)	60.3-3.10 (3.27-3.10)	47.6-1.95 (2.06-1.95)	45.6-2.20 (2.32-2.20)
Observed reflections	146,382 (20,325)	2,435,819 (313,695)	257,814 (36,976)
Unique reflections	36,439 (5,219)	146,661 (21,138)	52,885 (7,580)
Completeness (%)	100.0 (100.0)	100.0 (100.0)	100.0 (99.9)
Average redundancy	4.0 (3.9)	16.6 (14.8)	4.9 (4.9)
R_{merge}[2] (%)	10.4 (48.8)	16.1 (134.8)	13.0 (46.6)
R_{pim}[3] (%)	6.0 (28.2)	4.0 (36.1)	6.6 (23.5)
<I / σ(I)>	9.4 (2.7)	15.6 (2.4)	8.7 (3.2)
Monomers per AU	8	8	4
Refinement			
Resolution (Å)	60.1-3.10	47.6-1.95	45.6-2.20
R_{cryst}[4] (%)	20.7	16.8	19.4
R_{free} (%)	25.8	23.1	26.1
Number of atoms	16,154	17,795	8,665
Twin fraction	NA[5]	NA[5]	0.09
rmsd bond lengths (Å)	0.006	0.011	0.018
rmsd bond angles (°)	1.05	1.63	1.78
Average B-factor (Å^2)	81.8	30.1	35.9
Ramachandran-plot[6]			
Favored (%)	95.2	96.8	95.2
Allowed (%)	4.4	3.1	4.7
Outliers (%)	0.4	0.1	0.1
Maximum likelihood based estimated coordinate error (Å)	0.27	0.13	0.18

[1] Values in parenthesis refer to the highest resolution shell

[2] $R_{merge} = \sum_{hkl}\sum_{i}\left|I_i - \langle I\rangle\right| \Big/ \sum_{hkl}\sum_{i} I_i$

[3] $R_{pim} = \sum_{hkl}\left[1/(N-1)\right]^{1/2}\sum_{i}\left|I_i - \langle I\rangle\right| \Big/ \sum_{hkl}\sum_{i} I_i$ (173)

[4] $R_{cryst} = \sum_{hkl}\left|F_{obs} - F_{calc}\right| \Big/ \sum_{hkl} F_{obs}$

[5] NA = not applicable

[6] According to Molprobity, version 3.19 (218)

Table S 4-2. Data Collection and Refinement Statistics (*E. coli* and *B. pseudomallei* FabI).

	ecFabI-NADH-CG400549	**ecFabI-NADH-PT166**	**bpFabI-NAD^+-PT155**
Data collection			
Cell dimensions			
a, b, c (Å)	80.1, 80.1, 320.2	79.7, 79.7, 330.2	74.3, 76.0, 89.4
α, β, γ (°)	90, 90, 120	90, 90, 120	90, 90, 90
Space group	$P6_122$	$P6_122$	I222
Resolution[1] (Å)	47.1-1.80 (1.90-1.80)	47.7-1.95 (2.06-1.95)	38.0-1.84 (1.94-1.84)
Observed reflections	818,706 (97,180)	306,907 (46,321)	108,611 (14,641)
Unique reflections	56,987 (7,945)	46,243 (6,503)	22,291 (3,219)
Completeness (%)	98.7 (96.6)	99.5 (98.6)	100.0 (100.0)
Average redundancy	14.4 (12.2)	6.6 (7.1)	4.9 (4.5)
R_{merge}[2] (%)	12.5 (109.7)	9.6 (64.7)	6.9 (26.1)
R_{pim}[3] (%)	3.2 (30.4)	4.0 (25.6)	3.5 (13.7)
<I / σ(I)>	12.6 (2.3)	12.6 (2.7)	14.6 (5.0)
Monomers per AU	2	2	1
Refinement			
Resolution (Å)	69.4-1.80	69.0-1.95	38.0-1.84
R_{cryst}[4] (%)	17.5	17.6	13.7
R_{free} (%)	20.7	21.2	16.2
Number of atoms	4,057	3,943	2,367
Twin fraction	NA[5]	NA[5]	NA[5]
rmsd bond lengths (Å)	0.012	0.015	0.008
rmsd bond angles (°)	1.60	1.77	1.14
Average B-factor (Å^2)	33.0	37.9	13.8
Ramachandran-plot[6]			
Favored (%)	97.4	97.4	97.3
Allowed (%)	2.6	2.6	2.7
Outliers (%)	0.0	0.0	0.0
Maximum likelihood based estimated coordinate error (Å)	0.08	0.09	0.18

[1] Values in parenthesis refer to the highest resolution shell

[2] $$R_{merge} = \sum_{hkl}\sum_{i}\left|I_i - \langle I\rangle\right| \Big/ \sum_{hkl}\sum_{i} I_i$$

[3] $$R_{pim} = \sum_{hkl}\left[1/(N-1)\right]^{1/2}\sum_{i}\left|I_i - \langle I\rangle\right| \Big/ \sum_{hkl}\sum_{i} I_i \quad (173)$$

[4] $$R_{cryst} = \sum_{hkl}\left|F_{obs} - F_{calc}\right| \Big/ \sum_{hkl} F_{obs}$$

[5] NA = not applicable

[6] According to Molprobity, version 3.19 (218)

Table S 4-3. EcFabI kinetic parameters for the mechanistic model in Figure 4-2B.

Parameter	Estimate	Rationale
K_S	4.25 mM for cro-CoA	Approximated based on a previously reported K_m value (175).
K_{NADH}	7.8 μM	Based on a previously reported K_d value (175).
K_{NAD}	1.8 mM	Based on a previously reported K_d value (175).
$k_{on,S}$	$6 \cdot 10^8$ M^{-1} min^{-1}	This arbitrary estimate is within an order of magnitude of the diffusion-limited rate constant, which represents the theoretical ceiling. The value will only affect the kinetic system if it is low enough to be rate limiting (approx. $6 \cdot 10^5$ M^{-1} min^{-1}).
$k_{on,NADH}$	$9 \cdot 10^7$ M^{-1} min^{-1}	This value approximates the $K_{m,NADPH}^{app}$ previously obtained with 500 μM cro-CoA (175).
$k_{off,\ NAD}$	$8 \cdot 10^3$ min^{-1}	We noticed that the dissociation rate of PT52 from saFabI was similar to ecFabI. Thus, we made the assumption that the K_i is identical for the two FabI homologues. Based on this assumption, we determined the value of $k_{off,\ NAD}$ that best replicates the experimental progress curves. Consistently, the ratio of $k_{off,\ NAD}$ for ecFabI to $k_{off,\ NADP}$ for saFabI is calculated to be very similar to the ratio of $k_{off,\ NADH}$ for ecFabI to $k_{off,\ NADPH}$ for saFabI (188).
k_{cat}	600 min^{-1} for cro-coA	Based on a previously reported k_{cat} value (175).

4.10.2 Supplemental Figures

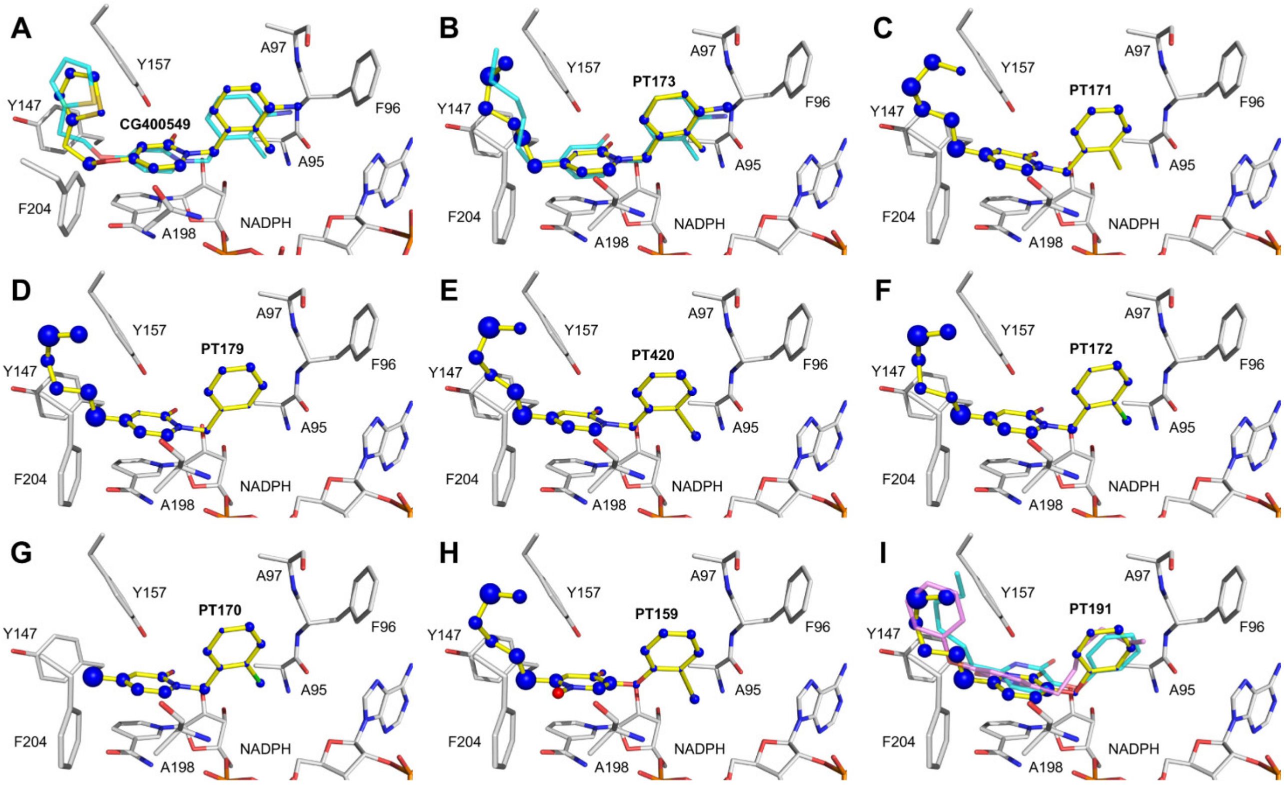

Figure S 4-1. Putative binding modes of pyridone inhibitors bound to saFabI. All pyridone inhibitors investigated in this study (Table 4-1) were docked into the saFabI binding pocket as described in the Experimental Procedures section. The radii of the blue (red) spheres represent the value of the favorable (unfavorable) per-atom score, as determined by DrugScore^X. Selected residues of the saFabI binding pocket (CG400549-I structure; according to the score, the more 'open' subunit C was selected for the bulky CG400549 compound, whereas subunit A was preferred for the other inhibitors) are depicted as gray sticks along with the putative inhibitor binding mode (yellow sticks). **(A)** Comparison of the generated CG400549 docking pose (yellow stick model) with the experimentally observed binding mode (cyan stick model). The best-ranked docking pose differs only slightly from the CG400549 binding geometry observed in the crystal structure (rmsd = 0.71 Å). **(B)** Comparison of the generated PT173 docking pose (yellow) with the experimental binding geometry (cyan). The top-ranked docking pose is very similar to the PT173 binding geometry observed in the crystal structure (rmsd = 0.83 Å). **(C)** Putative binding mode of PT171 (best-ranked pose). **(D)** Putative binding mode of PT179. The six highest-ranked docking poses were excluded due to the lack of the central hydrogen bonding network between the inhibitor, Tyr157 and NADPH. **(E)** Putative binding mode of PT420 (best-ranked pose). **(F)** Putative binding mode of PT172 (top-ranked pose). **(G)** Putative binding geometry of PT170. The best-ranked docking pose was excluded via visual inspection due to the absence of a hydrogen bond with Tyr157 and the cofactor. **(H)** Putative binding mode of PT159 (best-ranked pose). **(I)** Docking results for PT191. The FlexX docking procedure exclusively generated "unexpected" binding poses (the best-ranked pose is shown as pink stick model) without the central hydrogen bonding network. We attribute this to the free NH group and the low affinity of this particular C-substituted 2-pyridone (Table 4-1). However, docking of the tautomeric hydroxypyridine form of PT191, which likely exists in equilibrium with the pyridone form (235), resulted in the "expected" binding mode (cyan sticks; best-ranked docking pose was observed with subunit C of CG400549-I). Interestingly, the most favorable score was achieved when mutating PT179 in its putative binding mode (panel D) to PT191 (yellow sticks; subunit A of CG400549-I) (DrugScore of -261,110 compared to -246,554 and -225,496 for the best-ranked docking poses with the pyridone and hydroxypyridine forms of PT191, respectively).

5 Protons and Hydrides - Wherefrom and Whereto: From a Chemical Binding Pocket Analysis to a Biological Substrate Recognition Process

This chapter is based on the following publication:

Schiebel, J., Chang, A., Merget, B., Baxter, M. V., Bommineni, G. R., Yu, W., Spagnuolo, L. A., Tareilus, M., Tonge, P. J., Kisker, C., and Sotriffer, C. A. (in preparation‡) Protons and Hydrides - Wherefrom and Whereto: From a Chemical Binding Pocket Analysis to a Biological Substrate Recognition Process.

Author contributions with respect to data collection:

Schiebel, J.:	X-ray crystallography, molecular dynamics simulations, docking
Chang, A.:	Enzyme kinetics, mutagenesis
Merget, B.:	Molecular dynamics simulations (mutants)
Bommineni, G.R.:	Synthesis of inhibitors
Yu, W.:	Radioactive dissociation assay (results not available yet)
Spagnuolo, L.A.:	Synthesis of inhibitors
Baxter, M.V.:	Enzyme kinetics, mutagenesis
Tareilus, M.:	X-ray crystallography (ecFabI-NAD$^+$-PT449, saFabI-NADP$^+$-PT449)

‡The printed version might be subject to some changes prior to submission

Protons and Hydrides - Wherefrom and Whereto: From a Chemical Binding Pocket Analysis to a Biological Substrate Recognition Process

Johannes Schiebel,[1,2] Andrew Chang,[3] Benjamin Merget,[1] Gopal R. Bommineni,[3] Weixuan Yu,[3] Lauren A. Spagnuolo,[3] Michael V. Baxter,[3] Mona Tareilus,[2] Peter J. Tonge,[3] Caroline Kisker,[2] Christoph A. Sotriffer[1,*]

[1]Institute of Pharmacy and Food Chemistry, University of Wuerzburg, Am Hubland, D-97074 Wuerzburg, Germany

[2]Rudolf Virchow Center for Experimental Biomedicine, Institute for Structural Biology, University of Wuerzburg, Josef-Schneider-Str. 2, D-97080 Wuerzburg, Germany

[3]Institute for Chemical Biology & Drug Discovery, Department of Chemistry, Stony Brook University, Stony Brook, New York 11794-3400, USA

5.1 Abstract

One third of all drugs in clinical use target enzymatic processes thus highlighting their importance towards future drug development efforts. Based on the close relationship between inhibition and catalysis, it is key to understand enzymatic substrate recognition and its turnover. Although the *Staphylococcus aureus* enoyl-acyl carrier protein (ACP) reductase (saFabI), which is involved in bacterial fatty acid biosynthesis, constitutes a very promising drug target for the development of novel, urgently needed anti-staphylococcal agents, the substrate binding mode and catalytic mechanism remained unclear for this enzyme. Using a combined crystallographic, kinetic and computational approach, we explored the chemical properties of the saFabI binding cavity resulting in a consistent mechanistic model for substrate binding and turnover. A water-network, which links the active site with a water basin inside the homo-tetrameric protein, is likely crucial for the closure of a flexible loop as well as for an effective hydride and proton transfer during catalysis. Based on our results, we derived a new model for the FabI-ACP complex that reveals how the ACP-bound acyl-substrate is injected into the FabI binding crevice. These findings facilitate the development of novel FabI inhibitors that target the FabI-ACP interface and disrupt the interaction between these two proteins.

5.2 Introduction

Understanding the functionality of enzymes is of particular importance since one third of all currently used drugs target such proteins (209). Enzymes are tailored to stabilize the transition state (TS) of the catalyzed reaction, which should, according to Fischer's lock-and-key model, exhibit a perfect shape complementarity to the corresponding binding pocket (238). Based on this model, one would assume that enzyme catalysis is readily understood using the growing number of structural data. However, substrate binding and turnover are often accompanied by induced-fit effects, which are insufficiently characterized at the structural level (239). Many enzymes harbor flexible loops that close upon substrate binding and are most likely required for precise substrate orientation, avoidance of the release of reaction intermediates and exclusion of water from the binding-site (240). Members of the short-chain dehydrogenase/reductase (SDR) superfamily contain such a flexible loop, termed the substrate binding loop (SBL) (105). Two distinct SDR proteins are involved in the bacterial fatty acid biosynthesis (FAS-II) pathway, namely the β-ketoacyl-ACP reductase (FabG) and the enoyl-ACP reductase (FabI, EC 1.3.1.9/10) (51). Since the FAS-II acyl substrates are attached to the small acidic acyl carrier protein (ACP) via a 4'-phosphopantetheine linker (PPant, Figure 5-1A), protein-protein interactions are additionally involved in substrate recognition and turnover. However, little is known about the interaction of ACP with FAS-II enzymes. This additional complexity in the substrate recognition process has led to conflicting reports concerning the mechanism of FabI proteins, for which two fundamentally different substrate binding modes were suggested (70,107).

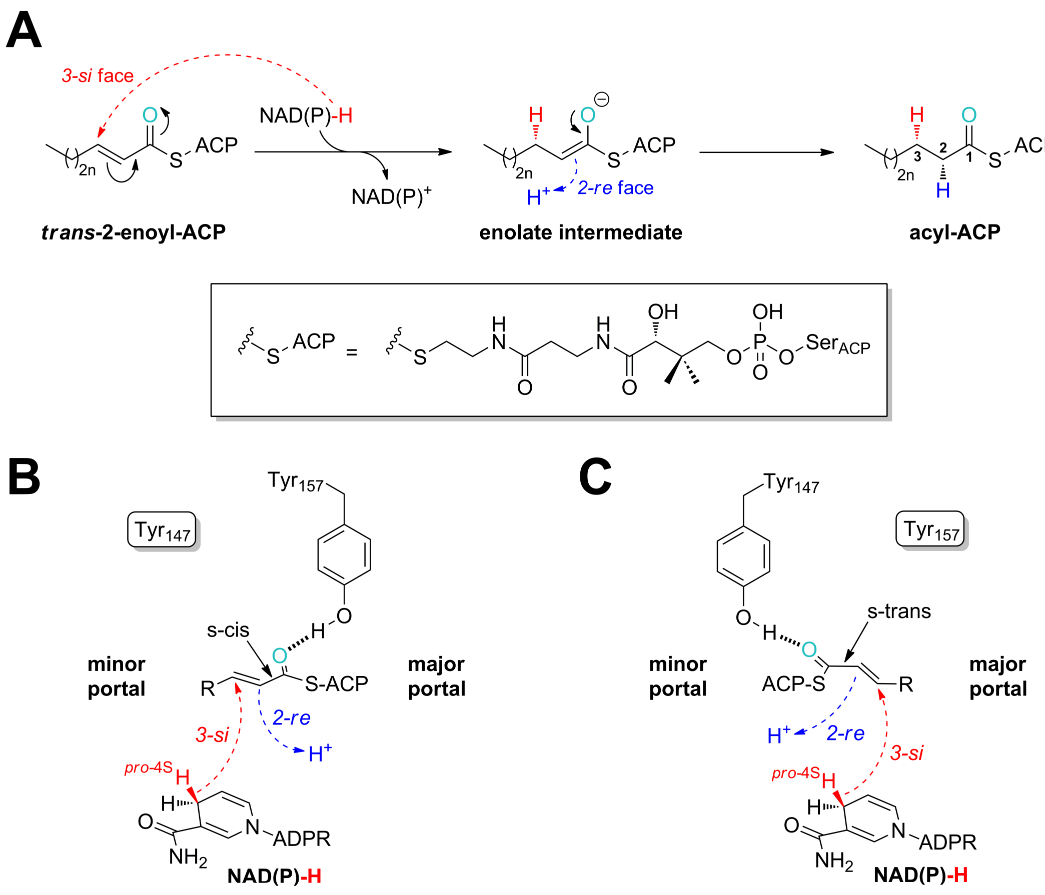

Figure 5-1. The FabI-catalyzed reaction (107,112,113). (A) Syn-addition of H_2 by a 2-step mechanism (n = 0-8). Dashed arrows indicate an attack from below the paper plane. The *pro*-4S hydride of NAD(P)H (highlighted in red) is transferred from the 3-*si* face. In a second step, the formed enolate intermediate is protonated stereospecifically from the *re* face at C2 (the proton is shown in blue). The thioester oxygen, which is hydrogen bonded to either Tyr157 (panel B) or Tyr147 (panel C), is indicated in cyan. During the reaction, the substrate is attached to ACP via a phosphopantetheine moiety depicted in the box. **(B)** Substrate delivery via the major portal. Given that the cofactor is located below the substrate in the chosen view (Figure 5-2B), the *trans*-2-enoyl-ACP has to be in the s-cis conformation to enable the correct stereochemical outcome in a scenario where ACP binds close to the major portal, and the thioester carbonyl is, thus, bound to Tyr157. Dashed arrows indicate attack vectors from below. **(C)** Substrate delivery via the minor portal. If ACP is located at the minor portal, the thioester carbonyl will be hydrogen bonded to Tyr147 and thus the substrate has to be in the s-trans conformation for consistency with the observed stereochemistry.

Enoyl-ACP reductases catalyze the last step of the FAS-II elongation pathway - the reduction of the *trans*-2-enoyl-ACP double bond (51). According to an ordered bi-bi mechanism, binding of the cofactor NAD(P)H precedes substrate binding (51). The catalyzed reaction proceeds via the transfer of the *pro*-4S hydride of NAD(P)H from the 3-*si* face to the C3 carbon of the C2-C3 enoyl-ACP double bond followed by the stereospecific protonation of the formed enolate intermediate via the 2-*re* face (Figure 5-1A) (70,112,113). To enable an effective hydride transfer, the catalytic triad residue Lys164 likely plays a crucial role in the correct positioning of the cofactor's reactive nicotinamide ring (residues will be numbered according to the *Staphylococcus aureus* homologue throughout the manuscript) (70). NAD(P)H is known to bind at the bottom of an elongated cavity with two channels leading to the solvent - a minor portal adjacent to the nicotinamide ring and a major portal next to the adenine ring (Figure 5-2B) (70). However, it is currently unclear whether the enoyl-substrate enters via the minor or major portal (70,107). A structure of the substrate analog *trans*-2-hexadecenoyl-(*N*-acetylcysteamine)-thioester (C_{16}-NAC) bound to the FabI homologue of

Mycobacterium tuberculosis (InhA) indicated that ACP should be located at the major portal (70). However, in an *Escherichia coli* FabI (ecFabI) - NAD$^+$ - *trans*-2-dodecenoyl-ACP (DD-ACP) structure, ACP was oriented for substrate delivery to proceed via the minor portal. Based on this structure which lacked the ACP amino acid side chains, the enoyl-substrate and the PPant linker due to the lack of electron density in a presumably very flexible complex, a model of the FabI-ACP complex was generated via molecular dynamics (MD) simulations (107). According to this model the thioester carbonyl oxygen would interact with the catalytic residue Tyr147 and the partial C1-C2 double bond has to be in s-trans conformation due to the defined stereochemical outcome of the reaction (Figure 5-1C) (107,112,113). However, if the ACP is located at the major portal, the substrate would be in the energetically more favorable s-cis conformation, and the thioester carbonyl would be hydrogen bonded to Tyr157, complementing the catalytic triad (Figure 5-1B) (70,107,113).

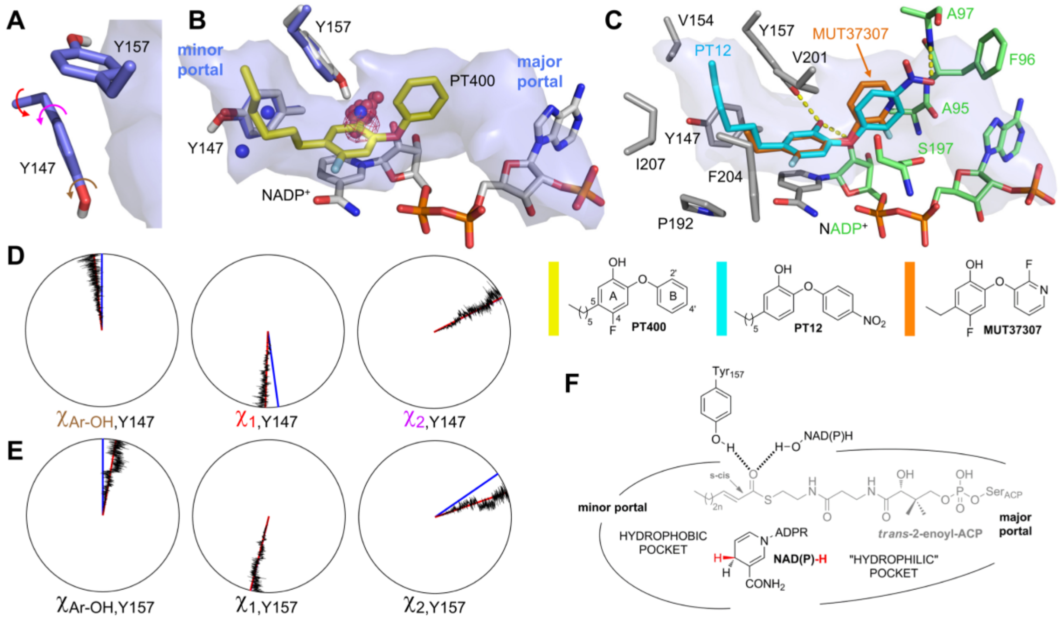

Figure 5-2. SaFabI binding pocket characteristics. (A) The catalytic tyrosines Tyr157 and Tyr147 and their orientation with respect to the binding pocket. Povme (241) was used to calculate the binding pocket volume indicated in blue surface representation (PT400-bound structure). **(B)** Hydrogen bonding hotspot. PT400 (yellow) binds to the saFabI cavity and is hydrogen bonded to Tyr157 (gray; saFabI-NADP$^+$-PT400 structure). The protonated Tyr147 and Tyr157 residues are shown for the representative structure of the largest cluster from a hierarchical clustering analysis of the saFabI$_4$-NADP$^+$-PT400 MD simulation (Figure S 5-3). Red (blue) spheres are shown for all oxygen (nitrogen) FabI inhibitor atoms within a radius of 3.5 Å around Tyr147 or Tyr157, respectively (for this purpose, all structurally known inhibitor-bound FabI complexes were superimposed on the saFabI-NADP$^+$-PT400 structure). The water occupancy map for one monomer of the saFabI$_4$-NADP$^+$ MD simulation is depicted as red mesh at the 50% level. **(C)** Probing the pocket characteristics with diphenyl ether inhibitors. The lipophilic, left subpocket (defined by the residues shown in gray) is occupied by hydrophobic alkyl chains. In contrast, the 4'-nitro substituent of PT12 as well as the fluoropyridine moiety of MUT37307 highlight the less hydrophobic character of the right subpocket (residues defining this part of the pocket are indicated in green; saFabI-NADP$^+$-PT12 structure). **(D, E)** Dials plots for Tyr147 and Tyr157. The dihedral angles C_ε-C_ζ-O-H (Ar-OH), χ_1 and χ_2 (indicated by the arrows in panel A) are exemplarily plotted for one monomer of the saFabI$_4$-NADP$^+$-PT400 trajectory. Red lines indicate the simulation averages ($\chi_{Ar\text{-}OH}$(Y147/Y157) = -7 ± 11°/11 ± 11°, χ_1 (Y147/Y157) = -178 ± 8°/-167 ± 7°, χ_2 (Y147/Y157) = 63 ± 10°/71 ± 10°) whereas blue lines depict the corresponding values for the crystal structure (for $\chi_{Ar\text{-}OH}$ the reference values were set to 0° since no hydrogen atoms were observed during the crystallographic experiments, χ_1 (Y147/Y157) = 172°/-166°, χ_2 (Y147/Y157) = 63°/56°). **(F)** Summary of the saFabI binding pocket properties. The expected substrate binding mode based on these observations is indicated in gray.

During our efforts to develop inhibitors against the drug target *S. aureus* FabI (saFabI) for which three drug candidates reached clinical trials (103), we identified a close relationship between catalysis and inhibition (188,242). Hence, small-molecule inhibitors can be used as chemical probes to explore substrate recognition and catalysis of this enzyme. Using a combined crystallographic, kinetic and computational approach, we can clearly show that Tyr157 stabilizes the enolate intermediate, which in turn is likely protonated via a water-chain that is replenished via a water chamber inside the homo-tetrameric enzyme. Consequently, we re-analyzed the ecFabI-NAD$^+$-DD-ACP structure which led to a new FabI-ACP model fully consistent with our findings and supporting the notion that the ACP should be located at the major portal. This newly derived model of substrate recognition and turnover will enhance our fundamental understanding of FabI catalysis and aid in the design of new inhibitors that can disrupt its interaction with the ACP-substrate.

5.3 Results and Discussion

5.3.1 Analysis of the SaFabI Binding Pocket Characteristics

Small-molecule inhibitors are valuable tools to investigate the mechanism of enzymatic reactions (239,242). In the case of saFabI, diphenyl ether-based inhibitors (188) were used to probe substrate binding and turnover for this important drug target. These TS-analogues trigger the full closure of the SBL (19) and establish an elongated binding pocket in contact with solvent via the minor and major portals (Figure 5-2B). Given the conserved binding mode of the diphenyl ethers (188), substituents in the 5-position of the A-ring can be used to explore the chemical properties of the left part of the pocket (left subpocket) (Figure 5-2C, surrounded by gray residues), whereas substituted B-rings are ideal probes for the right part of the pocket (right subpocket) (Figure 5-2C, surrounded by green residues). Thus, we kinetically investigated a series of diphenyl ethers (Table 5-1) and solved five associated saFabI-NADP$^+$-inhibitor structures (with the inhibitors PT12, PT400, PT404, MUT37307 (102), and PT449). Due to the very hydrophobic environment of the left subpocket, lipophilic alkyl chains are optimal substituents at the 5-position (Figure 5-2B and Figure 5-2C, Table 5-1), whereas the more hydrophilic 5-nitro and 5-fluoro substituents led to a decrease in binding affinity by one order of magnitude compared to more hydrophobic similarly sized 5-substituents (188). A similar trend was observed for ecFabI (102) indicating that the hydrophobicity of the left subpocket is conserved across species and that this pocket is ideally suited to bind the hydrophobic enoyl chain of the substrate. In contrast, the right subpocket is less hydrophobic as highlighted by the tolerance for the hydrophilic B-rings of PT12 and MUT37307 (Figure 5-2C, Table 5-1). Our crystal structures reveal that the 4'-nitro groups of PT12 and PT404 are hydrogen bonded to the amide nitrogen of Ala97 at a distance of 3.0 ± 0.1 Å (Figure 5-2C and Figure S 5-1A). Importantly, the three saFabI inhibitors, which are currently investigated in clinical trials, were also suggested to interact with the backbone of Ala97 (chapter 4), thus defining an important hydrophilic anchor in the right subpocket and a possible contribution to PPant-binding. In agreement with this suggestion, the clinical candidate MUT056399, which carries a hydrophilic 4'-amide group, displays high affinity towards saFabI (Table 5-1). The lower affinity of the inhibitor PT18 (Table 5-1) indicates the importance of the carbonyl oxygen being separated by just one atom from the B-ring to enable the hydrogen bond with Ala97 as observed for PT12 (Figure 5-2C).

Table 5-1. Kinetic parameters for saFabI inhibition by diphenyl ether analogues [a]

Name	Structure	k_{on} (x 10^{10} M^{-1} hr^{-1})	k_{off} (hr^{-1})	K_i (nM)
PT449	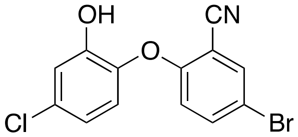	0.25	0.43	0.17
PT104 [b]	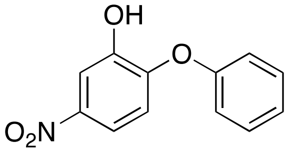	0.61	9.03	1.49
PT01 [b]	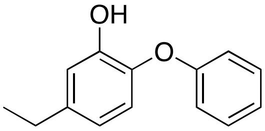	1.01	0.94	0.09
PT411	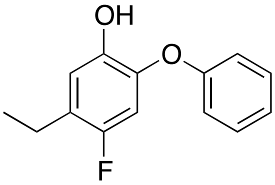	0.61	0.55	0.09
MUT37307	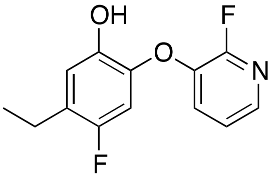	0.17	0.60	0.35
MUT056399	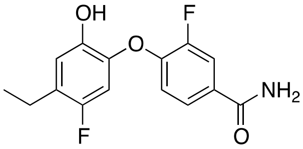	0.34	0.27	0.08
PT04 [b]	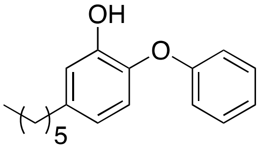	1.30	0.13 ± 0.04 [c]	0.01 [d]
PT12	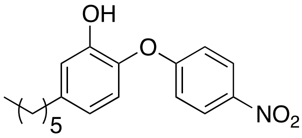	1.69	0.86	0.05
PT18	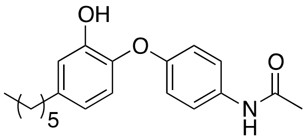	0.67	9.98	1.50

PT400	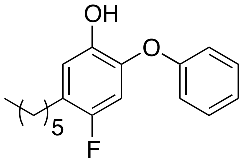	NA	NA	NA

a. Determined via single point progress curve analysis, as described in (188)
b. Data obtained from (188)
c. Calculated by fitting the ^{32}P-NAD-based dissociation curve as described in (188)
d. Determined using the k_{off} value obtained from the ^{32}P-NAD dissociation assay as described in (188)

Based on these experimental observations we speculated that the substrate enters the protein via the major portal (Figure 5-1B and Figure 5-2F) and performed five different 16 ns MD simulations using our saFabI-NADP$^+$-PT400 structure. Since saFabI is a tetramer in its ligand-bound state but can exist as a dimer in the apo-form (19), MD simulations were conducted for different oligomeric states of the protein (indicated by a subscript) including or excluding cofactor and/or inhibitor. We refer to the simulations as saFabI$_4$-NADP$^+$-PT400, saFabI$_1$-NADP$^+$-PT400, saFabI$_4$-NADP$^+$, saFabI$_4$ and saFabI$_2$ (details about the trajectories are given in the supplement). The orientation and dynamic behavior of the Tyr147 and Tyr157 hydroxyl groups are of particular importance for inhibitor and substrate recognition since the substrate thioester carbonyl oxygen has to be held in a fixed position by one of these two residues to enable the precise orientation of the enoyl-ACP double bond with respect to the NAD(P)H *pro*-4S hydride. As expected for tyrosine OH-groups (243), an analysis of the five MD trajectories revealed that the hydroxyl hydrogens of both active site tyrosines are exclusively located almost within the phenyl-ring plane (in both cases, the C_ε-C_ζ-O-H dihedral angle approximates 0° and was rarely found to be ~180° for Tyr147; see also Figure 5-2D and Figure 5-2E). In addition, the average χ_1 and χ_2 torsion angles are close to the crystallographically observed values and are very stable along the MD trajectories, leading to the precise orientation of the OH hydrogens. Preciseness in the orientation of catalytic residues seems to be a crucial component of enzymatic activity (240). In agreement, the saFabI catalytic triad residues were found to be amongst the least flexible binding-site residues in the saFabI$_4$-NADP$^+$-PT400 simulation (Figure S 5-2 and Figure S 5-3D). Importantly, only the Tyr157 but not the Tyr147 hydroxyl group points towards the saFabI binding pocket and, thus, displays an ideal geometry to bind the substrate thioester carbonyl group (Figure 5-2A). Accordingly, all investigated diphenyl ether inhibitors bind with their hydroxyl groups to the oxyanion hole formed by Tyr157 and the 2'-OH of the nicotinamide ribose, which likely mimics the interaction with the enolate intermediate (Figure 5-2 and Figure S 5-1). The resulting hydrogen bonds were conserved during the saFabI$_4$-NADP$^+$-PT400 MD simulation to 79% and 67%, respectively, leading to low rmsd values for the PT400 A-ring (1.30 ± 0.55 Å; all-atom fit) including the 5-hexyl group (1.47 ± 0.40 Å) compared to the B-ring (2.11 ± 1.11 Å). If PT400 was omitted during the MD simulation (saFabI$_4$-NADP$^+$), a water molecule binds to the oxyanion hole instead (Figure 5-2B). An analysis of all structurally characterized inhibitor-bound FabI-complexes revealed that all inhibitors from 8 different scaffold classes bind with an oxygen or nitrogen atom (rarely water-mediated) to this oxyanion hole, whereas only two polar atoms are found in the vicinity of Tyr147 (spheres in Figure 5-2B). These findings are therefore highly indicative of substrate delivery via the major portal (Figure 5-1B and Figure 5-2F), which also explains why Tyr147 is not conserved in the *M. tuberculosis* homologue InhA, where this residue is a phenylalanine (70).

5.3.2 Putative Substrate Binding Modes

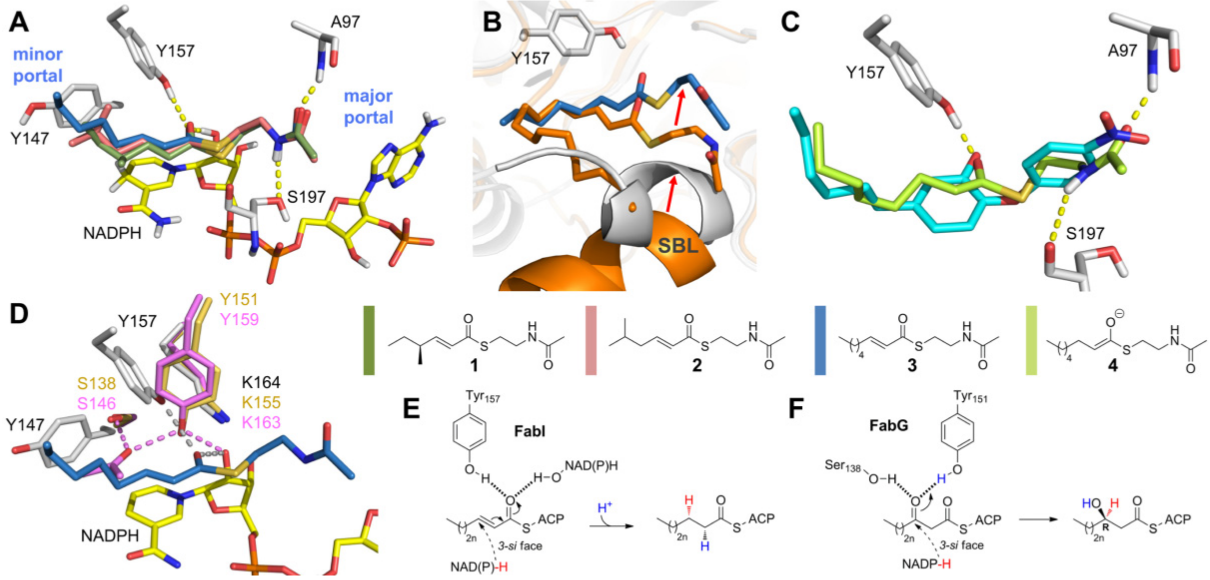

Figure 5-3. Putative substrate binding mode. (A) Enoyl-substrate analogs bound to saFabI-NADPH (gray). The selected docking poses for *S*-*trans*-4-methyl-2-hexenoyl-NAC (1), *trans*-5-methyl-2-hexenoyl-NAC (2) and *trans*-2-octenoyl-NAC (3) are depicted (color code according to the legend). **(B)** Comparison with the InhA-NAD$^+$-C$_{16}$-NAC complex (orange). The putative saFabI-NADPH-3 complex is shown in gray and blue, respectively. Red arrows indicate shifts in the substrate binding mode and SBL conformations. **(C)** Model of the octanoyl-NAC enolate intermediate (4) bound to saFabI-NADP$^+$ (gray). The inhibitor PT12 is shown as reference (cyan). **(D)** Superposition of saFabI (gray; saFabI-NADP$^+$-PT400 structure), FabG (light brown; PDB-code: 1Q7B) and 7α-hydroxysteroid dehydrogenase (HSDH) (pink; PDB-code: 1FMC). The proposed substrate binding modes (for HSDH, the carbonyl group of the reaction product 7-oxo glycochenodeoxycholic acid is shown), hydrogen bonding networks and catalytic triad residues are depicted. **(E, F)** Substrate binding to FabI and FabG, respectively. The geometrically different oxyanion holes of FabI and FabG likely bind the thioester carbonyl and β-keto oxygens, respectively.

Since the proceeding chemical reaction aggravates the structural characterization of enzyme-substrate complexes, we decided to use our validated computational docking approach to generate meaningful substrate binding modes. An octanoyl-NAC enolate intermediate (**4**, Figure 5-3) was docked into the saFabI-NADP$^+$-PT400 structure (omitting PT400) whereas four different substrate analogs (*S*-*trans*-4-methyl-2-hexenoyl-NAC = **1**, *trans*-5-methyl-2-hexenoyl-NAC = **2**, *trans*-2-octenoyl-NAC = **3**, *trans*-2-octenoyl-PPantMe = oct-PPantMe) were docked into the same receptor containing NADPH (details are given in the Methods section). Putative binding poses were selected based on the DrugScore^X score and the following three criteria: (1) the thioester carbonyl group has to bind to Tyr157 or Tyr147; (2) to fulfill the stereochemical requirements (112,113), the C1-C2 bond of the substrate has to be in s-cis (Figure 5-1B) or s-trans (Figure 5-1C) conformation, respectively; and (3) the C3 atom of the substrate has to be adjacent to the reactive *pro*-4S NADPH hydride. As expected, all selected binding modes exhibit an interaction between the thioester carbonyl and the oxyanion hole formed by Tyr157 and the nicotinamide ribose 2'-OH (Figure 5-3A and Figure 5-3C, interaction distances are given for **3** throughout the manuscript: 3.2 Å and 2.7 Å, respectively). Remarkably, even when forcing the hydroxyl hydrogen of Tyr147 to point towards the binding pocket with an artificial, energetically unfavorable Tyr147-OH torsion angle of 120° (243), the docking program generated no poses where the thioester carbonyl binds to this residue. Similar to the PT12 and PT404 4'-nitro substituents, the amide group of the substrate analogs interacts with the Ala97 backbone nitrogen (d = 2.9 Å) and is additionally bound to Ser197 (Figure 5-3A and Figure 5-3C). Overall, the created binding modes confirmed our expectations derived from the chemical mapping of the binding pocket (Figure 5-2F). A comparison with the InhA-NAD^+-C_{16}-NAC structure revealed consistency with the experimental substrate binding mode (Figure 5-3B). Interestingly, the InhA SBL and the substrate are located more towards the solvent indicating that this complex is catalytically inactive, which is in agreement with the fact that NAD^+ was used during co-crystallization (70).

5.3.3 Hydride Transfer and Proton Delivery

The putative saFabI-NADPH-**3** complex is consistent with the transfer of the *pro*-4S hydride to the C3 atom of the substrate in the s-cis conformation (d = 3.9 Å), whereas the thioester carbonyl should be protected from reduction (d = 5.0 Å, Figure 5-3E and Figure 5-4A). However, the question remains how the enolate-like TS is stabilized by the action of FabI. Clearly, the oxyanion hole is ideally suited to stabilize the evolving negative charge of the enolate. The 2'-OH of the nicotinamide ribose is involved in a hydrogen-bonding network consisting of Lys164 and two structurally and temporally conserved water molecules presumably leading to a delocalization of the evolving negative charge of the enolate (Figure 5-4A). In contrast to FabI, the negative charge is developing on the β-keto group in the case of the related FabG protein (51). Since the β-carbon of the FabG β-ketoacyl-ACP substrate should be similarly positioned with respect to the reactive *pro*-4S hydride as the FabI enoyl-ACP substrate C3 carbon, one would expect that the oxyanion hole has to be shifted two carbon atoms towards the minor portal in the case of FabG (Figure 5-3E and Figure 5-3F). Indeed, as for the classical SDR protein 7α-hydroxysteroid dehydrogenase (HSDH) (244), the oxyanion hole is created directly above the reactive NADPH hydride (Figure 5-3D). This is achieved by a substitution of Tyr147 by a serine and the exchange of the YX_6K-motif in FabI to YX_3K in FabG (51). Both FabI and FabG contain a SBL and the closure of a similar loop in triosephosphate isomerase (TIM) was proposed to be responsible for the stabilization of the two transition states (240,245). In this regard, the desolvation of the binding-site, which can be effectively achieved by the gradual closure of a flexible loop, was suggested to transfer the substrate from solvent into a protein cavity characterized by a much lower dielectric constant resulting in a strengthening of electrostatic interactions (238,245). The negative charge of the enolate generated during the FabI-catalyzed reaction might therefore be most effectively stabilized upon full closure of the SBL. Importantly, a strong electrostatic interaction develops between the enolate and the evolving positive charge on the $NAD(P)^{\delta+}$-H nicotinamide ring (Figure 5-4B). Several enzymes take advantage of positively charged moieties to stabilize negatively charged intermediates including enolates (245,246). Electrostatic interactions in a desolvated protein environment might thus be key contributors to lower the transition state energy of enzyme-catalyzed reactions.

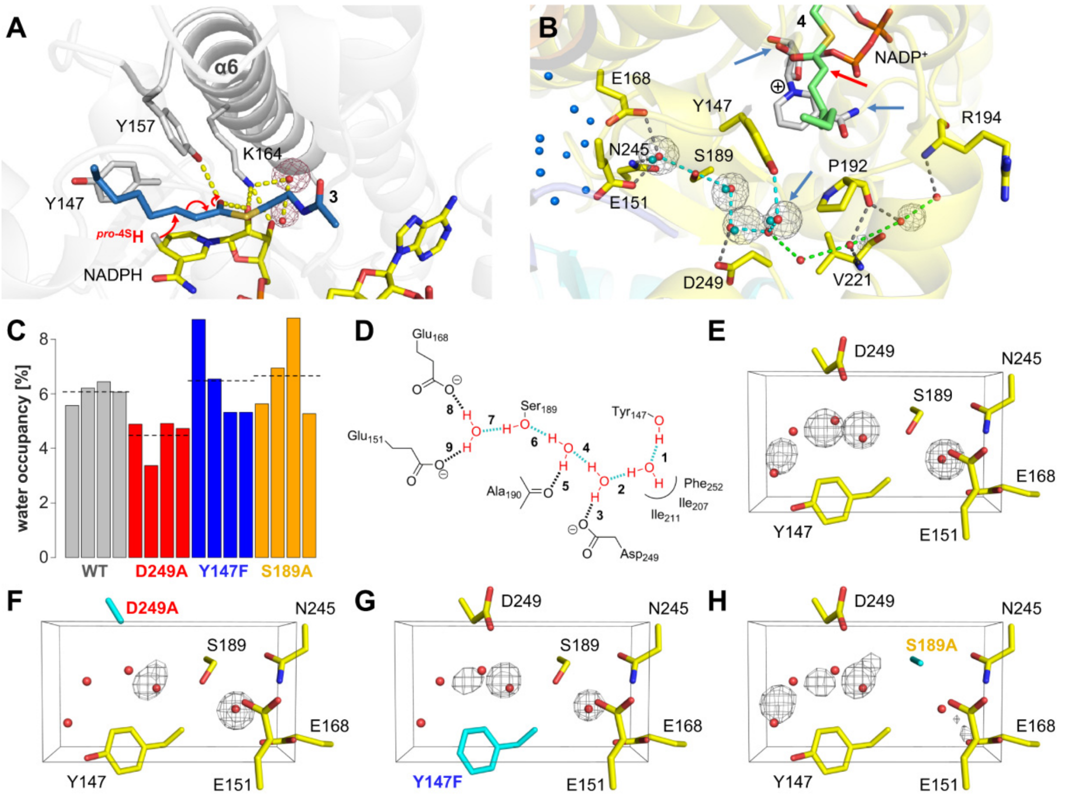
A
α6
Y157
K164
Y147
3
pro-4SH
NADPH
B
4
NADP+
E168
Y147
R194
N245
S189
P192
E151
D249
V221
C
water occupancy [%]
0
2
4
6
8
WT
D249A
Y147F
S189A
D
Glu168
Ser189
Tyr147
Glu151
Ala190
Phe252
Ile207
Ile211
Asp249
1
2
3
4
5
6
7
8
9
E
D249
N245
S189
E168
Y147
E151
F
D249A
N245
S189
E168
Y147
E151
G
D249
N245
S189
E168
Y147F
E151
H
D249
N245
S189A
E168
Y147
E151

Figure 5-4. Hydride and proton transfer. (A) Hydride transfer. The *pro*-4S hydride of NADPH is transferred to the C3-atom of the substrate (indicated by red arrows; the putative saFabI-NADPH-**3** complex is shown, see also Figure 5-3). Two highly conserved water molecules bound to Lys164 are depicted as red spheres. The corresponding water occupancy maps for one monomer of the saFabI$_4$-NADP$^+$-PT400 MD trajectory are depicted as red meshes at the 50% level. **(B)** Water-wire originating from Tyr147. In the saFabI-NADP$^+$-PT400 structure, a chain of water molecules (red spheres) connects Tyr147 with a water basin inside the tetramer (blue spheres; cyan dashes) and with the bulk solvent (green dashes), respectively. Whereas the water-chain towards the interior of the tetramer is highly conserved during the saFabI$_4$-NADP$^+$-PT400 MD simulation (occupancy maps are shown as gray meshes at 50%), the water-wire towards the exterior seems not to be established permanently. Blue arrows indicate possible proton sources and the red arrow the C2 atom of the enolate intermediate (**4** shown in green, see Figure 5-3), which is protonated during the reaction. Cyan spheres represent water molecules of the ecFabI-NAD$^+$-PT449 structure towards the inside of the tetramer. **(C)** Overall water occupancies for the four monomers of the wild-type and mutant saFabI$_4$-NADP$^+$-PT400 MD simulations in a box surrounding the water-chain. Water occupancies were calculated for 5376 grid points within the boxes depicted in panels E-H and averaged to yield the plotted overall water occupancy per monomer (shown as individual bars). Mean values for each tetramer are indicated by horizontal dashed lines. **(D)** Schematic representation of the water-network towards the inside of the homo-tetramer. Simulation-averaged distances and occupancies of the hydrogen bonding interactions in the saFabI$_4$-NADP$^+$-PT400 MD simulation (monomer 2) are given as: 2.8 ± 0.1 Å, 76% (1); 2.8 ± 0.1 Å, 69% (2); 2.7 ± 0.1 Å, 80% (3); 2.8 ± 0.1 Å, 88% (4); 2.8 ± 0.1 Å, 55% (5); 2.8 ± 0.1 Å, 76% (6); 2.7 ± 0.1 Å, 96% (7); 2.7 ± 0.1 Å, 95% (8); 2.7 ± 0.1 Å, 96% (9). **(E-H)** Water occupancies for the wild-type and variant (D249A, Y147F, S189A; highlighted in cyan) saFabI$_4$-NADP$^+$-PT400 MD simulations. The corresponding water occupancy maps (averaged for all monomers) are shown as gray meshes at the 50% level.

Since the saFabI enzyme has evolved to stabilize the enolate intermediate, its slow intrinsic rate of dissociation may limit the rate of catalysis. Thus, an alternate route to dissociation via protonation of the enolate intermediate is very important. To effectively enable protonation of this intermediate in the desolvated saFabI binding pocket, a defined water-mediated connection to bulk solvent can be envisioned. Indeed, our saFabI structures reveal a conserved water-chain originating from Tyr147 and extending towards the inside of the homo-tetramer and the exterior of the protein (Figure 5-4B). We therefore propose the following model: After the transfer of the hydride, the natural fluctuations along the reaction coordinate will cause a slight opening of the SBL, which is further triggered by the re-hydration of the binding-site via this water-chain. The water molecule directly bound to Tyr147 will be the first to enter the active site and due to steric reasons will only be able to intercalate between the enolate and nicotinamide, thus enabling the stereospecific protonation from the 2-*re* face as observed for ecFabI and InhA (Figure 5-1B and Figure 5-4B) (112,113). In principle, the NADP$^+$ amide group could be alternatively responsible for the protonation step, but its hydrogen atoms are involved in a tight hydrogen bonding network. In addition, an enol formed by protonation of the enolate oxygen via the oxyanion hole cannot be the final product dissociating from the enzyme due to the defined stereochemical outcome of the reaction (113). In fact, it has been proposed that water-networks linking substrate binding-sites with bulk solvent might be a general feature of all enzymes to enable protonation steps as well as dehydration and rehydration of the active site upon substrate binding and product release, respectively (247).

To improve our understanding of such networks, we investigated the FabI water-wire using a combined experimental and computational approach. Interestingly, our saFabI$_4$-NADP$^+$-PT400 MD simulation clearly indicates that only the water-chain towards the water chamber inside the tetrameric protein is conserved over time (Figure 5-4B, cyan dashes). Accordingly, the crystallographically observed water molecule that defines the branch of the water-wire towards the exterior of the protein is quickly released, leading to a network consisting of four water molecules and Ser189 (Figure 5-4D), which is similarly present in our ecFabI structure (Figure 5-4B, cyan spheres). Residues Tyr147, Glu168 (rarely an aspartate), Ser189 and Asp249 involved in the formation of the water-chain are strictly conserved within the FabI-familiy (mycobacterial enoyl-reductases are an exception and harbor a different water-system (70)). Thus, we explored the kinetic and dynamic behavior of the saFabI Y147F, S189A and D249A variants. A comparison of wild-type and mutant saFabI$_4$-NADP$^+$-PT400 MD simulations (Table S 5-1), clearly indicates that the water occupancies and, thus, the stability of the directed water-chain towards the interior of the tetramer are reduced for all three mutants (Figure 5-4E-H) although the overall water occupancy in this region of the protein (characterizing the complete water content of the boxes depicted in Figure 5-4E-H) remains similar to the wild-type level for Y147F and S189A (Figure 5-4C). Accordingly, the catalytic efficiency decreased for each of the water-channel mutants (Table 5-2). Both thermal shift assays and CD-spectra suggest that each mutant comprises a folded and stable structure (Table 5-3 and Figure S 5-4). Pyridone- and diphenyl ether-based TS analogues (chapter 4) were used to probe the ability of the mutant saFabI enzymes to stabilize the TS of the hydride transfer. Thermal shifts of the S189A and D249A ternary complexes are significantly diminished, suggesting increased TS energies (Table 5-3). Moreover, the increased $K_{m,\ \text{oct-CoA}}$ suggests decreased binding affinity for the acyl-CoA substrate. Since these residues are located outside of the active site and substrate binding pocket, these findings suggest that the water-chain may be crucial for SBL closure and, consequently, hydride transfer. Although one could argue that these mutations might cause slight structural perturbations that may be transferred to the active site, the remote locations and drastic effects of the mutated residues suggest that more global processes are compromised. The particularly dramatic effect of the D249A mutation (> 10,000-fold reduced catalytic efficiency) is consistent with our prediction that this residue has the greatest impact on water occupancy (Figure 5-4). We propose that water molecules, which are trapped in between the entering substrate and the left subpocket, cannot properly leave the binding-site via the disrupted water-channel of the D249A and S189A variants thereby hindering substrate binding and the closure of the SBL. In agreement with this hypothesis, mutations of residues that are up to 20 Å away from the active site of dihydrofolate reductase (DHFR) were suggested to impair catalytic activity by changing the mobility of loop regions that are important for catalysis (238).

Table 5-2. Kinetic characterization of saFabI water-channel mutants.

	$K_{m,oct\text{-}CoA}$ (µM) [a,b]	k_{cat} (min^{-1}) [a]	$k_{cat}/K_{m,oct\text{-}CoA}$ (min^{-1} μM^{-1})
wt saFabI [c]	20.7 ± 2.7	2645.4 ± 107.3	127.8 ± 17.5
saFabI D249A	> 100		0.012 ± 0.001 [d]
saFabI S189A	> 100		1.50 ± 0.04 [d]
saFabI Y147F	44.2 ± 14.5	723.9 ± 73.3	16.4 ± 5.6

a. $K_{m,oct\text{-}CoA}$ and k_{cat} values were determined at a fixed NADPH concentration (350 µM)
b. Oct-CoA = *trans*-2-octenoyl-CoA
c. Data obtained from (19).
d. Estimated based on linear slope of the Michaelis-Menten plot at low oct-CoA concentrations

Table 5-3. Thermal shifts of saFabI water-channel mutants upon ternary complex formation. [a, b, c]

	Wild-type saFabI	saFabI D249A	saFabI S189A	saFabI Y147F
E	62.60	63.40	61.20	63.20
E-NADPH-CG400549	71.20	64.60	64.20	71.20
E-$NADP^+$-PT119	70.40	63.60	61.80	72.20

a. Values correspond to T_m measurements (°C)
b. Experiments were performed in duplicate. Data variability is approximately ± 0.2 °C.
c. PT119 is a representative potent diphenyl ether (188), whereas CG400549 is a representative potent 2-pyridone (chapter 4).

Interestingly, the Y147F saFabI variant maintains a thermal shift similar to the wild-type enzyme upon ternary complex formation with a TS analogue (Table 5-3). Thus, the TS energy for the hydride transfer is likely unchanged in this mutant relative to wild-type. One of the TS mimics is more enolate-like (PT119) and the other more substrate-like (CG400549) (chapter 4). Thus, the 2-fold increased $K_{m,\ oct\text{-}CoA}$ (Table 5-2) may also uniquely be reflected in the higher thermal shift of the E-$NADP^+$-PT119 complex relative to E-NADPH-CG400549 (Table 5-3) indicating that substrate binding affinity is altered more than the enolate binding affinity. Given an increased $K_{m,\ oct\text{-}CoA}$ and unchanged TS energy, a smaller barrier to hydride transfer is expected. The opposing experimental observation of a smaller k_{cat} for the Y147F variant likely reflects a shift in the rate limiting step. This result suggests that we successfully and rationally increased the barrier to enolate protonation, thereby making it the new bottleneck step in saFabI catalysis.

5.3.4 Protein Fluctuations Relevant for Substrate Recognition

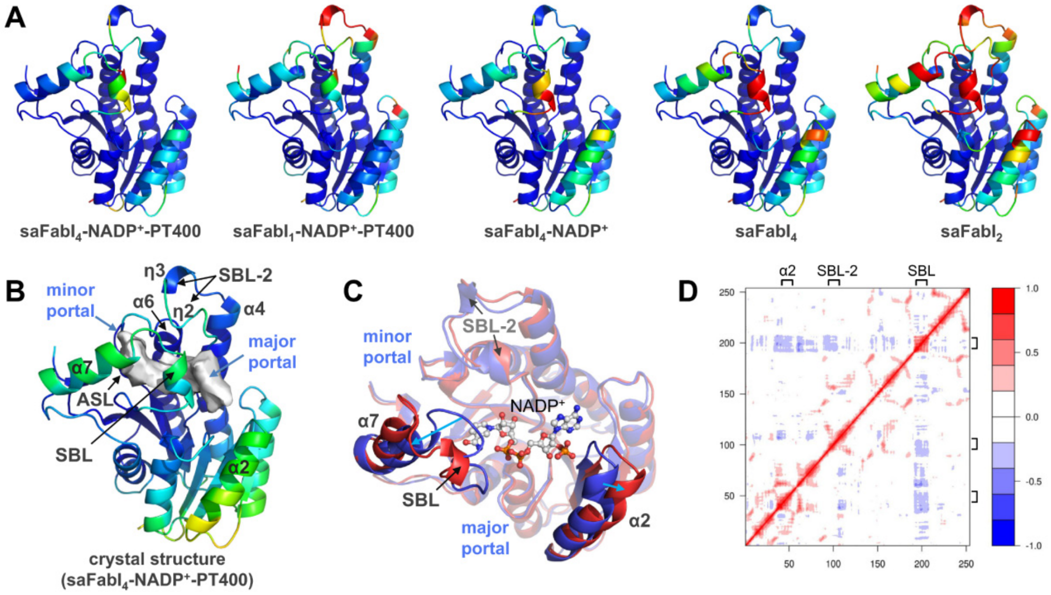

Figure 5-5. Conformational variability of saFabI. (A) Visualization of the B-factors for the five wild-type MD simulations. B-factors were averaged over the four monomers and plotted on monomer 3 of the saFabI-NADP$^+$-PT400 structure. Colors indicate the B-factor value of each residue (blue to red = 5 to 85 Å^2). **(B)** Visualization of the B-factor for the saFabI-NADP$^+$-PT400 crystal structure. B-factors were averaged over the four monomers and plotted on monomer 3 of the structure. Colors indicate the B-factor value of each residue (blue to red = 20 to 85 Å^2). **(C)** Essential dynamics of saFabI (calculated with ptraj and IED (248)). The first (blue) and last (red) frames along the principal mode of the 16 ns saFabI$_2$ MD trajectory are shown for one monomer exemplarily. Blue arrows indicate the anti-correlated movement of the SBL and helix α2. NADP$^+$ of the saFabI-NADP$^+$-PT400 structure is shown as reference (colored ball-and-stick model). See also Movie S 5-1. **(D)** Dynamic cross-correlation map (shown for the same monomer of the saFabI$_2$ MD simulation). This graph was generated using the statistical framework R.

Although the presented results concerning the FabI binding-site clearly indicate that the substrate should be delivered via the major portal, the ecFabI-NAD$^+$-DD-ACP structure suggested that the ACP residue Ser36 carrying the substrate is located adjacent to the minor portal (107). To resolve this issue, we first had a closer look at the intrinsic protein fluctuations since protein-protein interactions usually require structural adaptations (249). The MD trajectories of the saFabI apo-enzyme (NADP$^+$ and PT400 omitted) are characterized by significantly increased simulation-averaged rmsd values and standard deviations compared to the ternary complex simulations indicating an enhanced conformational variability and mobility (Table S 5-2 and Figure S 5-5). A comparison of the B-factors for the five different MD trajectories (Figure 5-5A) revealed that this behavior can mainly be attributed to the increasing flexibility of the SBL, the attached helix α7 as well as helix α2. In line with our previous structural observation that rearrangements of two loops (substrate binding loop 2 = SBL-2; active site loop = ASL) and of the attached helices α4 and α6 are involved in a dimer-tetramer transition (19), we additionally observed enhanced B-factors for these regions when simulating the monomeric or dimeric protein molecule (most pronounced for η3; Figure 5-5A). While the substantial mobility of the SBL confirmed our expectations, we were rather surprised to observe enhanced B-factors for helix α2. Indeed, the experimental B-factors of the PT400-bound saFabI structure emphasized the mobility of this helix (Figure 5-5B). In addition, our recently reported saFabI structure in complex with NADPH and a substrate-like pyridone inhibitor (chapter 4) reveals a more opened α2 conformation compared to the saFabI-$NADP^+$-diphenyl ether structures (Figure S 5-6D). Importantly, dynamic cross-correlation maps and essential dynamics analyses revealed an anti-correlated opening movement of the SBL and helix α2, which was most pronounced for the $saFabI_2$-simulation (Figure 5-5C and Figure 5-5D, Movie S 5-1). This concerted opening results in a widening of the major portal that might facilitate the binding of the cofactor and the substrate (see also Figure S 5-6 and Supplemental Results). In addition, the flexible α2 and SBL regions provide an ideal platform for the interaction with ACP adjacent to the major portal.

5.3.5 Location and Binding Process of ACP-substrates

Since all our results clearly indicate that ACP delivers the enoyl-substrate via the major portal, we revisited the ecFabI-NAD^+-DD-ACP structure (PDB-entry 2FHS). Importantly, we found that ACP not only contacts the FabI molecule in the asymmetric unit, which was interpreted as biologically relevant interaction partner (Figure 5-6A-B, yellow), but also interacts with a symmetry-related FabI (Figure 5-6A-B, gray). Since the complex with the symmetry-related monomer, in contrast to the original interpretation (107), enables the binding of four ACP molecules per homo-tetramer without any clashes (Figure 5-6D-E), this could likely be the biologically relevant assembly. We superimposed a decanoyl-ecACP structure (PDB-entry 2FAE) onto the partial ACP model of the 2FHS-structure to create a full model for the FabI-ACP complex (Figure 5-6B), which displays a much larger interaction surface for the assembly with the symmetry-related monomer compared to the original FabI-ACP complex (344 vs. 93 $Å^2$ according to the PISA-server (157), Figure 5-6C). In this new complex the ACP is located at the major portal and interacts with the SBL and helix α2 as proposed by our MD simulations (Figure 5-6F). An analysis of all structurally known ACP complexes (PDB-entries 3NY7, 3EJB, 3EJD, 3EJE, 1F80, 4ETW, 4DXE, 2XZ0, 2XZ1) indicated that ACP helix $\alpha2_{ACP}$, which includes Ser36 carrying the substrate at its N-terminus, is consistently involved in the protein-protein interface (76) with frequent contributions from the N-terminal part of helix $\alpha3_{ACP}$. Since these helices contain three conserved acidic regions (including 2-4 acidic residues each; red ACP portions in Figure 5-6F), the interaction interface of the FAS-II enzymes is required to be electropositive (76). FabI proteins harbor several basic residues surrounding the major portal, which are distributed over three secondary structure elements - α2 with 2-4 basic residues, the SBL including the attached N-terminus of helix α7 with 1-4 basic residues and the loop containing residues 17-18 with up to two basic amino acids (Figure 5-6F). Whereas in the original FabI-ACP model only the N-terminus of helix $\alpha2_{ACP}$ was able to interact with FabI, the new model permits the interaction of the full helix $\alpha2_{ACP}$ and the N-terminus of $\alpha3_{ACP}$ with the basic FabI interface surrounding the major portal. Based on the original model, the ecFabI residues Lys201, Arg204 and Lys205 (part of helix α7) were mutated to analyze the proposed interface (107). Unfortunately all three residues would be involved in the interaction of FabI with the ACP molecule through both the minor and the major portal and therefore also supported the original model. We note that for the closely related FabG protein stereochemistry alone can reveal the location of

ACP since the positions of the *pro*-4S hydride donor and β-keto acceptor groups are fixed as depicted in Figure 5-3F. Indeed, the R-β-hydroxyacyl-ACP is formed during the FabG-catalyzed reaction (250), providing evidence that ACP is located at the major portal as we propose for FabI.

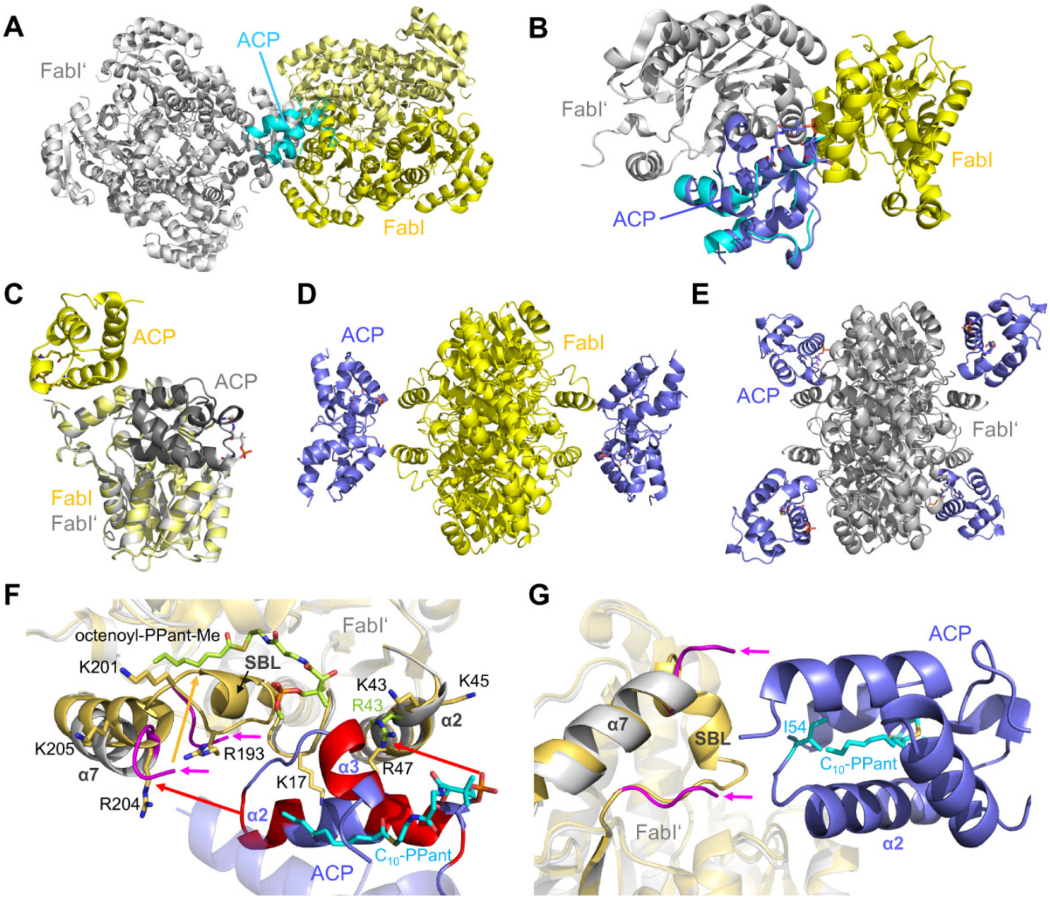

Figure 5-6. The ecFabI-ACP encounter complex. (A) Symmetry-related ecFabI homo-tetramer (gray) within the ecFabI-NAD$^+$-DD-ACP structure (yellow, PDB-code: 2FHS; two FabI monomers and one ACP in the asymmetric unit). The partial ACP model is depicted in cyan. **(B)** ACP environment in the 2FHS-structure. To derive a full ACP model, decanoyl-ecACP (lilac, PDB-code: 2FAE) was superimposed onto the partial ACP model of the 2FHS-structure considering only main chain atoms. **(C)** Superposition of the two crystallographically feasible FabI-ACP interaction models. The originally proposed model is depicted in yellow, the model derived from the interaction with a symmetry related FabI monomer is colored in gray. **(D, E)** FabI-ACP clash-test. The simultaneous interaction of the FabI homo-tetramer with four ACP substrates will lead to severe clashes for the original model (panel D) (107), whereas no clashes are observed for the new model (panel E). These figures were created by superimposing both models (panel C) on each subunit of the full FabI homo-tetramer. **(F)** ACP binds close to the major portal. According to the new model, the conserved acidic ACP patches (depicted in red) interact with basic FabI regions mainly located on helices α2, α7 and the SBL (golden sticks; PDB-code: 1QSG). The disordered SBL of the 2FHS-structure is highlighted in magenta. The 1QSG ecFabI-NAD$^+$-triclosan structure (golden) displays a closed SBL and was superimposed onto the FabI monomer of the new model (gray) as a reference. Red and golden arrows indicate the proposed movements of ACP and the SBL upon substrate injection, respectively. The putative *trans*-2-octenoyl-PPantMe binding mode is depicted in green. **(G)** Proposed substrate delivery. The ACP residue Ile54 (cyan) is located in the FabI-ACP interface and likely contributes to the binding of the substrate inside the ACP-fold (cyan).

A comparison of the new FabI-ACP complex with the putative substrate binding modes suggests that ACP has to move by approximately 12 Å to reach the relatively conserved basic residue at position 43 (indicated by red arrows in Figure 5-6F), which should be ideally suited to bind to the PPant phosphate group in the final complex based on distance considerations.

Hence, we propose that the new FabI-ACP model is not in a catalytically competent state but rather constitutes the initial encounter complex prior to substrate injection (Figure 5-6F). In line with this suggestion, the SBL was found to be disordered in the 2FHS-structure and no electron density was observed for the cofactor or substrate (107). This is not very surprising since the oxidized cofactor was used during the crystallization of the complex. We thus propose that binding of the reduced cofactor will initiate the formation of the catalytically competent complex via the concerted closure of the SBL and injection of the substrate to the FabI binding-site. The highly conserved ACP residue Ile54, which displayed the largest chemical shift perturbation in NMR experiments with FabG and ACP (76), contacts the acyl-substrate within the ACP-fold and is located close to the SBL in the FabI-ACP complex indicating that this residue might be involved in this concerted process (Figure 5-6G). In FabI, the conserved basic residue at position 194 (193 for ecFabI) might also be crucial for this process since it can interact electrostatically with the ACP and was suggested to function as a hinge for SBL closure together with a hydrogen bond acceptor at position 205 (153). Whereas ACP in the initial encounter complex mainly interacts with basic residues located on helix α2, the closure of the SBL might enable ACP to move closer to the newly created positively charged amino acid patch surrounding this loop (indicated by the red and golden arrows in Figure 5-6F). We note that the essential dynamics observed for the SBL and helix α2 might be directly involved in this substrate recognition process.

5.3.6 Concluding Remarks

In the course of these studies we analyzed the chemical binding pocket properties and conformational dynamics of saFabI and applied this knowledge to clarify the catalytic mechanism of this important drug target involving hydride and proton transfer steps. Ultimately, this led to a model where we clearly show that the FabI-ACP encounter complex is formed via the major portal and not as previously suggested through the minor portal. The vastly improved knowledge about substrate binding and turnover can now facilitate medicinal chemistry efforts aiming to mimic important substrate moieties within the adaptable FabI binding pocket or to block the essential interaction of this enzyme with ACP. Addressing Ala97, that likely stabilizes the terminal PPant peptide (Figure 5-3A), can be one strategy to design new saFabI inhibitors, which has already proven successful during the development of three drug candidates which are currently in clinical trials for the treatment of MRSA infections (103).

5.4 Methods

5.4.1 Crystallization, Data Collection and Structure Determination

SaFabI was purified and crystallized as described previously (19,188). Briefly, protein samples (15 mg/ml in 20 mM citrate pH 5.6, 280 mM NaCl, 280 mM potassium glutamate and 1 mM EDTA; 19 mg/ml in 20 mM citrate pH 5.6, 250 mM NaCl, 250 mM potassium glutamate and 1 mM EDTA for PT449) were incubated for 2 hours at 4 °C with a 10-fold molar excess of $NADP^+$ (dissolved in water) and a 15-20-fold molar excess of inhibitor (dissolved in DMSO). Using the vapor diffusion method, crystals were obtained in 0.1 M Na/K-phosphate pH 6.5 and 39 - 47% 2-methyl-2,4-pentanediol (MPD) (Table S 5-3). For diffraction experiments, crystals were directly flash-frozen without the addition of a cryoprotectant. Similarly, ecFabI (purified as described previously (109), 13 mg/ml in 20 mM PIPES pH 7.5, 200 mM NaCl and 1 mM EDTA) was incubated with a 10-fold molar excess of NAD^+ (dissolved in water) and a 20-fold molar excess of PT449 (dissolved in DMSO). Crystals grew in a precipitant solution composed of 0.1 M CAPS pH 10.5, 0.08 M NH_4Ac and 20% PEG 3350 and were cryo-protected using the mother liquid supplemented by 20% ethylene glycol.

Diffraction data were collected at beamline 14.1 of the BESSY II synchrotron (λ = 0.918 Å, T = 100 K) using a MarMosaic 225 (PT12, PT400, PT404, MUT37307) or Pilatus 6M detector (PT449), integrated with Imosflm (178) or XDSAPP (215), respectively, and scaled with Scala (179). After molecular replacement with Phaser (180) (search models: PDB-entries 4ALK and 1QSG for saFabI and ecFabI, respectively), alternate cycles of model building in Coot (182) and refinement using Refmac 5 (181) led to the final models. Since the electron density for the ecFabI amino acid region 193-210 was only weak, this part of the protein could not be fully modeled. Data collection and refinement statistics are given in Table S 5-3. All structural figures were prepared using PyMOL (174).

5.4.2 Site-Directed Mutagenesis, Expression and Purification of SaFabI Variants

Site-directed mutagenesis was performed using the QuikChange Mutagenesis Kit from Stratagene to construct the D249A, S189A and Y147F mutants from a pET-16b plasmid containing the wild-type *fabI* gene. The primers are listed in Table S 5-4. Expression and purification of the variants were performed as described for the wild-type enzyme (19).

5.4.3 Steady-State Kinetics

Kinetic experiments were performed as described previously (19). Briefly, reaction velocities were measured by monitoring the oxidation of NAD(P)H to $NAD(P)^+$ at 340 nm ($\varepsilon = 6220\ M^{-1}\ cm^{-1}$). Kinetic parameters for saFabI D249A, S189A and Y147F were determined by measuring initial velocities at varying concentrations of *trans*-2-octenoyl CoA and a constant concentration of NADPH (350 µM).

5.4.4 Inhibition Kinetics

Progress curves at a single inhibitor concentration were used to determine the kinetics and thermodynamics of inhibition by the compounds in Table 5-1, as described previously (188).

5.4.5 Thermal Shift Assay

ThermoFluor experiments were carried out in 96-well plates (Concord) using the CFX96 Real-Time PCR Detection System and C1000 Thermal Cycler (Bio-Rad), as described previously (188).

5.4.6 Circular Dichroism

Prior to analysis, saFabI was dialyzed in low salt buffer (10 mM potassium phosphate pH 7.5, 100 mM KCl) to a concentration of 5-10 µM. Circular dichroism (CD) was performed using a Chirascan CD spectrophotometer (Applied Photophysics) at 20°C. The cells had a path length of 1 cm, and spectra were recorded from 260 to 200 nm for far-UV.

5.4.7 Molecular Dynamics Simulations

All eight MD simulations conducted were based on the saFabI-NADP$^+$-PT400 structure. The full homo-tetramer (subunits E-H, referred to as monomers 1-4) was simulated for the wild-type protein as well as the Y147F, S189A and D249A variants with bound NADP$^+$ and PT400. Moreover, simulations were initiated using the tetrameric complex structure without PT400 or NADP$^+$ and PT400, respectively. Since saFabI can exist as a dimer in the apo form (19), we also simulated the dimeric protein lacking both ligands (subunits F-G). As a reference, we additionally performed a simulation for the monomeric saFabI-NADP$^+$-PT400 complex (subunit G). For the setup of the MD simulations only those water molecules of the binding pocket and water-chain were included from the original structure, which had clear electron density (56 waters for the tetrameric protein). The binding-site of the protein was defined by residues 93-99, 102, 121, 146-147, 154-157, 160, 164, 190-193, 195, 197-204, 207 and NADP$^+$. Guided by visual inspection, the most likely asparagine, glutamine and histidine conformations and protonation states were assigned (in particular His247 was assumed to be doubly protonated due to its interactions with Glu151 and Glu244').

The MD simulations were performed according to a standard procedure of the working group of Prof. Christoph A. Sotriffer as, for instance, described in references (236,237) explaining the partially similar wording. Using the tleap module of AMBER11 (251), hydrogens were added and ff99SB force field parameters assigned to the protein atoms. Atomic charges for NADP$^+$ and PT400 were determined with Gaussian 03 (252) using the RESP methodology (253) at the HF/6-31G* level. The AMBER11 parmchk module (254) was used to assign the missing force field parameters according to the GAFF force field (255). The correct GAFF atom and bond types were determined using antechamber (254). A short energy minimization over 200 steps using a generalized Born implicit solvent model was performed with the SANDER module of AMBER11 (251). Using tleap, the minimized systems were then solvated in a box of TIP3P water molecules and neutralized using sodium counter ions. The wild-type and mutant simulations were performed using the SANDER module of AMBER11 (251) or the PMEMD module of AMBER12 (256), respectively. First, the solvent molecules were disordered in a 25 ps constant-volume simulation, keeping the protein atoms fixed using the ibelly option. This was achieved by heating the systems from 100 to 300 K over 20 ps and then cooling back to 100 K within 5 ps, applying the Berendsen weak coupling algorithm with a 0.5 ps time constant. In a second step, the whole system was allowed to move freely and was heated gradually to 300 K over 25 ps. To enable a time step of 2 fs during the following MD run, all bonds involving hydrogen atoms were constrained by the SHAKE algorithm (257). Moreover, the constant-volume periodic boundary conditions were switched to constant-pressure by applying isotropic position scaling with a reference pressure of 1 bar and a relaxation time of 1 ps. In addition, the temperature was fixed by coupling to a heat bath with a time constant of 1 ps. An 8 Å cutoff was used for van der Waals interactions and long-range electrostatic interactions were treated using the particle mesh Ewald method (258). Coordinates were saved at intervals of 1 ps and MD trajectory data were collected over a period of 16 ns for each system. Processing and analyses of the trajectories were performed using the ptraj module of AMBER11, carnal of AMBER7 and VMD (259). Hierarchical clustering analysis was conducted using SYBYL-X (Tripos, St. Louis, 2009), version 1.0 (225).

5.4.8 Computational Docking

Putative substrate binding poses were generated using our validated approach described previously for the docking of pyridone inhibitors to saFabI (chapter 4). Briefly, binding poses were produced using FlexX (BioSolveIT, Sankt Augustin, 2009), version 3.1.4 (220), and rescored with DrugScore^X (G. Neudert and G. Klebe, University of Marburg, 2008) (221). The most likely binding mode was selected based on the DrugScore^X score and the selection criteria specified in the results section. Re-docking of PT400 yielded rmsd values below 0.77 Å for the 10 best-ranked poses (0.60 Å for the top-ranked pose) and thus confirms the reliability of our approach.

During the docking procedure, the hydroxyl dihedral angles of Tyr147 and Tyr157 were set to 0° or 120° and 0°, respectively. An octanoyl-NAC enolate intermediate (**4** in Figure 5-3) was docked into the saFabI-NADP$^+$-PT400 structure (omitting PT400) whereas the *S*-*trans*-4-methyl-2-hexenoyl-NAC (anteiso, **1**), *trans*-5-methyl-2-hexenoyl-NAC (iso, **2**), *trans*-2-octenoyl-NAC (**3**) and *trans*-2-octenoyl-PPantMe substrate analogs were docked into the same receptor containing the reduced cofactor NADPH (derived from a superimposition with a NADPH-bound saFabI structure; saFabI-NADPH-CG400549 structure, subunit C; see also chapter 4). For the five compounds mentioned above, the docking poses with rank 1, 18, 5, 2 and 1 (with respect to the DrugScore^X score) were chosen for further analysis, respectively.

5.5 Associated Content

5.5.1 Supporting Information

The supplement contains four tables, six figures, a movie and supporting results.

5.6 Author Information

5.6.1 Corresponding Author

*E-mail: sotriffer@uni-wuerzburg.de

5.6.2 Notes

The authors declare no competing financial interest.

5.7 Acknowledgments

We thank the staff at the BESSY II beamline 14.1 (Berlin) for technical support. This work was supported in part by NIH grants GM102864, AI044639 and AI070383 to P.J.T., and through the Deutsche Forschungsgemeinschaft to C.K. (SFB630 and Forschungszentrum FZ82) and C.A.S. (SFB630). J.S. was supported by a grant of the German Excellence Initiative to the Graduate School of Life Sciences, University of Würzburg.

5.8 Supplementary Information

5.8.1 Supplemental Tables

Table S 5-1. Simulation averages of the rmsd values for the tetrameric wild-type and mutant saFabI MD simulations (saFabI$_4$-NADP$^+$-PT400) with respect to the saFabI-NADP$^+$-PT400 starting structure [Å].

rmsd (vs. X-ray)	D249A	Y147F	S189A	wild-type
C$_\alpha$ atoms of all residues	1.29 ± 0.17	1.14 ± 0.09	1.27 ± 0.13	1.25 ± 0.12

Table S 5-2. Simulation averages of the rmsd values for the five wild-type saFabI MD simulations with respect to the saFabI-NADP$^+$-PT400 starting structure [Å].

rmsd (vs. X-ray)	saFabI$_2$		saFabI$_4$		saFabI$_4$-NADP$^+$		saFabI-NADP$^+$-PT400		saFabI$_4$-NADP$^+$-PT400	
	all atoms	C$_\alpha$ atoms	all atoms	C$_\alpha$ atoms	all atoms	C$_\alpha$ atoms	all atoms	C$_\alpha$ atoms	all atoms	C$_\alpha$ atoms
all protein residues	2.55 ± 0.32	1.97 ± 0.31	2.15 ± 0.22	1.61 ± 0.18	1.74 ± 0.18	1.26 ± 0.15	1.87 ± 0.15	1.25 ± 0.14	1.72 ± 0.15	1.25 ± 0.12
less flexible residues [a]	1.71 ± 0.16	1.18 ± 0.13	1.62 ± 0.15	1.19 ± 0.11	1.46 ± 0.13	1.05 ± 0.09	1.60 ± 0.12	1.04 ± 0.08	1.44 ± 0.11	1.01 ± 0.08
flexible residues [b]	4.52 ± 0.67	3.78 ± 0.70	3.52 ± 0.42	2.71 ± 0.39	2.50 ± 0.35	1.85 ± 0.33	2.70 ± 0.34	1.91 ± 0.36	2.52 ± 0.27	1.94 ± 0.25
β-strands [c]	1.01 ± 0.11	0.69 ± 0.10	1.41 ± 0.15	1.09 ± 0.13	1.13 ± 0.13	0.85 ± 0.10	0.79 ± 0.08	0.46 ± 0.05	1.12 ± 0.11	0.85 ± 0.10

[a] the most flexible regions (residues 3-7, 40-47, 99-113, 152-156 and 194-210) were omitted during fitting and rmsd calculation

[b] rmsd for the most flexible regions with fitting according to [a]

[c] rmsd for β-strand residues only (37 residues)

Table S 5-3. Data Collection and Refinement Statistics.

	saFabI-NADP$^+$-PT12	saFabI-NADP$^+$-PT400	saFabI-NADP$^+$-PT404
Inhibitor	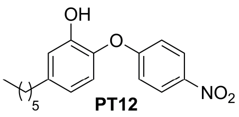 PT12	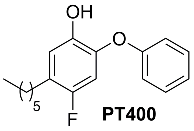 PT400	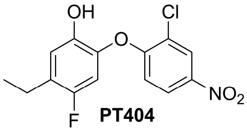 PT404
Crystallization			
Protein concentration (mg/ml)	15.0	15.0	15.0
Crystallization condition	0.1 M K/Na-phosphate pH 6.5 47% MPD	0.1 M K/Na-phosphate pH 6.5 39% MPD	0.1 M K/Na-phosphate pH 6.5 47% MPD
Cryoprotectant	none	none	none
Data collection			
Cell dimensions			
a, b, c (Å)	89.4, 94.8, 94.8	90.4, 94.9, 94.9	89.2, 94.9, 94.9
α, β, γ (°)	98.3, 111.4, 97.5	98.2, 97.2, 112.5	98. 5, 111.5, 97.3
Space group	P1	P1	P1
Resolution[a] (Å)	40.8-2.30 (2.42-2.30)	38.6-2.02 (2.13-2.02)	40.7-2.15 (2.27-2.15)
Observed reflections	266,684 (38,821)	360,497 (52,058)	327,098 (47,457)
Unique reflections	120,978 (17,617)	181,260 (26,181)	148,864 (21,614)
Completeness (%)	96.8 (96.1)	97.8 (97.0)	97.5 (96.7)
Average redundancy	2.2 (2.2)	2.0 (2.0)	2.2 (2.2)
R_{merge}[b] (%)	10.7 (43.5)	5.7 (37.6)	11.0 (41.7)
R_{pim}[c] (%)	9.6 (39.1)	5.7 (37.6)	9.8 (37.4)
<I / σ(I)>	6.1 (2.0)	7.5 (2.0)	6.0 (2.1)
Monomers per AU	8	8	8
Refinement			
Resolution (Å)	40.8-2.30	38.4-2.02	40.7-2.15
R_{cryst}[d] (%)	15.2	14.5	17.0
R_{free} (%)	21.3	18.5	23.0
Number of atoms	17,717	18,217	18,382
rmsd bond lengths (Å)	0.010	0.013	0.012
rmsd bond angles (°)	1.68	1.78	1.74
Average B-factor (Å^2)	38.7	33.5	23.3
Ramachandran-plot[e]			
Favored (%)	95.7	96.6	96.3
Allowed (%)	4.1	3.4	3.4
Outliers (%)	0.2	0.0	0.3
Maximum likelihood based estimated coordinate error (Å)	0.15	0.10	0.13

	saFabI-NADP$^+$-MUT37307	**saFabI-NADP$^+$-PT449**	**ecFabI-NAD$^+$-PT449**
Inhibitor	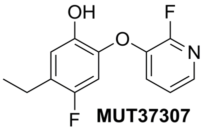 **MUT37307**	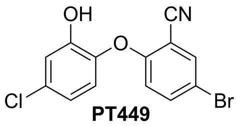 **PT449**	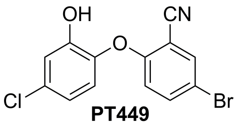 **PT449**
Crystallization			
Protein concentration (mg/ml)	15.0	19.0	13.0
Crystallization condition	0.1 M K/Na-phosphate pH 6.5 41% MPD	0.1 M K/Na-phosphate pH 6.5 47% MPD	0.08 M NH_4Ac 0.1 M CAPS pH 10.5 20% PEG 3350
Cryoprotectant	none	none	20% ethylene glycol
Data collection			
Cell dimensions			
a, b, c (Å)	90.0, 94.7, 94.8	90.1, 95.2, 95.2	79.1, 79.1, 322.3
α, β, γ (°)	98.1, 97.4, 112.2	98.4, 97.5, 111.5	90, 90, 120
Space group	P1	P1	$P6_122$
Resolution[a] (Å)	33.6-1.80 (1.90-1.80)	46.6-2.15 (2.27-2.15)	47.0-2.00 (2.11-2.00)
Observed reflections	1,011,220 (146,182)	543,061 (80,880)	794,472 (114,237)
Unique reflections	254,237 (36,744)	152,227 (22,139)	41,818 (5,947)
Completeness (%)	97.5 (96.4)	98.2 (97.6)	100.0 (100.0)
Average redundancy	4.0 (4.0)	3.6 (3.7)	19.0 (19.2)
R_{merge}[b] (%)	7.1 (61.7)	9.7 (56.0)	13.7 (124.6)
R_{pim}[c] (%)	4.1 (35.7)	6.1 (34.1)	3.2 (29.0)
<I / σ(I)>	11.4 (2.3)	8.3 (2.2)	16.2 (2.4)
Monomers per AU	8	8	2
Refinement			
Resolution (Å)	33.6-1.80	46.6-2.15	68.5-2.00
R_{cryst}[d] (%)	14.0	17.4	16.6
R_{free} (%)	17.0	22.7	20.6
Number of atoms	18,237	17,357	3,996
rmsd bond lengths (Å)	0.015	0.012	0.015
rmsd bond angles (°)	1.87	1.68	1.75
Average B-factor ($Å^2$)	28.8	36.8	41.6
Ramachandran-plot[e]			
Favored (%)	97.2	96.6	97.3
Allowed (%)	2.8	3.4	2.7
Outliers (%)	0.0	0.0	0.0
Maximum likelihood based estimated coordinate error (Å)	0.06	0.14	0.10

[a] Values in parenthesis refer to the highest resolution shell

[b] $R_{merge} = \sum_{hkl}\sum_{i}\left|I_i - \langle I \rangle\right| \Big/ \sum_{hkl}\sum_{i} I_i$

[c] $R_{pim} = \sum_{hkl}\left[1/(N-1)\right]^{1/2}\sum_{i}\left|I_i - \langle I \rangle\right| \Big/ \sum_{hkl}\sum_{i} I_i$ (173)

[d] $R_{cryst} = \sum_{hkl}\left|F_{obs} - F_{calc}\right| \Big/ \sum_{hkl} F_{obs}$

[e] According to Molprobity (172)

Table S 5-4. Nucleotide primers for site-directed mutagenesis

Name	Primer sequence
D249A forward	5' CAGGTGAAAATATTCATGTAGCGAGCGGATTCCACGCAATTAA 3'
D249A reverse	5' TTAATTGCGTGGAATCCGCTCGCTACATGAATATTTTCACCTG 3'
S189A forward	5' CGCGTTAATGCAATTGCGGCTAGTCCAATCCG 3'
S189A reverse	5' CGGATTGGACTAGCCGCAATTGCATTAACGCG 3'
Y147F forward	5' GCATTGTTGCAACAACATTTTTAGGTGGCGAATTCGC 3'
Y147F reverse	5' GCGAATTCGCCACCTAAAAATGTTGTTGCAACAATGC 3'

5.8.2 Supplemental Figures

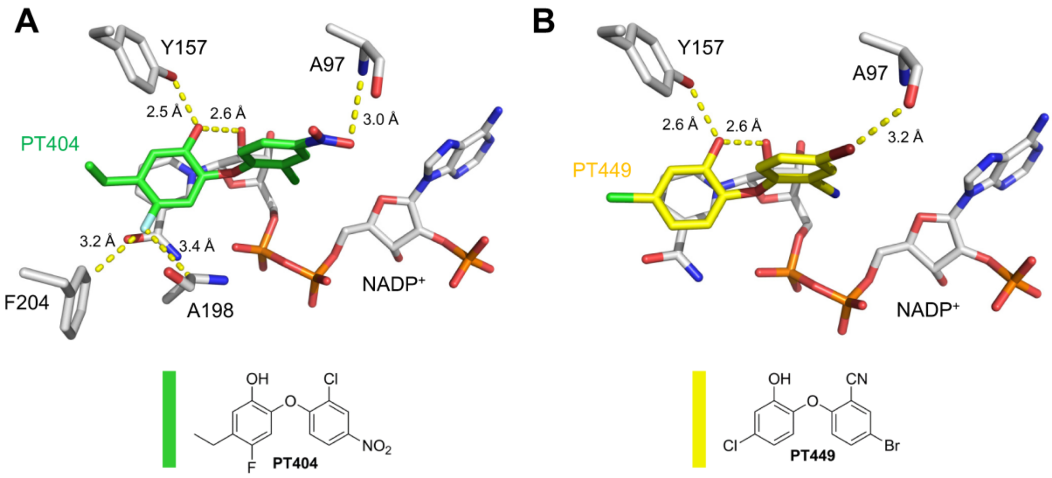

Figure S 5-1. Inhibitor binding modes. **(A)** SaFabI inhibition by PT404 (green). Direct interactions are highlighted by yellow dashed lines. The PT404 A-ring hydroxyl group is hydrogen bonded to the Tyr157 hydroxyl group and the 2'-OH of the nicotinamide ribose at distances of 2.50 ± 0.05 Å and 2.57 ± 0.03 Å, respectively. The 4'-nitro group interacts with the amide nitrogen of Ala97 at a distance of 2.99 ± 0.10 Å. In addition, the 4-F substituent forms weak hydrogen bonds with one of the two Phe204 C_ε hydrogens as well as with the Ala198 C_α hydrogen (distances of 3.20 ± 0.12 Å and 3.38 ± 0.05 Å, respectively; for details about such interactions see also reference (152)). **(B)** SaFabI inhibition by PT449 (yellow). As for PT404, the OH group of PT449 is bound to Tyr157 and the 2'-OH of the $NADP^+$ nicotinamide ribose at distances of 2.59 ± 0.14 Å and 2.64 ± 0.10 Å, respectively. Furthermore, a linear halogen bond is formed between the Ala97 carbonyl oxygen and the 4'-Br group of PT449 at a distance of 3.16 ± 0.11 Å (152).

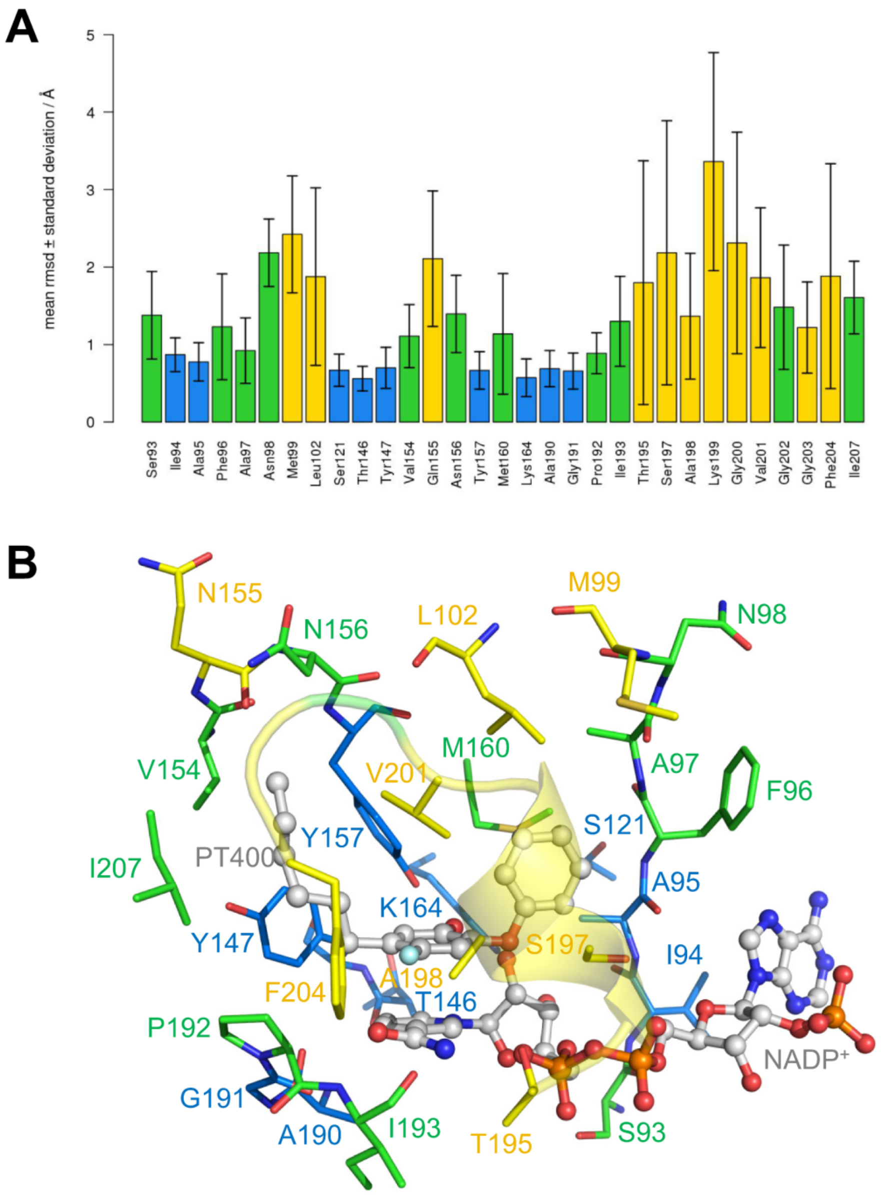

Figure S 5-2. SaFabI binding pocket mobility. (A) Per-residue rmsd values for the binding-site residues. The calculation of the rmsd values was based on an all-atom fit of the 31 binding-site residues for the saFabI$_4$-NADP$^+$-PT400 MD snapshots. Conformational variability is indicated by the rmsd values, whereas the flexibility of the individual residues is represented by the corresponding standard deviations. This graph was generated using R. **(B)** Binding-site residue classification by flexibility. This classification is based on per-residue root mean square fluctuations (rmsf). Rigid, medium flexible and the most flexible residues are depicted as blue, green and yellow sticks, respectively (the same color code was also used for panel A). To enable a classification in three similarly sized groups, 0.6 and 1.0 Å rmsf-cutoffs were chosen. The SBL is shown in transparent cartoon representation and the cofactor and inhibitor as ball-and-stick model.

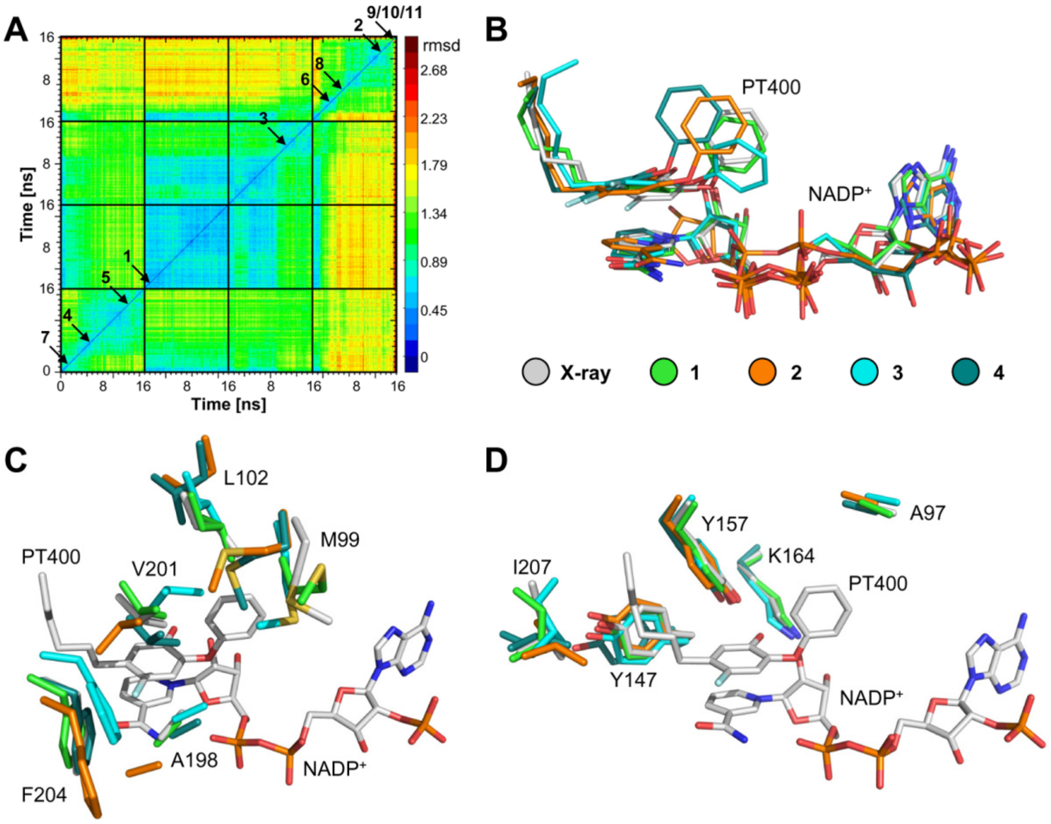

Figure S 5-3. Hierarchical clustering analysis. (A) Combined 2D-rmsd plot for the C$_\alpha$-atoms of the 31 binding-site residues of the four monomers within the saFabI$_4$-NADP$^+$-PT400 MD simulation. The binding pockets of monomers 1 to 4 are represented by the black-framed squares. Calculation of rmsd values was performed in 100 ps intervals. Black arrows indicate the chosen cluster representatives (numbered consecutively according to cluster size; cluster 1 accounts for 44% of all snapshots, 2 = 13.7%, 3 = 11.1%, 4 = 9.7%, 5 = 9.6%, 6 = 4.1%, 7 = 3.5%, 8 = 2.7%, 9 = 0.6%, 10 = 0.5%, 11 = 0.4%). **(B)** Representative inhibitor and cofactor geometries. The binding modes of PT400 and NADP$^+$ are shown for clusters 1-4 (colored according to the legend). The ligands of the saFabI-NADP$^+$-PT400 crystal structure are shown as a reference in gray. **(C)** Conformations of selected flexible binding-site residues for the first four cluster representatives. **(D)** Conformations of selected rigid binding-site residues for the first four cluster representatives.

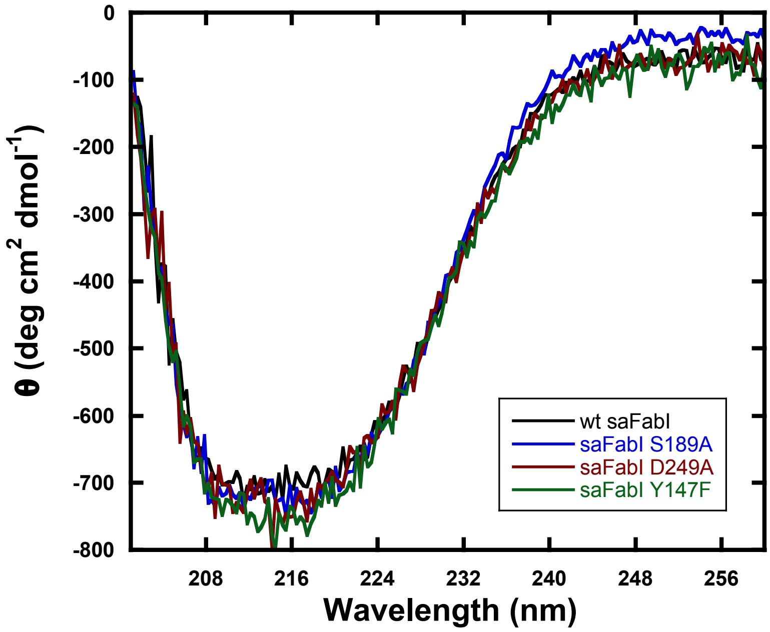

Figure S 5-4. CD spectra showing a similar folding pattern for the water channel mutants compared to the wild-type saFabI enzyme.

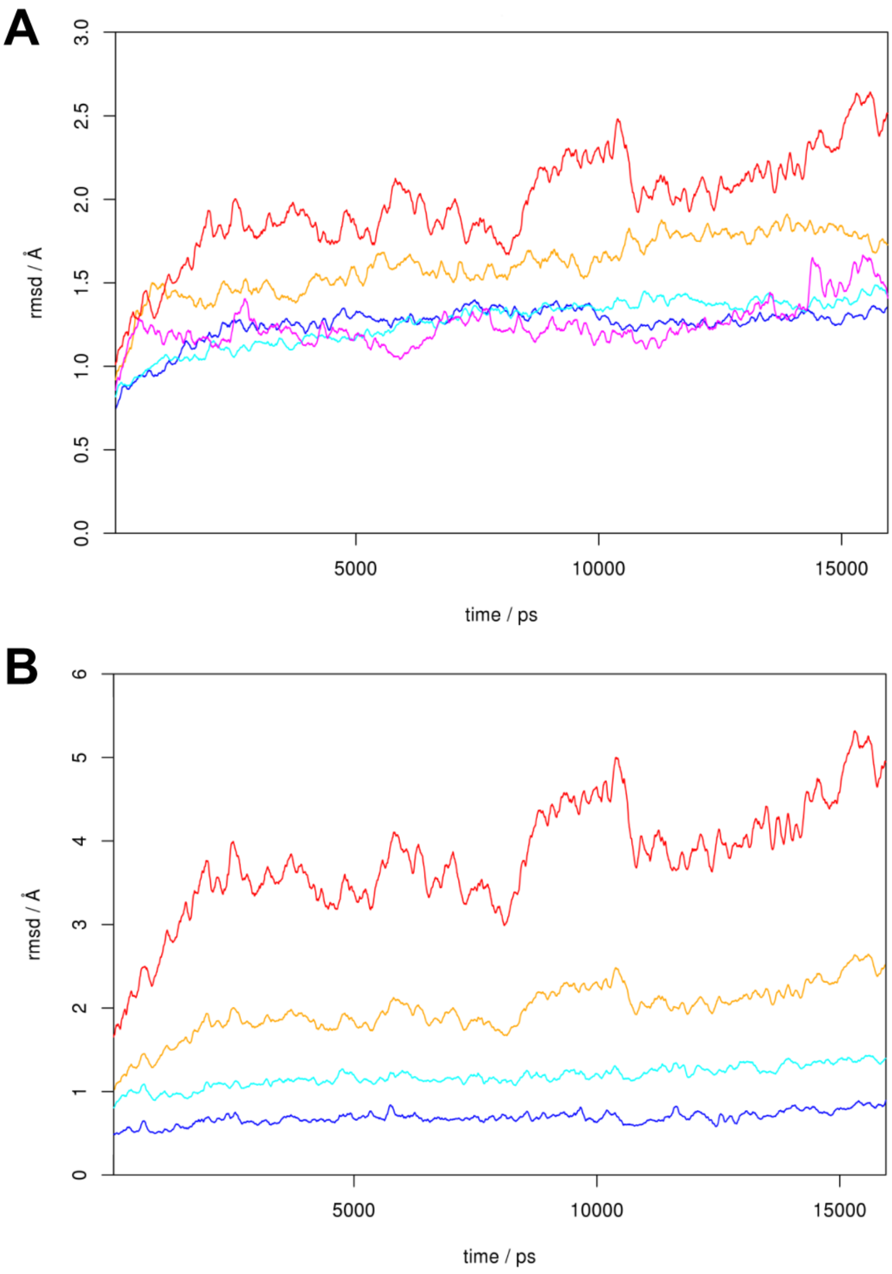

Figure S 5-5. Trajectory rmsd values. (A) Rmsd values for the five wild-type MD simulations (saFabI$_4$-NADP$^+$-PT400, blue; saFabI$_1$-NADP$^+$-PT400, magenta; saFabI$_4$-NADP$^+$, cyan; saFabI$_4$, orange; saFabI$_2$, red). Calculations were performed using all protein C$_\alpha$-atoms. **(B)** Rmsd values for selected atoms of the saFabI$_2$ simulation. Calculations were performed using all protein C$_\alpha$-atoms (orange, 254 atoms per monomer), all C$_\alpha$-atoms excluding the most flexible residues (see below) (cyan, 204 atoms per monomer) or the C$_\alpha$-atoms of β-strand residues only (blue, 37 atoms per monomer). In addition, rmsd values for the most flexible saFabI residues (3-7, 40-47, 99-113, 152-156 and 194-210) were calculated based on a fitting procedure using all C$_\alpha$-atoms excluding those residues (red, 50 atoms per monomer), which allows an evaluation of the conformational variability of these protein regions. Both plots were generated using R and averaging over 100 ps (260).

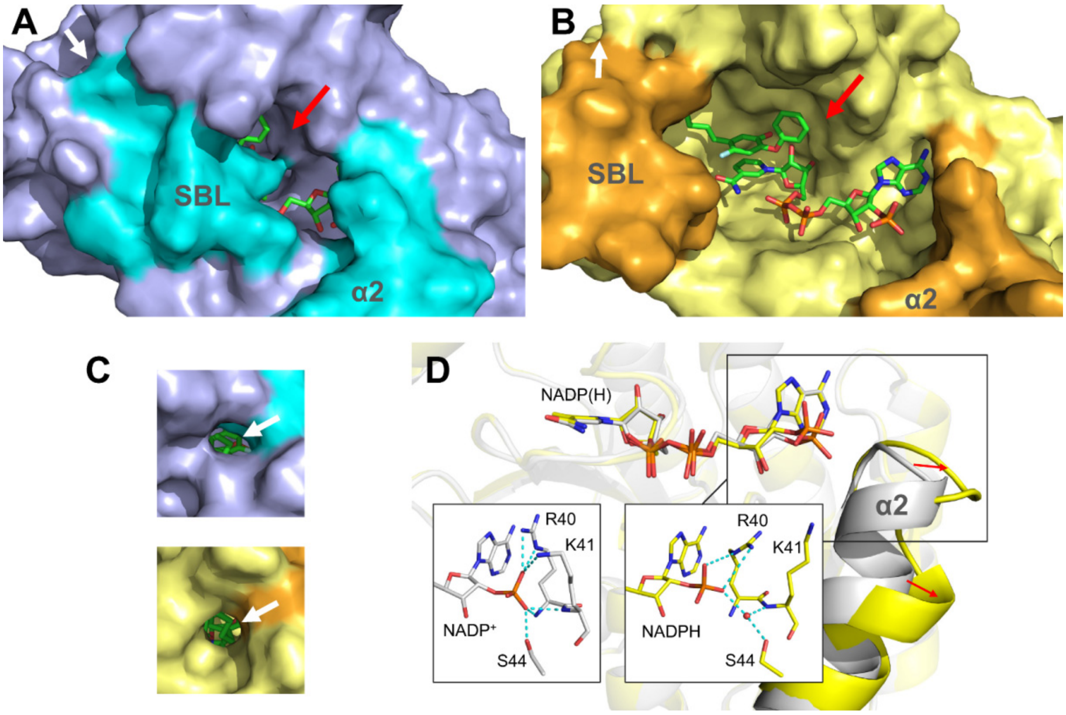

Figure S 5-6. Cofactor and substrate binding process. (A) Closed state of the major portal. Red and white arrows indicate the location of the major and minor portal, respectively. The saFabI-NADP$^+$-PT400 crystal structure is shown in blue surface representation with the SBL and helix α2 indicated in cyan (including hydrogens added using tleap). PT400 and NADP$^+$ are shown as green sticks. **(B)** Opened state of the major portal. The structural representative of a hierarchical clustering analysis of the saFabI$_2$ MD trajectory with the most opened major portal (t = 14.7 ns, same monomer as in Figure 5-5C-D and Movie S 5-1) is shown in yellow surface representation with the SBL and helix α2 highlighted in orange. The same scale and view was used as for panel A. PT400 and NADP$^+$ are shown as reference in green. **(C)** Minor portal opening. The minor portals of the structures shown also in panels A and B are depicted using the same color code and scale. **(D)** Conformational variability of the saFabI helix α2. The conformations of helix α2 as well as the interactions with the NADP(H) 2'-phosphate (19) differ between the saFabI-NADP$^+$-PT400 (gray) and saFabI-NADPH-CG400549 (yellow; see also chapter 4) structures. Red arrows indicate the shift of helix α2 in the CG400549-bound structure.

5.8.3 Supplemental Movies

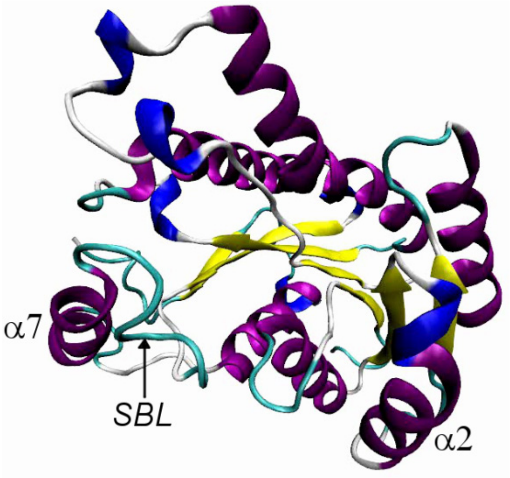

Movie S 5-1. Essential dynamics of saFabI (calculated with ptraj and IED (248)). The dynamics along the principal mode of the 16 ns saFabI$_2$ MD trajectory are shown for one monomer exemplarily (colored according to its secondary structure). The view is similar to that depicted in Figure 5-5C. Please note the widening of the central binding cavity located on top of the β-sheet (yellow) via the anti-correlated movements of the helix α2 and the SBL (labeled in the still frame during the first four seconds of the movie). This movie was produced using VMD and has been smoothed (trajectory smoothing window size = 10 frames).

5.8.4 Supplemental Results and Discussion

5.8.4.1 Inhibition of SaFabI

During the development of the drug candidate MUT056399 by Mutabilis, MUT37307 was found to be one of the most promising FabI inhibitors amongst a large series of diphenyl ether inhibitors (102). Both compounds contain more hydrophilic B-rings leading to lowered clogD values and, thus, to the decoupling of the FabI activity from a non-specific mode of action. We solved the structure of saFabI in complex with NADP$^+$ and MUT37307 revealing the binding mode of this promising compound. Interestingly, the fluoropyridine B-ring does not engage in direct interactions with the protein but is well tolerated at this position (Figure 5-2C, Table 5-1). MUT056399, MUT37307, PT400 and PT404 share the same phenolic A-ring comprising a 4-fluoro and 5-ethyl group. The former substituent was suggested to act as a metabolic regulator (119) and did not affect the affinity significantly (Table 5-1 - PT01 and PT04 compared to PT411 and PT400, respectively). Since fluorine has only a slightly increased atomic radius compared to hydrogen, it is well tolerated in a small side pocket created by Phe204 and Ala198 without affecting the closed state of the substrate binding loop (Figure S 5-1A). The PT404 fluoro-substituent contacts one of the Phe204 C_ε-H atoms at a C-F distance of 3.20 ± 0.12 Å. Moreover, a direct weak hydrogen bonding interaction of the F with the Cα-H of Ala198 was observed at a C-F distance of 3.38 ± 0.05 Å.

In order to strengthen the linear halogen bond observed between the 4'-Cl substituent of the antimicrobial agent triclosan and the Ala97 carbonyl oxygen (19,152), we introduced a 4'-Br substituent combined with the potent 2'-CN group leading to PT449. However, compared to the corresponding analogue lacking the bromine substituent (PT447) (188), PT449 displayed a 3-fold increased K_i value although a halogen bond was observed with preferable geometry (152) for saFabI (d = 3.16 ± 0.11 Å, Figure S 5-1B) and ecFabI (d = 3.26 Å). Importantly, the reduced affinity towards saFabI arises purely from a slowed association (k_{on}) while the dissociation kinetics are unchanged (k_{off}). The transition state barrier to association and, thus, K_i might be increased due to the bulky bromine substituent, which needs to be placed into the saFabI binding crevice (Figure S 5-1B).

5.8.4.2 Molecular Dynamics Simulations

We initiated eight saFabI MD simulations for mainly three reasons: (1) To learn more about the dynamics involved in the inhibition of saFabI (saFabI$_4$-NADP$^+$-PT400 and saFabI$_1$-NADP$^+$-PT400 simulations), (2) to explore the process of cofactor and substrate binding as well as product release (saFabI$_4$-NADP$^+$, saFabI$_4$ and saFabI$_2$ simulations), and (3) to investigate the catalytic mechanism of this important drug target (all wild-type and mutant simulations). The MD trajectories of saFabI excluding cofactor and PT400 displayed larger conformational variability and mobility as highlighted by the simulation-averaged rmsd values and standard deviations, respectively (Table S 5-2). In particular the apo-simulations were characterized by a rising rmsd over time indicating a directional movement as described in the main text (Figure 5-5 and Figure S 5-5A). However, when omitting the most flexible regions participating in these motions during the calculation of the rmsd values, this effect was diminished (Table S 5-2, Figure S 5-5B).

To gain insights into the motions characterizing the binding-site, we analyzed the dynamic behavior of the corresponding amino acids. Although we only explicitly discuss the dynamic profile of the binding-site residues for the saFabI$_4$-NADP$^+$-PT400 simulation, similar observations were made for all trajectories. As expected, the SBL residues (amino acids 194-204) sealing the binding-site displayed the largest conformational diversity and mobility as revealed by an analysis of the per-residue rms deviations and fluctuations (Figure S 5-2). Interestingly, Leu102, which was found to be present in an alternative, more opened state in our diphenyl ether-bound saFabI structures, also showed enhanced fluctuations. Moreover, Met99 is characterized by an increased conformational variability and mobility. This residue was shown to be involved in conferring selectivity to two clinical trial inhibitors towards the saFabI homologue (chapter 4) and, thus, its flexibility might change upon binding of such compounds contacting Ala97. Importantly, most residues surrounding the reactive site of the cofactor including the catalytic triad residues (amino acids 190-193, 146-147, 157 and 164) were found to be rather rigid facilitating the precise relative orientation of substrate and cofactor and, thus, enabling the proceeding of the catalyzed reaction from a stereoelectronic perspective. In addition, the amino acid stretch including residues 93-97 displays relatively low rmsd values and standard deviations and might, thus, act as a platform for the binding of the PPant moiety of the substrate.

These trends were confirmed by a hierarchical clustering analysis based on the 2D-rmsd values for all four subunits of the saFabI$_4$-NADP$^+$-PT400 simulation (Figure S 5-3A). Whereas monomers 1-3 displayed relatively homogenous binding-site snapshots, monomer 4 was characterized by increased heterogeneity and, thus, accounted for over 50% of all cluster representatives. A detailed analysis of the dynamics sampled by this monomer revealed that the anti-correlated opening of the binding-site (Figure 5-5C) partially occurs for this subunit (data not shown). The MD trajectory for this monomer might, thus, represent the start of an inhibitor dissociation process. Interestingly, the electron density of the starting crystal structure was less well defined for this monomer compared to all other subunits. Hence, subtle structural perturbations might have led to the relatively quick dissociation in the light of the high experimental residence time of PT400. Figure S 5-3 shows selected residues of the structural representatives for the four largest clusters of the hierarchical clustering analysis (numbered consecutively from 1 to 4) compared to the crystal structure. The enhanced conformational diversity of the PT400 B-ring described in the main text is clearly visible in Figure S 5-3B. Moreover, the cluster representatives 2 and 4 reveal that Leu102 can indeed be present in a more opened state (Figure S 5-3C). In contrast, the enhanced Met99 mobility is particularly due to extensive side chain motions. The catalytic triad residues, however, were found to be in a relatively conserved conformation for all clusters. In summary, the sampled conformations of the binding-site residues and in particular the cluster representatives may serve as an ideal starting point for the development of new saFabI inhibitors since induced-fit effects are very dominant for saFabI (19,188) (chapter 4).

5.8.4.3 Cofactor Binding Process

Given the limited size of both portals towards the closed saFabI binding pocket (Figure S 5-6A and Figure S 5-6C, top), it is unclear how the much larger cofactor may actually enter this crevice. The anti-correlated opening of the SBL and helix α2 described in the main text may not only be important for substrate recognition but could additionally facilitate binding of NADPH (Figure 5-5C, Movie S 5-1). Indeed, with respect to the closed character of the starting crystal structure that likely resembles a state close to the TS sampled during the hydride transfer of the reaction, the most opened structural representative of a hierarchical clustering analysis of the saFabI_2 MD snapshots displays a vastly enlarged major portal opening (Figure S 5-6B), whereas the minor portal remains in its relatively closed state (Figure S 5-6C, bottom). Our structures of saFabI in complex with the more substrate-like 2-pyridone inhibitors (chapter 4) indeed are characterized by a more opened conformation of helix α2 compared to the diphenyl ether-bound structures (Figure S 5-6D). Interestingly, the structural variation of helix α2 entails a change in the recognition pattern of the additional NADPH 2'-phosphate by the RKXXS-motif located at the N-terminus of this helix. The specificity for NADPH compared to the commonly used reducing agent NADH is unique for saFabI and closely related homologues (19). An important question, thus, is whether the flexibility of helix α2 may contribute to NADPH specificity and cofactor binding. We assumed that the nature of the cofactor would not affect binding of the diphenyl ether. This was the basis for directly measuring residence times using the saFabI R40Q/K41N/S44L mutant (188), which overlapped well with values measured via progress curve analysis in the wild-type enzyme. Moreover, the dissociation rate of PT52 (k_{off} = 0.03 min^{-1}) from the E (wild-type)-NAD^+-PT52 ternary complex is very similar to that from E (wild-type)-NADP^+-PT52. Interestingly, the onset and degree of inhibition both increased in the presence of NADH/NAD^+ relative to NADPH/NADP^+. This is most likely attributed to a 2-fold slower rate of dissociation of NAD^+ from the wild-type enzyme compared to NADP^+. Consistently, the dissociation rate of NAD^+ from *E. coli* FabI is estimated to be 4-fold slower than the dissociation of NADP^+ from saFabI (188) (chapter 4). Thus, the higher binding affinity of NADPH/NADP^+ to saFabI is mostly the result of a faster rate of association. The observed mobility of helix α2 explains why the selectivity for NADPH is based on an enhanced association rate. The additional negative charges of the NADPH 2'-phosphate may be attracted by the more solvent-exposed RKXXS-motif taking advantage of the long-range character of electrostatic interactions (Figure S 5-6D). Indeed, this phenomenon has been described as electrostatic steering and can particularly lead to an increase in on-rates (44,261). However, bound NADP^+ may be more quickly released from the wild-type saFabI enzyme compared to NAD^+ due to the transient character of these interactions (Figure S 5-6D) and since charge-assisted hydrogen bonds are not as favorable when exposed to bulk solvent (152).

5.8.4.4 Substrate Recognition

An important question concerning the binding of the substrate is whether FabI recognizes its correct interaction partner based on slightly varying ACP conformations for different FAS-II intermediates or just after injection of each substrate (76). During our kinetic experiments, we found that the octenoyl-CoA substrate and its saturated octanoyl-CoA product bind with similar affinity to the enzyme (estimated $K_{d,\ \text{octenoyl-CoA}}$ = 100 µM (188), $K_{i,\ \text{octanoyl-CoA}}$ = 96 ± 21 µM). The inability of saFabI to differentiate these two CoA-species indicates that substrate recognition has to occur at the ACP level prior to substrate delivery, which is much more efficient than scanning all substrates inside the binding pocket.

6 Acyl Channel Opening Reveals How the Condensing Enzyme KasA from *Mycobacterium tuberculosis* Recognizes Mycolic Acid Precursors

This chapter is based on the following publication:

Schiebel, J., Kapilashrami, K., Fekete, A., Bommineni, G. R., Schaefer, C. M., Mueller, M. J., Tonge, P. J., and Kisker, C. (in preparation[‡]) Acyl Channel Opening Reveals How the Condensing Enzyme KasA from *Mycobacterium tuberculosis* Recognizes Mycolic Acid Precursors.

Author contributions with respect to data collection:

Schiebel, J.:	X-ray crystallography, mass spectrometric analysis
Kapilashrami, K.:	Inhibition kinetics
Fekete, A.:	Mass spectrometric analysis (experimental details not shown)
Bommineni, G. R.:	Synthesis of thiolactomycin analogs
Schaefer, C. M.:	Protein expression

[‡] The printed version might be subject to some changes prior to submission

Acyl Channel Opening Reveals How the Condensing Enzyme KasA from *Mycobacterium tuberculosis* Recognizes Mycolic Acid Precursors[*]

Johannes Schiebel[1,2], Kanishk Kapilashrami[3], Agnes Fekete[4], Gopal R. Bommineni[3], Christin M. Schaefer[1], Martin J. Mueller[4], Peter J. Tonge[3], Caroline Kisker[1]

From the [1]Rudolf Virchow Center for Experimental Biomedicine, Institute for Structural Biology, University of Wuerzburg, D-97080 Wuerzburg, Germany

[2]Institute of Pharmacy and Food Chemistry, University of Wuerzburg, Am Hubland, D-97074 Wuerzburg, Germany

[3]Institute for Chemical Biology & Drug Discovery, Department of Chemistry, Stony Brook University, Stony Brook, NY 11794-3400, USA

[4]Julius-von-Sachs Institute of Biosciences, Biocenter, Department of Pharmaceutical Biology, University of Wuerzburg, D-97082 Wuerzburg, Germany

To whom correspondence should be addressed: Caroline Kisker, Rudolf Virchow Center for Experimental Biomedicine, Institute for Structural Biology, University of Wuerzburg, D-97080 Wuerzburg, Germany, Tel.: +49 931 3180381, Fax: +49 931 3187320, E-mail: caroline.kisker@virchow.uni-wuerzburg.de

6.1 Keywords

induced-fit substrate recognition**;** enzyme dynamics**;** β-ketoacyl-ACP synthase; KasA; KAS enzyme; condensing enzyme; phospholipid; type 2 fatty acid biosynthesis; mycolic acid synthesis; *Mycobacterium tuberculosis*; thiolactomycin

6.2 Capsule

Background: Although induced-fit binding is central to molecular recognition, in most cases the structural basis for this process remains to be elucidated.
Results: We characterized the dynamics of substrate recognition for the important drug target *M. tuberculosis* KasA.
Conclusion: KasA binds extra-long fatty acid substrates via the induced-fit concerted opening of a hydrophobic cavity.
Significance: The improved understanding of induced-fit effects is crucial for inhibitor design.

6.3 Summary

The survival of *Mycobacterium tuberculosis* depends critically on C_{60}-C_{90} mycolic acids - one of nature's longest fatty acids. However, despite considerable effort, little is known about how enzymes involved in mycolic acid biosynthesis recognize and bind their hydrophobic fatty acyl substrates. The condensing enzyme KasA is pivotal for the synthesis of very long (C_{38-42}) fatty acids, that are the precursors of mycolic acids. To probe the mechanism of substrate and inhibitor recognition by KasA, we determined the structure of this protein in complex with a long chain phospholipid, and with several thiolactomycin derivatives that were designed as substrate analogs. Our structures provide consecutive snapshots along the reaction coordinate for the enzyme-catalyzed reaction, and support an induced-fit mechanism in which a wide cavity is established through the concerted opening of three gatekeeping residues and several α-helices. The stepwise characterization of the binding process provides mechanistic insight into the induced-fit molecular recognition in this system and serves as an excellent foundation for the development of high affinity KasA inhibitors.

6.4 Introduction

Mycobacterium tuberculosis is dependent on mycolic acids, long-chain C_{60-90} α-alkyl-β-hydroxy fatty acids that are essential components of the unusually waxy mycobacterial cell wall, which confers pathogenicity, intrinsic antibiotic resistance and the ability to persist within the human macrophage (23). The biosynthesis of mycolic acids requires the presence of two distinct fatty acid synthesis pathways, the mammalian-like type I (FAS-I)[5] and the bacterial type II (FAS-II) systems (Figure 6-1). The C_{16-18} acyl-CoA primers produced by the FAS-I system are elongated by the FAS-II pathway to C_{50-56} mycolic acid precursors (meromycolic acids) (11). In contrast to the FAS-I system, which consists of one large multifunctional dimer, the FAS-II system is constituted by monofunctional enzymes, which can be targeted selectively (22). After its activation within the mycobacterial cell, the first-line anti-tuberculosis drug isoniazid inhibits the enoyl-ACP reductase InhA, thereby validating the FAS-II pathway as a promising target for the development of novel antibiotics (Figure 6-1) (69).

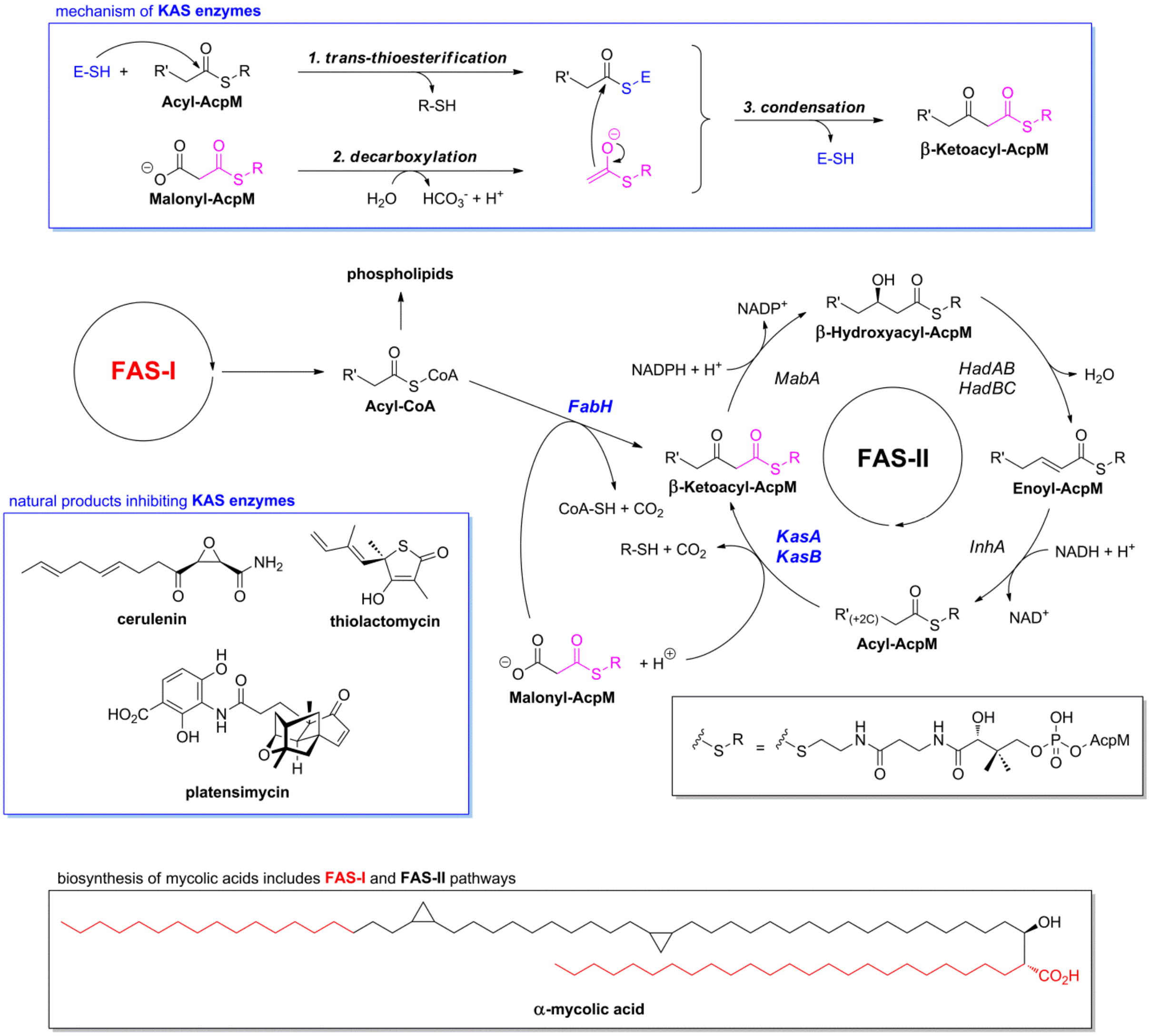
mechanism of KAS enzymes
E-SH +
Acyl-AcpM
1. trans-thioesterification
R-SH
Malonyl-AcpM
2. decarboxylation
H2O
HCO3- + H+
3. condensation
E-SH
β-Ketoacyl-AcpM
phospholipids
FAS-I
Acyl-CoA
FabH
CoA-SH + CO2
NADP+
NADPH + H+
MabA
β-Hydroxyacyl-AcpM
HadAB
HadBC
H2O
FAS-II
β-Ketoacyl-AcpM
Enoyl-AcpM
KasA
KasB
R-SH + CO2
InhA
NADH + H+
NAD+
Acyl-AcpM
Malonyl-AcpM
+ H+
AcpM
natural products inhibiting KAS enzymes
cerulenin
thiolactomycin
platensimycin
biosynthesis of mycolic acids includes FAS-I and FAS-II pathways
α-mycolic acid

Figure 6-1. Mycolic Acid Biosynthesis in *Mycobacterium tuberculosis*. FAS-I, which is also responsible for phospholipid biogenesis, generates C_{16-18} and C_{24-26} acyl-CoA substrates *de novo* (11). Subsequently, FAS-II elongates the C_{16-18} acyl-CoA primers to the very long C_{50-56} meromycolate chains (upper part of the depicted mycolic acid; the terminal portion synthesized via FAS-I is highlighted in red), which are attached to the shorter C_{24-26} aliphatic α-branch originating from FAS-I (lower part of the mycolic acid) to yield the mature mycolic acids (23). α-Mycolic acid is the most frequent mycolic acid in *M. tuberculosis* (11). Three β-ketoacyl-ACP synthases are involved in the FAS-II system, namely FabH, KasA and KasB (highlighted in blue). They are inhibited by the natural products cerulenin, thiolactomycin and platensimycin (shown in the lower blue box) and catalyze a Claisen condensation reaction between acyl-AcpM (acyl-CoA for FabH) and malonyl-AcpM via the 3-step mechanism depicted in the upper box (13,59). The reduction of the generated β-keto group to a methylene group is achieved via the subsequent actions of MabA, HadAB/BC and InhA (8,68).

Like InhA, the KasA enzyme is also essential for mycobacterial survival and is thus an attractive drug target (135). This homo-dimeric β-ketoacyl-ACP synthase (KAS) catalyzes a Claisen condensation reaction between acyl-AcpM and malonyl-AcpM in each elongation cycle of the FAS-II pathway, during which the substrates are attached to Ser41 of the small acidic acyl carrier protein (ACP; AcpM in *M. tuberculosis*) via a phosphopantetheine linker (Figure 6-1) (75). The KasA catalytic triad consisting of Cys171, His311 and His345 facilitates the formation of the new carbon-carbon bond via a 3-step mechanism (Figure 6-1) (13,59,60,140). During this process, the active site cysteine is acylated and subsequently attacked by the decarboxylated malonyl-AcpM to yield a β-ketoacyl-AcpM which is extended by two carbon atoms. The acylated enzyme intermediate is mimicked by a C171Q KasA variant in which Gln171 forms hydrogen bonds with the KasA oxyanion hole (17,131,262). This acyl-enzyme mimic is particularly important for future drug design as the natural products thiolactomycin (TLM) and platensimycin inhibit KAS enzymes by binding preferentially to the acyl-enzyme (Figure 6-1) (59,131,132). Interestingly, the antibiotic TLM, which has been shown to possess efficacy in *Serratia marcescens* and *Klebsiella pneumoniae* murine models of infection (137), inhibits both classes of condensing enzymes, the KAS I/II enzymes (FabB/F in *Escherichia coli*, KasA/B in *M. tuberculosis*) that participate in the elongation cycle and the FAS-II initiating KAS III enzymes (FabH) (24,58,136). TLM and similar antibacterials, which interact with multiple targets, are ideal lead compounds because single-target mutations will not lead to full resistance (4).

For the development of improved TLM-based drug candidates it is critical to understand the substrate recognition process, catalytic mechanism and inhibition of KAS enzymes. Clearly, a certain amount of flexibility is an important requirement for FAS-II enzymes in order to bind and process their long chain hydrophobic substrates. This is supported by the observation that the FAS-II enoyl-ACP reductases are highly flexible proteins prior to substrate binding (19,207,263). In the present work, we probe the KasA ligand binding mechanism using TLM-analogs substituted at the 3-position which were designed to mimic the two KasA substrates acyl-AcpM and malonyl-AcpM. We reveal a unique process of substrate binding including extensive structural changes which can be triggered by one of our most potent inhibitors (16), laying the foundation for the development of new anti-mycobacterial agents.

6.5 Experimental Procedures

6.5.1 Expression and Purification

Following a previously described procedure, the proteins KasA and C171Q KasA were expressed in *Mycobacterium smegmatis* mc^{2}155 and subsequently purified using affinity, anion exchange and size-exclusion chromatography (17,59).

6.5.2 Crystallization and Data Collection

Crystallizations were performed using the vapor diffusion method. Prior to crystallization, KasA (8.6 mg/ml) was incubated for 2 hours with a 200-fold molar excess of TLM5 (dissolved in DMSO). Crystals grew in 10% PEG 3350, 0.2 M K/Na-tartrate and 1.5 mM TCEP. Two separate crystals were exposed to a cryoprotectant solution that additionally contained 30% ethylene glycol and 40 mM TLM5 and soaked for 1 (KasA - TLM5 - I) and 5 min (KasA - TLM5 - II), respectively. Using a MarMosaic 225 detector, diffraction data were collected to 2.4 and 2.7 Å at the ESRF beamline ID 23-2 (λ = 0.873 Å, T = 100 K) and BESSY II beamline 14.1 (λ = 0.918 Å, T = 100 K), respectively.

Similarly, C171Q KasA was incubated with a 20-fold molar excess of TLM, TLM18 (dissolved in DMSO), TLM3, TLM4, TLM5 and TLM6 (dissolved in isopropanol). Crystals of space group $P2_12_12_1$ grew under varying conditions (Table S 6-1), were briefly transferred into a cryoprotectant solution (Table S 6-1) and cryocooled in liquid nitrogen. Diffraction data were collected to resolutions between 1.5 Å and 2.0 Å at MX beamline 14.1 (BESSY II) using a MarMosaic 225 detector (λ = 0.918 Å, T = 100 K). Data collection statistics are given in Table S 6-1.

6.5.3 Structure Determination

Data were integrated with XDS (KasA - TLM5 - I) (183), XDSAPP (C171Q KasA - TLM) (215) or Imosflm (178), respectively. Scaling was performed using Scala (179). For the Phaser molecular replacement (180), we used our previously determined TLM-bound KasA and C171Q KasA structures (lacking all ligands) as search models (PDB-entries 2WGE and 2WGG) (17). Alternate cycles of model building and maximum likelihood refinement (including preceding TLS-refinement (200)) were performed with Coot (182) and Refmac 5 (181). Based on the electron density maps, inhibitor binding sites could be identified unambiguously. As reported in our preliminary study, inhibitor densities were lower but sufficient for KasA compared to C171Q KasA (17). Hence, we used a 200-fold molar inhibitor excess during the co-crystallization of the KasA - TLM5 complex. In addition, soaking (for 1 and 5 min; KasA - TLM5 - I and II structures, respectively) was performed to enhance inhibitor occupancy. As expected, the TLM5 electron density improved with longer soaking times whereas the resolution dropped from 2.4 to 2.7 Å. Refinement statistics are given in Table S 6-1.

To avoid model bias, omit maps were calculated prior to inclusion of the respective ligand. Distances and angles are given as mean values for both subunits and as mean values ± standard deviations if multiple structures were analyzed. All structural figures were prepared with PyMol (174).

6.5.4 Lipidomics

Two different and equally successful protocols were used to extract bound ligands from the protein samples. Ten µl KasA (100 µM), C171Q KasA (150 µM) or buffer reference samples were incubated for 30 min at 20 °C with 10 µl of a papain solution (1 mg/ml in 50 mM PIPES pH 7.0, 300 mM NaCl and 10 mM DTT). Alternatively, the samples were treated for 5 min at 55 °C with 10 µl of a 10 M urea solution. After the addition of 30 µl isopropanol, 10 min sonication and centrifugation, the supernatants were analyzed by LC-MS.

To analyze the phospholipid content of the KasA expression host, liquid cultures of *M. smegmatis* mc^{2}155 with induced C171Q KasA expression were prepared as described previously (17). Thirty mg of wet cell pellet were treated with 1 ml Folch solution (chloroform : methanol = 2 : 1) and subjected to 10 ultrasonic pulses. After centrifugation and separation from the cell debris, the supernatant was evaporated and the pellet dissolved in methanol and analyzed by LC-MS. Further details are provided in the Supplemental Experimental Procedures.

6.5.5 Synthesis of 3-Substituted TLM-Derivatives

Enantiomerically pure 5(*R*)-TLM and TLM analogs were synthesized using a reported protocol (16) and will be reported in a separate publication.

6.5.6 Inhibition Kinetics

Binding of TLM18 to wild-type and mutant KasA was quantified by monitoring changes in the intrinsic tryptophan fluorescence of the enzyme using 280 nm excitation and 337 nm emission as described previously (16). Briefly, the data were collected using a Quanta Master fluorimeter (Photon Technology International). Inhibitors were dissolved in DMSO and titrated into 1 µM solutions of KasA and C171Q KasA in buffer (50 mM Tris-HCl, 150 mM NaCl, 1 mM dithiothreitol, pH 8.5).

6.6 Results

6.6.1 KasA Inhibition by 3-Substituted TLM-Derivatives

Thiolactomycin (TLM) is a natural product that binds preferentially to the KasA acyl-enzyme with low micromolar affinity (59). To improve the affinity of TLM for KasA, elucidate the validity of KasA as a drug target and to develop chemical tools to investigate the substrate binding and catalytic mechanism of KasA, we designed and synthesized two classes of 3-substituted TLM-derivatives that display structural features reminiscent of either the acyl- or the malonyl-AcpM substrates for the enzyme (16). The linear, hydrophobic 3-substituents of TLM3, TLM4 and TLM18 were attached to the thiolactone scaffold to mimic the long acyl chain of acyl-AcpM (Figure 6-2A, upper box). In contrast, the 1,3-dioxo group of malonyl-AcpM is more closely reproduced by TLM5 and TLM6 carrying 3-acetyl and 3-trifluoroacetyl moieties (Figure 6-2A, lower box). Therefore, to facilitate our mechanistic studies, we used the previously recognized malonyl-mimicking features of TLM and optimized the interactions by incorporating an additional exocyclic carbonyl group (Figure 6-2A, lower box) (132,138).

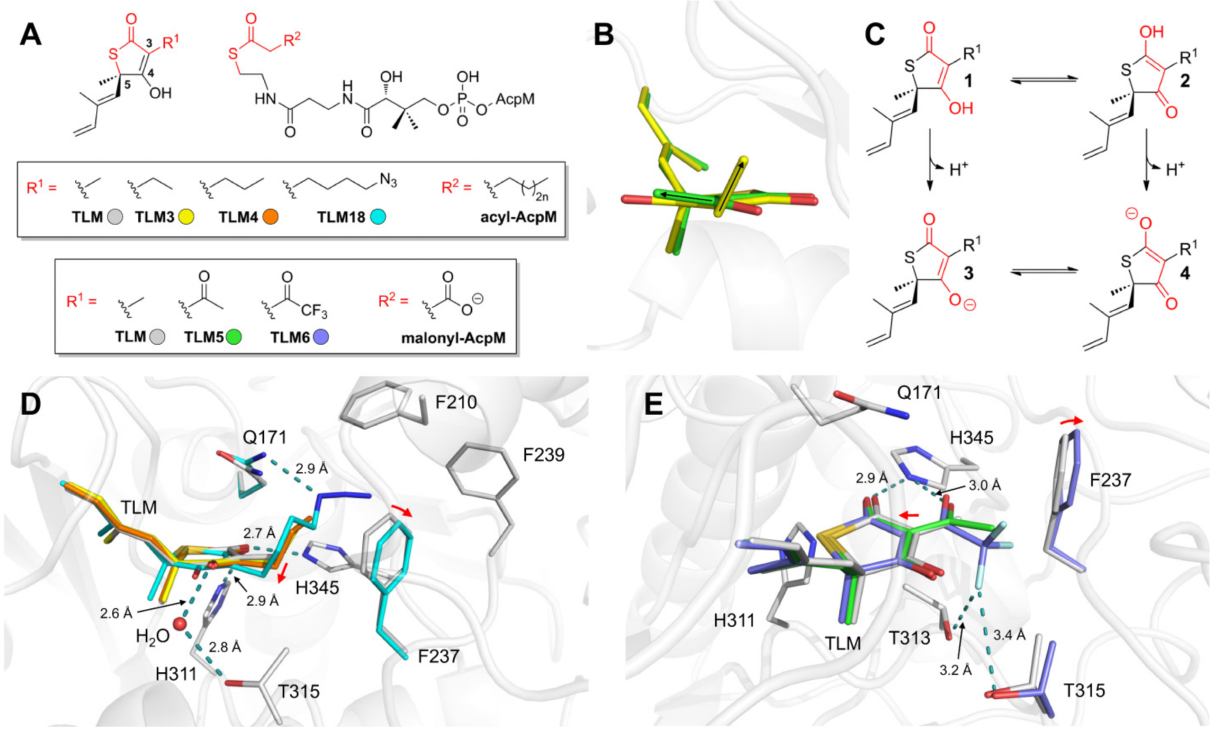

Figure 6-2. KasA Inhibition by Thiolactomycin Substrate Analogs. (A) TLM-derivatives studied here which were designed to resemble the natural KasA substrates. Corresponding moieties are depicted in red. The 3-substituents R^1 were chosen to either mimic the hydrophobic linear chain (R^2) of acyl-AcpM (TLM3, 4 and 18) or the malonyl-group of malonyl-AcpM (TLM5 and 6). **(B)** Comparison of the TLM3 (yellow) and TLM5 (green) binding poses. The binding modes of the two inhibitor groups (see panel A) vary with respect to the orientation of the 3-substituent (indicated by black arrows). **(C)** Possible TLM species. TLM and its derivatives are vinylogous acids (the vinylogous system is highlighted in red) and might, therefore, be present in a deprotonated form at physiological pH (236). The two tautomers of protonated TLM (1 and 2) and the resonance structures of deprotonated TLM (3 and 4) are shown. **(D)** Acyl-AcpM analogs bound to C171Q KasA. As reference, the TLM structure is depicted in gray. Significantly deviating binding site residue conformations are shown for the inhibitor structure with the largest variance. The color code is depicted in panel A. Conformational changes and the differences in the TLM-binding pose are indicated by red arrows. **(E)** Malonyl-AcpM analogs bound to C171Q KasA. As reference, the TLM structure is shown in gray. The inhibitor color code is described in panel A.

We subsequently solved the structures of the C171Q KasA acyl-enzyme mimic in complex with these TLM-derivatives with resolutions of up to 1.5 Å. The basic TLM binding mode is conserved for all investigated inhibitors with the isoprenoid chain intercalating between two peptide bonds and the thiolactone carbonyl group hydrogen bonded to His345 and His311 (Figure 6-2D and Figure 6-2E) (17).

To reduce steric clashes between the new 3-position substituents and the KasA binding site, small but significant shifts in the TLM binding mode can be observed including rearrangements of water molecules and slight conformational changes mainly observed for Phe237 and its adjacent residues Phe210, Ala215, Met216 and Phe239 (Figure 6-2D and Figure 6-2E). In addition, TLM5 and 6 move slightly away from Phe237 thereby increasing the hydrogen bonding distance between the thiolactone carbonyl and His345 from 2.74 ± 0.07 Å to 2.93 ± 0.04 Å but simultaneously enabling the formation of a hydrogen bond between the acetyl carbonyl oxygen and His345 at a distance of 2.96 ± 0.08 Å (Figure 6-2E). The observation of this bifurcated three-centered hydrogen bond between the 1,3-dioxo group and His345 rationalizes the observed 2 to 4-fold gain in affinity compared to TLM (16) and validates these compounds as good malonyl-AcpM analogs. In accordance, the carboxyl group of platensimycin, which was also suggested to mimic the malonyl-substrate, was found to be located at a comparable position in an *E. coli* FabF structure (PDB-entry 2GFX) (131). The additional weak hydrogen bonds between one of the TLM6 fluorines and the hydroxyl groups of Thr313 and Thr315 might explain why this compound displayed the most potent K_i^* value (460 nM (16)) of the investigated inhibitor series (Figure 6-2E).

In contrast to these malonyl-AcpM analogs, the inhibitors TLM3, 4 and 18 are characterized by a 4 to 18-fold decrease in affinity with respect to TLM (Table 6-1) (16). However, the residence time, which was suggested to be a particularly important kinetic quantity for the prediction of *in vivo* drug efficacy (10,45), increased 4-fold for TLM3 with a value of 33 min for this C171Q KasA slow-onset inhibitor. Consistently, our structures also emphasize that this subset of compounds behaves differently compared to TLM5 and 6 (Figure 6-2B). Slight changes in the central TLM binding mode enable the extension of the more hydrophobic 3-substituents into an orthogonal direction towards an aromatic box consisting of Phe210, Phe237, Phe239 and His345 (Figure 6-2B and Figure 6-2D). In addition, the TLM18 azide group forms a hydrogen bond to Gln171 and takes part in a π - π stacking interaction with Phe237 and His345. However, these interactions seem to be overcompensated by desolvation costs for the additional azide since the binding affinity of TLM18 is reduced compared to TLM (K_i^* = 34 µM compared to 1.9 µM, respectively) (Table 6-1 and (16)).

Table 6-1. Interaction kinetics for TLM18 with wild-type and C171Q KasA.

Compound	**Kinetic constants**					
	KasA	**C171Q KasA**				
	K_d *(µM)*	*Slow-onset*	K_i *(µM)*	K_i^* *(µM)*	k_{on} *(sec^{-1})*	k_{off} *(sec^{-1})*
TLM*	226.0±9.0	Yes	175.4±3.0	1.9±0.3	0.18±0.002	0.0020±0.0001
TLM3*	330.0±4.0	Yes	357.0±35.0	7.1±1.3	0.025±0.002	0.0005±0.0001
TLM4*	233.0±7.0	Yes	305.0±8.0	16.0±2.0	0.012±0.002	0.0011±0.0001
TLM5*	25.6±0.5	Yes	8.2±0.8	0.9±0.2	0.035±0.010	0.0039±0.0003
TLM6*	21.8±2.1	Yes	12.1±0.6	0.46±0.05	0.145±0.03	0.0056±0.0002
TLM18	112.0±3.0	Yes	384.0±12.0	34.0±3.0	0.025±0.005	0.0024±0.0002

*data reproduced from (16)

We note that the geometry of the observed interactions for all investigated complexes indicates that the thiolactone ring might be present as the enolate with the negative charge delocalized between the thiolactone carbonyl oxygen and the C-4 hydroxyl group (Figure 6-2C). The short distance of the thiolactone carbonyl oxygen to His311 (2.85 ± 0.07 Å) clearly indicates the presence of a hydrogen bond (Figure 6-2D). However, the thiolactone carbonyl double bond is not optimally oriented for hydrogen bond formation given that the lone pairs of electrons are in the plane of the bond (152). Taken together with the observation of a short (2.58 ± 0.15 Å) and therefore likely charge-assisted hydrogen bond between the TLM hydroxyl oxygen in the 4-position and a conserved water molecule bound below the thiolactone plane (Figure 6-2D), it seems likely that TLM-analogs bind in a delocalized and deprotonated fashion to KasA (structures 3 and 4 in Figure 6-2C). This is consistent with the knowledge that TLM and its analogs are vinylogous acids which can be deprotonated at physiological pH (Figure 6-2C, according to the program Moka (264) the predicted pK_a of TLM is 5.94) (236). In this regard, His311, which is believed to act as a general base during catalysis (13), may facilitate deprotonation of the tautomeric form of the inhibitors where the hydroxyl group is located next to the thiolactone sulfur (tautomer 2 in Figure 6-2C).

6.6.2 Identification of a Phospholipid Bound to KasA

The electron density maps of our C171Q KasA structures also indicated the presence of a long-chain molecule close to the active site (Figure 6-3). Due to the need to add polyethylene glycol (PEG) during C171Q KasA crystallization, we initially interpreted this density as a long PEG chain (17). However, the observation that this molecule was present in protein crystals obtained in the absence of PEG suggested that it was a host-derived lipid. Intriguingly, using mass spectrometry, we demonstrated that, in contrast to wild-type KasA, the C171Q variant protein samples contained significant amounts of phospholipids (Table 6-2 and Table S 6-2, Figure S 6-1). Co-purification and crystallization of these phospholipids with C171Q KasA suggested that they bound specifically to the enzyme. Three main phospholipids are observed with respect to the identity of the head group (Figure 6-3), while the acyl chains are primarily palmitic (16:0) and tuberculostearic acids (19:0) (Table 6-2). Interestingly, the latter methyl-branched fatty acid is a lipid component of Actinomycetales such as mycobacteria and can be used for the diagnosis of tuberculosis meningitis (265,266). The C171Q variant preferably binds glycerophospholipids containing acyl chains with 16, 17 and 19 carbon atoms (Table 6-2), which likely were co-purified from the expression host *Mycobacterium smegmatis* mc^2155 and crystallized with the C171Q KasA protein. Importantly, the major 19:0,16:0

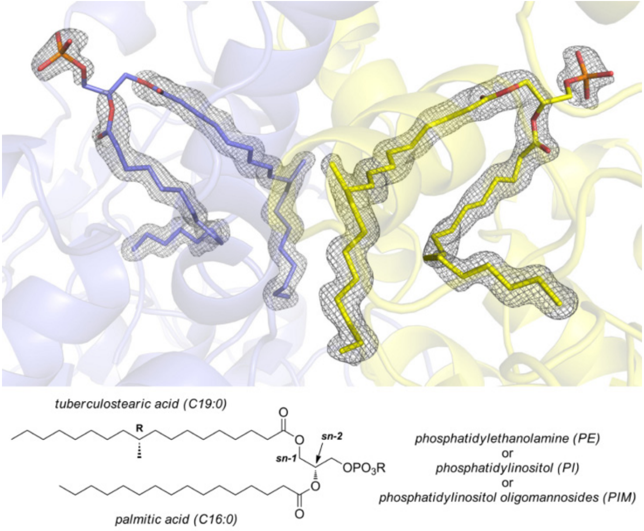
tuberculostearic acid (C19:0)
R
O
O
sn-2
sn-1
OPO3R
O
O
phosphatidylethanolamine (PE)
or
phosphatidylinositol (PI)
or
phosphatidylinositol oligomannosides (PIM)
palmitic acid (C16:0)

Figure 6-3. Identification of a Phospholipid Bound to C171Q KasA. The $2F_o$-F_c omit map for an initially unknown ligand is depicted for the C171Q KasA - TLM5 structure at 1σ. Using mass spectrometry, this molecule was identified as a phospholipid with different head groups and acyl chains. Among the fatty acid chains, a preference for tuberculostearic acid and palmitic acid is apparent.

phospholipids perfectly fit the observed electron density with 16:0 attached to the central glycerol hydroxyl group (*sn*-2) and 19:0 at the terminal position (*sn*-1), which is in agreement with the previous finding that mycobacterial phospholipids are mainly comprised of fatty acids with 18 or 19 carbons at position *sn*-1 and with 16 carbon atoms at position *sn*-2 (Figure 6-3) (266,267). For model building we used a 19:0,16:0 phospholipid without a head group since it was not visible in the electron density presumably due to its exposed position at the C171Q KasA surface (Figure 6-3).

Table 6-2. Mass-spectrometric identification of phosphatidylethanolamines (PEs) and phosphatidylinositols (PIs) bound to C171Q KasA and present in the total lipid extracts of *M. smegmatis* mc^{2}155.

	mol% of PE and PIs	
	C171Q KasA	*M. smegmatis*
(16:0,19:0)PI	60.35 ± 0.52	34.65 ± 4.34
(16:0,17:0)PI	20.34 ± 0.35	4.09 ± 0.55
(16:1,19:0)PI	7.66 ± 0.35	1.98 ± 0.14
(16:0,16:1)PI	3.91 ± 0.07	0.48 ± 0.20
(16:1,17:0)PI	3.49 ± 0.13	0.32 ± 0.07
(16:0,19:0)PE	1.55 ± 0.22	11.75 ± 1.96
(16:0,16:0)PE	1.16 ± 0.06	14.20 ± 0.39
(16:0,18:1)PI	0.98 ± 0.09	1.61 ± 1.06
(16:0,16:1)PE	0.42 ± 0.06	1.93 ± 0.61
(16:0,19:1)PE	0.13 ± 0.02	0.50 ± 0.13
(19:0,19:0)PE	n.d.[a]	13.51 ± 1.44
(16:0,18:1)PE	n.d.	5.65 ± 2.74
(16:0,18:0)PE	n.d.	3.07 ± 0.33
(18:0,19:0)PE	n.d.	1.81 ± 0.23
(19:0,17:0)PE	n.d.	1.13 ± 0.11
(18:1,19:0)PE	n.d.	1.05 ± 0.29
(16:1,18:1)PE	n.d.	0.72 ± 0.34
(19:0,19:1)PE	n.d.	0.54 ± 0.05
(16:1,18:1)PI	n.d.	0.32 ± 0.09
(16:0,17:1)PE	n.d.	0.23 ± 0.07
(18:0,18:1)PE	n.d.	0.23 ± 0.03
(18:0,19:1)PI	n.d.	0.14 ± 0.10
(18:1,19:1)PI	n.d.	0.07 ± 0.10

[a] n.d. = not detected

6.6.3 Location of the KasA Substrate Binding Sites

Clearly, the identified phospholipid represents a very long acyl chain bound to KasA and defines the long KasA acyl-binding channel which is created by hydrophobic residues mainly located in the capping region - a part of the KAS enzymes which is formed by genetically variable insertions (Figure 6-4A, Figure 6-5 and Figure S 6-2) (17). A similar location of the cavity has also been observed in the *E. coli* FabB (ecFabB) C_{12}-acyl-enzyme structure (Figure 6-4A) (13).

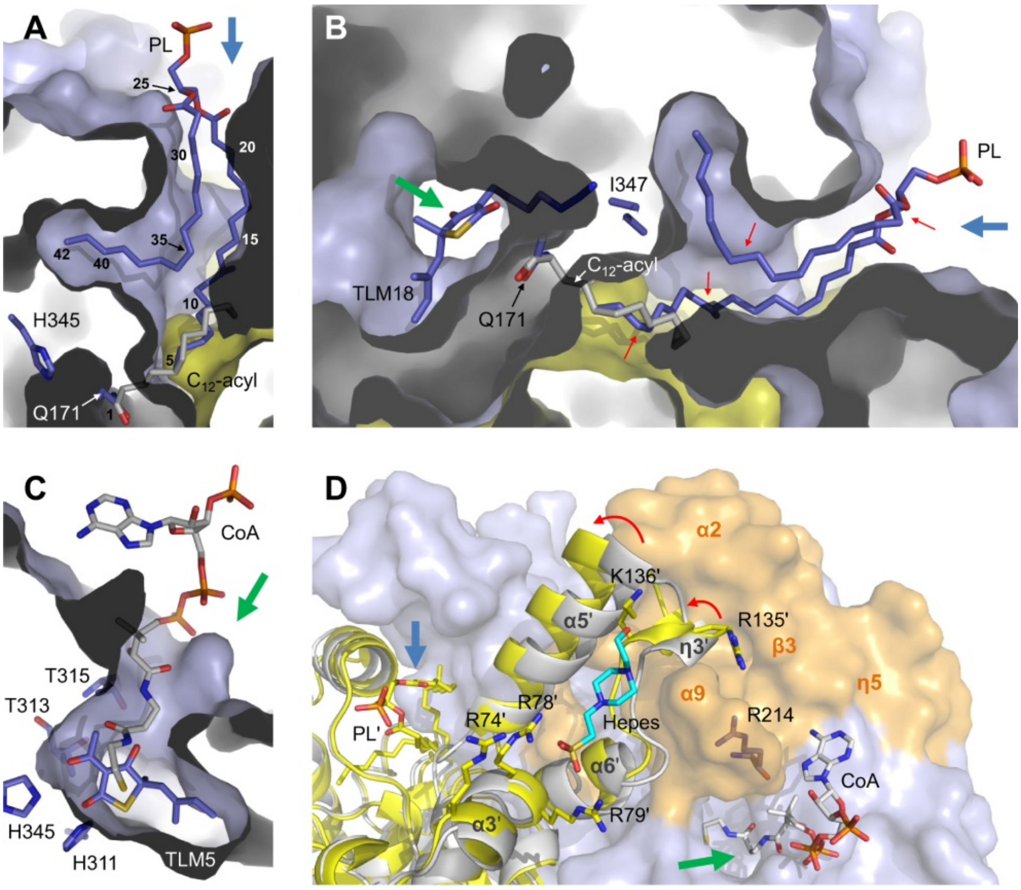

Figure 6-4. Location of the KasA Acyl- and Phosphopantetheine-channels. (A) The acyl-binding channel. The two KasA subunits are shown as blue and yellow surfaces. An intersection of the KasA dimer reveals an acyl-channel containing the phospholipid (PL) molecule. The solvent-exposed opening of this channel is indicated by a blue arrow. The structure of an *E. coli* FabB acyl-intermediate (PDB-entry 1EK4) was superimposed on C171Q KasA - TLM5 (13). The respective C_{12}-acyl chain is depicted in gray and the carbon atom count for the KasA acyl chains resulting from this comparison is provided adjacent to the phospholipid (42 = 4 [missing to reach Gln171] + 18 [19:0 methyl-branched acyl chain of the phospholipid] + 4 [glycerol of phospholipid] + 16 [16:0 acyl chain]). The location of the KasA active site is indicated by Gln171 and His345 in stick representation. **(B)** KasA substrate binding sites. This intersection of the C171Q KasA - TLM18 structure shows both binding channels. The channel entrances are indicated by a blue and green arrow, respectively (see also panel A and C). Red arrows indicate the locations of major kinks in the observed phospholipid conformation. For Ile347 only the terminal side chain methyl group in its alternate conformation is shown. **(C)** The phosphopantetheine-binding channel. A superposition of the active site cysteines from KasA and *E. coli* FabH (PDB entries 2WGE and 2EFT) shows that the CoA molecule bound in the FabH structure, is pointing towards the KasA active site (15-17). The CoA molecule, which resembles the phosphopantetheinylated AcpM, is depicted in gray along with an intersection of the C171Q KasA - TLM5 structure. The entrance of the phosphopantetheine-channel is indicated by a green arrow. **(D)** Proposed AcpM binding site. Basic residues located on α3' and η3' likely bind to the acidic AcpM protein, which is believed to deliver its substrate to the adjacent subunit (18). A HEPES buffer molecule (shown in cyan) bound to the α3' basic patch was observed for the C171Q KasA and C171Q KasA - TLM structures. The flexible regions of KasA are highlighted by red arrows in one subunit (C171Q KasA - TLM5 is shown in yellow, KasA - TLM (PDB-entry 2WGE) shown in gray) and as orange surface in the other subunit (see also Figures 5, 6 and S2). Blue and green arrows indicate the openings towards the acyl- and phosphopantetheine-pockets, respectively.

To characterize the phosphopantetheine-channel, which is additionally necessary for the binding of both AcpM-substrates (236), we superimposed the active site cysteines of KasA and a coenzyme A (CoA) bound *E. coli* FabH structure (Figure 6-4C) (15). Consistently, the CoA molecule points into the cavity which contains the TLM-inhibitors underlining their potential as substrate analogs. We recently validated this model by NMR-experiments showing interligand NOEs between a pantetheine analog and TLM bound to KasA simultaneously (16). According to this model, and in line with FabF docking studies (68), Thr313 and Thr315, which are strictly conserved for KAS I and II enzymes (Figure S 6-2) and were proposed to be involved in ACP-substrate binding (141), contact the terminal phosphopantetheine peptide carbonyl oxygen (Figure 6-4C), which is represented by one of the TLM6 fluorines (Figure 6-2E).

In a recent kinetic study, Borgaro et al. proposed that the binding of the acidic ACP protein to one ecFabB monomer leads to the delivery of its substrate to the active site of the adjacent subunit (18). They identified several basic amino acids on the protein surface that are important for ACP binding. Similarly, the corresponding KasA arginines 74', 78' and 79' on α-helix 3', as well as Arg135', Lys136' and Arg214 (the prime designates the second KasA monomer) are ideally positioned to interact with the AcpM molecule. In this orientation the bound AcpM would then permit the entrance of the substrates via the phosphopantetheine-tunnel opening (indicated by the green arrow in Figure 6-4D) of the neighboring monomer. In two of our nine crystal structures, a negatively charged HEPES molecule is bound to this basic KasA patch where the acidic AcpM is expected to bind (cyan stick model in Figure 6-4D). Importantly, we exclude the possibility that one or both substrates are delivered through the acyl-pocket opening (blue arrow in Figure 6-4D) due to distance considerations to reach the active site cysteine. An entrance through the acyl-pocket opening would require to bridge the large distance between the phospholipid head group and the active site cysteine of ~30 Å (corresponding to 25 atoms) by the phosphopantetheine linker which has a maximal length of ~16 Å (14 atoms) (Figure 6-1, Figure 6-4A and Figure 6-4B).

6.6.4 Structural Explanation for the KasA Substrate Preferences

The mycobacterial β-ketoacyl-ACP synthases KasA and KasB are striking examples of enzymes that produce very hydrophobic meromycolates with up to 56 carbon atoms in length in a cytosolic, i.e. hydrophilic environment. KasA was found to extend short FAS-I primers to $C_{38\text{-}42}$ monounsaturated acyl chains, whereas KasB can produce full-length meromycolates (268). The unambiguous identification of phospholipids bound to the acyl-channel of C171Q KasA sheds light on the observed substrate preferences of this enzyme. Remarkably, the number of carbon atoms between the mutated active site cysteine and the terminal end of the *sn*-2 phospholipid acyl chain coincides with the maximal acyl chain length of 42 carbons generated by KasA (Figure 6-4A). We assume that the C_{42} chain cannot be further elongated because the acyl-channel is capped by the peptide backbone of residues 239-241, thus explaining why KasA is not able to produce full-length meromycolic acids. Consistently, phospholipids mimicking the C_{44} acyl-enzyme intermediate (e.g. (19:0,19:0)PE and (19:0,18:0)PE) do not bind to C171Q KasA although they are present in the total lipid extract of *M. smegmatis* (Table 6-2).

Furthermore, we observed that the phospholipid does not bind in an extended manner but rather contains several kinks as pre-defined by the geometry of the surrounding KasA cavity (Figure 6-4B). This non-linear architecture of the acyl-channel might facilitate the binding of unsaturated primers as exemplified by the presence of phospholipids with unsaturated fatty acids (Table 6-2). Indeed, it has been proposed that the *cis* ω-19 double bond is already introduced at the C_{22} stage of meromycolate synthesis (11) and the observed non-linear shape of the acyl-cavity could thus facilitate the binding of kinked unsaturated substrates with a migration of the *cis* double bond by two carbon atoms along the channel in each new elongation round.

In contrast to KasA, its homolog KasB produces full meromycolates with up to 56 carbons (268). Unfortunately, the available KasB crystal structure was not solved in its 'open' acyl-channel conformation as observed for C171Q KasA and thus the preference for longer substrates cannot be directly deduced (22,269). However, most residues that create the 'open' C171Q KasA acyl-binding pocket are conserved in KasB. Among the few differences between KasA and KasB, E124F, P201R and I347V are particularly interesting. The first two residues are located at the opening of the acyl-pocket and might elongate the cavity in KasB. In contrast, Ile347 lies between the aromatic box containing the hydrophobic TLM 3-substituents (Figure 6-2D) and the terminal part of the hypothetical C_{42}-acyl chain (Figure 6-4B), suggesting that the acyl chain could be extended towards the aromatic box and TLM binding site in KasB due to distinct sequence variations (I145Y, G200T, I347V). The hydrophobic 3-substitutent of TLM18 might mimic this alternative acyl binding mode (Figure 6-4B).

6.6.5 Acyl-Channel Opening Mechanism

Our structures unambiguously establish the location of all substrate binding sites which immediately leads to two important questions - how does KasA achieve the uptake of its hydrophobic substrates given that neither the long acyl chain nor its lipophilic binding pocket should be exposed to solvent for too long and why do phospholipids not bind equally well to the wild-type enzyme? To address these questions, we solved the structure of TLM5 bound to wild-type KasA. Intriguingly, this malonyl-AcpM analog induces conformational changes which define an intermediate state between the wild-type KasA - TLM structure (PDB entry 2WGE), which is characterized by a 'closed' acyl-channel, and the 'open' structure observed for the acyl-enzyme analog C171Q KasA which binds phospholipids (17). A per-residue rmsd plot of the three structures reveals five regions in close vicinity to the

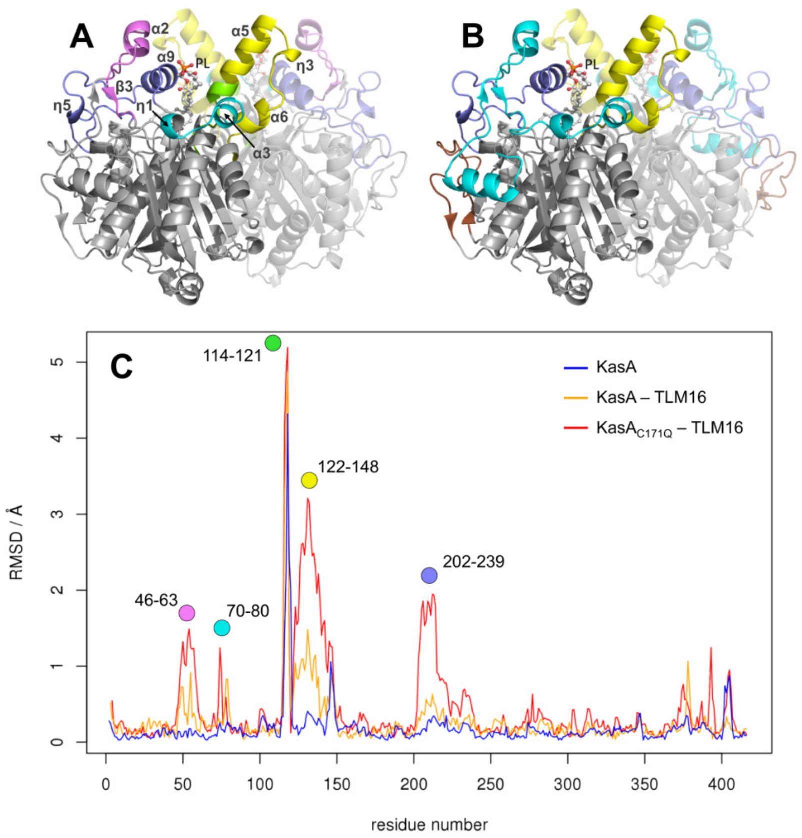

Figure 6-5. Flexible KasA Regions Involved in Substrate Recognition. (A) Flexible KasA regions surrounding the substrate binding sites. The highlighted regions (color coded as defined in panel C) exhibit different conformations in the KasA and C171Q KasA structures. For clarity, one of the two C171Q KasA -TLM5 monomers is shown in transparent colors. **(B)** KasA capping region. The three N-terminal KasA insertions (26-80, 115-145 and 200-240) are depicted in cyan, yellow and lilac, the C-terminal insertion (366-391) in brown. **(C)** Differences between KasA and C171Q KasA structures. The per-residue rmsd, calculated with Theseus, is shown for the KasA (PDB entry 2WGD), KasA - TLM5 - I and C171Q KasA - TLM5 structures (14). KasA - TLM (PDB entry 2WGE) was used as the reference structure. The five highlighted regions reveal significant differences between the investigated structures.

substrate binding sites which differ in their conformation between the enzyme and acyl-enzyme states (Figure 6-5). This is the first time that a partially 'open' acyl-channel has been observed, thus revealing that the acyl-substrate interacts with KasA through an induced-fit binding mechanism. Although adaptive substrate recognition is a well-known phenomenon, structural information about the dynamics of such processes is rare (239).

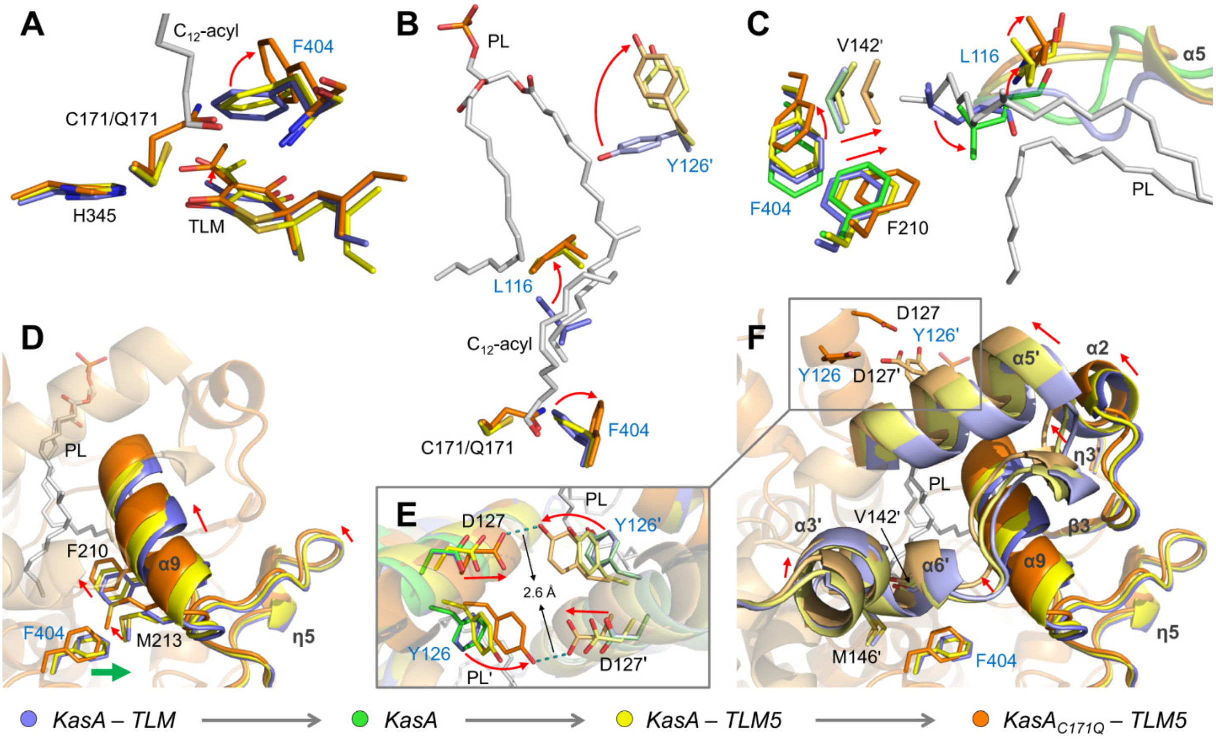

Figure 6-6. The KasA Acyl-substrate Recognition Mechanism. (A-F) The phospholipid and C$_{12}$-acyl chain (Figure 6-4) are shown in gray. Gatekeeper residues Leu116, Phe404 and Tyr126' are labeled in blue. Red arrows indicate the stepwise conformational changes apparent from the structures KasA - TLM (lilac, PDB-entry 2WGE), KasA (green, PDB-entry 2WGD), KasA - TLM5 - I (yellow) and C171Q KasA - TLM5 (orange). For the second subunit, pale colors were used. The phosphopantetheine-channel opening is indicated by a green arrow (Figure 6-4). Panel E contains a detailed view of the KasA dimer interface along a 2-fold axis of symmetry. The conformational changes observed for Tyr126 and Asp127 lead to a short hydrogen bond in both subunits.

We characterized this mechanism and the associated conformational changes in a stepwise manner using the four different structures KasA - TLM (PDB-entry 2WGE), apo KasA (PDB-entry 2WGD), KasA - TLM5 - I (nomenclature of all structures according to Table S 6-1) and C171Q KasA - TLM5 of which only the final 'open' state permits the binding of long acyl chains. Similar to the KasA - TLM complex, the unliganded KasA structure is almost 'closed' (Figure 6-5). The conformational changes towards the 'open' state can be triggered by either the C171Q mutation, which mimics acylation of the active site cysteine (C171Q KasA - TLM5) or by the binding of TLM5 (KasA - TLM5 - I). Since the natural malonyl-substrate preferably binds to the 'open' acyl-enzyme state during catalysis (Figure 6-1) (262), its close analog TLM5 seems to have the capability to select for or to actively induce a partially opened conformation in the wild-type enzyme. The improved potency of this inhibitor (16) might be the cause for these conformational changes, which enabled us to trap an intermediate state between the wild-type and acyl-enzyme forms. In contrast, similar rearrangements were not observed with TLM which has a lower affinity (16,17). Compared to the 'closed' state, the three subsequent structures are characterized by a Phe404 conformation in which the phenyl-ring plane is rotated by 5°, (-)19° and 59°, respectively (henceforth, we will indicate the stepwise changes observed for these three structures compared to the 'closed' KasA - TLM state using the following notation: 5° → 19° → 59°) (Figure 6-6A and Figure 6-6C). The introduction of the C171Q mutation that mimics acylation of the active site cysteine as well as the binding of TLM5 in a slightly different orientation compared to TLM, apparently induce the rotation of the Phe404 phenyl-ring. This conserved residue was suggested to play an important role as a gatekeeper between the active site cysteine and the acyl-binding cavity opening upon acylation (17).

The alteration in the Phe404 conformation induces a cascade of structural changes (Figure 6-6). Initially, the adjacent residues Phe210, Met213, Val142' and Met146' are shifted due to the rotation of Phe404 (Figure 6-6C, Figure 6-6D and Figure 6-6F). Compared to the 'closed' reference state, the C_α atom of Phe210 moves by 0.4 → 0.5 → 1.8 Å and the C_α atom of Val142' by 0.1 → 0.6 → 1.6 Å. Together with Ile347, these three residues comprise a binding cavity for Leu116 in the initial KasA - TLM structure. Due to the subsequent shift and tightening of this pocket, Leu116 is successively expelled from the acyl-channel (Leu116 C_α moves by 1.5 → 3.3 → 4.3 Å) (Figure 6-6C), which creates space for the binding of an acyl chain and, hence, Leu116 can be regarded as a second gatekeeper residue. This observation validates experimentally a similar proposal by Schaefer et al. based on a molecular dynamics simulation (236).

Simultaneously, the Phe404-induced shifts of Phe210 and Met213 directly lead to a movement of an entire range of residues including amino acids 202-239 (rmsd change of 0.2 → 0.4 → 1.1 Å) and therefore helix α9 (residues 204-211) (Figure 6-5, Figure 6-6D and Figure S 6-2). In particular, the conformational change of residues 212-216 causes a widening of the phosphopantetheine-pocket which accounts for the enhanced TLM affinity towards the acyl-enzyme intermediate (17). Helix α9 is in close proximity to a region containing residues 46-63 (including α2 and β3) and 122'-148' (including α5', α6' and the 3_{10}-helix η3') which consequently move in a similar direction supported by the spatial rearrangements of Val142' and Met146', which in turn are triggered by the rotation of the Phe404 phenyl-ring plane (rmsd values change by 0.1 → 0.5 → 1.0 Å and 0.4 → 0.9 → 2.1 Å, respectively) (Figure 6-6F). The extensive alterations in helices α5' and α6' in turn induce a slight shift of helix α3' (rmsd change of 0.2 → 0.4 → 0.6 Å) and, together with the movement of Leu205 located on helix α9, the extrusion of Tyr126' from the acyl-binding channel, which is stabilized in this final conformation by a hydrogen bond to Asp127 (Figure 6-6E and Figure 6-6F). During this process, the distance between the hydroxyl group of Tyr126' and the Asp127 carboxyl oxygen decreases from 11.5 Å via 10.9 Å and 5.6 Å to ultimately 2.6 Å. Related via a 2-fold axis of symmetry, the exact same modifications are observed between Tyr126 and Asp127', which indicates that the proposed cascade of conformational changes, and therefore the opening of the substrate binding pockets, take place in the neighboring monomer at the same time.

Importantly, Tyr126' may be envisioned as a third gatekeeper that protects the hydrophobic acyl-cavity from solvent exposure by its hydrophilic OH group. According to the proposed mechanism, all three gatekeepers (Phe404, Leu116 and Tyr126') exit concertedly from the acyl-channel to permit the simultaneous uptake of an acyl chain as exemplified by the C171Q KasA bound phospholipid (Figure 6-6B, Movie S 6-1 and Movie S 6-2). This concerted process is facilitated by considerable shifts of the helices surrounding both acyl-channels and would avoid excessive exposure of the hydrophobic channel to the solvent (Figure 6-5A, Movie S

6-1). Interestingly, these helices are part of the capping region, a genetically variable part of the KAS enzymes, that may have evolved specifically to enable the binding of meromycolate precursors to KasA (Figure 6-5B and Figure S 6-2) (68). The vastly different but also flexible FabH capping domain, which is formed from insertions located at distinct sites in the primary sequence (Figure S 6-2), has similarly been suggested to be involved in substrate binding (263,270). Moreover, a sequence alignment of the KAS enzymes shows that the three gatekeeping residues are conserved in KasB, thus suggesting that a similar substrate recognition mechanism may be present in this enzyme (Figure S 6-2). Consistent with this proposal, it has been suggested that Leu115 (corresponding to Leu116 in KasA) has to undergo conformational changes upon binding of cerulenin, which contains a long hydrophobic chain (Figure 6-1) (269).

6.7 Discussion

To address the question of how the β-ketoacyl-ACP synthase KasA ensures the binding of very hydrophobic long-chain mycolic acid precursor molecules, we utilized analogs of the natural product TLM that recapitulate key aspects of the structure of the two KasA substrates, acyl-AcpM and malonyl-AcpM. Our structural data support an induced-fit substrate binding mechanism which involves the concerted rearrangement of three gatekeeping residues. This mechanism includes the movement of several helices thereby creating the acyl-binding pocket and thus accounting for the ability of the C171Q KasA acyl-enzyme mimic to bind phospholipids that are similar in size to the C_{42} acyl chain of the natural substrate (Table 6-2, Movie S 6-1 and Movie S 6-2).

Strikingly, these conformational changes take place in the KasA region where AcpM is expected to bind (Figure 6-4D) (18), and thus it is likely that AcpM binding initiates this process. Based on this hypothesis, we propose the following mechanism: The acidic AcpM protein interacts via the helices α2 and α3 with the basic KasA surface region containing helices α9, α3', α5', η3' and α6' and thereby delivers both substrates through the phosphopantetheine-tunnel (green arrow in Figure 6-4D) of the adjacent subunit. Since all the KasA helices mentioned above undergo conformational changes during the acyl-channel opening process, it is tempting to speculate that AcpM might be the trigger for the observed substrate binding mechanism and specifically could induce the opening of the three gatekeepers. The acyl-substrate could thus be injected simultaneously to the opening of the acyl-pocket upon AcpM binding, ensuring that neither the hydrophobic acyl-chain, nor the acyl-cavity are exposed to the solvent. In support of this hypothesis we observe that the acyl chain itself is not able to induce these conformational changes as exemplified by the absence of the phospholipids in the wild-type KasA binding cavity. Furthermore, our model explains why acyl-CoA substrates are not efficiently processed by KasA (18). In contrast, the FabH enzyme has a fundamentally different capping region (Figure S 6-2) which likely accounts for the altered specificity towards acyl-CoA primers (270).

In conjunction with the proposed substrate binding mechanism, our C171Q KasA structures provide an excellent model for the investigation of the 3-step catalytic mechanism. In particular, the decarboxylation step of KAS enzymes has not been fully elucidated due to the lack of structural information to establish the location of the malonyl group. The 1,3-dioxo TLM5 moiety is an excellent mimic of the malonyl group, and consistent with previous studies, is hydrogen bonded to His345 in the active site (141). However, it is not possible to distinguish between the two oxo groups - i.e. which of the two represents the malonyl carboxylate thus leading to the two geometric possibilities depicted in Figure 6-7C and Figure 6-7D. These possibilities represent the two conflicting mechanistic models which have been proposed for the decarboxylation reaction - either His311 or Phe237, which are both strictly conserved among KAS I and II enzymes (Figure S 6-2), were suggested to trigger the decarboxylation of malonyl-ACP (59,132,141).

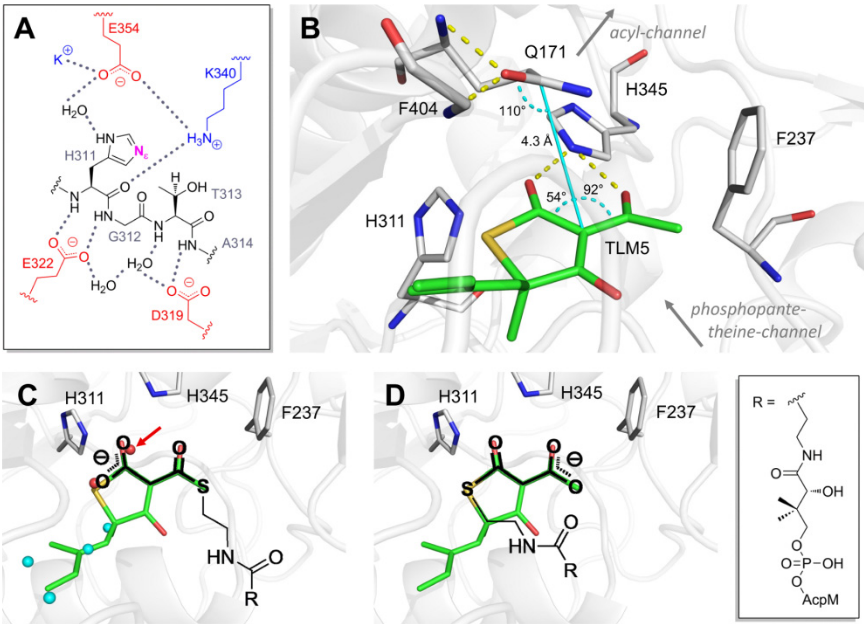

Figure 6-7. Mechanistic Insights. (A) Hydrogen bond network surrounding His311. Positively (Lys340; depicted in blue) and negatively (Asp319, Glu322 and Glu354; depicted in red) charged amino acids, which were proposed to be important for decarboxylation (141), interact with His311 via a complex hydrogen bonding network, which includes a potassium ion located in a conserved cation binding site (Figure S 6-3). This environment likely leads to the modulation of the electronic properties of the His311 ε-nitrogen (magenta) to a catalytically ideal state (139). **(B)** Mechanistic consequences of TLM5 being a malonyl-AcpM analog. His345 binds to the 1,3-dioxo group of TLM5, which mimics the malonyl group of the natural substrate. The side chain amide carbonyl oxygen of Gln171 is located in the oxyanion hole formed by residues 171 and 404 (the side chain of Phe404 is omitted for clarity). The proposed attack vector geometry of the acetyl-carbanion forming via decarboxylation is depicted in cyan. **(C-D)** Geometric possibilities for malonyl-AcpM binding. Two different models of malonyl-AcpM binding to KasA via the phosphopantetheine-tunnel are displayed on top of TLM5. In addition, panel C depicts six water molecules of the C171Q KasA apo structure which are not present in the binary complex. Water molecules which are likely displaced by the malonyl-substrate are colored in red, water molecules which might still be present upon malonyl-AcpM binding are highlighted in cyan. The red arrow indicates the water which was suggested to attack the carboxylate group of malonyl-AcpM (271).

In the orientation depicted in Figure 6-7C the ε-nitrogen of His311 could trigger the decarboxylation, whereas this role is indicated for one of the Phe237 π-faces in the alternative case (Figure 6-7D). For both models decarboxylation leads to the generation of the carbanion at the carbon atom located between the two TLM5 carbonyl groups (Figure 6-7B). Interestingly, the evolving carbanion could approach the acylated cysteine with a Buergi-Dunitz trajectory of 110° (Figure 6-7B), which is within the expected range of 100 - 110° for the transition state attack vector angle of a carbonyl group by a nucleophile (Nu → C=O) (272,273). For similar stereoelectronic reasons, the carbanion should attack the Cys171 thioester carbonyl with an obtuse angle as assumed for the related aldol reactions (274). Thus, we reason that the malonyl-group of the AcpM-substrate is positioned with the carboxylate pointing towards His311 (enolate attack angle of 92° vs. 54°, see also Figure 6-7B and 7C) and therefore exclude the possibility depicted in Figure 6-7D. Strikingly, all residues, which were proposed to play an important role during decarboxylation (the charged amino acids Asp319, Glu322, Lys340 and Glu354, which are conserved amongst KAS I/II proteins) (141) and an octahedrally bound potassium ion identified in this study (Figure S 6-3), are involved in a complex hydrogen bonding network contacting His311 (Figure 6-7A) and might thus be responsible to tailor the catalytically ideal His311 electronic state (139). Since the residues participating in catalysis are different for KAS III enzymes and other thiolase superfamily members such as chalcone synthase (CHS), these enzymes presumably operate via an alternative reaction mechanism (13,60,141,246). In particular, the catalytic residue His345 is replaced by an asparagine in FabH proteins and the residues corresponding to Asp319, Glu322, Lys340 and Glu354 as well as the cation binding site are not conserved (Figure S 6-2) (141).

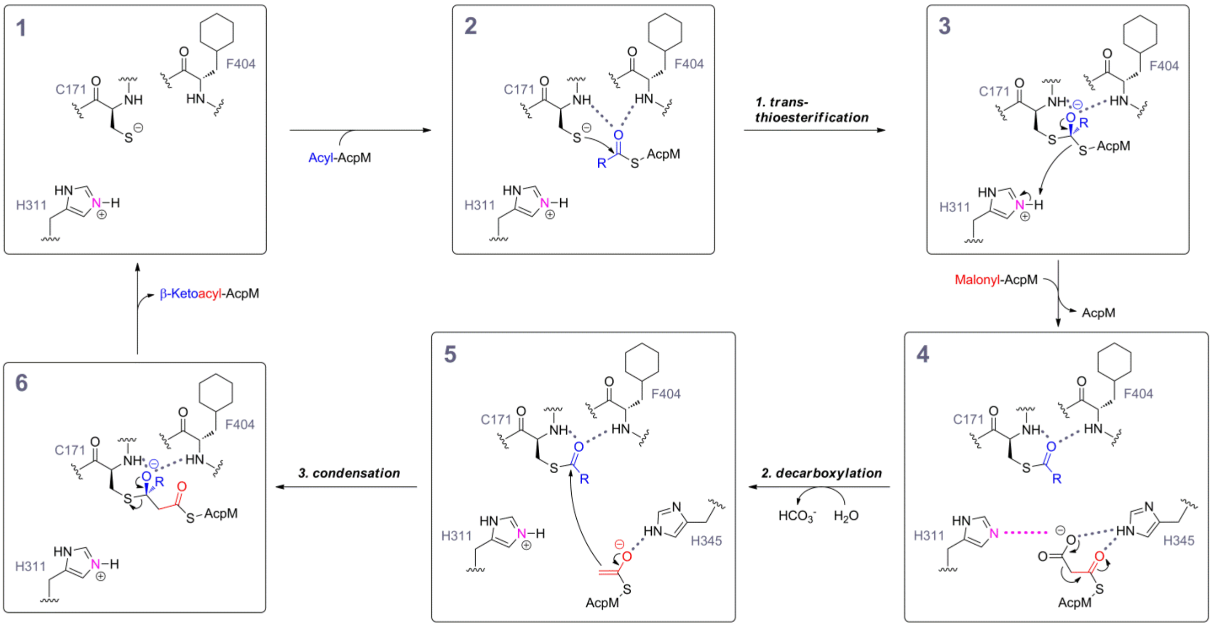

Figure 6-8. Proposed KasA Reaction Mechanism. This mechanistic scheme is strongly supported by our structural work and builds on previous studies (51,139,141,262,271). Gray dashed lines indicate hydrogen bonds. It was proposed that the dipole moment of helix α8 acidifies Cys171 (Figure S 6-2) (68) leading to a zwitterionic His311H$^+$-Cys171$^-$ ion pair in the free enzyme (box 1) which activates Cys171 for the nucleophilic attack of the acyl-AcpM (box 2) (139). The His311 ε-nitrogen (depicted in magenta as in Figure 6-7A) likely destabilizes the malonyl-AcpM carboxylate during decarboxylation as highlighted by the dashed line in magenta, in box 4. In contrast to a previous hypothesis regarding the decarboxylation reaction (271), our KasA binary complex structures contain no appropriately positioned water molecule which could be activated by the His311 ε-nitrogen to trigger the decarboxylation reaction directly (box 4). Consequently, we suggest that the initial product is CO_2 which can then be hydrated after decarboxylation (in between steps 4 and 5). The evolving enolate (box 5) is stabilized by the neutral His345 which is protonated at its ε-nitrogen since the δ-nitrogen is hydrogen bonded to the backbone NH of Ile347 (139). Geometric considerations based on our structures suggest that the nucleophilic attacks of Cys171 and of the acetyl-carbanion occur from the Si- and Re-faces of the thioester carbonyl groups, respectively (boxes 2 and 5; see also Figure 6-7).

Based on our structural results concerning the binding mode of the malonyl group and taking previous findings into account (139,141,262,271), we propose the mechanism depicted in Figure 6-8. A mechanistic study of the mammalian fatty acid synthase β-ketoacyl synthase domain, which shares the Cys-His-His catalytic triad and the important active site residues with KAS I enzymes (138), revealed that bicarbonate is the product of the condensation reaction (262). Subsequently, a similar outcome has been proposed and confirmed for *Streptococcus pneumoniae* FabF (spFabF) where it was shown that ^{14}C-labeled bicarbonate is incorporated into malonyl-ACP in the reverse reaction of the condensing enzyme (271).

Thus, an activated water molecule either directly attacks the carboxylate of malonyl-ACP or hydrates CO_2 after decarboxylation (262). The identification of a structured water molecule bound to the ε-nitrogen of His311 (according to the KasA numbering) in most apo KAS I/II crystal structures, has previously been used to support this mechanism (51,271). Indeed, our C171Q KasA apo structure confirms the presence of such a water molecule (indicated by the red arrow in Figure 6-7C). However, in the binary complex it is displaced by the thiolactone oxygen of TLM5 mimicking one of the malonyl-AcpM carboxylate oxygens. Assuming a neutral His311 (deprotonated at N_ε) prior to decarboxylation, as proposed for ecFabB and spFabF (13,51,271), we suggest that the ε-nitrogen lone pair electrons directly destabilize the adjacent malonyl-AcpM carboxylate (Figure 6-8 - box 4, dashed line in magenta) leading to the transfer of the negative charge to the thioester carbonyl which in turn is stabilized by His345. After decarboxylation, one of the water molecules surrounding the substrate might re-enter the binding site and could hydrate the CO_2 molecule facilitated by a His311-mediated activation (Figure 6-7C). In support, an ecFabB H298Q mutant was decarboxylation deficient whereas a H298E mutant displayed residual decarboxylation activity at pH values between 6 and 8, which highlights the necessity for an electron-rich lone pair at the position of the His311 ε-nitrogen (corresponding to ecFabB His298) enabling both decarboxylation and binding of a water molecule (141).

Most enzymes are inherently flexible systems tailored to accommodate substrates and undergo catalysis (275). In light of the fact that the free energy of the transition state along the reaction coordinate has to be lowered efficiently, it is not very surprising that the dynamics of substrate binding and catalysis is also reflected in the inhibition of enzymes (209,238,239). This is nicely illustrated by recent studies concerning the induced-fit binding of peptide deformylase (PDF) and enoyl-ACP reductase (FabI) inhibitors (19,188,239). For instance, the picomolar affinity of diphenyl ether FabI inhibitors can be related to their capability to mimic the transition state of the catalyzed reaction and to trigger the correlated ordering of a flexible loop (19,188). In the present study we reveal snapshots of the dynamic process which is involved in the recognition of very long chain fatty acyl substrates by the important drug target KasA. This investigation of induced-fit substrate recognition and turnover has important implications for the design of optimized KasA inhibitors. For instance, TLM 3-acyl substituents can trigger the opening of the phosphopantetheine and acyl-channels in the wild-type KasA enzyme. This observation now suggests ways in which these inhibitors can be tailored in order to occupy the hydrophilic and hydrophobic cavities in the active site, thus leading to compounds with improved affinity for KasA and ultimately to the development of urgently needed drug candidates for the treatment of tuberculosis.

6.8 Acknowledgements

We thank the staff at the ESRF beamline ID 23-2 (Grenoble) and at the BESSY II beamline 14.1 (Berlin) for technical support. The lipid analysis was performed in cooperation with the Metabolomics Core Facility at University of Wuerzburg. Furthermore, we thank Andreas Schlosser, Silke Leimkühler and Manfred Weiss for their helpful support during the identification of the unknown ligand and cation, Hermann Schindelin for critical reading and discussion of the manuscript, our collaboration partner Christoph A. Sotriffer for help with the prediction of the TLM pK_a as well as Wook Lee and Bernd Engels for fruitful discussions regarding the catalytic mechanism of KAS enzymes.

6.9 Footnotes

*This work was supported in part by NIH grants GM102864, AI044639 and AI070383 to P.J.T., and through the Deutsche Forschungsgemeinschaft to C.K. (SFB630 and Forschungszentrum FZ82). J.S. was supported by a grant of the German Excellence Initiative to the Graduate School of Life Sciences, University of Würzburg.

[1] Rudolf Virchow Center for Experimental Biomedicine, Institute for Structural Biology, University of Wuerzburg, D-97080 Wuerzburg, Germany

[2] Institute of Pharmacy and Food Chemistry, University of Wuerzburg, Am Hubland, D-97074 Wuerzburg, Germany

[3] Institute for Chemical Biology & Drug Discovery, Department of Chemistry, Stony Brook University, Stony Brook, NY 11794-3400, USA

[4] Julius-von-Sachs Institute of Biosciences, Department of Pharmaceutical Biology, University of Wuerzburg, D-97082 Wuerzburg, Germany

[5] The abbreviations used are: ACP, acyl carrier protein; AcpM, acyl carrier protein of *M. tuberculosis*; CHS, chalcone synthase; CoA, coenzyme A; DMSO, dimethyl sulfoxide; FAS-I, type I fatty acid biosynthesis; FAS-II, type II fatty acid biosynthesis; KAS, β-ketoacyl-ACP synthase; KasA, *M. tuberculosis* β-ketoacyl-ACP synthase I; LC-MS, liquid chromatography - mass spectrometry; NMR, nuclear magnetic resonance; NOE, Nuclear Overhauser Effect; PE, phosphatidylethanolamine; PEG, polyethylene glycol; PI, phosphatidylinositol; PIM, phosphatidylinositol oligomannosides; PL, phospholipid; TCEP, tris(2-carboxyethyl)phosphine; TLM, thiolactomycin.

6.10 Supplementary Information

6.10.1 Supplemental Tables

Table S 6-1. Data Collection and Refinement Statistics.

	KasA - TLM5 - I	KasA - TLM5 - II	C171Q KasA
Crystallization			
Protein concentration (mg/ml)	8.6	8.6	8.1
Crystallization condition	0.2 M K/Na-tartrate 10% PEG 3350 1.5 mM TCEP	0.2 M K/Na-tartrate 10% PEG 3350 1.5 mM TCEP	0.1 M HEPES pH 7.5 40% PEG 200
Cryoprotectant	30% ethylene glycol	30% ethylene glycol	none
Data collection			
Cell dimensions			
a, b, c (Å)	77.6, 77.6, 147.7	77.2, 77.2, 146.9	74.2, 89.1, 183.5
α, β, γ (°)	90, 90, 120	90, 90, 120	90, 90, 90
Space group	$P3_121$	$P3_121$	$P2_12_12_1$
Resolution[a] (Å)	49.2-2.40 (2.53-2.40)	49.4-2.70 (2.85-2.70)	32.9-1.70 (1.79-1.70)
Observed reflections	148,026 (17,845)	78,398 (11,448)	555,297 (79,724)
Unique reflections	20,763 (2,978)	14,534 (2,084)	134,076 (19,388)
Completeness (%)	99.8 (99.9)	100.0 (100.0)	100.0 (100.0)
Average redundancy	7.1 (6.0)	5.4 (5.5)	4.1 (4.1)
R_{merge}[b] (%)	9.9 (59.6)	13.6 (58.0)	8.7 (56.4)
R_{pim}[c] (%)	3.7 (25.3)	6.3 (26.5)	4.8 (31.7)
<I / σ(I)>	13.9 (2.7)	9.2 (2.5)	10.5 (2.3)
Monomers per AU	1	1	2
Refinement			
Resolution (Å)	67.2-2.40	66.9-2.70	91.7-1.70
R_{cryst}[d] (%)	16.4	17.6	14.3
R_{free} (%)	21.6	24.2	17.0
Number of atoms	3,172	3,139	7,276
rmsd bond lengths (Å)	0.010	0.016	0.019
rmsd bond angles (°)	1.52	1.66	1.82
Average B-factor (Å^2)	52.2	42.3	19.5
Ramachandran-plot[e]			
Favored (%)	95.9	96.4	97.2
Allowed (%)	3.9	3.1	2.8
Outliers (%)	0.2	0.5	0.0
Maximum likelihood based estimated coordinate error (Å)	0.15	0.23	0.05

	C171Q KasA - TLM	**C171Q KasA - TLM3**	**C171Q KasA - TLM4**
Crystallization			
Protein concentration (mg/ml)	8.1	4.6	7.1
Crystallization condition	0.1 M HEPES pH 7.5 30% PEG 400	20 % PEG 3350	0.1 M HEPES pH 7.5 0.2 M NaCl 13% isopropanol
Cryoprotectant	5% PEG 400	25 % ethylene glycol	30% glycerol
Data collection			
Cell dimensions			
a, b, c (Å)	74.3, 89.3, 183.0	74.7, 89.3, 183.5	74.5, 89.5, 183.3
α, β, γ (°)	90, 90, 90	90, 90, 90	90, 90, 90
Space group	$P2_12_12_1$	$P2_12_12_1$	$P2_12_12_1$
Resolution[a] (Å)	48.5-1.95 (2.06-1.95)	36.1-1.80 (1.90-1.80)	33.8-1.75 (1.84-1.75)
Observed reflections	370,790 (53,438)	469,728 (66,187)	512,768 (73,736)
Unique reflections	87,684 (12,482)	114,325 (16,510)	123,806 (17,911)
Completeness (%)	98.3 (97.0)	99.9 (100.0)	99.9 (100.0)
Average redundancy	4.2 (4.3)	4.1 (4.0)	4.1 (4.1)
R_{merge}[b] (%)	8.4 (41.1)	10.1 (51.0)	8.0 (47.3)
R_{pim}[c] (%)	4.6 (22.4)	5.6 (29.1)	4.5 (26.3)
<I / σ(I)>	15.6 (3.7)	9.1 (2.4)	11.3 (2.9)
Monomers per AU	2	2	2
Refinement			
Resolution (Å)	91.5-1.95	91.7-1.80	91.7-1.75
R_{cryst}[d] (%)	13.8	16.0	14.0
R_{free} (%)	17.3	19.6	16.6
Number of atoms	7,131	7,295	7,303
rmsd bond lengths (Å)	0.014	0.014	0.018
rmsd bond angles (°)	1.64	1.64	1.86
Average B-factor (Å^2)	19.8	25.9	19.9
Ramachandran-plot[e]			
Favored (%)	97.0	97.7	97.2
Allowed (%)	3.0	2.3	2.8
Outliers (%)	0.0	0.0	0.0
Maximum likelihood based estimated coordinate error (Å)	0.07	0.06	0.05

	C171Q KasA - TLM18	**C171Q KasA - TLM5**	**C171Q KasA - TLM6**
Crystallization			
Protein concentration (mg/ml)	8.1	7.1	4.9
Crystallization condition	0.1 M Mg-formate 15% PEG 3350	0.2 M KSCN 15% PEG 3350	0.1 M Tris pH 7.5 15% PEG 6000
Cryoprotectant	27% ethylene glycol	25% ethylene glycol	25% ethylene glycol
Data collection			
Cell dimensions			
a, b, c (Å)	74.3, 88.9, 184.3	74.3, 89.1, 183.6	74.5, 89.1, 183.8
α, β, γ (°)	90, 90, 90	90, 90, 90	90, 90, 90
Space group	$P2_12_12_1$	$P2_12_12_1$	$P2_12_12_1$
Resolution[a] (Å)	33.7-1.80 (1.90-1.80)	28.5-1.50 (1.58-1.50)	36.0-1.80 (1.90-1.80)
Observed reflections	565,025 (81,773)	730,880 (92,296)	463,195 (66,841)
Unique reflections	113,762 (16,455)	194,886 (28,227)	113,933 (16,471)
Completeness (%)	100.0 (100.0)	99.9 (99.8)	100.0 (100.0)
Average redundancy	5.0 (5.0)	3.8 (3.3)	4.1 (4.1)
R_{merge}[b] (%)	11.3 (61.1)	6.8 (43.6)	9.9 (58.9)
R_{pim}[c] (%)	5.6 (29.9)	4.0 (28.2)	5.6 (33.2)
<I / σ(I)>	10.0 (2.5)	11.1 (2.6)	10.2 (2.3)
Monomers per AU	2	2	2
Refinement			
Resolution (Å)	92.2-1.80	91.8-1.50	91.9-1.80
R_{cryst}[d] (%)	13.9	13.6	14.5
R_{free} (%)	16.8	15.6	17.3
Number of atoms	7,387	7,518	7,269
rmsd bond lengths (Å)	0.016	0.016	0.017
rmsd bond angles (°)	1.71	1.78	1.73
Average B-factor ($Å^2$)	24.1	23.6	20.0
Ramachandran-plot[e]			
Favored (%)	97.1	97.2	96.7
Allowed (%)	2.9	2.7	3.3
Outliers (%)	0.0	0.1	0.0
Maximum likelihood based estimated coordinate error (Å)	0.05	0.03	0.06

[a] Values in parenthesis refer to the highest resolution shell

[b] $$R_{merge} = \sum_{hkl}\sum_{i}\left|I_i - \langle I\rangle\right| \Big/ \sum_{hkl}\sum_{i} I_i$$

[c] $$R_{pim} = \sum_{hkl}\left[1/(N-1)\right]^{1/2}\sum_{i}\left|I_i - \langle I\rangle\right| \Big/ \sum_{hkl}\sum_{i} I_i$$ (173)

[d] $$R_{cryst} = \sum_{hkl}\left|F_{obs} - F_{calc}\right| \Big/ \sum_{hkl} F_{obs}$$

[e] According to Molprobity (172)

Table S 6-2. Mass-spectrometric quantification of PEs and PIs bound to wild-type KasA, C171Q KasA and in the total lipid extracts of *M. smegmatis* mc^{2}155.

	amount of PE and PIs		
	KasA (pmol/nmol protein)	C171Q KasA (pmol/nmol protein)	*M. smegmatis* (pmol/mg pellet)
(16:0,19:0)PI	59.84	2042.34 ± 585.82	752.22 ± 222.19
(16:0,17:0)PI	28.57	690.78 ± 206.10	88.85 ± 27.18
(16:1,19:0)PI	n.d.[a]	256.52 ± 68.71	42.70 ± 10.37
(16:0,16:1)PI	n.d.	132.67 ± 39.17	9.58 ± 3.48
(16:1,17:0)PI	n.d.	116.81 ± 29.70	6.61 ± 0.91
(16:0,19:0)PE	n.d.	50.27 ± 9.34	244.38 ± 24.07
(16:0,16:0)PE	n.d.	39.20 ± 11.86	302.62 ± 55.58
(16:0,18:1)PI	n.d.	33.52 ± 10.91	31.71 ± 20.81
(16:0,16:1)PE	n.d.	13.68 ± 2.58	38.92 ± 6.85
(16:0,19:1)PE	n.d.	4.40 ± 0.78	10.27 ± 1.33
(19:0,19:0)PE	n.d.	n.d.	291.83 ± 80.70
(16:0,18:1)PE	n.d.	n.d.	110.33 ± 42.82
(16:0,18:0)PE	n.d.	n.d.	65.04 ± 10.99
(18:0,19:0)PE	n.d.	n.d.	39.14 ±11.17
(19:0,17:0)PE	n.d.	n.d.	24.41 ± 6.44
(18:1,19:0)PE	n.d.	n.d.	21.30 ± 2.82
(16:1,18:1)PE	n.d.	n.d.	14.13 ± 4.86
(19:0,19:1)PE	n.d.	n.d.	11.72 ± 3.08
(16:1,18:1)PI	n.d.	n.d.	6.54 ± 1.50
(18:0,18:1)PE	n.d.	n.d.	4.86 ± 0.22
(16:0,17:1)PE	n.d.	n.d.	4.60 ± 0.64
(18:0,19:1)PI	n.d.	n.d.	2.78 ± 2.01
(18:1,19:1)PI	n.d.	n.d.	1.29 ± 1.82

[a] n.d. = not detected

6.10.2 Supplemental Figures

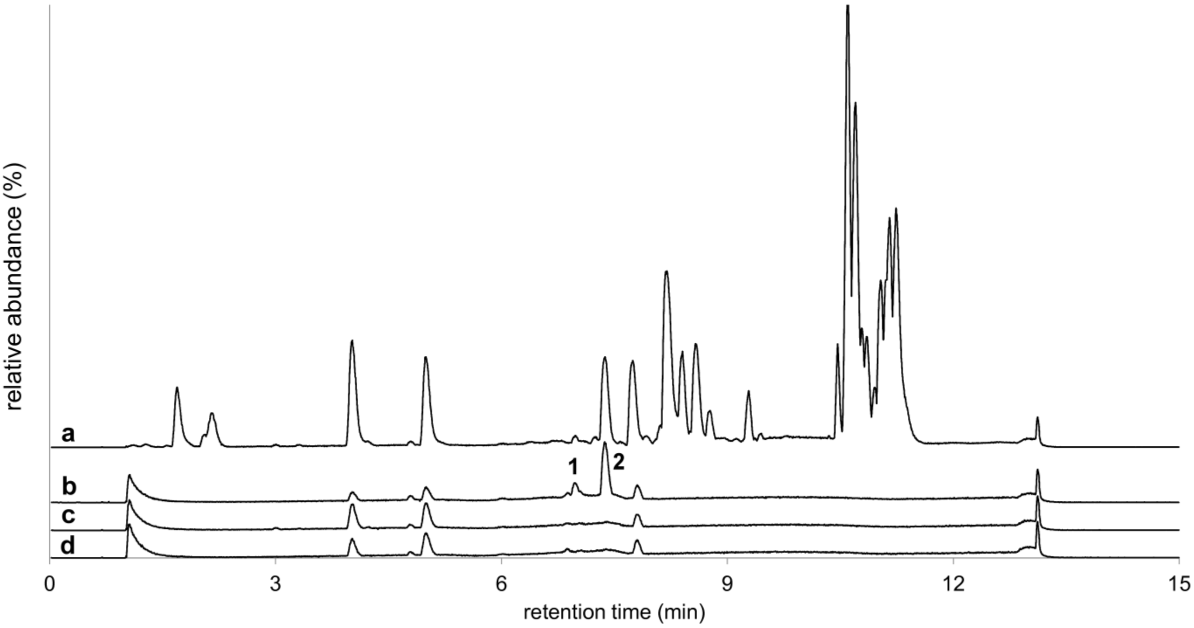

Figure S 6-1. Total ion chromatogram (TIC) of lipid extracts of *M. smegmatis* pellets (a) and protein fractions (b-c). TICs are depicted for samples of *M. smegmatis* total lipid extract (a), C171Q KasA variant (b), wild-type KasA protein (c) and the extraction buffer (d). Peaks unique for C171Q KasA and detectable in the total lipid extract of *M. smegmatis* were identified measuring the exact mass of deprotonated ions (accuracy of 3 mDa) and fragments of molecule ions (presence of fatty acyl chains). Identified lipids shown in the TICs are 1 = (16:0,17:0)PI, 2 = (16:0,19:0)PI.

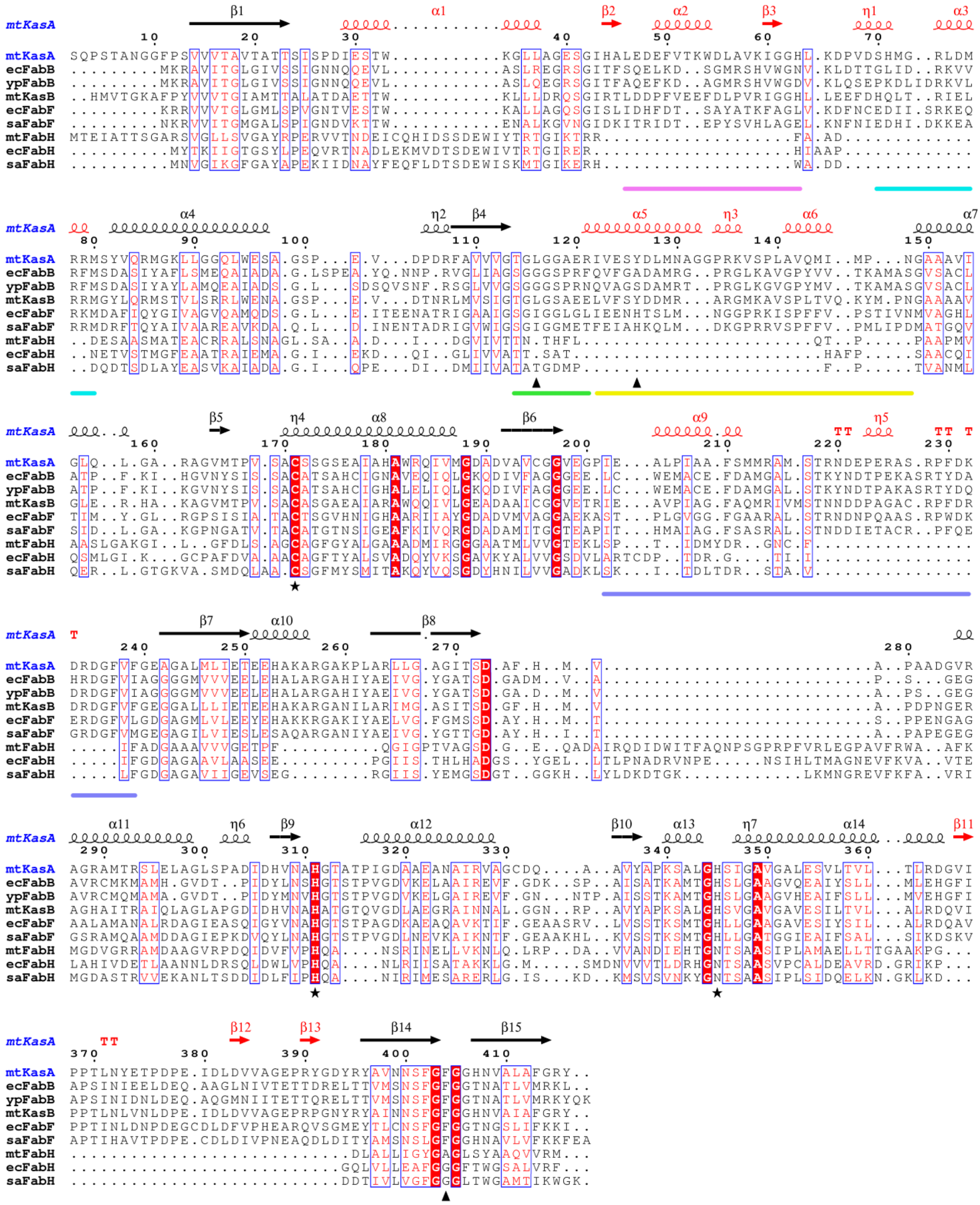

Figure S 6-2. Sequence Alignment of KAS Enzymes. Secondary structure matching (SSM) alignment of β-ketoacyl-ACP synthases I, II and III (PDB-entries: 2WGE, 2VB7, 3OYT, 2GP6, 1KAS, 2GQD, 1M1M, 3IL9, 3IL7) was performed by PDBe Fold (149). The bacterial sources are indicated by the first two letters of the protein names (mt = *Mycobacterium tuberculosis*, ec = *Escherichia coli*, yp = *Yersinia pestis*, sa = *Staphylococcus aureus*). The KasA secondary structure calculated with DSSP is depicted above the aligned sequences (150). The secondary structure elements accentuated in red reflect the N- and C-terminal KasA insertions. Flexible KasA regions contributing to acyl-substrate recognition are highlighted below the aligned sequences as bars colored in magenta, cyan, green, yellow and lilac (the same color code as in Figure 6-5). The catalytic and gatekeeper residues are indicated by black stars and triangles, respectively. This Figure was prepared using ESPript (151).

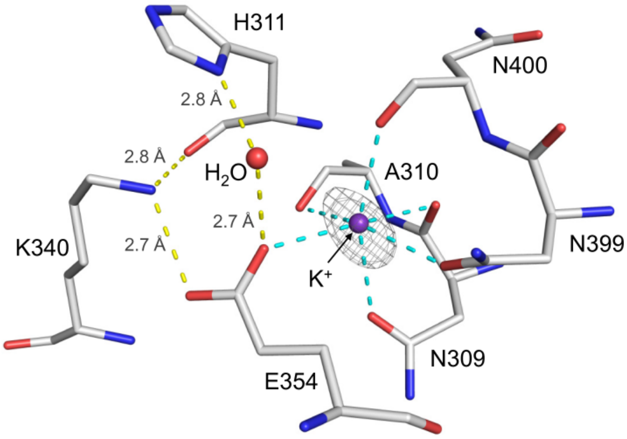

Figure S 6-3. Potassium Cation Binding Site. A potassium ion is bound close to His311 in all obtained KasA structures. The octahedral K^+ binding site (highlighted with cyan dashes) consists of the main chain carbonyl oxygens of Asn309, Ala310 and Asn400 (distances of 2.76 ± 0.02 Å, 2.97 ± 0.05 Å and 2.71 ± 0.03 Å for all C171Q KasA-structures) and the side chain oxygens of Asn309, Glu354 and Asn399 (distances of 2.68 ± 0.04 Å, 2.58 ± 0.04 Å and 2.59 ± 0.04 Å). A water molecule and Lys340 connects the K^+ ion with the catalytic residue His311 via Glu354. Similar cation binding sites are present in all structurally characterized KAS I and II enzymes (141). However, the identification of the bound cation has, to our knowledge, never been addressed thoroughly and most studies interpreted the cation density as NH_4^+, Na^+ or Mg^{2+} depending on the crystallization conditions (17,68,141). We unambiguously identified a potassium cation by analyses of the cation binding site and coordination geometry (276-278), crystal diffraction data and results from inductively-coupled plasma optical emission spectrometry (ICP-OES). An anomalous difference omit map (λ = 1.7 Å) is depicted at 5σ as a gray mesh.

6.10.3 Supplemental Movies

Movie S 6-1. Opening Movement of the Gatekeeping Units. Using LSQMAN, the frames for this animation were produced by the calculation of 'semi-plausible' intermediate states (morphing with internal coordinates including C_α and side chain atoms) between the structures KasA - TLM (PDB-entry 2WGE), KasA (PDB-entry 2WGD), KasA - TLM5 - I and C171Q KasA - TLM5 (148). The phospholipid molecules (which only were observed for the final state but are displayed throughout the animation for clarity) are shown as ball-and-stick models in gray, the gatekeeping residues Leu116, Phe404 and Tyr126' as yellow sticks, Asp127' as orange stick model and the two subunits of KasA as a C_α ribbon model in cyan and green, respectively.

Movie S 6-2. Acyl-Channel Opening Mechanism. This movie was produced using the same trajectory as for Movie S 6-1 and shows an intersection of KasA. The phospholipid molecules (which only were observed for the final state but are displayed throughout the animation for clarity) are shown as ball-and-stick models in gray, the gatekeeping residues Leu116, Phe404 and Tyr126' as yellow sticks, Asp127' as orange stick model and the two subunits of KasA in cyan and green surface representation, respectively.

6.10.4 Supplemental Experimental Procedures

6.10.4.1 Lipidomics

Processing of chromatograms and peak detection were performed using the MassLynx software (version 4.1, Waters, Manchester, U.K.). Defined lipid species were searched for in the samples based on their exact m/z in the low energy function and two integral fragments (fatty acyl side chains) in the high energy function with an error tolerance of 3 mDa. The main lipid species were diacyl-glycero-3-phosphoethanolamines (PEs) and diacyl-glycero-3-phosphoinositols (PIs) with acyl side chains of hexadecanoate (C16:0), hexadecenoate (C16:1), hexadecadienoate (C16:2), hexadecatrienoate (C16:3), heptadecanoate (C17:0), heptadecenoate (C17:1), octadecanoate (C18:0), octadecenoate (C18:1), octadecadienoate (C18:2), octadecatrienoate (C18:3), nonadecanoate (C19:0), nonadecenoate (C19:1). The species defined as their m/z and RT were then assembled into an automated method within QuanLynx embedded in MassLynx for the systematic integration of the identified lipid species in the extracts. For quantification of the PIs and PEs in the injected samples, 25 ng of (16:0,18:0)PI and (18:1,18:1)PE were used as internal standards.

7 Discussion

7.1 *S. aureus* FabI

7.1.1 Substrate, Cofactor and Inhibitor Recognition

The enoyl-ACP reductase FabI catalyzes the NAD(P)H-dependent reduction of the *trans*-2-enoyl-ACP double bond (51). In contrast to classical FabI proteins, the *S. aureus* homologue uses NADPH instead of NADH for this purpose (78,108). Thus, we investigated the molecular basis for this unique cofactor specificity and revealed that an RKXXS-motif is responsible for the favorable binding of the additional 2'-phosphate of NADPH (chapter 2, Figure 2-7). Due to the long-range character of the electrostatic interactions between the negatively charged cofactor and the positively charged residues Arg40 and Lys41, cofactor specificity is mainly conferred via an increased k_{on} value (chapter 5). The electrostatically steered binding process of the bulky NADPH cofactor (261) presumably is accompanied by structural rearrangements (e.g. of helix α2) leading from a wide major portal opening (Figure 2-5A-E, Figure 4-9 and Figure S 5-6) to a more closed form of the enzyme. Although a structure of the binary saFabI-NADPH complex is needed to finally prove this hypothesis, a study of *Debaryomyces hansenii* xylose reductase points out that NADPH has the ability to pre-form the enzyme conformation that is required for the binding of the substrate (279).

According to the ordered bi-bi mechanism observed for FabI (51), the cofactor is bound first and is followed by the substrate. Based on the chemical and dynamic properties of the saFabI binding crevice, the substrate binding mode was established using a validated docking approach (Figure 5-3A). The presented studies clearly reveal that the enoyl-ACP thioester carbonyl of the substrate binds to an oxyanion hole formed by the Tyr157 hydroxyl group and the 2'-OH of the NADPH nicotinamide ribose (Figure 5-3E). In addition, the terminal phosphopantetheine peptide is hydrogen bonded to Ser197 and the backbone of Ala97, which may serve as a polar anchor in the predominantly hydrophobic saFabI binding pocket (Figure 5-3A). Taken together with the known stereochemistry of the catalyzed reaction (Figure 5-1) (112,113,280), the relative orientation of cofactor and substrate unambiguously suggests how the reaction has to proceed mechanistically (chapter 5). Furthermore, a structurally and temporally conserved chain of water molecules towards a water-basin inside the homo-tetrameric enzyme was found to be important for hydride and proton transfer (Figure 5-4B). Similar water-networks connecting the active site with bulk solvent are commonly observed for enzymatic systems (247). Such water-chains might therefore be essential for the desolvation and re-hydration of the binding site upon substrate uptake and product release as well as for the delivery or uptake of protons needed for or formed during the catalytic reaction, respectively (247). Thus it is not very surprising that the D249A mutant, which led to the disruption of the FabI water-chain (Figure 5-4F), displayed a severely compromised catalytic activity.

Such a mutant, which hinders water molecules from flowing out of or into the binding pocket, likely will also be characterized by impaired loop dynamics (comparable to a blocked air-pump). For many enzymes it was suggested that the closure of a flexible loop accompanies the catalytic reaction. Loop closure might, thus, be an important mechanism to lower the energy of the transition state by placing the substrate into a desolvated protein environment (240). The FabI substrate binding loop (SBL) may fulfill a similar function and it is therefore particularly interesting to investigate the conformational states that are sampled along the reaction coordinate of substrate binding and turnover. Remarkably, the saFabI binding site is completely rearranged in the apo enzyme with respect to the presumably fully 'closed' state of the diphenyl ether bound structures (Figure 2-5). Since inhibitor binding can be assumed to closely resemble substrate recognition (239), different inhibitors were used as a tool to sample and provide several structural snapshots for induced-fit ligand binding and substrate turnover (Figure 4-9). These snapshots were highly informative since the conformational states involved in such processes are rarely known at the molecular level due to their transient nature (239). MD-simulations of saFabI with removed cofactor and inhibitor (PT400) consistently recapitulated key features of the crystallographically observed states (Figure 4-7, Figure 5-5 and Figure S 5-6). Given the lipophilicity and size of the enoyl-substrate, the observed structural variations will be required for substrate uptake, but may in addition be involved in the recognition process of the acyl carrier protein (ACP) carrying this cargo. Based on a FabI-ACP complex structure (107), a reinterpreted model for the interaction between FabI and ACP could be derived (Figure 5-6), which is fully consistent with the chemical binding site characteristics, the proposed mechanism, and the conformational adaptability of saFabI (chapter 5).

A comparison of saFabI with FabI proteins from other bacteria revealed unique properties of the *S. aureus* homologue, which can be related to its exceptional mobility (chapter 2, Figure 2-2C). SaFabI undergoes a dimer-tetramer transition upon ligand uptake that might cause the observed positive cooperativity of cofactor and substrate binding (Figure 2-6, Figure S 2-3, Figure S 2-5). Based on a comparison of the ternary saFabI-NADP(H)-inhibitor complexes with the apo-structures, it can be assumed that cofactor and enoyl-ACP binding to one subunit triggers structural rearrangements of two loop regions establishing the full tetramer interface and thereby facilitating the same conformational changes in the neighboring monomers (Figure 2-5G and Figure 2-6). Consistently, these loops were found to display enhanced flexibility in MD-simulations of monomeric and dimeric saFabI assemblies compared to simulations of the homo-tetramer (Figure 5-5A). For both, crystal structures (Figure 2-5G) and MD-simulations (Figure 5-5A), the conformational change of the SBL-2 propagates from the dimer-dimer interface (Figure 2-6) to the amino acid stretch 95-97, which contributes to the binding of the phosphopantetheine (Figure 5-2C and Figure 5-3C).

These unique characteristics of saFabI might have evolved to enable the turnover of branched-chain substrates required for the production of branched-chain fatty acids (BCFA) (chapter 2). Indeed, in contrast to classical FabI enzymes, the *S. aureus* homologue is qualified to process branched first-round substrates efficiently (Table 2-3). Importantly, BCFAs are required for the fitness of *Staphylococci* and related BCFA-producing bacteria (146,166). Since the human blood serum only contains a minimal amount of BCFA (147), the uptake of exogenous fatty acids might not fully satisfy the requirements of such bacteria during infection. A key question thus is whether unsaturated fatty acids can effectively replace branched-chain fatty acids to allow *S. aureus* growth *in vivo* despite the inhibition of FAS-II. Very recently, Sun *et al.* explicitly showed that the survival of *Listeria monocytogenes*, a pathogen that produces BCFAs (86), is compromised during an infection if BCFAs are lacking (281). Hence, it seems very likely that the need of *S. aureus* for the rarely occurring

BCFAs provides a rationale why this organism, in contrast to other Gram-positive bacteria such as *Streptococci*, developed a strategy to limit the uptake of exogenous fatty acids (chapter 1.3.4) (89) and, thus, is sensitive to the inhibition of the FAS-II pathway as demonstrated by the *in vivo* efficacy of several saFabI inhibitors (chapter 4) (92,100,101). Indeed, the lack of a block of the AccABCD function by exogenous fatty acids in the case of *S. aureus* led to a residual proportion of 37.7% BCFAs amongst all fatty acids of this organism when supplying oleic acid in the growth medium (89). Similarly, *B. subtilis* requires at least 28% BCFA for growth (86) and thus a minimal amount of approx. 30% BCFAs may be essential for BCFA-producing bacteria in general. Hence, the fatty acid profile of the human blood serum containing only 1% BCFAs does not fulfill the requirements of these bacteria (147) assuming that they have not developed a mechanism to accumulate BCFAs (90). In summary, these findings suggest that saFabI remains a valid drug target for the development of antibacterials that interfere with the integrity of the bacterial cell membrane, which is a known concept for antibiotics such as polymyxins (Table 1-1).

7.1.2 Molecular Determinants of Affinity and Selectivity

The numerous saFabI structures in complex with different diphenyl ether and pyridone inhibitors solved in this thesis served as a basis to rationalize the inhibitory and kinetic characteristics of these compounds (in particular chapters 3 and 4). Using various 4-, 5-, 2'-, 3'- and 4'-substituents, the saFabI binding cavity was probed thoroughly, providing a platform to design molecules with improved pharmacological properties. Similar to the thioester carbonyl of the substrate (Figure 5-3), all investigated inhibitors were found to be hydrogen bonded to the oxyanion hole formed by Tyr157 and the 2'-OH of the NADP(H) nicotinamide ribose (e.g. Figure 3-6). This result extends to all structurally characterized FabI-inhibitor complexes (Figure 5-2B) underlining the hotspot characteristics of the oxyanion hole. Guided by this central interaction, all analyzed inhibitors display a conserved overall binding mode. For instance, B-ring 2'-substituents were uniformly found to be directed towards a small pocket formed by the cofactor, Ala95 and Ser197 (Figure 3-8). This highlights that even though saFabI is a remarkably flexible enzyme, shape complementarity remains a fundamental principle. PT119, which carries a 5-hexyl and a 2'-cyano substituent on the diphenyl ether scaffold, constitutes an impressive example underlining the potential of this simple concept. Compared to 5-methyl-2-phenoxyphenol (PT53), the larger 5- and 2'-substituents of PT119 nicely fill additional side pockets (Figure 3-7B and Figure 3-8) leading to a 40-fold increase in affinity and residence time (Table 3-1).

Despite the structural similarity between diphenyl ether and pyridone saFabI inhibitors, diphenyl ethers are slow-binding inhibitors whereas pyridones display rapid-reversible characteristics (Figure 4-3). Moreover, these two scaffolds target different states of the catalytic cycle - pyridones preferably interact with the E-NADPH complex and diphenyl ethers with E-NADP$^+$ after product release (Figure 4-2B). This differing mechanism of inhibition likely explains the slow onset of saFabI inhibition by diphenyl ethers since the binary E-NADP$^+$ complex generated via catalysis is present at a much lower concentration compared to E-NADPH (chapter 4). Thus, the closure of the SBL presumably is not the slow step of diphenyl ether binding. Accordingly, the opening of the SBL was found to occur on the ns-timescale in an MD-simulation of saFabI excluding cofactor and inhibitor. The distinct modes of inhibition additionally suggest that pyridone and diphenyl ether-bound structures may represent different states along the reaction coordinate of the hydride transfer reaction. Whereas pyridones are more substrate-like, diphenyl ethers closely resemble the transition state of the reaction (Figure 4-2D). In line with this hypothesis, the corresponding crystal structures differ with respect to the conformation of the SBL (Figure 4-9). A comparison of the diphenyl ether and pyridone inhibitors is also very informative with respect to their spectrum of antibacterial activity (chapter 4). Whereas the clinical candidate CG400549 displays a *Staphylococcus*-restricted spectrum, diphenyl ethers such as MUT056399 are active against a broader range of pathogenic bacteria (4,31,102). On a molecular basis, the specificity of CG400549 can be explained by the enlarged saFabI cavity, which facilitates binding of the bulky CG400549 inhibitor and is likely also required for the synthesis of BCFAs (Figure 4-5).

For future drug design projects it is key to unravel the molecular determinants conferring high affinity to saFabI inhibitors. In combination with the observed SAR-profile, a close inspection of all structures presented here reveals that small substituents are tolerated sterically at the 4- and 2'-positions of the basic bisaryl system. However, in line with an SAR-study of *Bacillus anthracis* FabI (6), larger 5- and 3'/4'-groups can be used since they extend towards the minor and major portal, respectively (Figure 3-7A and Figure 5-2C). Consistently, an SAR-study with a large series of diphenyl ethers indicated that different substituents are tolerated at the B-ring 4'-position (102).

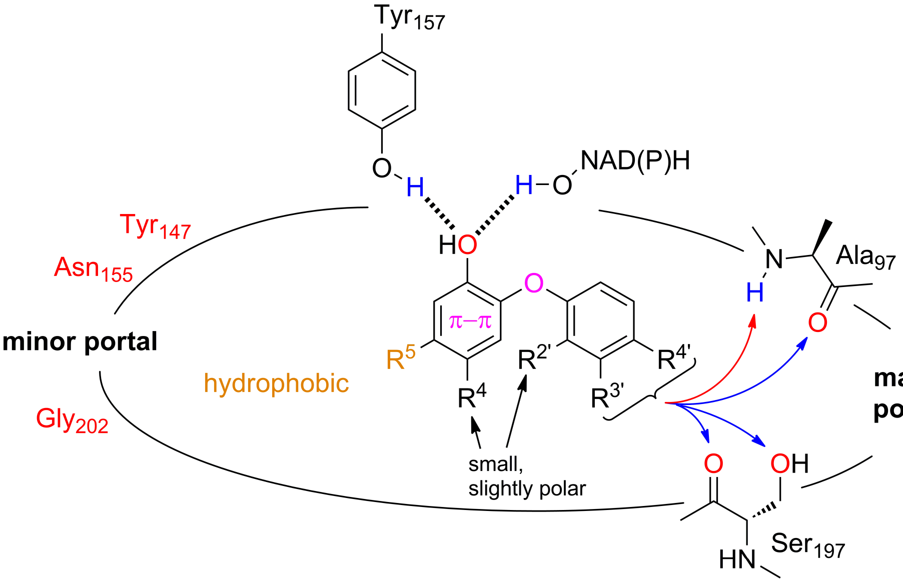

Figure 7-1. Determinants of saFabI affinity. This scheme summarizes molecular features that led or may lead to enhanced saFabI affinity. Hydrogen bond donors are depicted in blue, hydrogen bond acceptors in red and hydrophobic features in orange. Additional important characteristics of the basic diphenyl ether or pyridone bisaryl system are highlighted in magenta. The scheme contains the results from the work presented here (in particular chapters 3 and 4) and knowledge derived from further computational analyses (e.g. hotspot analyses); in addition, it takes similar SAR-studies into account (5,6).

As highlighted above, potent saFabI inhibitors should contain a hydrogen bond acceptor that can bind to the oxyanion hole (Figure 7-1). Interestingly, the binding crevice of saFabI comprises two further polar amino acid patches towards the major and minor portal, respectively. The former hydrophilic region mainly consists of Ser197 and the backbone of Ala97, which are contacted by the phosphopantetheine moiety of the substrate (Figure 5-3A). In particular, Ala97 has been shown to provide an interaction platform for the potent inhibitors triclosan (Figure 2-4B and Table 3-1) and CG400549 (Figure 4-5A, Table 4-1). The

4'-chlorine of triclosan and the 3'-NH_2 group of CG400549 interact with the Ala97 carbonyl group via a halogen and hydrogen bond, respectively. Furthermore, naphthyridinones are ideally suited to interact with Ala97 in a dual hydrogen bonding network (Figure 4-1) (5,101). Thus, an elaborate choice of 3'- and 4'-substituents containing distinct hydrogen bond donors/acceptors or halogens/sulfur can lead to an improvement of affinity in particular for the *S. aureus* homologue, for which the interactions with Ala97 are protected from solvent by the side chain of Met99 (Figure 4-5D). At the minor portal, the backbone carbonyl oxygens of Asn155 and Gly202 as well as the free electron pair of the Tyr147 hydroxyl group might be additional anchor points for hydrogen bond donors (Figure 7-1). Accordingly, three water molecules were found to be present in this region of the ternary complex structures for inhibitors with small 5-substituents such as PT53 (Figure 3-7D). The finding that the 5-hexyl group of PT04 expels these water molecules suggests that hydrophilic moieties might be used at the terminus of this elongated alkyl chain to mimic the interactions observed for the expelled water molecules. Closer towards the bisaryl scaffold, however, high-affinity inhibitors commonly exhibit hydrophobic features including aromatic rings, alkyl groups or halogens (Figure 7-1, chapters 3 and 4) (5,6,102), which reflect the lipophilic properties of the corresponding part of the saFabI crevice accommodating also the fatty acyl chain (Figure 5-2C and Figure 5-3C). In contrast, small substituents are favorable at the 4- and 2'-positions. The SAR at these positions is slightly different for diphenyl ethers and pyridones, presumably due to the different SBL conformations (chapters 3 and 4). Whereas a 2'-CN group increases the affinity of diphenyl ethers, this group is less favorable for pyridones for which a 2'-methyl substituent provides a good choice. Finally, the characteristics and interactions of the bisaryl system itself are highly informative. The A-ring can engage in π-π stacking interactions with the nicotinamide ring of the cofactor and, thus, the electronic properties of this ring might influence binding affinity depending on the oxidation state of the cofactor. Furthermore, it should be noted that the nature of the atom linking the two aromatic rings of the basic bisaryl scaffold is of particular importance. In the biologically active conformation, the two rings display an approximately orthogonal geometry (Figure 3-6). As mentioned previously (9) and confirmed by a search of the Cambridge Structural Database (CSD), this is the preferred geometry for a bisaryl system with a bridging oxygen whereas a methylene bridge induces a "clamp-like" structure (Figure 7-2). Hence, the bridging oxygen seems to be ideally suited to pre-form the biologically active conformation as highlighted by the higher intrinsic potency of 4-pyridones compared to 2-pyridones (chapter 4). Similarly, early work with diphenyl ethers indicated that a bridging oxygen is superior compared to sulfur or methylene linkages (97,99), which can be related to an entropic advantage upon binding.

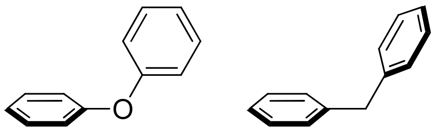

Figure 7-2. Preferred geometries of diphenylethers and diphenylmethanes (9).

7.1.3 Rational Residence Time Optimization - a Case Study with SaFabI

Drug-target kinetics are crucial during the lead optimization phase of a drug discovery project (chapter 1.2.4) (44). Importantly, the correlation between affinity and residence time observed for diphenyl ether saFabI inhibitors (Figure 3-5) permits the rationalization of the differing dissociation kinetics using the knowledge gained from the ground-state ternary complex structures (chapter 3). Thus, the saFabI SAR-profile can be extended to a structure-kinetic relationship (SKR; term used in (261)) (Figure 7-1). Since the k_{on} values are very similar among diphenyl ethers and pyridones (chapter 4), the transition state barrier to association seems to be relatively invariant suggesting that the slow-off behavior of diphenyl ethers is exclusively determined by their potent affinities (Figure 4-9A). Consequently, it is very important to answer the question where the higher intrinsic potency of diphenyl ethers with respect to pyridones originates from. As for many enzymes (238,245), the closure of the flexible SBL will lead to the extrusion of water molecules from the binding site and, thus, to a strengthening of electrostatic interactions via a lowered effective dielectric constant. The fully closed SBL for diphenyl ether-bound ternary complex structures (Figure 4-7A) and the resulting buried electrostatic interaction between the presumably deprotonated diphenyl ethers (see also chapter 3) and the positive charge of the oxidized cofactor might therefore explain the long residence times of these inhibitors. Within the investigated diphenyl ether series, the residence time was shown to increase using bulky, hydrophobic 5-substituents or small and slightly polar 2'-groups based on their good steric fit (chapter 3).

Since only little is known about the molecular principles that govern drug-target kinetics (44), this case study should also be discussed in more general terms. Based on a recent review, we point out that to date only one convincing strategy exists how to rationally modulate residence time (44). Schmidtke and coworkers demonstrated that water-shielded hydrogen bonds provide kinetic traps leading to a decrease in off-rates (261). Water molecules, which usually initiate the dissociation process, are hindered to access such buried interactions. In agreement, the closed SBL shields the saFabI binding site and thus the central hydrogen bonding network to the diphenyl ether inhibitors. In contrast, the rapid-reversible pyridone inhibitors do not induce the fully closed state of the SBL (Figure 4-7A). Moreover, elongating the diphenyl ether 5-alkyl substituent from methyl (PT53) to hexyl (PT04) leads to a progressively shielded central hydrogen bond and consequently to a 25-fold enhancement of residence time (Figure 3-7, Table 3-1). However, this concept may not be limited to hydrogen bonds since the buried electrostatic interaction between $NADP^+$ and the negatively charged phenolate oxygen likely contributes to the slow off-rates of diphenyl ethers. Furthermore, the introduction of a 2'-cyano group which binds to a water-shielded side pocket of the saFabI cavity results in a decrease of the dissociation constant (Figure 3-8, Table 3-1). Thus, the concept suggested by Schmidtke et al. may be extended to water-shielded interactions with electrostatic contributions in general, which seem to be thermodynamically (lowered dielectric constant) and kinetically (hindered water access) favored in a desolvated, buried environment. Importantly, this concept can be directly related to the functionality of many enzymes since shielding from water - often via flexible loops - seems to be a fundamental principle promoting enzymatic processes by stabilizing the transition state(s) of the reaction (238,240,245). At the transition state the shielding will be maximal explaining why transition state analogues frequently exhibit slow-off, tight-binding characteristics (209,239,282). Hence it is pivotal to implement the knowledge with respect to catalysis in the design of new drugs targeting enzymatic systems.

7.1.4 New Concepts for Inhibitor Design

Which strategies can be derived from these studies to further improve or to develop novel saFabI inhibitors? Clearly, one focus must be on lowering the logP value of such compounds without affecting the affinity towards the rather hydrophobic saFabI binding pocket too much. This is an important factor to enhance the bioavailability and to decouple the FabI-specific mode of action from a non-specific biocidal effect observed for more hydrophobic compounds such as triclosan (102). In this regard, the two additional hydrophilic patches located close to the major and minor portal, respectively, can provide a platform to rationally design inhibitors with lower lipophilicity (Figure 7-1). It will be pivotal to identify the right balance between hydrophobic moieties binding to the fatty acyl pocket and more hydrophilic substituents taking advantage of the interactions observed for the phosphopantetheine linker (Figure 5-3A). Interestingly, the amide group of the cofactor's nicotinamide ring is rotated slightly out-of-plane in all observed saFabI crystal structures thereby presenting the amide oxygen to the binding pocket (Figure 5-2). An appropriately positioned hydrogen bond donor might hence be able to bind to this acceptor. For pyridone inhibitors, electron-donating groups on the A-ring might decrease the logP value and concomitantly strengthen the central hydrogen bonding network by enhancing the nucleophilicity of the pyridone oxygen, which would, thus, more closely mimic the oxyanion of the enolate intermediate (Figure 4-2D). Consequently, the introduction of a 5-alkoxy substituent might further improve inhibitors that are based on the very promising 4-pyridone scaffold (see also chapter 4).

Assuming that future studies can establish the relevance of the saFabI dimer-tetramer transition during ligand binding *in vivo*, the central cavity of the homo-tetramer might be accessible and provide an additional target site remote from the actual substrate binding crevice (Figure 2-2A). In fact, the same cavity was suggested to be druggable in InhA (115). Targeting this pocket in the case of saFabI might be promising for mainly two reasons. Firstly, compounds that would block the association of two dimers might hinder the cooperative structural changes establishing the substrate binding sites upon ligand uptake (Figure 2-5 and Figure 2-6). Furthermore, molecules that would still allow the association of two saFabI dimers but block the exchange of water molecules between the active site and the cavity inside the tetramer via the conserved water-chain (Figure 5-4), likely will impair the motions that are involved in substrate recognition and turnover and hinder the delivery of protons for catalysis (chapter 5) (247).

An additional aspect, which could be considered for the development of new inhibitors, is the required interaction between FabI and ACP. In recent years considerable progress has been made in the design of molecules that disrupt protein-protein interactions, which are essential for most biological processes (283). The protein-protein interface revealed by the new FabI-ACP model might serve as an additional target site for the development of compounds that interfere with substrate binding to enoyl-ACP reductases at the ACP level. In summary, such strategies may guide future drug design studies to combat the increasing clinical problem of MRSA-infections.

7.2 *M. tuberculosis* KasA

7.2.1 Substrate and Inhibitor Recognition

In contrast to common bacterial FAS-II condensing enzymes, the mycobacterial KasA protein can synthesize very hydrophobic fatty acids with up to 42 carbon atoms in length (268). For this purpose KasA has to enable the binding of long-chain acyl-AcpM substrates. Using a combined crystallographic and mass-spectrometric approach, co-purified phospholipids were identified inside the acyl binding cavity of the KasA C171Q variant (Figure 6-3). These molecules clearly delineate the geometry and extraordinary length of this hydrophobic channel, providing a rationale for the observed substrate specificity (Figure 6-4A). Furthermore, structural snapshots of an induced-fit binding mechanism were revealed, which explain how the hydrophobic acyl-chain can enter the KasA binding site without excessive solvent exposure. This was a fortuitous finding since transient states along the reaction coordinate of substrate binding are rarely characterized for enzymatic systems although substrate recognition frequently involves conformational changes (239). Incremental structural changes in the capping region of KasA involving considerable movements of three gatekeeper residues (Leu116, Tyr126' and Phe404) lead to the opening of the acyl-binding channel (Figure 6-6). AcpM likely triggers this process and injects the attached acyl-chain into the evolving cavity (for details see chapter 6 and Figure 6-4D). A similar concerted process can also be envisioned for FabI proteins, which are involved in the same biosynthetic pathway. The new FabI-ACP model suggests that ACP might trigger the closure of the substrate binding loop thereby establishing the tube-like binding cavity, which simultaneously can take up the enoyl-substrate (for details see chapter 5 and Figure 5-6F). Hence, similar induced-fit processes that couple the formation of an elongated binding site with the uptake of the fatty acyl chain, might have evolved for most FAS-II enzymes to allow the binding of their large and hydrophobic substrates. Indeed, different conformational states of the substrate binding site are known for many FAS-II enzymes such as InhA (207), FabL (156), FabG (284) and FabH (15,263,270).

Compared to the lead compound thiolactomycin, TLM5 and TLM6 display enhanced affinities towards the wild-type and C171Q KasA forms (16), which could be rationalized by additional hydrogen bonding interactions with the catalytic triad residue His345 (Figure 6-2E). Furthermore, the binding mode of these compounds suggests how the second substrate of the ping-pong reaction, malonyl-AcpM, may be oriented with respect to the KasA catalytic triad residues and, thus, provides a molecular basis to clarify the mechanism of the decarboxylation reaction (Figure 6-8).

7.2.2 New Concepts for Inhibitor Design

The investigation of the substrate recognition and turnover process by the drug target KasA has important impacts on the design of optimized KasA inhibitors. To enhance the affinity of inhibitors via cation-π interactions, quaternary ammonium substituents have been successfully used in the past to address protein pockets with a high content of aromatic amino acids (152). Thus, the design of molecules with a positive charge placed appropriately in the KasA aromatic box binding TLM 3-substituents (Figure 6-2D) could help to increase the affinity of KasA inhibitors. As exemplified by the 3-trifluoroacetyl group of the most potent inhibitor TLM6 (Figure 6-2E) (16), the conserved threonines 313 and 315 involved in phosphopantetheine binding might additionally be ideal anchors for dual hydrogen bond acceptors. Most importantly, however, the 3-acetyl group of TLM5 induces a partial opening of the acyl-binding channel in the wild-type enzyme which might be filled by hydrophobic moieties. To achieve a pharmacologically reasonable balance between hydrophobic and hydrophilic groups, the phosphopantetheine binding cavity should be addressed simultaneously.

In addition, the sampled structural snapshots along the reaction coordinate of the acyl-transfer may provide good starting points for virtual screening studies. It should also be noted that thiolactomycin provides an ideal lead compound for the development of molecules that inhibit all three mycobacterial condensing enzymes in order to reduce the propensity for resistance formation (4). Molecules inhibiting KasA should therefore always be tested against KasB and mtFabH. To avoid the development of molecules with pharmacologically problematic properties, it should additionally be analyzed whether such inhibitors interfere with the human FAS-system. Using the knowledge with respect to substrate recognition, a long-term goal might also be to block the interaction between condensing enzymes and AcpM by small molecules in order to develop novel anti-TB drugs.

7.3 Interaction between ACP and FAS-II Enzymes

The established models for the binding of ACP-substrates to saFabI (chapter 5) and KasA (chapter 6) do not only facilitate the design of novel compounds interfering with the interaction between FAS-II enzymes and ACP but also suggest strategies how structural information of the corresponding complexes could be gained.

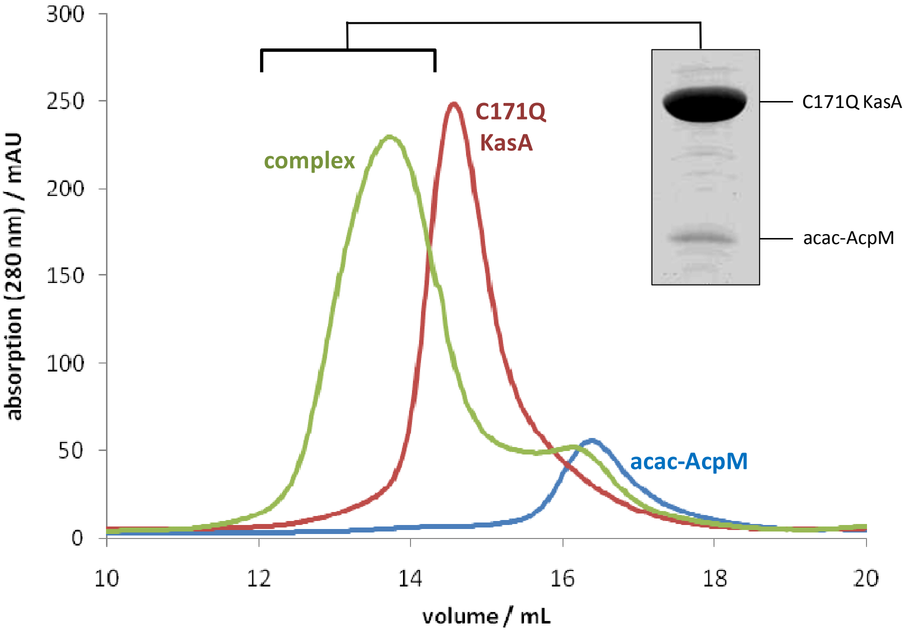

Figure 7-3. Interaction between the C171Q KasA variant and acetoacetyl-AcpM. Analytical size-exclusion chromatograms clearly indicate an interaction between these two components. Please note that the absorption at 280 nm and staining of the small, acidic AcpM is much weaker compared to KasA. Experiments were conducted in 20 mM Tris pH 7.8 and 200 mM NaCl with a C171Q KasA : acac-AcpM ratio of 1 : 2 (concentrations of 60 and 120 µM [according to photometric measurement, please see Chapter 9.2.2 for details], respectively).

Given that the C171Q KasA variant exhibits opened acyl- and phosphopantetheine-cavities (chapter 6) (17), malonyl-AcpM might easily access the binding site. Accordingly, analytical size-exclusion chromatography (aSEC) experiments indicated complex formation between the inactivated substrate analogue acetoacetyl-AcpM (acac-AcpM; Figure 7-4) and C171Q KasA (Figure 7-3; see chapter 9.2 for the purification of acac-AcpM). However, despite various attempts, the crystallization of the complex did not result in a structure with bound substrate. Thus, alternative strategies are necessary to finally obtain a KasA-AcpM complex structure. To further improve the stability of the resulting KasA-AcpM complex, the acetoacetyl-moiety could be extended to TLM5, which was shown to effectively mimic malonyl-AcpM (Figure 6-7C and Figure 7-4). Alternatively, a reactive chemical group might be attached to the phosphopantetheine linker of AcpM such that it selectively reacts with KasA amino acids (e.g. Thr313, Thr315 or Cys171) leading to a stable covalent complex. Finally, a study of Borgaro et al. suggests the usage of short peptides with the primary sequence of the AcpM helix α2 including Ser42 carrying the substrate (18). The reduction in size of the KasA interaction partner might facilitate crystal packing of the complex, in particular since the acyl carrier protein is known to be an intrinsically flexible protein (76).

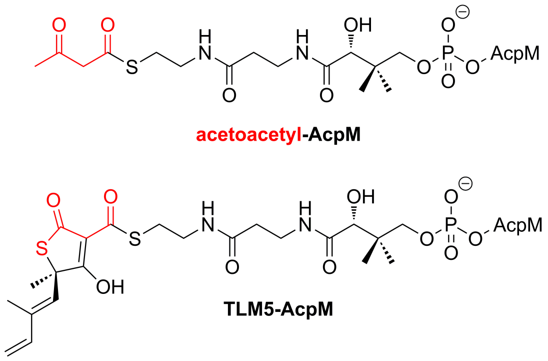

Figure 7-4. Malonyl-AcpM analogues for interaction studies with KasA. The acetoacetyl group of acetoacetyl-AcpM and the corresponding moiety of TLM5-AcpM is shown in red.

In contrast to the KasA interaction studies mentioned above, aSEC experiments with 150 µM saFabI and 300 µM crotonoyl-saACP (cro-saACP; see chapter 9.2 for the purification of cro-saACP) in the presence of 1.5 mM NADP$^+$ did not indicate complex formation (in 20 mM Tris pH 7.5 and 200 mM NaCl). However, co-crystallization of saFabI with cro-saACP and NADP$^+$ in a 1 : 3.5 : 10 ratio yielded a new crystal form using a precipitant solution composed of 0.1 M NaAc pH 4.5, 0.1 M MgCl$_2$ and 8% PEG 8000. Unfortunately, diffraction experiments with these very small crystals resulted in only a few weak reflections close to the center of the diffraction pattern indicating that the crystals contain protein molecules. Further optimization of these crystals might ultimately lead to the determination of a saFabI-saACP complex structure. The coupling of a potent inhibitor with ACP via a phosphopantetheine-like linker might be an even more promising strategy to achieve this goal. For instance, a comparison of the PT12-bound saFabI-structure with the putative enoyl-ACP substrate binding mode (Figure 5-3C) suggests that diphenyl ethers might be linked to ACP via a 4'-acyl moiety mimicking the phosphopantetheine (Figure 7-5). Similarly, isoniazid could be attached to AcpM as a warhead that could react with NAD$^+$ for interaction studies with the mycobacterial enoyl-reductase InhA (Table 1-2) (125). Even without the synthetically challenging coupling between an inhibitor and ACP, it might be worthwhile to use NAD(P)$^+$ and a diphenyl ether to trigger the closure of the SBL and thus to create the full electropositive surface for the interaction with ACP (Figure 5-6F). Alternatively, reproducing and soaking the encounter complex crystals of ecFabI-dodecenoyl-ACP (107) with NADH might initiate partial loop closure and substrate delivery and could, in principle, result in structural snapshots along the reaction coordinate. Moreover, trying to crystallize the FabI isoenzyme FabV in complex with its natural substrate could constitute a promising strategy since FabV is, in contrast to FabI, a monomer and thus crystal packing might occur more readily for the corresponding complex (118).

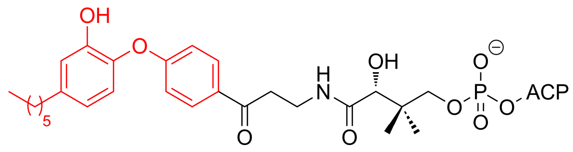

Figure 7-5. Diphenyl ether analogue coupled to ACP for the structural study of FabI-ACP complexes. The diphenyl ether moiety is depicted in red.

Complex structures between FAS-II enzymes and their natural ACP-substrates would reveal important information about substrate recognition and turnover that can be utilized in the development of novel drug candidates to combat multidrug-resistant pathogens.

8 References

1. Payne, D. J., Gwynn, M. N., Holmes, D. J., and Pompliano, D. L. (2007) Drugs for bad bugs: confronting the challenges of antibacterial discovery. *Nat Rev Drug Discov* **6**, 29-40
2. O'Shea, R., and Moser, H. E. (2008) Physicochemical properties of antibacterial compounds: Implications for drug discovery. *Journal of Medicinal Chemistry* **51**, 2871-2878
3. Simmons, K. J., Chopra, I., and Fishwick, C. W. (2010) Structure-based discovery of antibacterial drugs. *Nat Rev Microbiol* **8**, 501-510
4. Silver, L. L. (2011) Challenges of antibacterial discovery. *Clin Microbiol Rev* **24**, 71-109
5. Lu, X., Lv, M., Huang, K., Ding, K., and You, Q. (2012) Pharmacophore and Molecular Docking Guided 3D-QSAR Study of Bacterial Enoyl-ACP Reductase (FabI) Inhibitors. *Int J Mol Sci* **13**, 6620-6638
6. Tipparaju, S. K., Mulhearn, D. C., Klein, G. M., Chen, Y., Tapadar, S., Bishop, M. H., Yang, S., Chen, J., Ghassemi, M., Santarsiero, B. D., Cook, J. L., Johlfs, M., Mesecar, A. D., Johnson, M. E., and Kozikowski, A. P. (2008) Design and synthesis of aryl ether inhibitors of the Bacillus anthracis enoyl-ACP reductase. *ChemMedChem* **3**, 1250-1268
7. Payne, D. J., Warren, P. V., Holmes, D. J., Ji, Y., and Lonsdale, J. T. (2001) Bacterial fatty-acid biosynthesis: a genomics-driven target for antibacterial drug discovery. *Drug Discov Today* **6**, 537-544
8. Sacco, E., Covarrubias, A. S., O'Hare, H. M., Carroll, P., Eynard, N., Jones, T. A., Parish, T., Daffe, M., Backbro, K., and Quemard, A. (2007) The missing piece of the type II fatty acid synthase system from Mycobacterium tuberculosis. *Proc Natl Acad Sci U S A* **104**, 14628-14633
9. Brameld, K. A., Kuhn, B., Reuter, D. C., and Stahl, M. (2008) Small molecule conformational preferences derived from crystal structure data. A medicinal chemistry focused analysis. *J Chem Inf Model* **48**, 1-24
10. Lu, H., and Tonge, P. J. (2010) Drug-target residence time: critical information for lead optimization. *Curr Opin Chem Biol* **14**, 467-474
11. Takayama, K., Wang, C., and Besra, G. S. (2005) Pathway to synthesis and processing of mycolic acids in Mycobacterium tuberculosis. *Clin Microbiol Rev* **18**, 81-101
12. Maier, T., Leibundgut, M., and Ban, N. (2008) The crystal structure of a mammalian fatty acid synthase. *Science* **321**, 1315-1322
13. Olsen, J. G., Kadziola, A., von Wettstein-Knowles, P., Siggaard-Andersen, M., and Larsen, S. (2001) Structures of beta-ketoacyl-acyl carrier protein synthase I complexed with fatty acids elucidate its catalytic machinery. *Structure* **9**, 233-243
14. Theobald, D. L., and Wuttke, D. S. (2008) Accurate structural correlations from maximum likelihood superpositions. *PLoS Comput Biol* **4**, e43
15. Alhamadsheh, M. M., Musayev, F., Komissarov, A. A., Sachdeva, S., Wright, H. T., Scarsdale, N., Florova, G., and Reynolds, K. A. (2007) Alkyl-CoA disulfides as inhibitors and mechanistic probes for FabH enzymes. *Chem Biol* **14**, 513-524
16. Kapilashrami, K., Bommineni, G. R., Machutta, C. A., Kim, P., Lai, C. T., Simmerling, C., Picart, F., and Tonge, P. J. (2013) Thiolactomycin-Based beta-ketoacyl-AcpM synthase A (KasA) Inhibitors: Fragment-Based Inhibitor Discovery Using Transient 1D NOE NMR Spectroscopy. *J Biol Chem* **288**, 6045-6052

17. Luckner, S. R., Machutta, C. A., Tonge, P. J., and Kisker, C. (2009) Crystal structures of Mycobacterium tuberculosis KasA show mode of action within cell wall biosynthesis and its inhibition by thiolactomycin. *Structure* **17**, 1004-1013
18. Borgaro, J. G., Chang, A., Machutta, C. A., Zhang, X., and Tonge, P. J. (2011) Substrate recognition by beta-ketoacyl-ACP synthases. *Biochemistry* **50**, 10678-10686
19. Schiebel, J., Chang, A., Lu, H., Baxter, M. V., Tonge, P. J., and Kisker, C. (2012) Staphylococcus aureus FabI: Inhibition, Substrate Recognition, and Potential Implications for In Vivo Essentiality. *Structure* **20**, 802-813
20. Fischbach, M. A., and Walsh, C. T. (2009) Antibiotics for emerging pathogens. *Science* **325**, 1089-1093
21. Wright, G. D. (2007) The antibiotic resistome: the nexus of chemical and genetic diversity. *Nat Rev Microbiol* **5**, 175-186
22. Swanson, S., Gokulan, K., and Sacchettini, J. C. (2009) KasA, another brick in the mycobacterial cell wall. *Structure* **17**, 914-915
23. Bhatt, A., Molle, V., Besra, G. S., Jacobs, W. R., Jr., and Kremer, L. (2007) The Mycobacterium tuberculosis FAS-II condensing enzymes: their role in mycolic acid biosynthesis, acid-fastness, pathogenesis and in future drug development. *Mol Microbiol* **64**, 1442-1454
24. Schaeffer, M. L., Agnihotri, G., Volker, C., Kallender, H., Brennan, P. J., and Lonsdale, J. T. (2001) Purification and biochemical characterization of the Mycobacterium tuberculosis beta-ketoacyl-acyl carrier protein synthases KasA and KasB. *J Biol Chem* **276**, 47029-47037
25. Livermore, D. M. (1998) Beta-lactamase-mediated resistance and opportunities for its control. *J Antimicrob Chemother* **41 Suppl D**, 25-41
26. Courvalin, P. (2006) Vancomycin resistance in gram-positive cocci. *Clin Infect Dis* **42 Suppl 1**, S25-34
27. Uttley, A. H., Collins, C. H., Naidoo, J., and George, R. C. (1988) Vancomycin-resistant enterococci. *Lancet* **1**, 57-58
28. Fan, F., Yan, K., Wallis, N. G., Reed, S., Moore, T. D., Rittenhouse, S. F., DeWolf, W. E., Jr., Huang, J., McDevitt, D., Miller, W. H., Seefeld, M. A., Newlander, K. A., Jakas, D. R., Head, M. S., and Payne, D. J. (2002) Defining and combating the mechanisms of triclosan resistance in clinical isolates of Staphylococcus aureus. *Antimicrob Agents Chemother* **46**, 3343-3347
29. Pantosti, A., and Venditti, M. (2009) What is MRSA? *Eur Respir J* **34**, 1190-1196
30. Klevens, R. M., Edwards, J. R., Tenover, F. C., McDonald, L. C., Horan, T., and Gaynes, R. (2006) Changes in the epidemiology of methicillin-resistant Staphylococcus aureus in intensive care units in US hospitals, 1992-2003. *Clin Infect Dis* **42**, 389-391
31. Yum, J. H., Kim, C. K., Yong, D., Lee, K., Chong, Y., Kim, C. M., Kim, J. M., Ro, S., and Cho, J. M. (2007) In vitro activities of CG400549, a novel FabI inhibitor, against recently isolated clinical staphylococcal strains in Korea. *Antimicrob Agents Chemother* **51**, 2591-2593
32. Turnidge, J. D., Kotsanas, D., Munckhof, W., Roberts, S., Bennett, C. M., Nimmo, G. R., Coombs, G. W., Murray, R. J., Howden, B., Johnson, P. D., and Dowling, K. (2009) Staphylococcus aureus bacteraemia: a major cause of mortality in Australia and New Zealand. *Med J Aust* **191**, 368-373
33. Haddadin, A. S., Fappiano, S. A., and Lipsett, P. A. (2002) Methicillin resistant Staphylococcus aureus (MRSA) in the intensive care unit. *Postgrad Med J* **78**, 385-392
34. Ferber, D. (2010) Infectious disease. From pigs to people: the emergence of a new superbug. *Science* **329**, 1010-1011
35. Kaufmann, S. H. (2005) Robert Koch, the Nobel Prize, and the ongoing threat of tuberculosis. *N Engl J Med* **353**, 2423-2426

36. Dorman, S. E., and Chaisson, R. E. (2007) From magic bullets back to the magic mountain: the rise of extensively drug-resistant tuberculosis. *Nat Med* **13**, 295-298

37. WHO. (2012) World Health Organization: Global tuberculosis report 2012. *http://www.who.int/tb/publications/global_report/en/index.html*

38. Veyron-Churlet, R., Guerrini, O., Mourey, L., Daffe, M., and Zerbib, D. (2004) Protein-protein interactions within the Fatty Acid Synthase-II system of Mycobacterium tuberculosis are essential for mycobacterial viability. *Mol Microbiol* **54**, 1161-1172

39. Velayati, A. A., Masjedi, M. R., Farnia, P., Tabarsi, P., Ghanavi, J., Ziazarifi, A. H., and Hoffner, S. E. (2009) Emergence of new forms of totally drug-resistant tuberculosis bacilli: super extensively drug-resistant tuberculosis or totally drug-resistant strains in iran. *Chest* **136**, 420-425

40. Lipinski, C. A., Lombardo, F., Dominy, B. W., and Feeney, P. J. (2001) Experimental and computational approaches to estimate solubility and permeability in drug discovery and development settings. *Adv Drug Deliv Rev* **46**, 3-26

41. Verlinde, C. L., and Hol, W. G. (1994) Structure-based drug design: progress, results and challenges. *Structure* **2**, 577-587

42. Kuntz, I. D. (1992) Structure-based strategies for drug design and discovery. *Science* **257**, 1078-1082

43. Wiseman, V., Kim, M., Mutabingwa, T. K., and Whitty, C. J. (2006) Cost-effectiveness study of three antimalarial drug combinations in Tanzania. *PLoS Med* **3**, e373

44. Pan, A. C., Borhani, D. W., Dror, R. O., and Shaw, D. E. (2013) Molecular determinants of drug-receptor binding kinetics. *Drug Discov Today* **18**, 667-673

45. Copeland, R. A., Pompliano, D. L., and Meek, T. D. (2006) Drug-target residence time and its implications for lead optimization. *Nat Rev Drug Discov* **5**, 730-739

46. Lu, H., England, K., am Ende, C., Truglio, J. J., Luckner, S., Reddy, B. G., Marlenee, N. L., Knudson, S. E., Knudson, D. L., Bowen, R. A., Kisker, C., Slayden, R. A., and Tonge, P. J. (2009) Slow-onset inhibition of the FabI enoyl reductase from francisella tularensis: residence time and in vivo activity. *ACS Chem Biol* **4**, 221-231

47. Tummino, P. J., and Copeland, R. A. (2008) Residence time of receptor-ligand complexes and its effect on biological function. *Biochemistry* **47**, 5481-5492

48. Basavapathruni, A., Jin, L., Daigle, S. R., Majer, C. R., Therkelsen, C. A., Wigle, T. J., Kuntz, K. W., Chesworth, R., Pollock, R. M., Scott, M. P., Moyer, M. P., Richon, V. M., Copeland, R. A., and Olhava, E. J. (2012) Conformational adaptation drives potent, selective and durable inhibition of the human protein methyltransferase DOT1L. *Chem Biol Drug Des* **80**, 971-980

49. Anselmi, C., Grininger, M., Gipson, P., and Faraldo-Gomez, J. D. (2010) Mechanism of Substrate Shuttling by the Acyl-Carrier Protein within the Fatty Acid Mega-Synthase. *J Am Chem Soc* **132**, 12357-12364

50. Payne, D. J., Miller, W. H., Berry, V., Brosky, J., Burgess, W. J., Chen, E., DeWolf Jr, W. E., Jr., Fosberry, A. P., Greenwood, R., Head, M. S., Heerding, D. A., Janson, C. A., Jaworski, D. D., Keller, P. M., Manley, P. J., Moore, T. D., Newlander, K. A., Pearson, S., Polizzi, B. J., Qiu, X., Rittenhouse, S. F., Slater-Radosti, C., Salyers, K. L., Seefeld, M. A., Smyth, M. G., Takata, D. T., Uzinskas, I. N., Vaidya, K., Wallis, N. G., Winram, S. B., Yuan, C. C., and Huffman, W. F. (2002) Discovery of a novel and potent class of FabI-directed antibacterial agents. *Antimicrob Agents Chemother* **46**, 3118-3124

51. White, S. W., Zheng, J., Zhang, Y. M., and Rock. (2005) The structural biology of type II fatty acid biosynthesis. *Annu Rev Biochem* **74**, 791-831

52. Campbell, J. W., and Cronan, J. E., Jr. (2001) Bacterial fatty acid biosynthesis: targets for antibacterial drug discovery. *Annu Rev Microbiol* **55**, 305-332

53. Marrakchi, H., Laneelle, G., and Quemard, A. (2000) InhA, a target of the antituberculous drug isoniazid, is involved in a mycobacterial fatty acid elongation system, FAS-II. *Microbiology* **146 (Pt 2)**, 289-296
54. Zhang, Y. M., White, S. W., and Rock, C. O. (2006) Inhibiting bacterial fatty acid synthesis. *J Biol Chem* **281**, 17541-17544
55. Dessen, A., Quemard, A., Blanchard, J. S., Jacobs, W. R., Jr., and Sacchettini, J. C. (1995) Crystal structure and function of the isoniazid target of Mycobacterium tuberculosis. *Science* **267**, 1638-1641
56. Mendoza, D., Schujman, G. E., and Aguilar, P. S. (2002) Biosynthesis and Function of Membrane Lipids. in *Bacillus subtilis and its closest relatives* (Sonenshein, A. L., Hoch, J. A., and Losick, R. eds.), American Society for Microbiology, Washington, DC. pp 43-55
57. Qiu, X., Choudhry, A. E., Janson, C. A., Grooms, M., Daines, R. A., Lonsdale, J. T., and Khandekar, S. S. (2005) Crystal structure and substrate specificity of the beta-ketoacyl-acyl carrier protein synthase III (FabH) from Staphylococcus aureus. *Protein Sci* **14**, 2087-2094
58. Choi, K. H., Kremer, L., Besra, G. S., and Rock, C. O. (2000) Identification and substrate specificity of beta -ketoacyl (acyl carrier protein) synthase III (mtFabH) from Mycobacterium tuberculosis. *J Biol Chem* **275**, 28201-28207
59. Machutta, C. A., Bommineni, G. R., Luckner, S. R., Kapilashrami, K., Ruzsicska, B., Simmerling, C., Kisker, C., and Tonge, P. J. (2010) Slow onset inhibition of bacterial beta-ketoacyl-acyl carrier protein synthases by thiolactomycin. *J Biol Chem* **285**, 6161-6169
60. Zhang, H., Machutta, C. A., and Tonge, P. J. (2010) 8.07 - Fatty Acid Biosynthesis and Oxidation. in *Comprehensive Natural Products II* (Editors-in-Chief: Lew, M., and Hung-Wen, L. eds.), Elsevier, Oxford. pp 231-275
61. Marrakchi, H., Ducasse, S., Labesse, G., Montrozier, H., Margeat, E., Emorine, L., Charpentier, X., Daffe, M., and Quemard, A. (2002) MabA (FabG1), a Mycobacterium tuberculosis protein involved in the long-chain fatty acid elongation system FAS-II. *Microbiology* **148**, 951-960
62. Brown, A. K., Bhatt, A., Singh, A., Saparia, E., Evans, A. F., and Besra, G. S. (2007) Identification of the dehydratase component of the mycobacterial mycolic acid-synthesizing fatty acid synthase-II complex. *Microbiology* **153**, 4166-4173
63. Heath, R. J., and Rock, C. O. (1995) Enoyl-acyl carrier protein reductase (fabI) plays a determinant role in completing cycles of fatty acid elongation in Escherichia coli. *J Biol Chem* **270**, 26538-26542
64. Heath, R. J., and Rock, C. O. (2000) A triclosan-resistant bacterial enzyme. *Nature* **406**, 145-146
65. Heath, R. J., Su, N., Murphy, C. K., and Rock, C. O. (2000) The enoyl-[acyl-carrier-protein] reductases FabI and FabL from Bacillus subtilis. *J Biol Chem* **275**, 40128-40133
66. Massengo-Tiasse, R. P., and Cronan, J. E. (2008) Vibrio cholerae FabV defines a new class of enoyl-acyl carrier protein reductase. *J Biol Chem* **283**, 1308-1316
67. Lu, H., and Tonge, P. J. (2008) Inhibitors of FabI, an enzyme drug target in the bacterial fatty acid biosynthesis pathway. *Acc Chem Res* **41**, 11-20
68. Price, A. C., Rock, C. O., and White, S. W. (2003) The 1.3-Angstrom-resolution crystal structure of beta-ketoacyl-acyl carrier protein synthase II from Streptococcus pneumoniae. *J Bacteriol* **185**, 4136-4143
69. Sullivan, T. J., Truglio, J. J., Boyne, M. E., Novichenok, P., Zhang, X., Stratton, C. F., Li, H. J., Kaur, T., Amin, A., Johnson, F., Slayden, R. A., Kisker, C., and Tonge, P. J. (2006)

High affinity InhA inhibitors with activity against drug-resistant strains of Mycobacterium tuberculosis. *ACS Chem Biol* **1**, 43-53

70. Rozwarski, D. A., Vilcheze, C., Sugantino, M., Bittman, R., and Sacchettini, J. C. (1999) Crystal structure of the Mycobacterium tuberculosis enoyl-ACP reductase, InhA, in complex with NAD+ and a C16 fatty acyl substrate. *J Biol Chem* **274**, 15582-15589
71. Banerjee, A., Dubnau, E., Quemard, A., Balasubramanian, V., Um, K. S., Wilson, T., Collins, D., de Lisle, G., and Jacobs, W. R., Jr. (1994) inhA, a gene encoding a target for isoniazid and ethionamide in Mycobacterium tuberculosis. *Science* **263**, 227-230
72. Heath, R. J., White, S. W., and Rock, C. O. (2001) Lipid biosynthesis as a target for antibacterial agents. *Prog Lipid Res* **40**, 467-497
73. Lambalot, R. H., and Walsh, C. T. (1997) Holo-[acyl-carrier-protein] synthase of Escherichia coli. *Methods Enzymol* **279**, 254-262
74. Zhang, Y. M., Rao, M. S., Heath, R. J., Price, A. C., Olson, A. J., Rock, C. O., and White, S. W. (2001) Identification and analysis of the acyl carrier protein (ACP) docking site on beta-ketoacyl-ACP synthase III. *J Biol Chem* **276**, 8231-8238
75. Wong, H. C., Liu, G., Zhang, Y. M., Rock, C. O., and Zheng, J. (2002) The solution structure of acyl carrier protein from Mycobacterium tuberculosis. *J Biol Chem* **277**, 15874-15880
76. Zhang, Y. M., Wu, B., Zheng, J., and Rock, C. O. (2003) Key residues responsible for acyl carrier protein and beta-ketoacyl-acyl carrier protein reductase (FabG) interaction. *J Biol Chem* **278**, 52935-52943
77. Roujeinikova, A., Baldock, C., Simon, W. J., Gilroy, J., Baker, P. J., Stuitje, A. R., Rice, D. W., Slabas, A. R., and Rafferty, J. B. (2002) X-ray crystallographic studies on butyryl-ACP reveal flexibility of the structure around a putative acyl chain binding site. *Structure* **10**, 825-835
78. Xu, H., Sullivan, T. J., Sekiguchi, J., Kirikae, T., Ojima, I., Stratton, C. F., Mao, W., Rock, F. L., Alley, M. R., Johnson, F., Walker, S. G., and Tonge, P. J. (2008) Mechanism and inhibition of saFabI, the enoyl reductase from Staphylococcus aureus. *Biochemistry* **47**, 4228-4236
79. Heath, R. J., and Rock, C. O. (1996) Inhibition of beta-ketoacyl-acyl carrier protein synthase III (FabH) by acyl-acyl carrier protein in Escherichia coli. *J Biol Chem* **271**, 10996-11000
80. Cryle, M. J., and Schlichting, I. (2008) Structural insights from a P450 Carrier Protein complex reveal how specificity is achieved in the P450(BioI) ACP complex. *Proc Natl Acad Sci U S A* **105**, 15696-15701
81. Babu, M., Greenblatt, J. F., Emili, A., Strynadka, N. C., Reithmeier, R. A., and Moraes, T. F. (2010) Structure of a SLC26 anion transporter STAS domain in complex with acyl carrier protein: implications for E. coli YchM in fatty acid metabolism. *Structure* **18**, 1450-1462
82. Parris, K. D., Lin, L., Tam, A., Mathew, R., Hixon, J., Stahl, M., Fritz, C. C., Seehra, J., and Somers, W. S. (2000) Crystal structures of substrate binding to Bacillus subtilis holo-(acyl carrier protein) synthase reveal a novel trimeric arrangement of molecules resulting in three active sites. *Structure* **8**, 883-895
83. Marrakchi, H., Zhang, Y. M., and Rock, C. O. (2002) Mechanistic diversity and regulation of Type II fatty acid synthesis. *Biochem Soc Trans* **30**, 1050-1055
84. Massengo-Tiasse, R. P., and Cronan, J. E. (2009) Diversity in enoyl-acyl carrier protein reductases. *Cell Mol Life Sci* **66**, 1507-1517
85. O'Donnell, A. G., Nahaie, M. R., Goodfellow, M., Minnikin, D. E., and Hajek, V. (1985) Numerical analysis of fatty acid profiles in the identification of staphylococci. *J Gen Microbiol* **131**, 2023-2033

86. Kaneda, T. (1991) Iso- and anteiso-fatty acids in bacteria: biosynthesis, function, and taxonomic significance. *Microbiol Rev* **55**, 288-302
87. Willecke, K., and Pardee, A. B. (1971) Fatty acid-requiring mutant of bacillus subtilis defective in branched chain alpha-keto acid dehydrogenase. *J Biol Chem* **246**, 5264-5272
88. Balemans, W., Lounis, N., Gilissen, R., Guillemont, J., Simmen, K., Andries, K., and Koul, A. (2010) Essentiality of FASII pathway for Staphylococcus aureus. *Nature* **463**, E3; discussion E4
89. Parsons, J. B., Frank, M. W., Subramanian, C., Saenkham, P., and Rock, C. O. (2011) Metabolic basis for the differential susceptibility of Gram-positive pathogens to fatty acid synthesis inhibitors. *Proc Natl Acad Sci U S A* **108**, 15378-15383
90. Brinster, S., Lamberet, G., Staels, B., Trieu-Cuot, P., Gruss, A., and Poyart, C. (2009) Type II fatty acid synthesis is not a suitable antibiotic target for Gram-positive pathogens. *Nature* **458**, 83-86
91. Park, H. S., Yoon, Y. M., Jung, S. J., Yun, I. N., Kim, C. M., Kim, J. M., and Kwak, J. H. (2007) CG400462, a new bacterial enoyl-acyl carrier protein reductase (FabI) inhibitor. *Int J Antimicrob Agents* **30**, 446-451
92. Escaich, S., Prouvensier, L., Saccomani, M., Durant, L., Oxoby, M., Gerusz, V., Moreau, F., Vongsouthi, V., Maher, K., Morrissey, I., and Soulama-Mouze, C. (2011) The MUT056399 inhibitor of FabI is a new antistaphylococcal compound. *Antimicrob Agents Chemother* **55**, 4692-4697
93. Kremer, L., Nampoothiri, K. M., Lesjean, S., Dover, L. G., Graham, S., Betts, J., Brennan, P. J., Minnikin, D. E., Locht, C., and Besra, G. S. (2001) Biochemical characterization of acyl carrier protein (AcpM) and malonyl-CoA:AcpM transacylase (mtFabD), two major components of Mycobacterium tuberculosis fatty acid synthase II. *J Biol Chem* **276**, 27967-27974
94. Brown, A. K., Sridharan, S., Kremer, L., Lindenberg, S., Dover, L. G., Sacchettini, J. C., and Besra, G. S. (2005) Probing the mechanism of the Mycobacterium tuberculosis beta-ketoacyl-acyl carrier protein synthase III mtFabH: factors influencing catalysis and substrate specificity. *J Biol Chem* **280**, 32539-32547
95. Veyron-Churlet, R., Bigot, S., Guerrini, O., Verdoux, S., Malaga, W., Daffe, M., and Zerbib, D. (2005) The biosynthesis of mycolic acids in Mycobacterium tuberculosis relies on multiple specialized elongation complexes interconnected by specific protein-protein interactions. *J Mol Biol* **353**, 847-858
96. Ojha, A., Anand, M., Bhatt, A., Kremer, L., Jacobs, W. R., Jr., and Hatfull, G. F. (2005) GroEL1: a dedicated chaperone involved in mycolic acid biosynthesis during biofilm formation in mycobacteria. *Cell* **123**, 861-873
97. Sivaraman, S., Sullivan, T. J., Johnson, F., Novichenok, P., Cui, G., Simmerling, C., and Tonge, P. J. (2004) Inhibition of the bacterial enoyl reductase FabI by triclosan: a structure-reactivity analysis of FabI inhibition by triclosan analogues. *J Med Chem* **47**, 509-518
98. McMurry, L. M., Oethinger, M., and Levy, S. B. (1998) Triclosan targets lipid synthesis. *Nature* **394**, 531-532
99. Heath, R. J., Yu, Y. T., Shapiro, M. A., Olson, E., and Rock, C. O. (1998) Broad spectrum antimicrobial biocides target the FabI component of fatty acid synthesis. *J Biol Chem* **273**, 30316-30320
100. Park, H. S., Yoon, Y. M., Jung, S. J., Kim, C. M., Kim, J. M., and Kwak, J. H. (2007) Antistaphylococcal activities of CG400549, a new bacterial enoyl-acyl carrier protein reductase (FabI) inhibitor. *J Antimicrob Chemother* **60**, 568-574
101. Kaplan, N., Albert, M., Awrey, D., Bardouniotis, E., Berman, J., Clarke, T., Dorsey, M., Hafkin, B., Ramnauth, J., Romanov, V., Schmid, M. B., Thalakada, R., Yethon, J., and

Pauls, H. W. (2012) Mode of Action, In Vitro Activity, and In Vivo Efficacy of AFN-1252, a Selective Antistaphylococcal FabI Inhibitor. *Antimicrob Agents Chemother* **56**, 5865-5874

102. Gerusz, V., Denis, A., Faivre, F., Bonvin, Y., Oxoby, M., Briet, S., Lefralliec, G., Oliveira, C., Desroy, N., Raymond, C., Peltier, L., Moreau, F., Escaich, S., Vongsouthi, V., Floquet, S., Drocourt, E., Walton, A., Prouvensier, L., Saccomani, M., Durant, L., Genevard, J. M., Sam-Sambo, V., and Soulama-Mouze, C. (2012) From Triclosan toward the Clinic: Discovery of Nonbiocidal, Potent FabI Inhibitors for the Treatment of Resistant Bacteria. *J Med Chem* **55**, 9914-9928
103. Gerusz, V. (2010) Recent Advances in the Inhibition of Bacterial Fatty Acid Biosynthesis. in *Annual Reports in Medicinal Chemistry* (John, E. M. ed.), Academic Press. pp 295-311
104. Persson, B., Kallberg, Y., Oppermann, U., and Jornvall, H. (2003) Coenzyme-based functional assignments of short-chain dehydrogenases/reductases (SDRs). *Chem Biol Interact* **143-144**, 271-278
105. Grimm, C., Maser, E., Mobus, E., Klebe, G., Reuter, K., and Ficner, R. (2000) The crystal structure of 3alpha -hydroxysteroid dehydrogenase/carbonyl reductase from Comamonas testosteroni shows a novel oligomerization pattern within the short chain dehydrogenase/reductase family. *J Biol Chem* **275**, 41333-41339
106. Larkin, M. A., Blackshields, G., Brown, N. P., Chenna, R., McGettigan, P. A., McWilliam, H., Valentin, F., Wallace, I. M., Wilm, A., Lopez, R., Thompson, J. D., Gibson, T. J., and Higgins, D. G. (2007) Clustal W and Clustal X version 2.0. *Bioinformatics* **23**, 2947-2948
107. Rafi, S., Novichenok, P., Kolappan, S., Zhang, X., Stratton, C. F., Rawat, R., Kisker, C., Simmerling, C., and Tonge, P. J. (2006) Structure of acyl carrier protein bound to FabI, the FASII enoyl reductase from Escherichia coli. *J Biol Chem* **281**, 39285-39293
108. Heath, R. J., Li, J., Roland, G. E., and Rock, C. O. (2000) Inhibition of the Staphylococcus aureus NADPH-dependent enoyl-acyl carrier protein reductase by triclosan and hexachlorophene. *J Biol Chem* **275**, 4654-4659
109. Sivaraman, S., Zwahlen, J., Bell, A. F., Hedstrom, L., and Tonge, P. J. (2003) Structure-activity studies of the inhibition of FabI, the enoyl reductase from Escherichia coli, by triclosan: kinetic analysis of mutant FabIs. *Biochemistry* **42**, 4406-4413
110. Kwon, Y. J., Fang, Y., Xu, G. H., and Kim, W. G. (2009) Aquastatin A, a new inhibitor of enoyl-acyl carrier protein reductase from Sporothrix sp. FN611. *Biol Pharm Bull* **32**, 2061-2064
111. Stewart, M. J., Parikh, S., Xiao, G., Tonge, P. J., and Kisker, C. (1999) Structural basis and mechanism of enoyl reductase inhibition by triclosan. *J Mol Biol* **290**, 859-865
112. Saito, K., Kawaguchi, A., Seyama, Y., Yamakawa, T., and Okuda, S. (1981) Steric course of reaction catalyzed by the enoyl acyl-carrier-protein reductase of Escherichia coli. *Eur J Biochem* **116**, 581-586
113. Fillgrove, K. L., and Anderson, V. E. (2000) Orientation of coenzyme A substrates, nicotinamide and active site functional groups in (Di)enoyl-coenzyme A reductases. *Biochemistry* **39**, 7001-7011
114. Roujeinikova, A., Sedelnikova, S., de Boer, G. J., Stuitje, A. R., Slabas, A. R., Rafferty, J. B., and Rice, D. W. (1999) Inhibitor binding studies on enoyl reductase reveal conformational changes related to substrate recognition. *J Biol Chem* **274**, 30811-30817
115. Lindert, S., and McCammon, J. A. (2012) Dynamics of Plasmodium falciparum enoyl-ACP reductase and implications on drug discovery. *Protein Sci* **21**, 1734-1745

116. Bamber, A. I., and Neal, T. J. (1999) An assessment of triclosan susceptibility in methicillin-resistant and methicillin-sensitive Staphylococcus aureus. *J Hosp Infect* **41**, 107-109
117. Levy, C. W., Roujeinikova, A., Sedelnikova, S., Baker, P. J., Stuitje, A. R., Slabas, A. R., Rice, D. W., and Rafferty, J. B. (1999) Molecular basis of triclosan activity. *Nature* **398**, 383-384
118. Hirschbeck, M. W., Kuper, J., Lu, H., Liu, N., Neckles, C., Shah, S., Wagner, S., Sotriffer, C. A., Tonge, P. J., and Kisker, C. (2012) Structure of the Yersinia pestis FabV enoyl-ACP reductase and its interaction with two 2-pyridone inhibitors. *Structure* **20**, 89-100
119. Moreau, F., Denis, A., Faivre, F., Bonvin, Y., Gerusz, V., Briet, S., Oxoby, M., Desroy, N., Soulama-Mouze, C., Floquet, S., Genevard, J. M., Oliveira, C., and Escaich, S. (2008) Design, Synthesis and Antibacterial properties of new potent Aryloxy-phenol FabI Inhibitors. in *Intersci. Conf. Antimicrob. Agents Chemother*, American Society for Microbiology, Washington, DC.
120. Maity, K., Bhargav, S. P., Sankaran, B., Surolia, N., Surolia, A., and Suguna, K. (2010) X-ray crystallographic analysis of the complexes of enoyl acyl carrier protein reductase of Plasmodium falciparum with triclosan variants to elucidate the importance of different functional groups in enzyme inhibition. *IUBMB Life* **62**, 467-476
121. Heerding, D. A., Chan, G., DeWolf, W. E., Fosberry, A. P., Janson, C. A., Jaworski, D. D., McManus, E., Miller, W. H., Moore, T. D., Payne, D. J., Qiu, X., Rittenhouse, S. F., Slater-Radosti, C., Smith, W., Takata, D. T., Vaidya, K. S., Yuan, C. C., and Huffman, W. F. (2001) 1,4-Disubstituted imidazoles are potential antibacterial agents functioning as inhibitors of enoyl acyl carrier protein reductase (FabI). *Bioorg Med Chem Lett* **11**, 2061-2065
122. Seefeld, M. A., Miller, W. H., Newlander, K. A., Burgess, W. J., Payne, D. J., Rittenhouse, S. F., Moore, T. D., DeWolf, W. E., Jr., Keller, P. M., Qiu, X., Janson, C. A., Vaidya, K., Fosberry, A. P., Smyth, M. G., Jaworski, D. D., Slater-Radosti, C., and Huffman, W. F. (2001) Inhibitors of bacterial enoyl acyl carrier protein reductase (FabI): 2,9-disubstituted 1,2,3,4-tetrahydropyrido[3,4-b]indoles as potential antibacterial agents. *Bioorg Med Chem Lett* **11**, 2241-2244
123. Kitagawa, H., Kumura, K., Takahata, S., Iida, M., and Atsumi, K. (2007) 4-Pyridone derivatives as new inhibitors of bacterial enoyl-ACP reductase FabI. *Bioorg Med Chem* **15**, 1106-1116
124. Ling, L. L., Xian, J., Ali, S., Geng, B., Fan, J., Mills, D. M., Arvanites, A. C., Orgueira, H., Ashwell, M. A., Carmel, G., Xiang, Y., and Moir, D. T. (2004) Identification and characterization of inhibitors of bacterial enoyl-acyl carrier protein reductase. *Antimicrob Agents Chemother* **48**, 1541-1547
125. Rawat, R., Whitty, A., and Tonge, P. J. (2003) The isoniazid-NAD adduct is a slow, tight-binding inhibitor of InhA, the Mycobacterium tuberculosis enoyl reductase: adduct affinity and drug resistance. *Proc Natl Acad Sci U S A* **100**, 13881-13886
126. Zheng, C. J., Sohn, M. J., and Kim, W. G. (2009) Vinaxanthone, a new FabI inhibitor from Penicillium sp. *J Antimicrob Chemother* **63**, 949-953
127. Zheng, C. J., Sohn, M. J., Chi, S. W., and Kim, W. G. (2010) Methyl-branched fatty acids, inhibitors of enoyl-ACP reductase with antibacterial activity from Streptomyces sp. A251. *J Microbiol Biotechnol* **20**, 875-880
128. Cho, J. Y., Kwon, Y. J., Sohn, M. J., Seok, S. J., and Kim, W. G. (2011) Phellinstatin, a new inhibitor of enoyl-ACP reductase produced by the medicinal fungus Phellinus linteus. *Bioorg Med Chem Lett* **21**, 1716-1718

129. Brown, A. K., Taylor, R. C., Bhatt, A., Futterer, K., and Besra, G. S. (2009) Platensimycin activity against mycobacterial beta-ketoacyl-ACP synthases. *PLoS One* **4**, e6306

130. Slayden, R. A., Lee, R. E., Armour, J. W., Cooper, A. M., Orme, I. M., Brennan, P. J., and Besra, G. S. (1996) Antimycobacterial action of thiolactomycin: an inhibitor of fatty acid and mycolic acid synthesis. *Antimicrob Agents Chemother* **40**, 2813-2819

131. Wang, J., Soisson, S. M., Young, K., Shoop, W., Kodali, S., Galgoci, A., Painter, R., Parthasarathy, G., Tang, Y. S., Cummings, R., Ha, S., Dorso, K., Motyl, M., Jayasuriya, H., Ondeyka, J., Herath, K., Zhang, C., Hernandez, L., Allocco, J., Basilio, A., Tormo, J. R., Genilloud, O., Vicente, F., Pelaez, F., Colwell, L., Lee, S. H., Michael, B., Felcetto, T., Gill, C., Silver, L. L., Hermes, J. D., Bartizal, K., Barrett, J., Schmatz, D., Becker, J. W., Cully, D., and Singh, S. B. (2006) Platensimycin is a selective FabF inhibitor with potent antibiotic properties. *Nature* **441**, 358-361

132. Price, A. C., Choi, K. H., Heath, R. J., Li, Z., White, S. W., and Rock, C. O. (2001) Inhibition of beta-ketoacyl-acyl carrier protein synthases by thiolactomycin and cerulenin. Structure and mechanism. *J Biol Chem* **276**, 6551-6559

133. Pappenberger, G., Schulz-Gasch, T., Kusznir, E., Muller, F., and Hennig, M. (2007) Structure-assisted discovery of an aminothiazole derivative as a lead molecule for inhibition of bacterial fatty-acid synthesis. *Acta Crystallogr D Biol Crystallogr* **63**, 1208-1216

134. Gajiwala, K. S., Margosiak, S., Lu, J., Cortez, J., Su, Y., Nie, Z., and Appelt, K. (2009) Crystal structures of bacterial FabH suggest a molecular basis for the substrate specificity of the enzyme. *FEBS Lett* **583**, 2939-2946

135. Bhatt, A., Kremer, L., Dai, A. Z., Sacchettini, J. C., and Jacobs, W. R., Jr. (2005) Conditional depletion of KasA, a key enzyme of mycolic acid biosynthesis, leads to mycobacterial cell lysis. *J Bacteriol* **187**, 7596-7606

136. Brown, M. S., Akopiants, K., Resceck, D. M., McArthur, H. A., McCormick, E., and Reynolds, K. A. (2003) Biosynthetic origins of the natural product, thiolactomycin: a unique and selective inhibitor of type II dissociated fatty acid synthases. *J Am Chem Soc* **125**, 10166-10167

137. Miyakawa, S., Suzuki, K., Noto, T., Harada, Y., and Okazaki, H. (1982) Thiolactomycin, a new antibiotic. IV. Biological properties and chemotherapeutic activity in mice. *J Antibiot (Tokyo)* **35**, 411-419

138. McFadden, J. M., Medghalchi, S. M., Thupari, J. N., Pinn, M. L., Vadlamudi, A., Miller, K. I., Kuhajda, F. P., and Townsend, C. A. (2005) Application of a flexible synthesis of (5R)-thiolactomycin to develop new inhibitors of type I fatty acid synthase. *J Med Chem* **48**, 946-961

139. Lee, W., Luckner, S. R., Kisker, C., Tonge, P. J., and Engels, B. (2011) Elucidation of the Protonation States of the Catalytic Residues in mtKasA: Implications for Inhibitor Design. *Biochemistry* **50**, 5743-5756

140. Kremer, L., Dover, L. G., Carrere, S., Nampoothiri, K. M., Lesjean, S., Brown, A. K., Brennan, P. J., Minnikin, D. E., Locht, C., and Besra, G. S. (2002) Mycolic acid biosynthesis and enzymic characterization of the beta-ketoacyl-ACP synthase A-condensing enzyme from Mycobacterium tuberculosis. *Biochem J* **364**, 423-430

141. von Wettstein-Knowles, P., Olsen, J. G., McGuire, K. A., and Henriksen, A. (2006) Fatty acid synthesis. Role of active site histidines and lysine in Cys-His-His-type beta-ketoacyl-acyl carrier protein synthases. *FEBS J* **273**, 695-710

142. Kim, P., Zhang, Y. M., Shenoy, G., Nguyen, Q. A., Boshoff, H. I., Manjunatha, U. H., Goodwin, M. B., Lonsdale, J., Price, A. C., Miller, D. J., Duncan, K., White, S. W., Rock, C. O., Barry, C. E., 3rd, and Dowd, C. S. (2006) Structure-activity relationships at the 5-position of thiolactomycin: an intact (5R)-isoprene unit is required for activity against

the condensing enzymes from Mycobacterium tuberculosis and Escherichia coli. *J Med Chem* **49**, 159-171

143. Sievert, D. M., Rudrik, J. T., Patel, J. B., McDonald, L. C., Wilkins, M. J., and Hageman, J. C. (2008) Vancomycin-resistant Staphylococcus aureus in the United States, 2002-2006. *Clin Infect Dis* **46**, 668-674
144. Priyadarshi, A., Kim, E. E., and Hwang, K. Y. (2010) Structural insights into Staphylococcus aureus enoyl-ACP reductase (FabI), in complex with NADP and triclosan. *Proteins* **78**, 480-486
145. Madsen, S. M., Beck, H. C., Ravn, P., Vrang, A., Hansen, A. M., and Israelsen, H. (2002) Cloning and inactivation of a branched-chain-amino-acid aminotransferase gene from Staphylococcus carnosus and characterization of the enzyme. *Appl Environ Microbiol* **68**, 4007-4014
146. Singh, V. K., Hattangady, D. S., Giotis, E. S., Singh, A. K., Chamberlain, N. R., Stuart, M. K., and Wilkinson, B. J. (2008) Insertional inactivation of branched-chain alpha-keto acid dehydrogenase in Staphylococcus aureus leads to decreased branched-chain membrane fatty acid content and increased susceptibility to certain stresses. *Appl Environ Microbiol* **74**, 5882-5890
147. Holman, R. T., Adams, C. E., Nelson, R. A., Grater, S. J., Jaskiewicz, J. A., Johnson, S. B., and Erdman, J. W., Jr. (1995) Patients with anorexia nervosa demonstrate deficiencies of selected essential fatty acids, compensatory changes in nonessential fatty acids and decreased fluidity of plasma lipids. *J Nutr* **125**, 901-907
148. Kleywegt, G. J., and Jones, T. A. (1996) Phi/psi-chology: Ramachandran revisited. *Structure* **4**, 1395-1400
149. Krissinel, E., and Henrick, K. (2004) Secondary-structure matching (SSM), a new tool for fast protein structure alignment in three dimensions. *Acta Crystallogr D Biol Crystallogr* **60**, 2256-2268
150. Kabsch, W., and Sander, C. (1983) Dictionary of protein secondary structure: pattern recognition of hydrogen-bonded and geometrical features. *Biopolymers* **22**, 2577-2637
151. Gouet, P., Courcelle, E., Stuart, D. I., and Metoz, F. (1999) ESPript: analysis of multiple sequence alignments in PostScript. *Bioinformatics* **15**, 305-308
152. Bissantz, C., Kuhn, B., and Stahl, M. (2010) A medicinal chemist's guide to molecular interactions. *J Med Chem* **53**, 5061-5084
153. Maity, K., Banerjee, T., Prabakaran, N., Surolia, N., Surolia, A., and Suguna, K. (2011) Effect of substrate binding loop mutations on the structure, kinetics, and inhibition of enoyl acyl carrier protein reductase from plasmodium falciparum. *IUBMB Life* **63**, 30-41
154. Price, A. C., Zhang, Y. M., Rock, C. O., and White, S. W. (2004) Cofactor-induced conformational rearrangements establish a catalytically competent active site and a proton relay conduit in FabG. *Structure* **12**, 417-428
155. Kim, S. J., Ha, B. H., Kim, K. H., Hong, S. K., Shin, K. J., Suh, S. W., and Kim, E. E. (2010) Dimeric and tetrameric forms of enoyl-acyl carrier protein reductase from Bacillus cereus. *Biochem Biophys Res Commun* **400**, 517-522
156. Kim, K. H., Ha, B. H., Kim, S. J., Hong, S. K., Hwang, K. Y., and Kim, E. E. (2011) Crystal Structures of Enoyl-ACP Reductases I (FabI) and III (FabL) from B. subtilis. *J Mol Biol* **406**, 403-415
157. Krissinel, E. (2010) Crystal contacts as nature's docking solutions. *J Comput Chem* **31**, 133-143
158. Björklind, A., and Arvidson, S. (1978) Influence of Amino Acids on the Synthesis of an Extracellular Proteinase from Staphylococcus aureus. *Journal of General Microbiology* **107**, 367-375

159. Blanche, F., Cameron, B., Bernard, F. X., Maton, L., Manse, B., Ferrero, L., Ratet, N., Lecoq, C., Goniot, A., Bisch, D., and Crouzet, J. (1996) Differential behaviors of Staphylococcus aureus and Escherichia coli type II DNA topoisomerases. *Antimicrob Agents Chemother* **40**, 2714-2720
160. Parikh, S., Moynihan, D. P., Xiao, G., and Tonge, P. J. (1999) Roles of tyrosine 158 and lysine 165 in the catalytic mechanism of InhA, the enoyl-ACP reductase from Mycobacterium tuberculosis. *Biochemistry* **38**, 13623-13634
161. Liebeke, M., Meyer, H., Donat, S., Ohlsen, K., and Lalk, M. (2010) A metabolomic view of Staphylococcus aureus and its ser/thr kinase and phosphatase deletion mutants: involvement in cell wall biosynthesis. *Chem Biol* **17**, 820-830
162. Bennett, B. D., Kimball, E. H., Gao, M., Osterhout, R., Van Dien, S. J., and Rabinowitz, J. D. (2009) Absolute metabolite concentrations and implied enzyme active site occupancy in Escherichia coli. *Nat Chem Biol* **5**, 593-599
163. Altschul, S. F., Gish, W., Miller, W., Myers, E. W., and Lipman, D. J. (1990) Basic local alignment search tool. *J Mol Biol* **215**, 403-410
164. Fozo, E. M., and Quivey, R. G., Jr. (2004) Shifts in the membrane fatty acid profile of Streptococcus mutans enhance survival in acidic environments. *Appl Environ Microbiol* **70**, 929-936
165. Choi, K. H., Heath, R. J., and Rock, C. O. (2000) beta-ketoacyl-acyl carrier protein synthase III (FabH) is a determining factor in branched-chain fatty acid biosynthesis. *J Bacteriol* **182**, 365-370
166. Sun, Y., and O'Riordan, M. X. (2010) Branched-chain fatty acids promote Listeria monocytogenes intracellular infection and virulence. *Infect Immun* **78**, 4667-4673
167. Gloerich, J., van Vlies, N., Jansen, G. A., Denis, S., Ruiter, J. P., van Werkhoven, M. A., Duran, M., Vaz, F. M., Wanders, R. J., and Ferdinandusse, S. (2005) A phytol-enriched diet induces changes in fatty acid metabolism in mice both via PPARalpha-dependent and -independent pathways. *J Lipid Res* **46**, 716-726
168. Atshaves, B. P., McIntosh, A. L., Payne, H. R., Mackie, J., Kier, A. B., and Schroeder, F. (2005) Effect of branched-chain fatty acid on lipid dynamics in mice lacking liver fatty acid binding protein gene. *Am J Physiol Cell Physiol* **288**, C543-558
169. Legendre, S., Letellier, L., and Shechter, E. (1980) Influence of lipids with branched-chain fatty acids on the physical, morphological and functional properties of Escherichia coli cytoplasmic membrane. *Biochim Biophys Acta* **602**, 491-505
170. Silbert, D. F., Ladenson, R. C., and Honegger, J. L. (1973) The unsaturated fatty acid requirement in Escherichia coli. Temperature dependence and total replacement by branched-chain fatty acids. *Biochim Biophys Acta* **311**, 349-361
171. Ryzhkov, L. R. (1996) Radical Nature of Pathways to Alkene and Ester from Thermal Decomposition of Primary Alkyl Diacyl Peroxide. *J Org Chem* **61**, 2801-2808
172. Davis, I. W., Leaver-Fay, A., Chen, V. B., Block, J. N., Kapral, G. J., Wang, X., Murray, L. W., Arendall, W. B., 3rd, Snoeyink, J., Richardson, J. S., and Richardson, D. C. (2007) MolProbity: all-atom contacts and structure validation for proteins and nucleic acids. *Nucleic Acids Res* **35**, W375-383
173. Weiss, M. (2001) Global indicators of X-ray data quality. *Journal of Applied Crystallography* **34**, 130-135
174. DeLano, W. L. (2002) The PyMOL Molecular Graphics System on World Wide Web http://www.pymol.org.
175. Ward, W. H., Holdgate, G. A., Rowsell, S., McLean, E. G., Pauptit, R. A., Clayton, E., Nichols, W. W., Colls, J. G., Minshull, C. A., Jude, D. A., Mistry, A., Timms, D., Camble, R., Hales, N. J., Britton, C. J., and Taylor, I. W. (1999) Kinetic and structural characteristics of the inhibition of enoyl (acyl carrier protein) reductase by triclosan. *Biochemistry* **38**, 12514-12525

176. Cornish-Bowden, A. (2004) *Principles of Enzyme Kinetics*, 3 ed., Portland Press
177. Smirnova, N., and Reynolds, K. A. (2001) Branched-chain fatty acid biosynthesis in Escherichia coli. *J Ind Microbiol Biotechnol* **27**, 246-251
178. Leslie, A. G. W. (1992) Recent changes to the MOSFLM package for processing film and image plate data. *Joint CCP4 + ESF-EAMCB Newsletter on Protein Crystallography* **26**
179. Evans, P. (2006) Scaling and assessment of data quality. *Acta Crystallogr D Biol Crystallogr* **62**, 72-82
180. McCoy, A. J., Grosse-Kunstleve, R. W., Adams, P. D., Winn, M. D., Storoni, L. C., and Read, R. J. (2007) Phaser crystallographic software. *J Appl Crystallogr* **40**, 658-674
181. Murshudov, G. N., Vagin, A. A., and Dodson, E. J. (1997) Refinement of macromolecular structures by the maximum-likelihood method. *Acta Crystallogr D Biol Crystallogr* **53**, 240-255
182. Emsley, P., and Cowtan, K. (2004) Coot: model-building tools for molecular graphics. *Acta Crystallogr D Biol Crystallogr* **60**, 2126-2132
183. Kabsch, W. (1993) Automatic processing of rotation diffraction data from crystals of initially unknown symmetry and cell constants. *J. Appl. Cryst.* **26**, 795-800
184. Zwart, P. H., Grosse-Kunstleve, R. W., Lebedev, A. A., Murshudov, G. N., and Adams, P. D. (2008) Surprises and pitfalls arising from (pseudo)symmetry. *Acta Crystallogr D Biol Crystallogr* **64**, 99-107
185. Adams, P. D., Afonine, P. V., Bunkoczi, G., Chen, V. B., Davis, I. W., Echols, N., Headd, J. J., Hung, L. W., Kapral, G. J., Grosse-Kunstleve, R. W., McCoy, A. J., Moriarty, N. W., Oeffner, R., Read, R. J., Richardson, D. C., Richardson, J. S., Terwilliger, T. C., and Zwart, P. H. (2010) PHENIX: a comprehensive Python-based system for macromolecular structure solution. *Acta Crystallogr D Biol Crystallogr* **66**, 213-221
186. Painter, J., and Merritt, E. A. (2006) Optimal description of a protein structure in terms of multiple groups undergoing TLS motion. *Acta Crystallogr D Biol Crystallogr* **62**, 439-450
187. Schuttelkopf, A. W., and van Aalten, D. M. (2004) PRODRG: a tool for high-throughput crystallography of protein-ligand complexes. *Acta Crystallogr D Biol Crystallogr* **60**, 1355-1363
188. Chang, A., Schiebel, J., Yu, W., Bommineni, G. R., Pan, P., Baxter, M. V., Khanna, A., Sotriffer, C. A., Kisker, C., and Tonge, P. J. (2013) Rational Optimization of Drug-Target Residence Time: Insights from Inhibitor Binding to the Staphylococcus aureus FabI Enzyme-Product Complex. *Biochemistry* **52**, 4217-4228
189. Zhang, R., and Monsma, F. (2009) The importance of drug-target residence time. *Curr Opin Drug Discov Devel* **12**, 488-496
190. Archer, G. L. (1998) Staphylococcus aureus: a well-armed pathogen. *Clin Infect Dis* **26**, 1179-1181
191. Kluytmans, J., van Belkum, A., and Verbrugh, H. (1997) Nasal carriage of Staphylococcus aureus: epidemiology, underlying mechanisms, and associated risks. *Clin Microbiol Rev* **10**, 505-520
192. Chambers, H. F., and Deleo, F. R. (2009) Waves of resistance: Staphylococcus aureus in the antibiotic era. *Nat Rev Microbiol* **7**, 629-641
193. Oliveira, D. C., Tomasz, A., and de Lencastre, H. (2002) Secrets of success of a human pathogen: molecular evolution of pandemic clones of meticillin-resistant Staphylococcus aureus. *Lancet Infect Dis* **2**, 180-189
194. Walsh, C. (1999) Deconstructing vancomycin. *Science* **284**, 442-443
195. Weigel, L. M., Clewell, D. B., Gill, S. R., Clark, N. C., McDougal, L. K., Flannagan, S. E., Kolonay, J. F., Shetty, J., Killgore, G. E., and Tenover, F. C. (2003) Genetic analysis of a

high-level vancomycin-resistant isolate of Staphylococcus aureus. *Science* **302**, 1569-1571

196. Baldock, C., Rafferty, J. B., Sedelnikova, S. E., Baker, P. J., Stuitje, A. R., Slabas, A. R., Hawkes, T. R., and Rice, D. W. (1996) A mechanism of drug action revealed by structural studies of enoyl reductase. *Science* **274**, 2107-2110
197. Karlowsky, J. A., Kaplan, N., Hafkin, B., Hoban, D. J., and Zhanel, G. G. (2009) AFN-1252, a FabI inhibitor, demonstrates a Staphylococcus-specific spectrum of activity. *Antimicrob Agents Chemother* **53**, 3544-3548
198. am Ende, C. W., Knudson, S. E., Liu, N., Childs, J., Sullivan, T. J., Boyne, M., Xu, H., Gegina, Y., Knudson, D. L., Johnson, F., Peloquin, C. A., Slayden, R. A., and Tonge, P. J. (2008) Synthesis and in vitro antimycobacterial activity of B-ring modified diaryl ether InhA inhibitors. *Bioorg Med Chem Lett* **18**, 3029-3033
199. Mueller, U., Darowski, N., Fuchs, M. R., Forster, R., Hellmig, M., Paithankar, K. S., Puhringer, S., Steffien, M., Zocher, G., and Weiss, M. S. (2012) Facilities for macromolecular crystallography at the Helmholtz-Zentrum Berlin. *J Synchrotron Radiat* **19**, 442-449
200. Painter, J., and Merritt, E. A. (2006) TLSMD web server for the generation of multi-group TLS models. *Journal of Applied Crystallography* **39**, 109-111
201. Schrodinger, LLC. (2010) The PyMOL Molecular Graphics System, Version 1.3r1.
202. Morrison, J. F., and Walsh, C. T. (1988) The behavior and significance of slow-binding enzyme inhibitors. *Adv Enzymol Relat Areas Mol Biol* **61**, 201-301
203. Copeland, R. A., Basavapathruni, A., Moyer, M., and Scott, M. P. (2011) Impact of enzyme concentration and residence time on apparent activity recovery in jump dilution analysis. *Anal Biochem* **416**, 206-210
204. Wolfram Research, I. (2010) Mathematica Edition: Version 8.0. Wolfram Research, Inc., Champaign, Illinois
205. Marcinkeviciene, J., Jiang, W., Kopcho, L. M., Locke, G., Luo, Y., and Copeland, R. A. (2001) Enoyl-ACP reductase (FabI) of Haemophilus influenzae: steady-state kinetic mechanism and inhibition by triclosan and hexachlorophene. *Arch Biochem Biophys* **390**, 101-108
206. Copeland, R. A. (2011) Conformational adaptation in drug-target interactions and residence time. *Future Med Chem* **3**, 1491-1501
207. Luckner, S. R., Liu, N., am Ende, C. W., Tonge, P. J., and Kisker, C. (2010) A slow, tight binding inhibitor of InhA, the enoyl-acyl carrier protein reductase from Mycobacterium tuberculosis. *J Biol Chem* **285**, 14330-14337
208. Maschera, B., Darby, G., Palu, G., Wright, L. L., Tisdale, M., Myers, R., Blair, E. D., and Furfine, E. S. (1996) Human immunodeficiency virus. Mutations in the viral protease that confer resistance to saquinavir increase the dissociation rate constant of the protease-saquinavir complex. *J Biol Chem* **271**, 33231-33235
209. Schramm, V. L. (2011) Enzymatic transition states, transition-state analogs, dynamics, thermodynamics, and lifetimes. *Annu Rev Biochem* **80**, 703-732
210. Wang, L. Q., Falany, C. N., and James, M. O. (2004) Triclosan as a substrate and inhibitor of 3'-phosphoadenosine 5'-phosphosulfate-sulfotransferase and UDP-glucuronosyl transferase in human liver fractions. *Drug Metab Dispos* **32**, 1162-1169
211. Naimi, T. S., LeDell, K. H., Como-Sabetti, K., Borchardt, S. M., Boxrud, D. J., Etienne, J., Johnson, S. K., Vandenesch, F., Fridkin, S., O'Boyle, C., Danila, R. N., and Lynfield, R. (2003) Comparison of community- and health care-associated methicillin-resistant Staphylococcus aureus infection. *JAMA* **290**, 2976-2984
212. Heath, R. J., Rubin, J. R., Holland, D. R., Zhang, E., Snow, M. E., and Rock, C. O. (1999) Mechanism of triclosan inhibition of bacterial fatty acid synthesis. *J Biol Chem* **274**, 11110-11114

213. Seefeld, M. A., Miller, W. H., Newlander, K. A., Burgess, W. J., DeWolf, W. E., Jr., Elkins, P. A., Head, M. S., Jakas, D. R., Janson, C. A., Keller, P. M., Manley, P. J., Moore, T. D., Payne, D. J., Pearson, S., Polizzi, B. J., Qiu, X., Rittenhouse, S. F., Uzinskas, I. N., Wallis, N. G., and Huffman, W. F. (2003) Indole naphthyridinones as inhibitors of bacterial enoyl-ACP reductases FabI and FabK. *J Med Chem* **46**, 1627-1635
214. Liu, N., Cummings, J. E., England, K., Slayden, R. A., and Tonge, P. J. (2011) Mechanism and inhibition of the FabI enoyl-ACP reductase from Burkholderia pseudomallei. *J Antimicrob Chemother* **66**, 564-573
215. Krug, M., Weiss, M. S., Heinemann, U., and Mueller, U. (2012) XDSAPP: a graphical user interface for the convenient processing of diffraction data using XDS. *Journal of Applied Crystallography* **45**, 568-572
216. Smart, O. S., Womack, T. O., Sharff, A., Flensburg, C., Keller, P., Paciorek, W., Vonrhein, C., and Bricogne, G. (2011) Grade (http://www.globalphasing.com). Global Phasing Ltd., Cambridge, United Kingdom
217. Bruno, I. J., Cole, J. C., Kessler, M., Luo, J., Motherwell, W. D., Purkis, L. H., Smith, B. R., Taylor, R., Cooper, R. I., Harris, S. E., and Orpen, A. G. (2004) Retrieval of crystallographically-derived molecular geometry information. *J Chem Inf Comput Sci* **44**, 2133-2144
218. Chen, V. B., Arendall, W. B., 3rd, Headd, J. J., Keedy, D. A., Immormino, R. M., Kapral, G. J., Murray, L. W., Richardson, J. S., and Richardson, D. C. (2010) MolProbity: all-atom structure validation for macromolecular crystallography. *Acta Crystallogr D Biol Crystallogr* **66**, 12-21
219. Morrison, J. F. (1969) Kinetics of the reversible inhibition of enzyme-catalysed reactions by tight-binding inhibitors. *Biochim Biophys Acta* **185**, 269-286
220. Rarey, M., Kramer, B., Lengauer, T., and Klebe, G. (1996) A fast flexible docking method using an incremental construction algorithm. *J Mol Biol* **261**, 470-489
221. Velec, H. F., Gohlke, H., and Klebe, G. (2005) DrugScore(CSD)-knowledge-based scoring function derived from small molecule crystal data with superior recognition rate of near-native ligand poses and better affinity prediction. *J Med Chem* **48**, 6296-6303
222. Gohlke, H., Hendlich, M., and Klebe, G. (2000) Knowledge-based scoring function to predict protein-ligand interactions. *J Mol Biol* **295**, 337-356
223. Neudert, G., and Klebe, G. (2011) DSX: a knowledge-based scoring function for the assessment of protein-ligand complexes. *J Chem Inf Model* **51**, 2731-2745
224. CCG. (2010) Molecular Operating Environment (MOE), 2010.10. 1010 Sherbooke St. West, Suite #910, Montreal, QC, Canada, H3A 2R7
225. Tripos. (2009) SYBYL-X 1.0. 1699 South Hanley Rd., St. Louis, Missouri, 63144, USA
226. Neudert, G., and Klebe, G. (2011) fconv: Format conversion, manipulation and feature computation of molecular data. *Bioinformatics* **27**, 1021-1022
227. CLSI. (2006) Methods for Dilution Antimicrobial Susceptibility Tests for Bacteria That Grow Aerobically. in *Approved Standard M7-A5, 6 Ed.*, Clinical and Laboratory Standards Institute, Wayne, PA
228. Gerber, A. U., Vastola, A. P., Brandel, J., and Craig, W. A. (1982) Selection of aminoglycoside-resistant variants of Pseudomonas aeruginosa in an in vivo model. *J Infect Dis* **146**, 691-697
229. Westley, A. M., and Westley, J. (1996) Enzyme inhibition in open systems. Superiority of uncompetitive agents. *J Biol Chem* **271**, 5347-5352
230. Brenwald, N. P., and Fraise, A. P. (2003) Triclosan resistance in methicillin-resistant Staphylococcus aureus (MRSA). *J Hosp Infect* **55**, 141-144
231. Tipparaju, S. K., Joyasawal, S., Forrester, S., Mulhearn, D. C., Pegan, S., Johnson, M. E., Mesecar, A. D., and Kozikowski, A. P. (2008) Design and synthesis of 2-pyridones as

novel inhibitors of the Bacillus anthracis enoyl-ACP reductase. *Bioorg Med Chem Lett* **18**, 3565-3569

232. Takahata, S., Iida, M., Yoshida, T., Kumura, K., Kitagawa, H., and Hoshiko, S. (2007) Discovery of 4-Pyridone derivatives as specific inhibitors of enoyl-acyl carrier protein reductase (FabI) with antibacterial activity against Staphylococcus aureus. *J Antibiot (Tokyo)* **60**, 123-128
233. Shin, K. J., Roh, E. J., Chung, M. K., Cha, H. J., and Seo, S. H. (2011) Novel 3-phenoxy-4-pyrone, 3-phenoxy-4-pyridone, or 4-pyridone derivatives, method for preparing same, and antimicrobial composition containing same as an active ingredient. in *WO/2011/014008*, Korea
234. Ro, S., Son, K. H., Kim, Y. E., Chang, H. J., Park, S. B., Choi, J. R., and Cho, J. M. (2009) CG400549: Candidate for the Treatment of MRSA Infection. in *Intersci. Conf. Antimicrob. Agents Chemother*, American Society for Microbiology, San Francisco, CA
235. Forlani, L., Cristoni, G., Boga, C., Todesco, P. E., Del Vecchio, E., Selva, S., and Monari, M. (2002) Reinvestigation of the tautomerism of some substituted 2-hydroxypyridines. *ARKIVOC* **2002**, 198-215
236. Schaefer, B., Kisker, C., and Sotriffer, C. A. (2011) Molecular dynamics of Mycobacterium tuberculosis KasA: implications for inhibitor and substrate binding and consequences for drug design. *J Comput Aided Mol Des* **25**, 1053-1069
237. Sippel, M., and Sotriffer, C. A. (2010) Molecular dynamics simulations of the HIV-1 integrase dimerization interface: guidelines for the design of a novel class of integrase inhibitors. *J Chem Inf Model* **50**, 604-614
238. Benkovic, S. J., and Hammes-Schiffer, S. (2003) A perspective on enzyme catalysis. *Science* **301**, 1196-1202
239. Fieulaine, S., Boularot, A., Artaud, I., Desmadril, M., Dardel, F., Meinnel, T., and Giglione, C. (2011) Trapping conformational states along ligand-binding dynamics of peptide deformylase: the impact of induced fit on enzyme catalysis. *PLoS Biol* **9**, e1001066
240. Knowles, J. R. (1991) Enzyme catalysis: not different, just better. *Nature* **350**, 121-124
241. Durrant, J. D., de Oliveira, C. A., and McCammon, J. A. (2011) POVME: an algorithm for measuring binding-pocket volumes. *J Mol Graph Model* **29**, 773-776
242. Hiratake, J. (2005) Enzyme inhibitors as chemical tools to study enzyme catalysis: rational design, synthesis, and applications. *Chem Rec* **5**, 209-228
243. Kossiakoff, A. A., Shpungin, J., and Sintchak, M. D. (1990) Hydroxyl hydrogen conformations in trypsin determined by the neutron diffraction solvent difference map method: relative importance of steric and electrostatic factors in defining hydrogen-bonding geometries. *Proc Natl Acad Sci U S A* **87**, 4468-4472
244. Tanaka, N., Nonaka, T., Tanabe, T., Yoshimoto, T., Tsuru, D., and Mitsui, Y. (1996) Crystal structures of the binary and ternary complexes of 7 alpha-hydroxysteroid dehydrogenase from Escherichia coli. *Biochemistry* **35**, 7715-7730
245. Malabanan, M. M., Amyes, T. L., and Richard, J. P. (2010) A role for flexible loops in enzyme catalysis. *Curr Opin Struct Biol* **20**, 702-710
246. Jez, J. M., Ferrer, J. L., Bowman, M. E., Dixon, R. A., and Noel, J. P. (2000) Dissection of malonyl-coenzyme A decarboxylation from polyketide formation in the reaction mechanism of a plant polyketide synthase. *Biochemistry* **39**, 890-902
247. Meyer, E. (1992) Internal water molecules and H-bonding in biological macromolecules: a review of structural features with functional implications. *Protein Sci* **1**, 1543-1562
248. Mongan, J. (2004) Interactive essential dynamics. *J Comput Aided Mol Des* **18**, 433-436

249. Tobi, D., and Bahar, I. (2005) Structural changes involved in protein binding correlate with intrinsic motions of proteins in the unbound state. *Proc Natl Acad Sci U S A* **102**, 18908-18913

250. Glasfeld, A., Leanz, G. F., and Benner, S. A. (1990) The stereospecificities of seven dehydrogenases from Acholeplasma laidlawii. The simplest historical model that explains dehydrogenase stereospecificity. *J Biol Chem* **265**, 11692-11699

251. Case, D. A., Darden, T. A., Cheatham, T. E., Simmerling, C. L., Wang, J., Duke, R. E., Luo, R., Walker, R. C., Zhang, W., Merz, K. M., Roberts, B., Wang, B., Hayik, S., Roitberg, A., Seabra, G., Kolossvai, I., Wong, K. F., Paesani, F., Vanicek, J., Liu, J., Wu, X., Brozell, S. R., Steinbrecher, T., Gohlke, H., Cai, Q., Ye, X., Wang, J., Hsieh, M.-J., Cui, G., Roe, D. R., Mathews, D. H., Seetin, M. G., Sagui, C., Babin, V., Luchko, T., Gusarov, S., Kovalenko, A., and Kollman, P. A. (2010) AMBER 11. University of California, San Francisco.

252. Frisch, M. J., Trucks, G. W., Schlegel, H. B., Scuseria, G. E., Robb, M. A., Cheeseman, J. R., Montgomery, J. A., Jr., T. V., Kudin, K. N., Burant, J. C., Millam, J. M., Iyengar, S. S., Tomasi, J., Barone, V., Mennucci, B., Cossi, M., Scalmani, G., Rega, N., Petersson, G. A., Nakatsuji, H., Hada, M., Ehara, M., Toyota, K., Fukuda, R., Hasegawa, J., Ishida, M., Nakajima, T., Honda, Y., Kitao, O., Nakai, H., Klene, M., Li, X., Knox, J. E., Hratchian, H. P., Cross, J. B., Bakken, V., Adamo, C., Jaramillo, J., Gomperts, R., Stratmann, R. E., Yazyev, O., Austin, A. J., Cammi, R., Pomelli, C., Ochterski, J. W., Ayala, P. Y., Morokuma, K., Voth, G. A., Salvador, P., Dannenberg, J. J., Zakrzewski, V. G., Dapprich, S., Daniels, A. D., Strain, M. C., Farkas, O., Malick, D. K., Rabuck, A. D., Raghavachari, K., Foresman, J. B., Ortiz, J. V., Cui, Q., Baboul, A. G., Clifford, S., Cioslowski, J., Stefanov, B. B., Liu, G., Liashenko, A., Piskorz, P., Komaromi, I., Martin, R. L., Fox, D. J., Keith, T., Al-Laham, M. A., Peng, C. Y., Nanayakkara, A., Challacombe, M., Gill, P. M. W., Johnson, B., Chen, W., Wong, M. W., Gonzalez, C., and Pople, J. A. (2004) Gaussian 03. Wallingford CT

253. Bayly, C. I., Cieplak, P., Cornell, W., and Kollman, P. A. (1993) A well-behaved electrostatic potential based method using charge restraints for deriving atomic charges: the RESP model. *The Journal of Physical Chemistry* **97**, 10269-10280

254. Wang, J., Wang, W., Kollman, P. A., and Case, D. A. (2006) Automatic atom type and bond type perception in molecular mechanical calculations. *J Mol Graph Model* **25**, 247-260

255. Wang, J., Wolf, R. M., Caldwell, J. W., Kollman, P. A., and Case, D. A. (2004) Development and testing of a general amber force field. *J Comput Chem* **25**, 1157-1174

256. Case, D. A., Darden, T. A., Cheatham, T. E., Simmerling, C. L., Wang, J., Duke, R. E., Luo, R., Walker, R. C., Zhang, W., Merz, K. M., Roberts, B., Hayik, S., Roitberg, A., Seabra, G., Swails, J., Goetz, A. W., Kolossváry, I., Wong, K. F., Paesani, F., Vanicek, J., Wolf, R. M., Liu, J., Wu, X., Brozell, S. R., Steinbrecher, T., Gohlke, H., Cai, Q., Ye, X., Wang, J., Hsieh, M.-J., Cui, G., Roe, D. R., Mathews, D. H., Seetin, M. G., Salomon-Ferrer, R., Sagui, C., Babin, V., Luchko, T., Gusarov, S., Kovalenko, A., and Kollman, P. A. (2012) AMBER 12. University of California, San Francisco

257. Ryckaert, J.-P., Ciccotti, G., and Berendsen, H. J. C. (1977) Numerical integration of the cartesian equations of motion of a system with constraints: molecular dynamics of n-alkanes. *Journal of Computational Physics* **23**, 327-341

258. Darden, T., York, D., and Pedersen, L. (1993) Particle mesh Ewald: An N [center-dot] log(N) method for Ewald sums in large systems. *The Journal of Chemical Physics* **98**, 10089-10092

259. Humphrey, W., Dalke, A., and Schulten, K. (1996) VMD: visual molecular dynamics. *J Mol Graph* **14**, 33-38, 27-38

260. R Development Core Team. (2010) R: A language and environment for statistical computing. R Foundation for Statistical Computing, Vienna, Austria

261. Schmidtke, P., Luque, F. J., Murray, J. B., and Barril, X. (2011) Shielded hydrogen bonds as structural determinants of binding kinetics: application in drug design. *J Am Chem Soc* **133**, 18903-18910

262. Witkowski, A., Joshi, A. K., and Smith, S. (2002) Mechanism of the beta-ketoacyl synthase reaction catalyzed by the animal fatty acid synthase. *Biochemistry* **41**, 10877-10887

263. Sachdeva, S., Musayev, F. N., Alhamadsheh, M. M., Scarsdale, J. N., Wright, H. T., and Reynolds, K. A. (2008) Separate entrance and exit portals for ligand traffic in Mycobacterium tuberculosis FabH. *Chem Biol* **15**, 402-412

264. Milletti, F., Storchi, L., Sforna, G., and Cruciani, G. (2007) New and original pKa prediction method using grid molecular interaction fields. *J Chem Inf Model* **47**, 2172-2181

265. French, G. L., Teoh, R., Chan, C. Y., Humphries, M. J., Cheung, S. W., and O'Mahony, G. (1987) Diagnosis of tuberculous meningitis by detection of tuberculostearic acid in cerebrospinal fluid. *Lancet* **2**, 117-119

266. Okuyama, H., Kankura, T., and Nojima, S. (1967) Positional distribution of fatty acids in phospholipids from Mycobacteria. *J Biochem* **61**, 732-737

267. Walker, R. W., Barakat, H., and Hung, J. G. (1970) The positional distribution of fatty acids in the phospholipids and triglycerides of Mycobacterium smegmatis and M. bovis BCG. *Lipids* **5**, 684-691

268. Slayden, R. A., and Barry, C. E., 3rd. (2002) The role of KasA and KasB in the biosynthesis of meromycolic acids and isoniazid resistance in Mycobacterium tuberculosis. *Tuberculosis (Edinb)* **82**, 149-160

269. Sridharan, S., Wang, L., Brown, A. K., Dover, L. G., Kremer, L., Besra, G. S., and Sacchettini, J. C. (2007) X-ray crystal structure of Mycobacterium tuberculosis beta-ketoacyl acyl carrier protein synthase II (mtKasB). *J Mol Biol* **366**, 469-480

270. Qiu, X., Janson, C. A., Smith, W. W., Head, M., Lonsdale, J., and Konstantinidis, A. K. (2001) Refined structures of beta-ketoacyl-acyl carrier protein synthase III. *J Mol Biol* **307**, 341-356

271. Zhang, Y. M., Hurlbert, J., White, S. W., and Rock, C. O. (2006) Roles of the active site water, histidine 303, and phenylalanine 396 in the catalytic mechanism of the elongation condensing enzyme of Streptococcus pneumoniae. *J Biol Chem* **281**, 17390-17399

272. Burgi, H. B., Dunitz, J. D., Lehn, J. M., and Wipff, G. (1974) Stereochemistry of Reaction Paths at Carbonyl Centers. *Tetrahedron* **30**, 1563-1572

273. Wilmouth, R. C., Clifton, I. J., Robinson, C. V., Roach, P. L., Aplin, R. T., Westwood, N. J., Hajdu, J., and Schofield, C. J. (1997) Structure of a specific acyl-enzyme complex formed between beta-casomorphin-7 and porcine pancreatic elastase. *Nat Struct Biol* **4**, 456-462

274. Li, Y., Paddonrow, M. N., and Houk, K. N. (1990) Transition Structures for the Aldol Reactions of Anionic, Lithium, and Boron Enolates. *Journal of Organic Chemistry* **55**, 481-493

275. Richard, J. P. (2013) Enzymatic Rate Enhancements: A Review and Perspective. *Biochemistry* **52**, 2009-2011

276. Muller, P., Kopke, S., and Sheldrick, G. M. (2003) Is the bond-valence method able to identify metal atoms in protein structures? *Acta Crystallogr D* **59**, 32-37

277. Lu, C. H., Lin, Y. F., Lin, J. J., and Yu, C. S. (2012) Prediction of metal ion-binding sites in proteins using the fragment transformation method. *PLoS One* **7**, e39252

278. Harding, M. M. (2006) Small revisions to predicted distances around metal sites in proteins. *Acta Crystallogr D Biol Crystallogr* **62**, 678-682
279. Biswas, D., Pandya, V., Singh, A. K., Mondal, A. K., and Kumaran, S. (2012) Co-factor binding confers substrate specificity to xylose reductase from Debaryomyces hansenii. *PLoS One* **7**, e45525
280. Erb, T. J., Brecht, V., Fuchs, G., Muller, M., and Alber, B. E. (2009) Carboxylation mechanism and stereochemistry of crotonyl-CoA carboxylase/reductase, a carboxylating enoyl-thioester reductase. *Proc Natl Acad Sci U S A* **106**, 8871-8876
281. Sun, Y., Wilkinson, B. J., Standiford, T. J., Akinbi, H. T., and O'Riordan, M. X. (2012) Fatty acids regulate stress resistance and virulence factor production for Listeria monocytogenes. *J Bacteriol* **194**, 5274-5284
282. Schloss, J. V. (1988) Significance of slow-binding enzyme inhibition and its relationship to reaction-intermediate analogs. *Accounts of Chemical Research* **21**, 348-353
283. Wells, J. A., and McClendon, C. L. (2007) Reaching for high-hanging fruit in drug discovery at protein-protein interfaces. *Nature* **450**, 1001-1009
284. Price, A. C., Zhang, Y. M., Rock, C. O., and White, S. W. (2001) Structure of beta-ketoacyl-[acyl carrier protein] reductase from Escherichia coli: negative cooperativity and its structural basis. *Biochemistry* **40**, 12772-12781
285. Smith, P. K., Krohn, R. I., Hermanson, G. T., Mallia, A. K., Gartner, F. H., Provenzano, M. D., Fujimoto, E. K., Goeke, N. M., Olson, B. J., and Klenk, D. C. (1985) Measurement of protein using bicinchoninic acid. *Anal Biochem* **150**, 76-85
286. Mofid, M. R., Finking, R., Essen, L. O., and Marahiel, M. A. (2004) Structure-based mutational analysis of the 4'-phosphopantetheinyl transferases Sfp from Bacillus subtilis: carrier protein recognition and reaction mechanism. *Biochemistry* **43**, 4128-4136
287. Sunbul, M., Zhang, K., and Yin, J. (2009) Chapter 10 using phosphopantetheinyl transferases for enzyme posttranslational activation, site specific protein labeling and identification of natural product biosynthetic gene clusters from bacterial genomes. *Methods Enzymol* **458**, 255-275
288. Post-Beittenmiller, D., Jaworski, J. G., and Ohlrogge, J. B. (1991) In vivo pools of free and acylated acyl carrier proteins in spinach. Evidence for sites of regulation of fatty acid biosynthesis. *J Biol Chem* **266**, 1858-1865
289. Heath, R. J., and Rock, C. O. (1996) Regulation of fatty acid elongation and initiation by acyl-acyl carrier protein in Escherichia coli. *J Biol Chem* **271**, 1833-1836
290. Schaeffer, M. L., Agnihotri, G., Kallender, H., Brennan, P. J., and Lonsdale, J. T. (2001) Expression, purification, and characterization of the Mycobacterium tuberculosis acyl carrier protein, AcpM. *Biochim Biophys Acta* **1532**, 67-78
291. Gasteiger, E., Hoogland, C., Gattiker, A., Duvaud, S., Wilkins, M. R., Appel, R. D., and Bairoch, A. (2005) Protein Identification and Analysis Tools on the ExPASy Server. *John M. Walker (Editor): The Proteomics Protocols Handbook, Humana Press*, 571-607
292. Changsen, C., Franzblau, S. G., and Palittapongarnpim, P. (2003) Improved green fluorescent protein reporter gene-based microplate screening for antituberculosis compounds by utilizing an acetamidase promoter. *Antimicrob Agents Chemother* **47**, 3682-3687

9 Appendix

9.1 Abbreviations

AAS	acyl-ACP synthetase
acac	acetoacetyl
AccABCD	acetyl-CoA carboxylase
ACP	Acyl carrier protein
AcpM	Acyl carrier protein of *M. tuberculosis*
AFN	Affinium Pharmaceuticals
Ala (A)	alanine
APS	ammonium persulfate
Arg (R)	arginine
aSEC	analytical size-exclusion chromatography
ASL	active site loop
Asn (N)	asparagine
Asp (D)	aspartate
AU	asymmetric unit
BAT	branched-chain aminotransferase
BCA	bicinchoninic acid
BCFA	branched-chain fatty acid
BESSY	Berliner Elektronen-Speicherring Gesellschaft für Synchrotronstrahlung
BKD	branched-chain α-ketoacid dehydrogenase
BSA	bovine serum albumin
BSA	buried surface area
CA-MRSA	community-acquired methicillin-resistant *Staphylococcus aureus*
CD	circular dichroism
CG	CrystalGenomics
CHS	chalcone synthase
CoA	coenzyme A
cpm	counts per minute
CPP	5-chloro-2-phenoxyphenol
cro	crotonyl
CS	conformationally sensitive
CSD	Cambridge Structural Database
CV	column volume
Cys (C)	cysteine
DD	dodecenoyl
DH	β-hydroxyacyl-ACP dehydratase
DHFR	dihydrofolate reductase
DMSO	dimethyl sulfoxide
DNA	deoxyribonucleic acid
EDTA	ethylenediaminetetraacetic acid
EMBL	European Molecular Biology Laboratory

ENR	enoyl-ACP reductase
EPP	5-ethyl-2-phenoxyphenol
ER	enoyl-ACP reductase
ESI	electrospray ionization
ESRF	European Synchrotron Radiation Facility
FabA	β-hydroxyacyl-ACP dehydratase
FabB	β-ketoacyl-ACP synthase I
FabD	malonyl-CoA:ACP transacylase
FabF	β-ketoacyl-ACP synthase II
FabG	β-ketoacyl-ACP reductase
FabH	β-ketoacyl-ACP synthase III
FabI	*trans*-2-enoyl-ACP reductase
FabK	*trans*-2-enoyl-ACP reductase
FabL	*trans*-2-enoyl-ACP reductase
FabM	*trans*-2, *cis*-3-decenoyl-ACP isomerase
FabV	*trans*-2-enoyl-ACP reductase
FabZ	β-hydroxyacyl-ACP dehydratase
FAS-I	type-I fatty acid biosynthesis pathway
FAS-II	type-II fatty acid biosynthesis pathway
FDA	Food and Drug Administration
Gln (Q)	glutamine
Glu (E)	glutamate
Gly (G)	glycine
GroEL1	mycobacterial Hsp60 chaperone
GSK	GlaxoSmithKline
HadAB	β-hydroxyacyl-ACP dehydratase of *M. tuberculosis*
HadBC	β-hydroxyacyl-ACP dehydratase of *M. tuberculosis*
His (H)	histidine
HIV	human immunodeficiency virus
HSDH	7α-hydroxysteroid dehydrogenase
HTS	high-throughput screening
ICP-OES	inductively-coupled plasma optical emission spectrometry
IEC	ion exchange chromatography
Ile (I)	isoleucine
IMAC	immobilized metal affinity chromatography
INH	isoniazid
InhA	*trans*-2-enoyl-ACP reductase of *M. tuberculosis*
IPTG	isopropyl-β-D-1-thiogalactopyranoside
KAS	β-ketoacyl-ACP synthase
KasA	β-ketoacyl-ACP synthase I of *M. tuberculosis*
KasB	β-ketoacyl-ACP synthase II of *M. tuberculosis*
KatG	mycobacterial catalase/peroxidase
KR	β-ketoacyl-ACP reductase
KS	β-ketoacyl-ACP synthase
LB	Luria-Bertani

LC	liquid chromatography
Leu (L)	leucine
Lys (K)	lysine
MabA	β-ketoacyl-ACP reductase of *M. tuberculosis*
MALDI	matrix-assisted laser desorption/ionization
MAT	malonyl-acetyl transferase
MD	molecular dynamics
MDR	multidrug-resistant
Me	methyl
Met (M)	methionine
MetRS	methionyl-tRNA synthetase
mFAS	mammalian fatty acid synthase
MIC	minimal inhibitory concentration
MPD	2-methyl-2,4-pentanediol
MRSA	methicillin-resistant *Staphylococcus aureus*
MS	mass spectrometry
MSSA	methicillin-sensitive *Staphylococcus aureus*
MUT	Mutabilis
NA	not applicable
NAC	*N*-acetylcysteamine
NAD^+	nicotinamide adenine dinucleotide
NADH	nicotinamide adenine dinucleotide, reduced form
$NADP^+$	nicotinamide adenine dinucleotide phosphate
NADPH	nicotinamide adenine dinucleotide phosphate, reduced form
NCS	non-crystallographic symmetry
NIH	National Institutes of Health
NMR	nuclear magnetic resonance
NOE	Nuclear Overhauser Effect
oct	octenoyl
OD	optical density
PAGE	polyacrylamide gel electrophoresis
PDB	Protein Data Bank
PDF	peptide deformylase
PE	phosphatidylethanolamine
PEG	polyethylene glycol
Phe (F)	phenylalanine
PheRS	phenylalanyl-tRNA synthetase
PI	phosphatidylinositol
PIM	phosphatidylinositol oligomannosides
PK	pharmacokinetics
PL	phospholipid
PPant	4'-phosphopantetheine
PPTase	phosphopantetheinyl transferase
PRH	phosphate recognition helix
Pro (P)	proline

RESP	restrained electrostatic potential
rmsd	root mean square deviation
rmsf	root mean square fluctuation
rpm	rounds per minute
RT	retention time
SAR	structure-activity relationship
SBDD	structure-based drug design
SBL	substrate binding loop
SBL-2	substrate binding loop 2
SCFA	straight-chain fatty acid
SDR	short-chain dehydrogenase/reductase
SDS	sodium dodecyl sulfate
SEC	size exclusion chromatography
Ser (S)	serine
SFB	Sonderforschungsbereich (Collaborative Research Center)
SKR	structure-kinetic relationship
SSM	secondary structure matching
TB	tuberculosis
TCEP	tris(2-carboxyethyl)phosphine
TCL	triclosan
TDR	totally drug-resistant
TEMED	*N,N,N',N'*-tetramethylethylenediamine
TEV	tabacco etch virus
TG	Tris-glycine
Thr (T)	threonine
TIC	total ion chromatogram
TIM	triosephosphate isomerase
TLM	thiolactomycin
TLS	translation liberation screw
TMEDA	*N,N,N',N'*-tetramethylethylenediamine
TOF-MS	time-of-flight mass spectrometer
t_R	residence time
Trp (W)	tryptophan
TS	transition state
Tyr (Y)	tyrosine
UFA	unsaturated fatty acid
UPLC	ultra performance liquid chromatography
UV	ultraviolet light
Val (V)	valine
VIS	visible light
VMD	visual molecular dynamics
VRE	vancomycin-resistant *Enterococci*
VRSA	vancomycin-resistant *Staphylococcus aureus*
WHO	World Health Organization
XDR	extensively drug-resistant

9.2 Supplementary Materials and Methods

9.2.1 Expression and Purification of Crotonyl-saACP

S. aureus ACP (saACP) was purified similar to a previously described procedure (78). The pET23b plasmid containing the *acp* gene fused to a C-terminal His$_5$-tag was kindly provided by the group of Prof. Peter J. Tonge (Stony Brook University, USA). All media were supplemented with 100 µg/ml ampicillin. The plasmid was heat-shock transformed into *E. coli* BL21 (DE3) cells, which were cultivated overnight on an LB agar plate at 37 °C. 200 ml sterile LB-medium was inoculated with a single colony of the grown bacteria and shaken overnight with 200 rpm at 37 °C. 40 ml of this pre-culture were used to inoculate 2 l of fresh LB-medium. The culture was shaken with 200 rpm at 37 °C and when reaching an OD$_{600\ nm}$ of 0.8, isopropyl-β-D-1-thiogalactopyranoside (IPTG) was added to a final concentration of 0.5 mM. Following induction, the temperature was reduced to 25 °C and the bacteria were grown overnight. On the next day, cells were harvested at 4 °C with the centrifuge Avanti J-26 XP and the rotor JLA 8.1000 at 5,000 g, flash-frozen in liquid nitrogen and stored at - 80 °C.

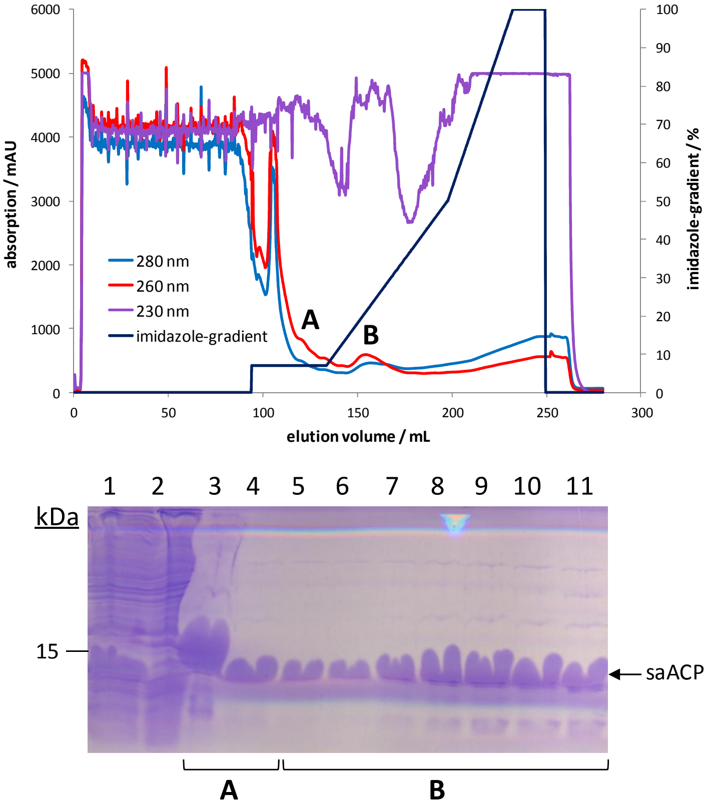

Figure 9-1. Purification of saACP via immobilized Ni^{2+} metal ion affinity chromatography (Ni^{2+}-IMAC). The chromatographic elution profile is shown at the top and the corresponding SDS-PAGE gel at the bottom. The letters A and B link the fractions shown in the gel with the corresponding peaks of the chromatogram. Lanes 1 and 2 of the gel contain the lysate and the flow-through, respectively. The UV-absorptions at 230 nm, 260 nm and 280 nm are highlighted in purple, red and blue, respectively. The gradient is shown in black.

20 g wet cell pellet was thawed and resuspended in 75 ml lysis buffer (20 mM Tris pH 7.9, 500 mM NaCl, 5 mM imidazole) including 3 µl DNaseI (Invitrogen). Subsequently, cells were lysed using a cell disruptor at a working pressure of 1.5 kbar (sonication did work equally well). Cell debris was removed via a further centrifugation step (centrifuge Avanti J-26 XP, rotor JA 25.50, 50,000 g) before the supernatant was loaded onto a 5 ml HisTrap FF crude

column (GE Healthcare). Using the Äkta purifier system (GE Healthcare), a step gradient from 5 mM to 40 mM imidazole (7% buffer B, 8 column volumes (CV)) was followed by linear gradients from 40 mM to 250 mM (approaching 50% B within 13 CV) and from 250 mM to 500 mM imidazole (approaching 100% B within 7 CV) (IMAC-buffer A = lysis buffer; IMAC-buffer B = 20 mM Tris pH 7.9, 500 mM NaCl, 500 mM imidazole). An 18% SDS-PAGE revealed that apo-saACP elutes as a single peak at an imidazole concentration of approximately 100 mM (20% B; Figure 9-1). Please note that the UV-absorption at 230 nm was measured since the small ACP protein does not contain any amino acids absorbing at a wavelength of 280 nm.

Fractions containing apo-saACP were pooled and dialyzed in reaction buffer (75 mM MES pH 6.0, 10 mM $MgCl_2$). Prior to the modification reaction, the protein concentration was determined via the BCA-assay (285) since the extinction coefficient of saACP at a wavelength of 280 nm is too low to allow a spectrophotometric approach. In order to modify Ser37 of saACP with the acylated phosphopantetheine moiety of crotonyl-CoA (cro-CoA), the phosphopantetheinyl transferase (PPTase) Sfp was used to catalyze this reaction (Figure 9-2).

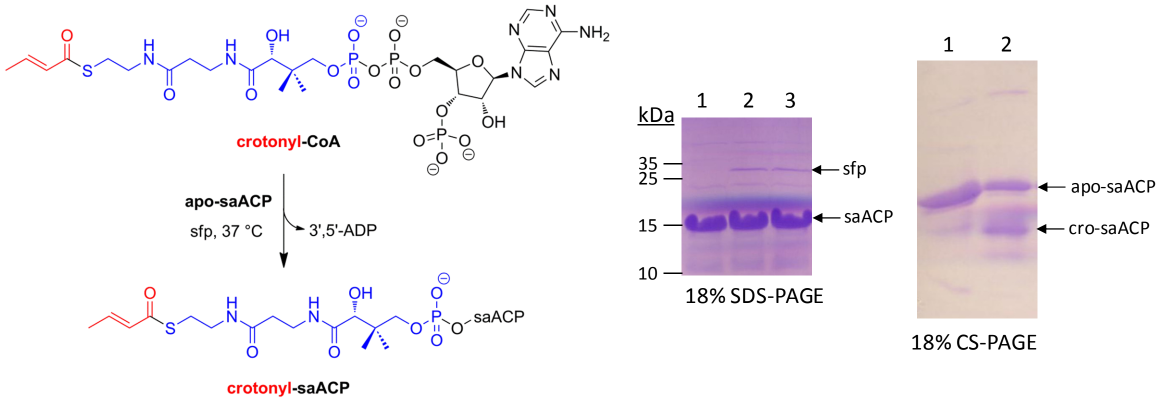

Figure 9-2. Acyl-phosphopantetheinylation of apo-saACP. The scheme on the left shows the chemical reaction to accomplish the coupling of apo-saACP with a defined substrate. An SDS-PAGE was not able to separate apo-saACP and cro-saACP. The respective gel is shown in the middle (lane 1 = saACP, lane 2 = reaction mixture after the addition of Sfp and cro-CoA to apo-saACP, lane 3 = reaction mixture after 2 h at 37 °C). In contrast, an 18% CS-PAGE could separate apo- from cro-saACP (shown on the right; lane 1 = reaction mixture after the addition of Sfp and cro-CoA to apo-saACP, lane 3 = reaction mixture after 2 h at 37 °C).

For this purpose Sfp (the corresponding pET29b(+) plasmid was kindly provided by Prof. Peter J. Tonge) was expressed and purified as described previously (286,287) with an additional final size-exclusion chromatography (SEC) step in a buffer composed of 10 mM Tris pH 7.5, 150 mM NaCl, 1 mM EDTA and 10% glycerol. The modification reaction mixture containing 77 µM apo-saACP, 179 µM cro-CoA and 0.78 µM Sfp was incubated for 2 h at 37 °C. Since an 18% SDS-PAGE was not capable of separating apo-saACP from the product of the reaction, an 18% conformationally sensitive polyacrylamide gel electrophoresis (CS-PAGE) experiment was used to analyze the success of the reaction (Figure 9-2), which indicated a yield of ≤ 50%. CS-PAGE is a method known for at least 20 years (63,288,289) and enables the separation of different ACP-intermediates based on the slightly different conformations induced by the individual acyl-chains (76). The corresponding gels were produced by consecutively polymerizing a CS-PAGE resolving gel (18% 29:1 acrylamide/bis-acryamide; 375 mM Tris pH 8.8; 0.5 M urea) and stacking gel solutions (5% 29:1 acrylamide/bis-acryamide; 125 mM Tris pH 6.8; 0.5 M urea) by the addition of 0.1% (w/v) ammonium persulfate (APS) and 0.1% (w/v) *N,N,N',N'*-tetramethylethylenediamine (TEMED or TMEDA, respectively). After the protein samples had been supplemented with loading buffer (5x loading buffer = 250 mM Tris pH 6.8, 0.5% (w/v) bromophenol blue, 50% glycerol and 250 mM urea), electrophoresis was carried out in 1x Tris-glycine buffer (TG-buffer = 25 mM Tris and 192 mM glycine). Staining was performed using a standard Coomassie solution (50% (w/v) methanol, 10% (w/v) acetic acid and 1% (w/v) Coomassie Brilliant Blue). To enhance the yield of the reaction, further experiments were conducted with acetyl-CoA, which revealed that a 100 : 3 : 400 ratio of saACP : Sfp : acyl-CoA (saACP concentration of 77 µM was also used in these experiments) in a modified buffer (75 mM Tris pH 7.5, 10 mM $MgCl_2$) resulted in much better yields (≥ 85%) after 3 h incubation of the reaction mixture at 37 °C. Alternatively, the reaction can be performed in 20 mM Tris pH 8.0, 10 mM $MgCl_2$ and 30 mM NaCl thereby allowing to skip the dialysis step prior to anion exchange chromatography (IEC). After dialysis in IEC-buffer A (20 mM Tris pH 8.0 and 50 mM NaCl), the modified protein sample was loaded onto a MonoQ 10/100 GL column (GE Healthcare). A very shallow NaCl-gradient was used to separate apo-saACP from cro-saACP (IEC-buffer B = 20 mM Tris pH 8.0 and 1 M NaCl; linear gradient from 0% to 5% B (1 CV) followed by a shallow gradient from 5% to 45% B (40 CV) and a steep gradient from 45% to 100% B (2 CV)). Apo- and cro-saACP eluted with their maxima at approximately 250 mM (21% B) and 280 mM NaCl (24% B), respectively. An 18% CS-PAGE was used to evaluate the success of the separation procedure (Figure 9-3).

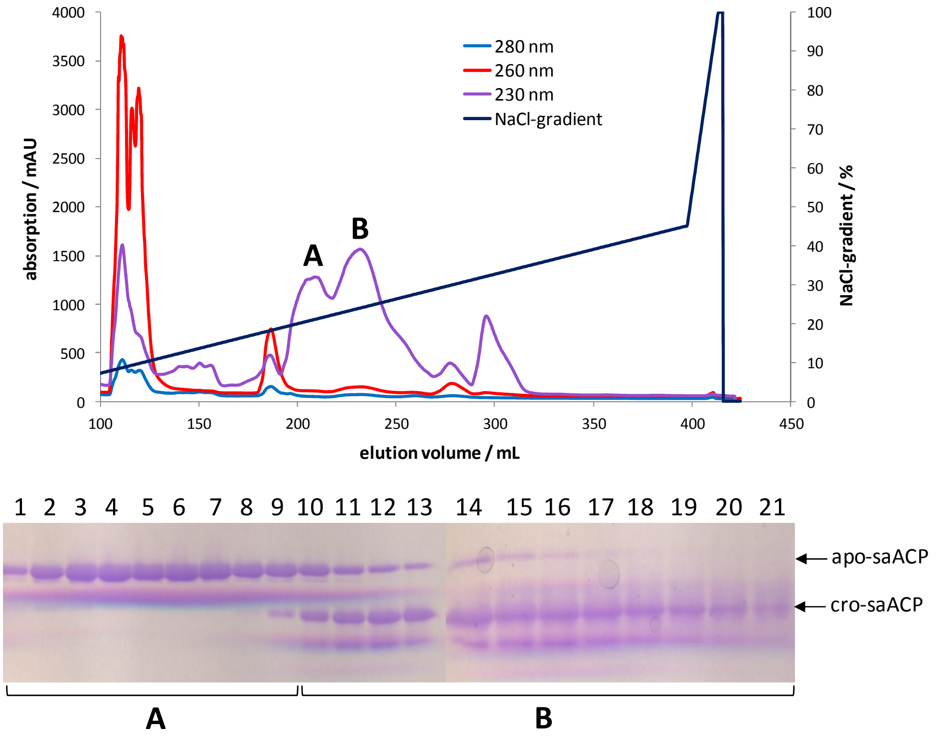

Figure 9-3. Separation of cro-saACP from apo-saACP via IEC. The chromatogram is shown at the top and the related 18% CS-PAGE gel at the bottom. The letters A and B indicate which lanes of the gel correspond to which peak in the elution profile. Curves corresponding to UV-absorptions at wavelengths of 230 nm, 260 nm and 280 nm are highlighted in purple, red and blue, respectively. The NaCl-gradient is depicted in black (percentage of buffer B).

Pooled fractions containing cro-saACP were loaded onto a HiLoad 26/60 Superdex 200 prep grade column pre-equilibrated with SEC-buffer (20 mM Tris pH 7.0, 150 mM NaCl, 1 mM EDTA). Cro-saACP eluted at a volume of approximately 245 ml. An 18% SDS-PAGE and CS-

PAGE was used to assess the purity of the samples (Figure 9-4). Finally, the pooled fractions containing relatively pure cro-saACP were concentrated to 0.5 mM (4.8 mg/ml), flash-frozen in liquid nitrogen and stored at - 80 °C.

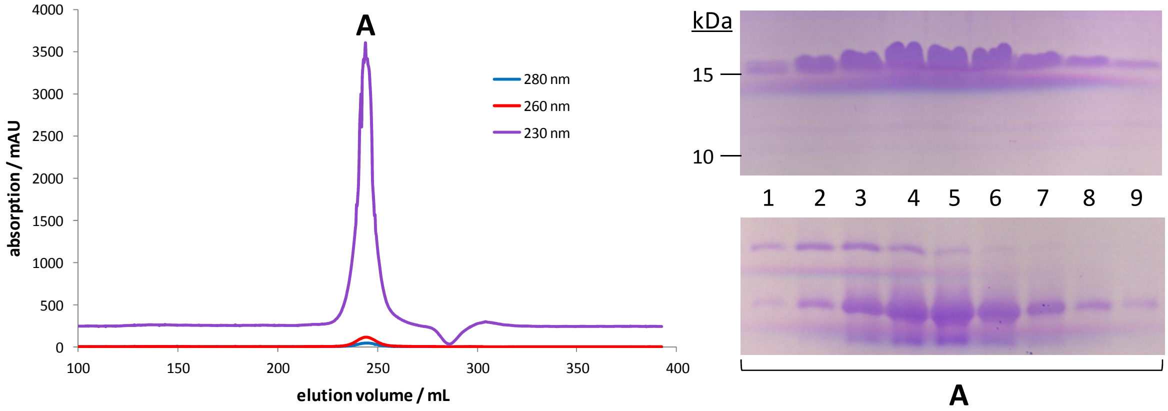

Figure 9-4. Isolation of cro-saACP via a final SEC-step. The chromatogram is shown on the left and the 18% SDS- (top) and CS-PAGE gels (bottom) on the right. Lanes 1 to 9 of both gels contain the same samples, which correspond to the main peak in the elution profile (indicated by the letter A). Purple, red and blue curves were obtained via measurements of the absorption at 230, 260 and 280 nm, respectively.

Mass-spectrometric experiments with cro-saACP (MALDI-TOF, conducted at Stony Brook University) indicated a mass of 10,150 Da (highest peak), which is close to the expected value of 10,122 Da. However, methods such as ESI-MS might be better suited to clearly confirm the nature of the purified saACP-substrate (personal communication).

9.2.2 Expression and Purification of Acetoacetyl-AcpM

The purification of acetoacetyl-AcpM (acac-AcpM) described here was guided by previously published protocols (59,75,290). The native AcpM protein was expressed in *E. coli* BL21 (DE3) cells. For this purpose, a pET24b(+) plasmid containing the *acp*-gene (obtained from the group of Prof. Peter J. Tonge) was heat-shock transformed into these cells, which were subsequently cultured on an LB-agar plate at 37 °C overnight. To select only those bacteria that took up the plasmid, solid and liquid media were supplemented with 50 µg/ml kanamycin. 40 ml of a 200 ml overnight culture were used to inoculate 2 l of sterile LB-medium, which was subsequently shaken with 200 rpm at 37 °C. After induction with 0.7 mM IPTG at an $OD_{600\ nm}$ of 0.9 and further growth for 3-4 h at 37 °C, cells were harvested by centrifugation (centrifuge Avanti J-26 XP, rotor JLA 8.1000, 5,000 g), flash-frozen in liquid nitrogen and stored at - 80 °C.

60 ml lysis buffer (20 mM Bis-Tris pH 6.5, 200 mM NaCl, 1 mM DTT) and 2 µl DNaseI (Invitrogen) were used to resuspend 13 g thawed cells. After the bacteria were lysed by one passage through a cell disruptor (1.5 kbar), cell debris was removed by centrifugation (centrifuge Avanti J-26 XP, rotor JA 25.50, 50,000 g). 60 ml ice-cold isopropanol was added dropwise to the lysate over a period of approximately 20 min. The resulting solution was slowly stirred for 2 h at 4 °C followed by the removal of aggregated protein via centrifugation (centrifuge Avanti J-26 XP, rotor JA 25.50, 10,000 g). By adding 120 ml dilution buffer (20 mM Bis-Tris pH 6.5, 1 mM DTT) the NaCl concentration of the supernatant was adjusted to 50 mM for the following IEC-step with the Äkta purifier system (GE Healthcare). The protein sample was loaded onto a 5 ml Q-sepharose XL column (GE Healthcare) and eluted by a shallow gradient from 50 mM to 1 M NaCl (25 CV; Q-buffer A = 20 mM Bis-Tris pH 6.5, 50

mM NaCl, 1mM DTT, Q-buffer B = 20 mM Bis-Tris pH 6.5, 1 M NaCl, 1 mM DTT). A mixture of holo-AcpM (= phosphopantetheinylated AcpM), apo-AcpM and acyl-AcpM co-eluted at approximately 400 mM NaCl (37% B) as indicated by an 18% SDS-PAGE analysis (Figure 9-5) (59).

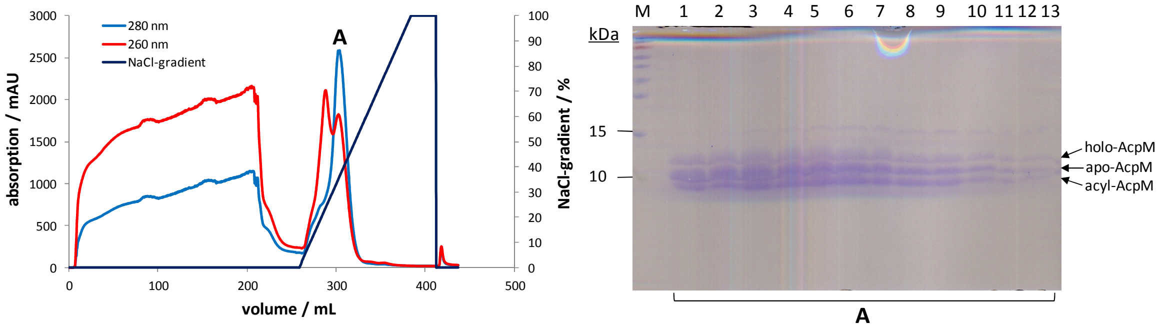

Figure 9-5. Isolation of a mixture of different AcpM-species via IEC. The chromatogram (left) and the related SDS-PAGE gel (right) are depicted. Lanes 1-13 of the gel correspond to peak A in the elution profile. Absorptions at 260 and 280 nm are colored red and blue, respectively. The NaCl-gradient is shown in black. M = marker, PageRuler^{TM} Prestained Protein Ladder (Fermentas).

The pooled fractions of peak A were dialyzed into IEC-buffer A (20 mM Tris pH 8.0, 50 mM NaCl) and loaded onto a MonoQ 10/100 GL column (GE Healtcare) using the sample pump P960 (GE Healtcare). A shallow NaCl-gradient enabled the separation of apo-AcpM (IEC-buffer B = 20 mM Tris pH 8.0, 1 M NaCl; linear gradient from 0% to 5% B (1 CV) followed by a shallow gradient from 5% to 45% B (40 CV) and a steep gradient from 45% to 100% B (2 CV)), which eluted first (peak A at approximately 17% B = 210 mM NaCl in Figure 9-6).

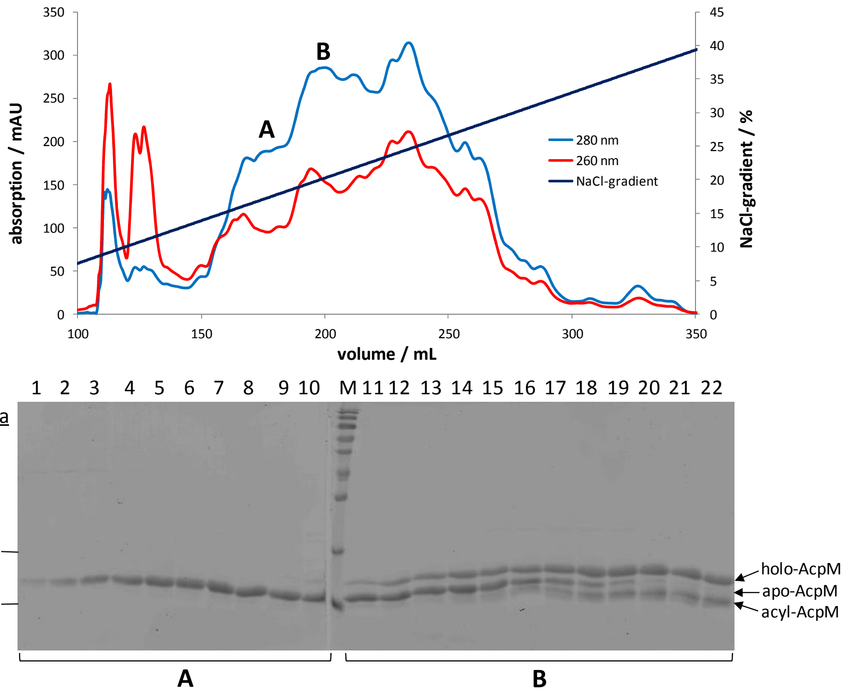

Figure 9-6. Isolation of apo-AcpM via IEC. Lanes of the 18% SDS-PAGE gel (bottom) corresponding to peaks A and B of the chromatogram (top) are labeled with A and B. UV-absorption was detected at wavelengths of 260 nm (red) and 280 nm (blue). For clarity, the elution profile is shown from 100 ml to 350 ml and the NaCl-gradient (in % buffer B) is colored in black. Two gels are depicted side by side (M = marker, PageRuler^{TM} Prestained Protein Ladder from Fermentas). Since the applied salt gradient was too steep during the first AcpM purification, the results are shown and discussed for the already optimized gradient.

After the pooled fractions containing only apo-AcpM were dialyzed into reaction buffer (50 mM Tris pH 8.5, 25 mM $MgCl_2$, 5 mM $MnCl_2$, 1 mM DTT), the protein concentration was determined using a photometric approach (NanoDrop ND 1000 from Peqlab). Because the AcpM extinction coefficient at 280 nm is relatively low according to theoretical calculations (ε = 2980 M^{-1} cm^{-1}) (291), acyl-AcpM samples were used to compare the photometric method with the BCA-assay. As the resulting concentrations varied by a factor of approximately 2 between the two different approaches, an acyl-AcpM sample was lyophilized to determine the "true" concentration for calibration of the BCA-assay and the photometric experiments. Resulting correction factors were 1.2 and 0.6, respectively. For the modification reaction catalyzed by the PPTase AcpS, a mixture of 0.58 mM apo-AcpM (0.96 mM measured photometrically), 6 µM AcpS and 0.72 mM acetoacetyl-CoA (acac-CoA, 1.2-fold molar excess) was incubated for 90 min at 30 °C. AcpS purified according to (73) was kindly provided by the group of Prof. Peter J. Tonge. Apo-AcpM and the formed acac-AcpM could be separated via 18% SDS-PAGE, which indicated a yield ≥ 60% (Figure 9-7). Hence, an approximately 2-fold molar excess of acac-CoA should be used to enable a more quantitative reaction (59). However, further small-scale experiments are recommended to derive the minimal amount of acac-CoA needed for a full conversion of apo-AcpM due to the high costs of CoA compounds.

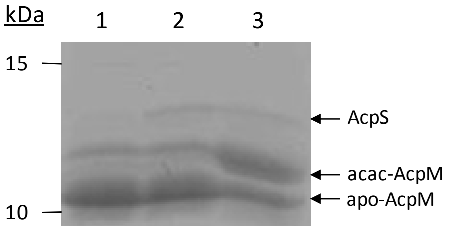

Figure 9-7. Acyl-Phosphopantetheinylation of apo-AcpM. This 18% SDS-PAGE gel section shows apo-AcpM (lane 1), apo-AcpM including AcpS and acac-CoA (lane 2) and the reaction mixture after 1.5 h of incubation (lane 3).

After the reaction, the protein sample was again dialyzed into IEC-buffer A to enable the isolation of acac-AcpM by MonoQ IEC performed as described above. Apo- and acac-AcpM could be separated and eluted with their maxima at approximately 290 mM (25% B) and 320 mM NaCl (28% B), respectively (Figure 9-8). Please note that the peaks corresponding to AcpM-species were shifted towards approximately 100 mM higher NaCl concentrations compared to the initial MonoQ run (Figure 9-6), which indicates that parameters such as temperature, sample composition and column condition might influence the exact elution profiles. Taken together with the findings for saACP (Figure 9-3), ACP-species seem to elute in the range of 200 to 400 mM NaCl (16 to 37% B) using the presented IEC protocol.

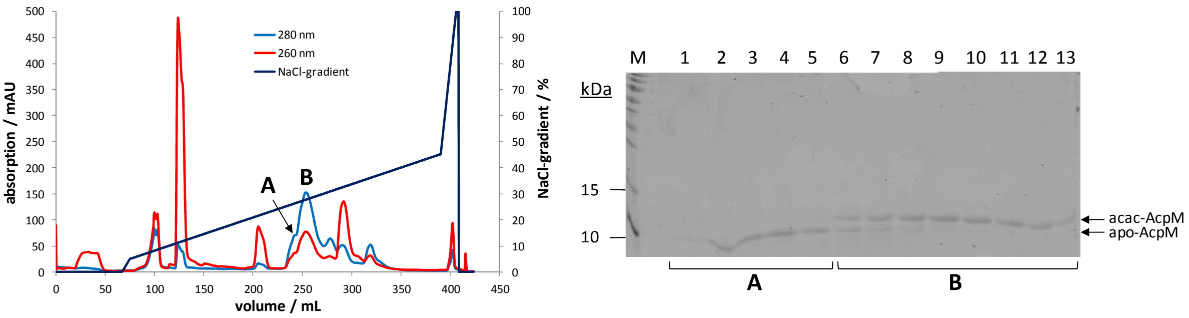

Figure 9-8. Separation of acac-AcpM and apo-AcpM via IEC. Labels A and B indicate those fractions of the 18% SDS-PAGE gel (right) that correspond to peaks A and B of the chromatogram (left). UV-absorption curves are shown at wavelengths of 260 nm (red) and 280 nm (blue). The NaCl-gradient profile is depicted in black. M = marker, PageRuler^{TM} Prestained Protein Ladder from Fermentas.

Fractions corresponding to peak B were pooled and loaded onto a HiLoad 26/60 Superdex 200 prep grade column equilibrated with SEC-buffer (20 mM Tris pH 7.4, 150 mM NaCl, 2 mM EDTA, 10% glycerol). Acac-AcpM eluted as a single peak at a volume of approximately 230 ml (Figure 9-9). Fractions containing relatively pure acac-AcpM were pooled, concentrated to 0.32 mM (0.54 mM determined via the photometric procedure), flash-frozen in liquid nitrogen and stored at - 80 °C.

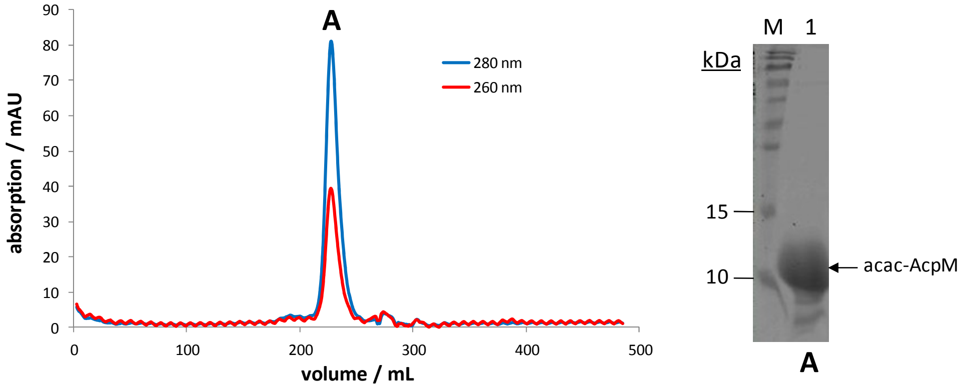

Figure 9-9. Final SEC purification step. The major peak A of the chromatogram (left) contains mainly acac-AcpM as shown by the 18% SDS-PAGE (right; pooled and concentrated peak A fractions). Red and blue curves represent the measured UV-absorption profiles at wavelengths of 260 and 280 nm, respectively. M = marker, PageRuler™ Prestained Protein Ladder from Fermentas.

Acac-AcpM was further analyzed by mass spectrometry (MALDI-TOF, Stony Brook University) indicating a mass of 13,059 Da (highest peak), which is close to the calculated value of 13,047 Da. However, ESI-MS might be better suited to determine the exact mass of the purified AcpM-species (personal communication).

9.3 DNA and Protein Sequences

9.3.1 SaFabI

For all shown sequences, the start and stop codons are underlined (dashed for the original start/stop codon), the His-tag is colored in green and mutations with respect to the reference gene are highlighted in red. The *safabI* gene (*S. aureus* N315, gene ID = 1123686) cloned into a pET16b plasmid (kindly provided by Prof. Peter J. Tonge) was found to have the following DNA base sequence(Seqlab, Goettingen):

ATGGGCCATCATCATCATCATCATCATCATCATCACAGCAGCGGCCATATCGAAGGTCGTCATATGTT
AAATCTTGAAAACAAAACTTATGTCATCATGGGAATCGCTAATAAGCGTAGTATTGCTTTTGGTGTCG
CTAAAGTTTTAGATCAATTAGGTGCTAAATTAGTATTTACTTACCGTAAAGAACGTAGCCGTAAAGAG
CTTGAAAAATTATTAGAACAATTAAATCAACCAGAAGCGCACTTATATCAAATTGATGTTCAAAGCGA
TGAAGAGGTTATTAATGGTTTTGAGCAAATTGGTAAAGATGTTGGCAATATTGATGGTGTATATCATT
CAATCGCATTTGCTAATATGGAAGACTTACGCGGACGCTTTTCTGAAACTTCACGTGAAGGCTTCTTG
TTAGCTCAAGACATTAGTTCTTACTCATTAACAATTGTGGCTCATGAAGCTAAAAAATTAATGCCAGA
AGGTGGTAGCATTGTTGCAACAACATATTTAGGTGGCGAATTCGCAGTTCAAAACTATAATGTGATG
GGTGTTGCTAAAGCGAGCTTAGAAGCAAATGTTAAATATTTAGCATTAGACTTAGGTCCAGATAATA
TTCGCGTTAATGCAATTTCAGCTGGTCCAATCCGTACATTAAGTGCAAAAGGTGTGGGTGGTTTCAAT
ACAATTCTTAAAGAAATCGAAGAGCGTGCACCTTTAAAACGTAATGTTGATCAAGTAGAAGTAGGTA
AAACTGCGGCTTACTTATTAAGTGATTTATCAAGTGGCGTTACAGGTGAAAATATTCATGTAGATAGC
GGATTCCACGCAATTAAATAA

The resulting protein sequence thus is:

MGHHHHHHHHHHSSGHIEGRHMLNLENKTYVIMGIANKRSIAFGVAKVLDQLGAKLVFTYRKERSRKEL
EKLLEQLNQPEAHLYQIDVQSDEEVINGFEQIGKDVGNIDGVYHSIAFANMEDLRGRFSETSREGFLLAQD
ISSYSLTIVAHEAKKLMPEGGSIVATTYLGGEFAVQNYNVMGVAKASLEANVKYLALDLGPDNIRVNAISA
GPIRTLSAKGVGGFNTILKEIEERAPLKRNVDQVEVGKTAAYLLSDLSSGVTGENIHVDSGFHAIK*

The *safabI* gene (*S. aureus* N315, gene ID = 1123686) was cloned into a pETM-11 plasmid (diploma thesis) resulting in the following DNA (Seqlab, Goettingen) and protein sequences:

ATGAAACATCACCATCACCATCACCCCATGAGCGATTACGACATCCCCACTACTGAGAATCTTTATTTT
CAGGGCGCCATGGTAAATCTTGAAAACAAAACTTATGTCATCATGGGAATCGCTAATAAGCGTAGTA
TTGCTTTTGGTGTCGCTAAAGTTTTAGATCAATTAGGTGCTAAATTAGTATTTACTTACCGTAAAGAAC
GTAGCCGTAAAGAGCTTGAAAAATTATTAGAACAATTAAATCAACCAGAAGCGCACTTATATCAAAT
TGATGTTCAAAGCGATGAAGAGGTTATTAATGGTTTTGAGCAAATTGGTAAAGATGTTGGCAATATT
GATGGTGTATATCATTCAATCGCATTTGCTAATATGGAAGACTTACGCGGACGCTTTTCTGAAACTTC
ACGTGAAGGCTTCTTGTTAGCTCAAGACATTAGTTCTTACTCATTAACAATTGTGGCTCATGAAGCTA
AAAAATTAATGCCAGAAGGTGGTAGCATTGTTGCAACAACATATTTAGGTGGCGAATTCGCAGTTCA
AAACTATAATGTGATGGGTGTTGCTAAAGCGAGCTTAGAAGCAAATGTTAAATATTTAGCATTAGAC
TTAGGTCCAGATAATATTCGCGTTAATGCAATTTCAGCTGGTCCAATCCGTACATTAAGTGCAAAAGG
TGTGGGTGGTTTCAATACAATTCTTAAAGAAATCGAAGAGCGTGCACCTTTAAAACGTAATGTTGATC
AAGTAGAAGTAGGTAAAACTGCGGCTTACTTATTAAGTGATTTATCAAGTGGCGTTACAGGTGAAAA
TATTCATGTAGATAGCGGATTCCACGCAATTAAATAA

MKHHHHHHPMSDYDIPTTENLYFQGAMVNLENKTYVIMGIANKRSIAFGVAKVLDQLGAKLVFTYRKER
SRKELEKLLEQLNQPEAHLYQIDVQSDEEVINGFEQIGKDVGNIDGVYHSIAFANMEDLRGRFSETSREGF
LLAQDISSYSLTIVAHEAKKLMPEGGSIVATTYLGGEFAVQNYNVMGVAKASLEANVKYLALDLGPDNIRV
NAISAGPIRTLSAKGVGGFNTILKEIEERAPLKRNVDQVEVGKTAAYLLSDLSSGVTGENIHVDSGFHAIK*

9.3.2 SaACP

The *saacp* gene (*S. aureus* NCTC8325, gene ID = 3919468) cloned into a pET23b plasmid (kindly provided by Prof. Peter J. Tonge) has the following DNA (Seqlab, Goettingen) and protein sequences:

ATGGTGGAAAATTTCGATAAAGTAAAAGATATCATCGTTGACCGTTTAGGTGTAGACGCTGATAAAG
TAACTGAAGATGCATCTTTCAAAGATGATTTAGGCGCTGACTCACTTGATATCGCTGAATTAGTAATG
GAATTAGAAGACGAGTTTGGTACTGAAATCCCTGATGAAGAAGCTGAAAAAATCAACACTGTTGGTG
ATGCTGTTAAATTTATTAACAGTCTTGAAAAACTCGAGCGCCACCACCACCACCATTGA

MVENFDKVKDIIVDRLGVDADKVTEDASFKDDLGADSLDIAELVMELEDEFGTEIPDEEAEKINTVGDAVK
FINSLEKLERHHHHH*

9.3.3 EcFabI

The *ecfabi* gene (*E. coli* BL21 (DE3), gene ID = 8180124) cloned into a pET23b plasmid (kindly provided by Prof. Peter J. Tonge) has the following DNA (Eurofins MWG DNA sequencing) and protein sequences:

ATGGGTTTTCTTTCCGGTAAGCGCATTCTGGTAACCGGTGTTGCCAGCAAACTATCCATCGCCTACGG
TATCGCTCAGGCGATGCACCGCGAAGGAGCTGAACTGGCATTCACCTACCAGAACGACAAACTGAA
AGGCCGCGTAGAAGAATTTGCCGCTCAATTGGGTTCTGACATCGTTCTGCAGTGCGATGTTGCAGAA
GATGCCAGCATCGACACCATGTTCGCTGAACTGGGGAAAGTTTGGCCGAAATTTGACGGTTTCGTAC
ACTCTATTGGTTTTGCACCTGGCGATCAGCTGGATGGTGACTATGTTAACGCCGTTACCCGTGAAGGC
TTCAAAATTGCCCACGACATCAGCTCCTACAGCTTCGTTGCAATGGCAAAAGCTTGCCGCTCCATGCT
GAATCCGGGTTCTGCCCTGCTGACCCTTTCCTACCTTGGCGCTGAGCGCGCTATCCCGAACTACAACG
TTATGGGTCTGGCAAAAGCGTCTCTGGAAGCGAACGTGCGCTATATGGCGAACGCGATGGGTCCGG
AAGGTGTGCGTGTTAACGCCATCTCTGCTGGTCCGATCCGTACTCTGGCGGCTTCCGGTATCAAAGA
CTTCCGCAAAATGCTGGCTCATTGCGAAGCCGTTACCCCGATTCGCCGTACCGTTACTATTGAAGATG
TGGGTAACTCTGCGGCATTCCTGTGCTCCGATCTCTCTGCCGGTATCTCCGGTGAAGTAGTCCACGTT
GACGGCGGTTTCAGCATCGCTGCAATGAACGAACTCGAACTGAAACTCGAGCACCACCACCACCACC
ACTGA

MGFLSGKRILVTGVASKLSIAYGIAQAMHREGAELAFTYQNDKLKGRVEEFAAQLGSDIVLQCDVAEDASI
DTMFAELGKVWPKFDGFVHSIGFAPGDQLDGDYVNAVTREGFKIAHDISSYSFVAMAKACRSMLNPGS
ALLTLSYLGAERAIPNYNVMGLAKASLEANVRYMANAMGPEGVRVNAISAGPIRTLAASGIKDFRKMLA
HCEAVTPIRRTVTIEDVGNSAAFLCSDLSAGISGEVVHVDGGFSIAAMNELELKLEHHHHHH*

9.3.4 KasA

The *kasa* gene (*M. tuberculosis* H37Rv, gene ID = 887269) cloned into a pFPCA1 plasmid (292) (kindly provided by Prof. Peter J. Tonge) has the following DNA (Eurofins MWG DNA sequencing) and protein sequences:

ATGGGCAGCAGCCATCATCATCATCATCACAGCAGCGGCCTGGTGCCGCGCGGCAGCCATATGGCTA
GCGTGAGTCAGCCTTCCACCGCTAATGGCGGTTTCCCCAGCGTTGTGGTGACCGCCGTCACAGCGAC
GACGTCGATCTCGCCGGACATCGAGAGCACGTGGAAGGGTCTGTTGGCCGGCGAGAGCGGCATCCA
CGCACTCGAAGACGAGTTCGTCACCAAGTGGGATCTAGCGGTCAAGATCGGCGGTCACCTCAAGGA
TCCGGTCGACAGCCACATGGGCCGACTCGACATGCGACGCATGTCGTACGTCCAGCGGATGGGCAA
GTTGCTGGGCGGACAGCTATGGGAGTCCGCCGGCAGCCCGGAGGTCGATCCAGACCGGTTCGCCGT
TGTTGTCGGCACCGGTCTAGGTGGAGCCGAGAGGATTGTCGAGAGCTACGACCTGATGAATGCGGG
CGGCCCCCGGAAGGTGTCCCCGCTGGCCGTTCAGATGATCATGCCCAACGGTGCCGCGGCGGTGAT
CGGTCTGCAGCTTGGGGCCCGCGCCGGGGTGATGACCCCGGTGTCGGCCTGTTCGTCGGGCTCGGA
AGCGATCGCCCACGCGTGGCGTCAGATCGTGATGGGCGACGCCGACGTCGCCGTCTGCGGCGGTGT
CGAAGGACCCATCGAGGCGCTGCCCATCGCGGCGTTCTCCATGATGCGGGCCATGTCGACCCGCAAC
GACGAGCCTGAGCGGGCCTCCCGGCCGTTCGACAAGGACCGCGACGGCTTTGTGTTCGGCGAGGCC
GGTGCGCTGATGCTCATCGAGACGGAGGAGCACGCCAAAGCCCGTGGCGCCAAGCCGTTGGCCCGA
TTGCTGGGTGCCGGTATCACCTCGGACGCCTTTCATATGGTGGCGCCCGCGGCCGATGGTGTTCGTG
CCGGTAGGGCGATGACTCGCTCGCTGGAGCTGGCCGGGTTGTCGCCGGCGGACATCGACCACGTCA

ACGCGCACGGCACGGCGACGCCTATCGGCGACGCCGCGGAGGCCAACGCCATCCGCGTCGCCGGTTGTGATCAGGCCGCGGTGTACGCGCCGAAGTCTGCGCTGGGCCACTCGATCGGCGCGGTCGGTGCGCTCGAGTCGGTGCTCACGGTGCTGACGCTGCGCGACGGCGTCATCCCGCCGACCCTGAACTACGAGACACCCGATCCCGAGATCGACCTTGACGTCGTCGCCGGCGAACCGCGCTATGGCGATTACCGCTACGCAGTCAACAACTCGTTCGGGTTCGGCGGCCACAATGTGGCGCTTGCCTTCGGGCGTTACTGA

MGSSHHHHHHSSGLVPRGSHMASVSQPSTANGGFPSVVVTAVTATTSISPDIESTWKGLLAGESGIHALEDEFVTKWDLAVKIGGHLKDPVDSHMGRLDMRRMSYVQRMGKLLGGQLWESAGSPEVDPDRFAVVVGTGLGGAERIVESYDLMNAGGPRKVSPLAVQMIMPNGAAAVIGLQLGARAGVMTPVSACSSGSEAIAHAWRQIVMGDADVAVCGGVEGPIEALPIAAFSMMRAMSTRNDEPERASRPFDKDRDGFVFGEAGALMLIETEEHAKARGAKPLARLLGAGITSDAFHMVAPAADGVRAGRAMTRSLELAGLSPADIDHVNAHGTATPIGDAAEANAIRVAGCDQAAVYAPKSALGHSIGAVGALESVLTVLTLRDGVIPPTLNYETPDPEIDLDVVAGEPRYGDYRYAVNNSFGFGGHNVALAFGRY*

9.3.5 AcpM

The *acpm* gene (*M. tuberculosis* H37Rv, gene ID = 888272) cloned into a pET24b plasmid (kindly provided by Prof. Peter J. Tonge) has the following DNA (Seqlab, Goettingen) and protein sequences:

ATGGTGCCTGTCACTCAGGAAGAAATCATTGCCGGTATCGCCGAGATCATCGAAGAGGTAACCGGTATCGAGCCGTCCGAGATCACCCCGGAGAAGTCGTTCGTCGACGACCTGGACATCGACTCGCTGTCGATGGTCGAGATCGCCGTGCAGACCGAGGACAAGTACGGCGTCAAGATCCCCGACGAGGACCTCGCCGGTCTGCGTACCGTCGGTGACGTTGTCGCCTACATCCAGAAGCTCGAGGAAGAAAACCCGGAGGCGGCTCAGGCGTTGCGCGCGAAGATTGAGTCGGAGAACCCCGATGCCGTTGCCAACGTTCAGGCGAGGCTTGAGGCCGAGTCCAAGTGA

MVPVTQEEIIAGIAEIIEEVTGIEPSEITPEKSFVDDLDIDSLSMVEIAVQTEDKYGVKIPDEDLAGLRTVGDVVAYIQKLEEENPEAAQALRAKIESENPDAVANVQARLEAESK*

10 Acknowledgements

First of all, I would like to express my gratitude to Prof. Caroline Kisker for her excellent guidance and mentoring. Her trust and support enabled me to pursue my research projects into different directions exploring my own scientific interests. In this regard, I would also like to thank my advisor Prof. Christoph A. Sotriffer for his cordial openness, brilliant ideas and the wonderful time in his group. I am also very thankful to Prof. Peter J. Tonge for his scientific input, the realization of new ideas and an unforgettable stay at Stony Brook. The support and knowledge my thesis committee provided was of utmost importance for my scientific development within the last three years.

In addition, I am extremely grateful to many different people because the success of most projects was a highly collaborative achievement. In particular, I would like to express my gratitude to everyone who contributed to the individual manuscripts. Moreover, I thank Dr. Sylvia Luckner and Dr. Maria Hirschbeck who introduced me to basic laboratory techniques and to our research field. I also really learned a lot from Prof. Hermann Schindelin and Dr. Jochen Kuper regarding X-ray crystallography and the experience and expertise of Dr. Petra Hänzelmann and Bodo Sander was extremely valuable during everyday lab life. I would also like to thank Gudrun Michels and Nicole Bader for their indispensable support in the acquisition of several materials. Discussions with Dr. Antje Schäfer and Christin Schäfer facilitated the resolution of expression problems in *M. smegmatis*. I would also like to express my gratitude to Dr. Benjamin Schaefer, Benjamin Merget, Michael Hein, David Zilian and Steffen Wagner for the introduction to several computational approaches, daily support and fruitful discussions. I am very grateful that I had the opportunity to work together with Dr. Andrew Chang and Dr. Kanishk Kapilashrami on these fascinating research topics. The scientific exchange and close cooperation was the fundament for many exciting findings. Furthermore, I thank all people of the working groups of Prof. Kisker, Prof. Schindelin, Prof. Sotriffer and Prof. Tonge for the great working atmosphere and an unforgettable time. In addition, the administrative and IT support provided by Petra Baron, Bernhard Fröhlich and Christian Weinberger was indispensable during my PhD work. I am also grateful to the Graduate School of Life Sciences Würzburg for the excellent structural framework and financial support. In this regard I would like to mention the Collaborative Research Center 630 (SFB 630) providing a very good possibility for scientific exchange in the research field of infectious diseases.

Finally, I would like to thank my parents, family and friends for their enduring support and interest in what I tried to accomplish during my PhD work. I am also incredibly grateful to my wife for her support, understanding, interest and simply that she provided the ideal basis for a time that I would not like to miss.

11 Curriculum Vitae

✉ johannes.schiebel@web.de

EDUCATION

Ph.D. (Dr. rer. nat.) in Life Sciences 2013 (expected)
Department of Structural Biology, University of Würzburg, Germany
Pharmaceutical Chemistry, University of Würzburg

Diploma in Chemistry March 2010
University of Würzburg
Overall grade: very good (with honors)

Intermediate Diploma in Chemistry October 2006
University of Marburg, Germany
Overall grade: very good (1.0)

University-entrance diploma (Abitur) June 2003
Gymnasium Feuchtwangen, Germany
Overall grade: 1.1

RESEARCH EXPERIENCE

Dissertation May 2010 - present
"Structure-Based Drug Design on Enzymes of the Fatty Acid Biosynthesis Pathway"

Supervision: Prof. Dr. Caroline Kisker (University of Würzburg)
Prof. Dr. Christoph A. Sotriffer (University of Würzburg)
Prof. Dr. Peter J. Tonge (Stony Brook University, USA)

Diploma Thesis June 2009 - March 2010
"Structural and Functional Characterization of the Inhibition of an Enoyl-ACP Reductase from *Staphylococcus aureus*"

Supervision: Prof. Dr. Caroline Kisker (University of Würzburg)

PROFESSIONAL EXPERIENCE

Member of the Collaborative Research Center 630 (SFB 630) May 2010 - present
"Recognition, Preparation and Functional Analysis of Agents against Infectious Diseases"

Teaching Assistant October 2008 - February 2009
Institute for Organic Chemistry, University of Würzburg

Civil Servant July 2003 - April 2004
Diakonie Feuchtwangen, Mobile Social Service

FELLOWSHIPS AND AWARDS

Fellow of the Graduate School of Life Sciences, University of Würzburg May 2010 - present
Funded by a grant of the German Excellence Initiative

Poster Awards October 2010, October 2011, November 2012
7th Joint Ph.D. Students Meeting of the SFBs 766, 630 and the FOR 854
6th International Symposium of the Graduate School of Life Sciences
Retreat of the Rudolf Virchow Center 2010

Faculty Award 2009/2010 July 2010
Faculty of Chemistry and Pharmacy, University of Würzburg

Fellow of the "Studienstiftung des Deutschen Volkes" November 2004 - March 2010
Funded by the German Federation

QUALIFICATIONS

Workshop Participations within the Graduate School of Life Sciences and through the "Studienstiftung des Deutschen Volkes" 2005 - present
Writing for Publication, Giving Academic Talks, Poster Design
Basic Italian Language Course (Rome, Italy)
"Genes & Genomes", "Diabetes mellitus", "Oceans and Climate Change"

Languages
German (native)
English (fluent)

VOLUNTARY SERVICE

Social Work 1997 - 2000, 2007 and 2010
Dürrwangen and Marburg, Germany
Organization and supervision of activities for child- and youth-groups

Environmental Work March 2007 - May 2007
Wallnau/Fehmarn, Germany
Public relations and maintenance of a nature reserve for water birds

Würzburg, 07/24/13
Place, Date *Signature*

12 List of Publications

Chang, A.*, **Schiebel, J.***, Yu, W., Bommineni, G. R., Pan, P., Baxter, M. V., Khanna, A., Sotriffer, C. A., Kisker, C., and Tonge, P. J. (2013) Rational Optimization of Drug-Target Residence Time: Insights from Inhibitor Binding to the *Staphylococcus aureus* FabI Enzyme-Product Complex. *Biochemistry* **52**, 4217-4228

Schiebel, J.*, Chang, A.*, Lu, H., Baxter, M. V., Tonge, P. J., and Kisker, C. (2012) *Staphylococcus aureus* FabI: Inhibition, Substrate Recognition, and Potential Implications for In Vivo Essentiality. *Structure* **20**, 802-813

Topf, C. M., **Schiebel, J.**, Kisker, C., and Holzgrabe, U. (2012) Von alten und neuen antimykobakteriellen Wirkstoffen - Die Fettsäuresynthese als Angriffspunkt. *Pharm Unserer Zeit* **41**, 64-70

Schiebel, J.*, Chang, A.*, Shah, S., Lu, Y., Liu, L., Pan, P., Hirschbeck, M. W., Tareilus, M., Eltschkner, S., Cummings, J. E., Knudson, S. E., Bommineni, G. R., Yu, W., Walker, S. G., Slayden, R. A., Sotriffer, C. A., Tonge, P. J., and Kisker, C. (in preparation) Molecular Basis for the Narrow-spectrum Activity of the Clinical Candidate CG400549 and the Rational Design of a Potent Broad-spectrum Pyridone-based FabI Inhibitor.

Schiebel, J., Chang, A., Merget, B., Bommineni, G. R., Yu, W., Spagnuolo, L. A., Baxter, M. V., Tareilus, M., Tonge, P. J., Kisker, C., and Sotriffer, C. A. (in preparation) Protons and Hydrides - Wherefrom and Whereto: From a Chemical Binding Pocket Analysis to a Biological Substrate Recognition Process.

Schiebel, J., Kapilashrami, K., Fekete, A., Bommineni, G. R., Schaefer, C. M., Mueller, M. J., Tonge, P. J., and Kisker, C. (in preparation) Acyl Channel Opening Reveals How the Condensing Enzyme KasA from *Mycobacterium tuberculosis* Recognizes Mycolic Acid Precursors.

Chang, A., Kapilashrami, K., Lu, Y., **Schiebel, J.**, Yu, W., Bommineni, G. R., Pan, P., Spagnuolo, L., Shah, S., Baxter, M. V., Tareilus, M., Kisker, C., Walker, S., Tonge, P. J. (in preparation) Drug-target Kinetics and Prolonged Antimicrobial Effects: Impact of Target Vulnerability and Turnover in Fatty Acid Biosynthesis and Core Metabolic Pathways.

*These authors contributed equally

13 Affidavit

I hereby confirm that my thesis entitled "Structure-Based Drug Design on Enzymes of the Fatty Acid Biosynthesis Pathway" is the result of my own work. I did not receive any help or support from commercial consultants. All sources and / or materials applied are listed and specified in the thesis.

Furthermore, I confirm that this thesis has not yet been submitted as part of another examination process neither in identical nor in similar form.

Würzburg, 07/24/13

Place, Date *Signature*

14 Eidesstattliche Erklärung

Hiermit erkläre ich an Eides statt, die Dissertation „Strukturbasiertes Wirkstoffdesign an Enzymen der Fettsäurebiosynthese“ eigenständig, d.h. insbesondere selbständig und ohne Hilfe eines kommerziellen Promotionsberaters, angefertigt und keine anderen als die von mir angegebenen Quellen und Hilfsmittel verwendet zu haben.

Ich erkläre außerdem, dass die Dissertation weder in gleicher noch in ähnlicher Form bereits in einem anderen Prüfungsverfahren vorgelegen hat.

Würzburg, den 24.07.2013

Ort, Datum *Unterschrift*